Universidade do Minho
Escola de Engenharia

Ricardo Jorge Brito Gonçalves Pereira

A new generation of microfluidic platforms based on smart and multifunctional materials

janeiro de 2023

A new generation of microfluidic platforms based on smart and multifunctional materials

Ricardo Jorge Brito Gonçalves Pereira

UMinho | 2023

Universidade do Minho
Escola de Engenharia

A new generation of microfluidic platforms based on smart and multifunctional materials

Ricardo Jorge Brito Gonçalves Pereira

Tese de Doutoramento
Engenharia de Materiais

Trabalho efetuado sob a orientação de
Doutora Vanessa Fernandes Cardoso
Professor Senentxu Lanceros-Méndez

janeiro de 2023

DIREITOS DE AUTOR E CONDIÇÕES DE UTILIZAÇÃO DO TRABALHO POR TERCEIROS

ACKNOWLEDGEMENTS

The completion of my dissertation was the product of extensive labor, hours of research, and reflection, all of which led to the achievement of this objective. However, in order to complete my project, I required the personal and professional accompaniment, assistance, and support of others. First, I want to thank the support of the Foundation for Science and Technology-FCT (grant SFRH/BD/140698/2018).

I would like to thank my supervisors, Dr Vanessa Cardoso and Professor Senentxu Lanceros-Mendez, for accepting the guidance of this project. I also thank you both, for your scientific knowledge, as well as your support, effort, availability and friendliness during these years.

A special thanks to my friends, André, Clarisse, Costa and Pedro, which were essential in the good and the bad times; they were always present to help me, even when the things appeared difficult, sometimes with real big gestures, sometimes with just a friendly word of encouragement, that made the difference.

I also thank the ESM research group for their support and welcome, which has always allowed me to develop my work, in the best way.

This work was partly made of trips and scientific stays, I would like to thank Professor Catherine Klapperich and her group at Boston University, for the great experience with them, it were unforgettable times, that I miss and cherish. I would also like to thank Professor Gerardo Hernandez, for the reception in the beautiful Heidelberg, at the Karlsruhe Institute of Technology, I learned a lot scientifically, I gained friends and experiences that I will keep forever.

I would also like to thank David Durán and his supervisors at the Centro de Cirugía de Mínima Invasión Jesús Usón, in Caceres, for the fantastic work and experience that we have developed together, which has allowed me to greatly expand my knowledge. Finally, I would like to thank BCMaterials, in Bilbao, for the support in the various works carried out and for the always very kind reception in the various visits made throughout the PhD.

I would like to leave a very special thanks to Paulina, we both started and finished this step, we went through its difficulties and ended up overcoming it, with total affection and unconditional support.

To my family, thank you from the bottom of my heart! Mom you are the best and I will never be able to thank you, for everything you do for me.

STATEMENT OF INTEGRITY

I hereby declare having conducted this academic work with integrity. I confirm that I have not used plagiarism or any form of undue use of information or falsification of results along the process leading to its elaboration.

I further declare that I have fully acknowledged the Code of Ethical Conduct of the University of Minho.

Abstract

A precise diagnostic is a key part of the clinical practice as it is essential to provide a correct clinical decision-making for both health professionals and policy makers in terms of public health. In this respect, the primary goal of this project is to develop new solutions that take advantage of the beneficial qualities of Portable Analytical Devices (PADs) and the microfluidic paper-based analytical devices (μPADS), while addressing their technological limitations such as the uncontrolled passive flow rate, the weak mechanical properties or the lack of simple functional reactions, that have a significant impact on their potential to achieve real-life applications and commercialization. To achieve such objective, different polymer-based substrates have been developed, characterized and tested for the printing of PADs and different fillers have been added to printable waxes aiming to induce multifunctionality on the PADs. In this context, poly(l-lactic acid) (PLLA), poly(vinylidene fluoride-*co*-trifluorethylene) (P(VDF-TrFE)), poly(D,L-lactic- *co*-glycolide) (PDLG), silk and silk fibroin, were processed in different morphologies. Each substrate revealed characteristics of great interest, such as the maximum capillary flow rate of PLLA oriented fiber substrates (70.2 ± 1.9 mm.min^{-1}), the high mechanical strength of P(VDF-TrFE) substrates (ranging from 71.4 ± 2.9 to 163.4 ± 5.1 MPa), the rapid degradation rate of PDLG (≈90 % weight loss in six weeks), or the stability of silk-based substrates which are capable of maintaining high accuracy after three utilizations, using different analytes (albumin, uric acid and glucose), with an minimum R^2 of 0.967.

The next objective of this project was to increase the versatility of the wax printing technique in terms of functional materials. Three different types of hydrophobic wax-based inks have been developed: magnetic, dielectric and conductive. Magnetic waxes (with Fe_3O_4 nanoparticles) exhibited an actuation capability with a deformation of ≈12 mm when a magnetic field of 105 mT was applied, and an energy harvesting aptitude with an energy density of about 9.7 mW.cm^{-3}. Active waxes with dielectric properties (with $BaTiO_3$ nanoparticles), exhibited optimized dielectric properties up to ε= 18 at 10 kHz. Conductive waxes (with carbon nanotubes and graphene) exhibited high electrical conductivity values (up to ≈ 2.5×10^{-4} S.m^{-1}), high gauge factor (up to 11), and a pressure sensitivity of (up to 0.17 MPa^{-1}).

In order to demonstrate the technological significance of the produced materials, two μPADS systems have been developed: i) a magnetic origami system completely printed on paper suitable for the detection of infectious diseases and magnetic biomarkers; and ii) a low-power thermal actuation system, based on the printing of conductive wax composites with integrated graphene nanoplatelets (GNP), that was able to work simultaneously as a barrier and as a heater. Thus the materials developed in this thesis hold great promise for the next generation of versatile, effective and accurate PADs and μPADS.

Keywords: Microfluidic; Multifunctional waxes; Point-of-care; Polymer-based substrates

Resumo

Um diagnóstico preciso é uma parte essencial da prática clínica uma vez que é crucial para uma correta tomada de decisão quer por parte profissionais de saúde quer pelos decisores políticos em termos de políticos de saúde pública.

O principal objetivo deste projeto foi o desenvolver novas soluções que aproveitassem, em simultâneo, as mais valias dos dispositivos analíticos portáteis (PADs) e dos dispositivos microfluídicos analíticos baseados em papel (μPADS), enquanto se procurava solucionar também as suas limitações tecnológicas como a sua taxa de fluxo passivo não controlada, as fracas propriedades mecânicas e a falta de reações funcionais, uma vez que todas estas limitações têm um impacto negativo na sua aplicabilidade/comercialização. Para alcançar este objetivo, foram desenvolvidos diferentes materiais de base polimérica e testados diversos reforços (promotores de multifuncionalidade). Nesse sentido foram usados o poli(L–ácido láctico) (PLLA), o poli(fluoreto de vinilideno – trifluoretileno) (P(VDF-TrFE)), o poli(D,L-láctico-co-glicólido) (PDLG) e a fibroína de seda com diferentes morfologias. Cada substrato polimérico evidenciou características de elevado interesse, tais como a velocidade e fluxo capilar dos substratos de fibras orientadas de PLLA (70.2 ± 1.9 $mm.min^{-1}$), a elevada resistência mecânica dos substratos de P(VDF-TRFE) quando molhados (de 71.4 ± 2.9 até 163.4 ± 5.1 MPa), a rápida taxa de degradação do substratos de PDLG, cerca de 90 % em seis semanas, e a elevada estabilidade da seda com a capacidade de manter uma elevada precisão após três utilizações, em diferentes reagentes (albumina, acido úrico e glucose), com um R^2 de 0.967. Outro dos objetivos deste trabalho foi o de aumentar as soluções proporcionadas pela técnica de impressão a cera utilizada no fabrico dos μPADs, tendo sido desenvolvidas ceras com propriedades magnéticas, dielétricas e condutoras. As ceras magnéticas (com a adição de nanopartículas de Fe_3O_4) evidenciaram uma boa capacidade de atuação (12 mm quando aplicado um campo de 105 mT) e uma elevada capacidade de recolha energética (cerca de 9.7 $mW.cm^{-3}$); as ceras ativas dielétricas (com a adição de nanopartículas de $BaTiO_3$) exibiram uma resposta dieléctrica optimizada (ε=18 a 10 kHz); e as ceras condutoras (com nanotubos de carbono e grafeno) mostraram uma elevada condutividade elétrica (até ≈2.5×10^{-4} $S.m^{-1}$), um *gauge factor* (GF) de 11 e uma pressão de sensibilidade (PS) de 0.17 MPa^{-1}.

Por fim e para demonstrar a aplicabilidade dos materiais desenvolvidos, foram desenvolvidas dois μPADS: i) um origami magnético totalmente impresso em papel para deteção de doenças infeciosas e biomarcadores magnéticos; e ii)

um sistema de aquecimento em papel, baseado na impressão de compósitos hidrofóbicos multifuncionais com nano-folhas de grafeno (GNP) integradas na matriz de cera. Os resultados deste projeto demonstram que os materiais desenvolvidos nesta tese poderão ser usados numa próxima geração de PADs e μPADs: versáteis, eficazes, e com elevada precisão.

Palavras chave: Ceras multifuncionais; Microfluídica; *Point-of-care*; Substratos de base polimérica

Index

List of Figures

List of tables

List of symbols

a	Distance between bending points
A	Electrode area
Bm	Magnetic field
C	Capacity
d	Thickness
d_{33}	Piezoelectric coefficient
ε	Electrical resistivity
ε_0	Vacuum permittivity
ε'	Real part of dielectric constant
ε_{break}	Stain-to-Failure
ε_{exp}	Experimental data measured
ε_{mod}	Predicted dielectric constant
εp	Porosity
εt	Strain
f	Frequency
F_β	β-phase content
G'	Storage modulus
G''	Loss modulus
GF	Gauge factor
HAC	Amplitude of the alternating current magnetic field
I	Current
Id	Mechanical displacement
It	Sample thickness
K_α	Absorption coefficient of α-PVDF
K_β	Absorption coefficient of β-PVDF
L	Distance between electrodes
M_{sat}	Magnetic saturation
pc	Percolation threshold
p	Filler content

P	Applied pressure
P_0	Harvested Power
PS	Compression applied
r	Surface electrical resistivity
R	Electrical resistance
Rl	Load resistance
R_0	Initial resistance
s	Universal critical exponent
t	Thickness of the piezoelectric layer
tan δ	Dielectric loss
tg	Storage modulus
Tm	Melting temperature
V	Voltage
ω	Angular frequency
wt.%	Weight percentage
Xc	Degree of crystallinity
Y	Young's modulus
Z	Vertical displacement
α_{33}	Transverse magnetoelectric voltage coefficient
ΔH_f	Melting enthalpy
ΔR	Electrical resistance variation
ΔV	Output voltage
σ	Electrical conductivity
σs	Stress
σ_0	Filler conductivity
σ_{break}	Ultimate tensile strength
δr	Relative percentage deviation

List of abbreviations

A

ATR Attenuated total reflection

ASSURED Affordable, Sensitive, Specific, User-friendly, Rapid and robust, Equipment-free and Deliverable to end-users

B

BM Basal medium

BSA Bovine serum albumin

BT Barium Titanate

C

CA Contact angle

CFO $CoFe_2O_4$

D

DAPI 4',6-diamidino-2-phenylindole

DLS Dynamic light scattering

DM Differentiation medium

DMEM Dulbecco's modified eagle's medium

DMF N, N-dimethylformamide

DMSO Dimethyl sulfoxide

DNA Deoxyribonucleic acid

DSC Differential scanning calorimetry

DTG Differential thermogravimetric

E

ECM Extracellular matrix

EDX Energy-dispersive X-ray spectroscopy

F

FBS Fetal bovine Serum

FDA Food and Drug Administration

FITC Phalloidin fluorescein isothiocyanate

FTIR Fourier transformed infrared spectroscopy

G

GDP Gross domestic product

GNP Graphene nanoplatelets

GO Graphene oxide

I

IoT Internet of things

ITU International Telecommunications Union

M

ME Magnetoelectric

MHC Myosin heavy chain

MOPAS Magnetic origami portable analytical system

MSNPs Mesoporous silica nanoparticles

MTS (3(4,5 dimethylthiazol 2 yl)5(3carboxymethoxyphenyl)2(4 sulfophenyl)-2H-tetrazolium)

MTT 3-(4,5-Dimethylthiazol-2-yl)-2,5-diphenyltetrazolium bromide

MWCNTs Multi-walled carbon nanotubes

N

NIPS Non-solvent induced phase separation

NMR Nuclear magnetic resonance

NdFeB Neodymium iron boron

O

O-ES Oriented electrospun fibre mats

P

P/S Penicillin/Streptomycin

PADs Portable analytical devices

PANI Poly(aniline)

PBS Phosphate Buffer Solution

PDI Perylenediimide derivative

PDMS Polydimethylsiloxane

PDLG Poly(D,L-lactide-co-glycolide)

PET Polyethylene terephthalate

PHBV Poly(3-hydroxybutyrate-co-3-hydroxyvalerate)

PGA Poly(glycolic acid)

PLLA Poly(L-lactic acid)

PLGA Poly(lactic-co-glycolic acid)

PMMA Polymethyl methacrylate

POC Point-of-care

PVC Polyvinyl polychloride

PVDF Poly(vinylidene fluoride)

P(VDF-TrFE) Poly(vinylidene fluoride-co-trifluoroethylene)

R

rGO Reduced graphene oxide

RNA Ribonucleic acid

RT-LAMP Reverse transcription loop-mediated isothermal amplification

RO-ES Randomly oriented electrospun fibre mats

S

SD Standard deviation

S.E.M. Standard error of the mean

SEM Scanning electron microscope

SERS Surface-enhanced raman scattering

SiNPs Silica nanoparticles

T

TE Tissue engineering

TEM Transmission electron microscopy

TIPS Temperature-induced phase separation

TGA Thermogravimetric analysis

V

VSM Vibrating sample magnetometer

W

W Wax

WHO World Health Organization

μ

μPADs Microfluidic paper analytical devices

Chapter 1. Introduction

1.1. Introduction

Global health is defined by the ability to provide equitable health care to all people worldwide [1,2]. However, access to health care and proper diagnostic tools is extremely unequal throughout the various regions of the planet.

This inequality is particularly evident in developing countries, as less than half of the population of Africa has access to modern health facilities. Many African countries spend less than a tenth of their gross domestic product (GDP) on their health care systems. Furthermore, there is a shortage of trained health care professionals and it is challenging to offer access to efficient diagnostic tools in developing countries, due to the lack of infrastructures that in the first phase allows making an effective clinical diagnosis and then to properly treat the population [3,4].

Therefore, it is urgent to develop diagnostic techniques, which allow to act quickly and without resorting to complex processes, representing a first approach to a patient's health problem [3].

New technologies could change how health care is provided in these areas, improving health care for people in remote areas. Similarly, easier access to reliable data helps both physicians and policymakers to make better-informed decisions about how to improve health services that can lead to changes in patient care towards more positive outcomes and improved cost-effectiveness for the health system [4].

Consequently, a mass implementation policy of portable analytical devices (PADs) in the medical field, in remote areas is needed, once it can be an essential component of medical systems in resource-limited locations where health care, transportation, and infrastructures are suboptimal. With PADs it is possible to cover the diagnostic or laboratory testing performed via health care services provided near or at the patient's location. For rapid results and can be easily implemented in remote settings that lack laboratory networks, thus allowing fast diagnosis and prompter treatment. In fact, they can be implemented in a variety of different locations such as homes, pharmacies, clinics, workplaces, ambulances, rural and remote hospitals or health clinics [5]. Moreover, diagnostic evaluation without the dependence on laboratory infrastructures avoids the logistics of complex sample transportation, strongly reducing handling times. Further, it comprises reasonably cheap, modest, hand-held tools that do not involve extensive training.

PADs have great importance in developing countries, but they are also progressively more applied in developed countries, as their successful implementation has been proven to be cost-effective and takes pressure away from the health care system [5].

Regarding the most recent scientific developments in this field, in the last decade an effort has been carried out to develop new technologies for diagnostic tools based on less expensive and complex processes [6].

PADs represent a promising platform for the development of fast, portable, disposable and cost-effective analytical tools not just for the medical field but also in other areas such as environmental monitoring and food safety, among others [7, 8]. Microfluidic paper analytical devices (μPADs) were first introduced in 2007 as an alternative to silicon, glass and polydimethylsiloxane (PDMS) materials, commonly used for prototyping and proof-of-concept studies [10]. Paper is typically made of cellulose fibres and has the advantage of being inexpensive, ubiquitous, biocompatible and scalable production-wise. In addition, cellulose's hydrophilicity, combined with patterned hydrophobic microfluidic barriers to create channels, allow samples to be guided via capillary flow from an inlet to a defined reaction place for subsequent analysis [10, 11]. Furthermore, the motivation behind the development of the μPADs and is supported by their potential to address the ASSURED (Affordable, Sensitive, Specific, User-friendly, Rapid and robust, Equipment-free and Deliverable to end-users) criteria for their development is defined by the World Health Organization (WHO), enabling local communities in developing regions to improve health care, environmental safety, animal health and food quality [9].

Nonetheless, although extensive academic developments, the use of PADs and μPADs in real-world applications is still relatively limited. This discrepancy may be related to the limited grade and properties of commercially available materials, including paper substrates with low storage stability, poor mechanical strength when wetted, and low control of fluid flow, as well as limited functional integrated tools (e.g, optical sensors, pressure sensors, micropumps, microvalves, heaters, or temperature sensors, among others). In this sense, various strategies have been developed for analyte control and manipulation (e.g. filtering, mixing, heating, separation, dilution) by using and/or integrating, for example, functional novel components into PADs and μPADs, such as diode valves, dissolvable sugar barriers and external electromagnets [11, 12].

Furthermore, there have been attempts to control the flow by tailoring the channels design, guiding the fluids either vertically or laterally through paper sheets using materials such as threads and yarns. However, the reported strategies have some limitations regarding their production, as they require specialized equipment for mass production [11].

Therefore, the commercialization of PADs and μPADs is noticeably lagging while the aforementioned problems remain unsolved, and this type of device may provide new solutions for more effective analysis with proper flow control [10, 13]. Thus, the development of new alternatives to devices based merely on

paper becomes essential, in order to combine proper absorption and flow rate with the ability to integrate materials that allow new responses, improved flow control and to allow analysis methods applicable in practical contexts and under a large variety of conditions [14].

This PhD thesis aims to address those issues by developing alternative materials with improved properties to both complement and replace paper. Natural and synthetic polymers featuring controlled physicochemical properties were developed to be used as novel microfluidic substrates with enhanced and even new and tailorable properties [15]. Concurrently, hydrophobic components are required to define the channels and confine the fluid flow within the hydrophilic substrates. In this context, multifunctional waxes, including magnetic, dielectric and conductive, were also developed as an alternative to the commercially passive materials used in printing technologies.

This work represents a contribution to the transition of PADs and μPADs from the laboratory into the user's hands, presenting the development of simple and low-cost systems, with integrated active characteristics, that can be produced in existing mass production facilities, allowing to accelerate their successful commercialization.

1.2. Microfluidics

The behaviour, precise control, and manipulation of fluids that are geometrically restricted to a tiny scale (usually sub-millimeter) at which surface forces dominate volumetric forces is referred as microfluidics [16].

Microfluidics is an interdisciplinary field that connects fluid dynamics, physics, and chemistry, among others [16]. The first advances in this technology were introduced around the 1950s. Particle separation and analysis techniques, such as gas and liquid chromatography were optimized in this period [17, 18]. It was discovered that with a reduction in channel size, it was possible to achieve better particle separation. Years later, the technique of capillary electrophoresis emerged to replace the initial techniques. It consists in the use of an agarose gel for the separation of electrically charged particles [19].

With the advances in microanalytical methods, the interest in combining them with microfluidic platforms also emerged. Another factor that contributed to the substantial advances in microfluidics was the need of the United States of America (USA) government to develop advanced defense programs, around the 1990s (the end of the Cold War) [16, 20]. One of the areas explored by this program was the development of microfluidic devices capable of detecting potential chemical and biological threats.

The last, but perhaps the most important factor in the progress of this technological area was the emergence of microelectronics. Associated with this area appeared lab-on-a-chip [21] and organ-on-a-chip [22] applications, small devices capable of incorporating various laboratory or biological functions into one single system [23]. Early applications of microfluidics arose associated with analyte separation and analysis due to the inherent advantages of miniaturization, including but not limited to the small amounts of sample and reagents required, short analysis times, the ability to integrate several components in one device and their low cost [21, 24].

Among the various specific characteristics of microfluidics systems, some prove to be of great importance for biomedical research. They will be discussed in the next sub-chapters.

1.2.1. Diminutive reagent utilization

A clear advantage of microfluidic devices when compared to other alternatives is that small volumes of reagents are required due to their typically small-scale channel in the micro- or even nanometer sizes. This advantage presents great significance when high-cost reagents, which requires complex processes of isolation and purification, are to be used [25, 26], or samples are limited in availability.

1.2.2. High surface to volume ratio

Associated with low reagent consumption arises the advantage of the extremely high surface to volume ratios provided by microfluidics systems. It allows fast mass and heat transfer, which is essential for several applications, as it is the case of biotransformation, selective temperature reactions and nano- and microparticle separation [26, 27].

1.2.3. High-throughput applications

With low working volumes and the capability to parallelize the reaction areas, these systems are suitable for high-throughput applications. Unlike conventional methods such as fluorescent activated cell sorting, microfluidic devices have outstanding capabilities for high parallelization reactions due to their reduced dimensions. Thus, a large amount of simultaneous experiments can be performed in a small system and provide proper statistically sound conclusions from a single run [29].

1.2.4. Portable systems

One of the main objectives of the development of microfluidics was to build a device that integrates all the instrumentation and the analysis capabilities of a laboratory in hand-held size to deliver a fully portable system. Reduced dimensions allow, to a certain extent, experiments at different locations of interest for true POC testing [30].

1.3. Conventional materials to fabricate microfluidic devices

One of the most important parameters to consider before developing a microfluidic system is the selection of the materials. Each material has certain characteristics as well as associated manufacturing techniques that influence the performance and price of each device. The most relevant will be described in the next sub-chapters along with their main advantages and limitations.

1.3.1. Silicon and glass

The first materials used in this area were silicon and glass which are usually processed by manufacturing techniques well known in the semiconductor industry such as bulk micromachining using chemical corrosion and dry corrosion, or surface micromachining [31]. Bulk micromachining produces structures within the substrate by selectively corroding it using photolithography to transfer a pattern from a mask to the surface. In turn, surface micromachining creates structures on top of the substrate, meaning that thin layers of silicon are deposited successively using chemical deposition techniques [31].

While silicon is transparent to infrared light but not to visible light, glass is optically transparent in the visible spectral range. Interesting properties of silicon and glass come from their high thermal and chemical stability. Also, like silicon, the chemical modifications of glass are based on silanol, allowing chemical surface modifications for specific applications [32]. However, the hardness of silicon and glass, its high cost and time to manufacture, as well as the difficulty in sealing the microfluidic structure and the integration of functional units, together with the non-permeability of gases, preclude its use in many applications [32].

Consequently, the development of microfluidic systems using other materials that can be easily manufactured and that are compatible with a wider range of applications has become a necessity [32].

1.3.2. Polymers

Polymer-based microfluidic systems are an interesting alternative because they are mostly inexpensive, easily mass-produced and chemically modifiable. An added benefit is the wide range of polymers available that offers great flexibility in the selection of materials with specific properties. According to their physical properties, polymers can be classified into thermosetting, thermoplastics and elastomers [33].

Heat-hardeners such as SU-8 resin are usually stable even at high temperatures, resistant to most solvents, biocompatible and show optical transparency and good mechanical properties [34]. SU-8 allows the manufacture of microstructures with a high height/width ratio using photolithography. When properly heated and exposed to ultraviolet light of a specific wavelength using inverse pattern high resolution photomasks, the unexposed parts, unlike the exposed parts, are soluble and thus removed after the process [34, 35]. SU-8 has been used directly as a structural material for the manufacture of functional units (such as electromechanical systems) and often as a template for the manufacture of PDMS based microfluidic systems, the most popular elastomer used for microfluidics [33].

During the process called replica molding, PDMS is poured into a thermally cured mold (at a temperature ranging from 40 to 100 °C) and easily peeled off due to its low surface tension. To seal open microfluidic channels, PDMS can be reversibly bonded to PDMS, glass or other substrates by simple contact or irreversibly using oxygen plasma surface treatments or a thin layer of uncoated PDMS as glue [20]. PDMS shows very interesting properties for the manufacture of functional units (such as valves and pumps) and/or for biotechnological applications because of its biocompatibility, high elasticity and low cost or for being a gas permeable porous matrix [36, 37]. However, nonspecific binding of hydrophobic molecules to the channel walls due to the high hydrophobicity of the PDMS surface along with the evaporation of water through the channels can cause a change in fluid concentration and composition. Several strategies, such as chemical surface modification or the use of continuous flows can be approached to overcome these limitations.

With respect to thermoplastics, due to their wide use in the industry, their thermoforming processing is very well established [35]. In this case, thousands of structures can be produced at a high rate and low-cost using metal or silicon molds and high temperatures. However, the manufacturing of this type of mold is time consuming and expensive and is therefore not widely used in research and prototyping [35].

Typical approaches to seal microchannels include high temperature bonding and glue [38]. Thermoplastics have the ability to be remodeled several times after reheating. Polymethyl methacrylate (PMMA), polystyrene, polyethylene terephthalate (PET) and polyvinyl polychloride (PVC) are typical thermoplastics used in the manufacturing of microfluidic systems [39]. Although these materials show

slightly better solvent compatibility than PDMS, they have poor gas permeability and their rigidity makes them difficult to manufacture as functional units.

In turn, although their melting temperatures are high (above 280 °C), perfluorinated polymers such as perfluoroalkoxy alkane (known as Teflon PFA) and polytetrafluoroethylene (known as Teflon PTFE) show good gas permeability, sufficient elasticity to make functional units, they are chemically inert to solvents and chemicals, they show low adsorption of non-specific proteins compared to PDMS and they have good cellular biocompatibility and good optical transparency [40]. Despite the positive characteristics presented above, their expensiveness and complex manufacturing methods are a barrier to their implementation and commercialization of devices. This becomes even more evident for applications that require disposable systems to avoid sample contamination and allow for *in situ* measurements [41].

As a result of these aspects, it has been a need to implement other materials with simpler, less expensive manufacturing processes that can be used by anyone, anywhere.

1.3.3. Paper

Cellulose is a linear polymer constituted of D-glucose units linked by β-(1,4) glycosidic bonds [42]. It is a renewable polymer, produced by trees, plants and some non-pathogenic bacteria, and is available at low-cost around the world [42]. It has a number of characteristics that makes it particularly attractive for the development of microfluidic devices, particularly for diagnostics and monitoring of pathologies [43].

Coupled with the advantage of a rapid, low-cost production process, the microstructure of paper itself is a huge benefit. Its porous structure allows not only filtering (depending on pore size, particle separation is possible), but even more importantly, to passively generate flows through the capillarity phenomenon causing the fluid to move without the need for external pumps or pressure [44].

Among the several commercially available papers, one of the most 3 used in this area is Whatman filter paper no.1 [45], having a structure consisting of non-oriented flattened fibers. Currently, other types of substrates developed especially for the microfluidic industry can be found. Millipore's Hi-Flow Plus membranes comprise several substrates with slightly different pore size structures. Two examples are the HF075, which filters out entities with a size of 500 μm or larger, and HP180 which filters out entities 400 μm or larger.

In addition to the characteristics presented above, paper has high biocompatibility and stability [44,46]. As a white material, it offers the necessary contrast for colorimetric detection methods. By combining these properties, it is possible to manufacture simple, portable, economic and highly efficient devices that

allow different biomedical applications [46]. It is thus easy to comprehend why there are several currently marketed microfluidic systems based on this raw material such as pregnancy tests [47] or for measuring the amount of glucose in blood [48], for detecting diseases such as malaria [49] or human immunodeficiency viruses [50], which are commercially available and implemented in our daily lives.

Despite all positive arguments regarding the use of this material for microfluidic systems, it is important to reinforce that these paper substrates serve just as a support material and do not allow any manipulation of the fluid. Besides that, paper has some inherent physical properties that cannot be precisely controlled, such as pore size, porosity, surface area, wettability, permeability and capillary flow rate, parameters that affect the performance of the device regarding fluid flow, color uniformity, and reagent immobilization [51].

Consequently, there is an interest in exploring and introducing new active materials for microfluidic applications.

1.3.4. Smart and bio-based polymers

A smart or active polymer is one that alters, significantly and selectively, one or more properties when an external stimulus such as a change in pH or temperature or when an electric or magnetic field is applied. Within this group, piezoelectric polymers are particularly interesting. They are capable of generating electrical signals by applying a mechanical force (direct piezoelectric effect) and undergoing mechanical deformation when subjected to an electric field (inverse piezoelectric effect) [52, 53]. The direct piezoelectric effect is typically used in sensor applications, while the inverse piezoelectric effect is used in actuator applications [54]. In conjunction with the active properties of smart polymer-based materials, they can be processed in various forms depending on the manufacturing method.

In fact, spheres and fibers can be obtained using electrospinning (Figure 1.1a), while porous films can be obtained by temperature-induced phase separation (TIPS) (Figure 1.1b) [54]. Hence, substrates can be processed with structures and morphologies similar to paper substrates.

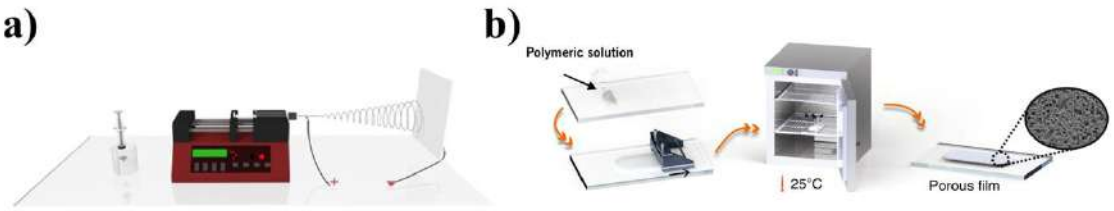

Figure 1.1. a) Schematic representation of electrospinning technique; b) Schematic representation of the preparation of porous films by TIPS [54].

However, synthetic polymers such as poly(L-lactic acid) (PLLA), polyvinylidene fluoride (PVDF), poly(3-hydroxybutyrate-co-3-hydroxyvalerate) (PHVB) or poly(D,L-lactide-co-glycolide) (PDLG) or even natural polymers such as silk fibroin show a highly hydrophobic nature, hampering their direct use as substrates for microfluidic applications. To overcome this limitation, approaches such as introducing hydrophilic entities (such as zeolites) into the polymer matrix, hydrolysis or plasma surface treatments may be used [55, 56]. These methodologies have already proven to be effective by increasing the surface energy of the polymers and simultaneously reducing their surface hydrophobicity.

Other natural polymers such as chitosan, lignin or collagen could potentially require a less prolonged surface treatment and be presented as alternatives to the materials mentioned above. However it would be necessary to evaluate their mechanical resistance during the printing process and again during the analytical tests, as the majority of the natural polymers tend to have poorer mechanical strength when compared to synthetic options [57].

Nevertheless, some of them could be used as an alternative to paper-based substrates, mimicking their excellent printability and capillarity characteristics, but also allowing to obtain substrates with a wide range of tailorable morphologies, capillary flow rates, biodegradabilities and mechanical resistances, taking also the advantage of the active properties which, at a later stage, could be used to improve the performance of the assays.

As referred previously, this work report on the development of alternative/complementary materials substrates to the conventional μPADs. For instance, given the hydrophilic nature of these substrates, hydrophobic boundaries with specific patterns are often required to restrict the fluid flow of the samples and reagents to specific pathway of the hydrophilic substrates. To address these goals, different strategies have been used such as photolithography, wax printing, inkjet printing and screen-printing. Folding several layers of patterned paper, origami inspired, has also been employed to obtain three-dimensional (3D) systems. Each of those approaches has its own benefits and limitations, so the choice is often based on

cost, fabrication time, equipment availability and also specific application demands. In this way, there will be described the most common printing techniques used to fabricate portable analytical devices.

1.4. Portable analytical devices applications

PADs have been applied in many areas such as medicine, environmental monitoring, biology and pharmaceuticals [36]. Some of the most attractive features of PADs arise from their ability to provide low-cost, robust, portable and user-friendly platforms for (bio)analytical assays. These devices can be produced on a large scale and be easily distributed around the world without the need for complex infrastructures or specialized technicians. These devices have versatile functionalities, which can be applied in fields as varied as biomedical, food and environmental quality control (Figure 1.2). Thus, in the next sections PADs developed for these purposes are presented.

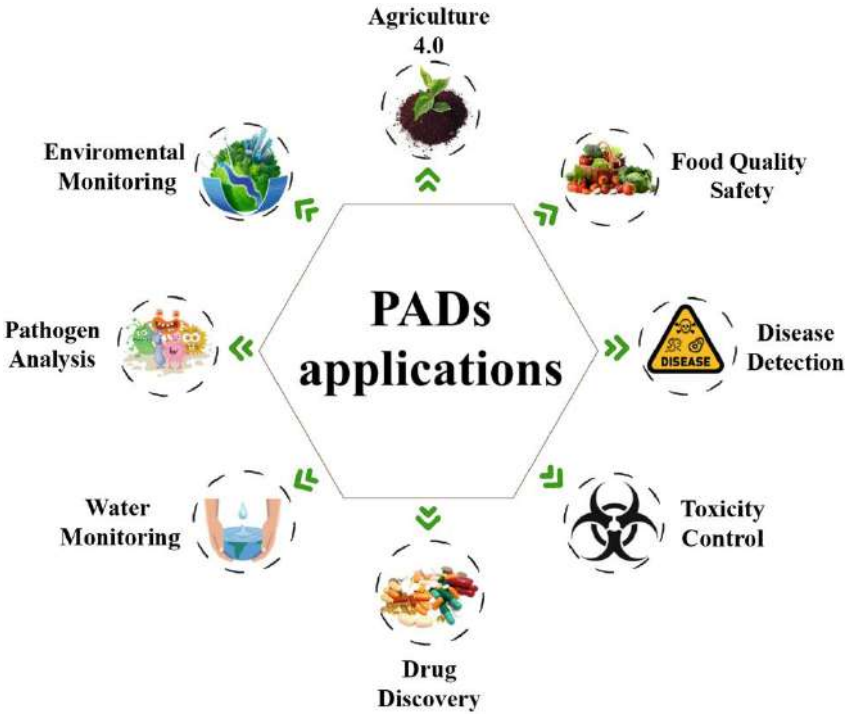

Figure 1.2. Schematic representation of different PADs areas of application.

Although the potential of PADs and the μPADs to be implemented in different applications has been recognized for a long time, it was more recently (when they were introduced as real alternatives to generate low cost and disposable biochemical sensing devices for multiple applications), that they have garnered more attention. Table 1.1 summarizes some relevant work carried out in different areas and their role on health diagnosis, environmental or food and beverage control.

Table 1.1. Some relevant and representative works on the use of microfluidic technology in different areas.

Health diagnosis	Analysis of biomolecules such as proteins, hormones, neurotransmitters and cells	[58-60]
	Analysis of small molecules and metabolites	[48, 61, 62]
	Nucleic acid analysis	[63, 64]
	Virus and infectious diseases	[65-67]
	Cancer biomarker detection	[47, 68, 69]
	Blood typing and blood filtering	[70, 71]
	Drug sensing	[72, 73]
Environmental diagnostics	Water, soil, air analysis, and heavy metal detection	[74-76]
Food and Beverage Control	Pesticide, foodborne detection, vegetables and wine quality analysis	[77, 78]

Research in medical diagnostic tools is gathering significant amount of efforts on PADs due to their critical importance and strong commercial possibilities. For instance, the commercialization of paper-based pregnancy tests, which represents one of the first lateral flow assays, was considered as one of the major breakthrough in this field [79-81].

A metabolite is any molecule involved in metabolic pathways of an organism and can be used for diagnosing diseases or monitoring homeostasis. Taking lactate as an example, its detection may be a form of diagnosing intra-abdominal sepsis. This has been achieved by fabricating screen-printed carbon microband electrodes from water-based ink containing lactate oxidase that are able to measure quantities of this metabolite [82]. Other lactate biosensors have also been developed with colorimetric approaches [83, 84]. Glucose detection in human serum has been achieved by the fabrication of an electrochemical μPADs with zinc oxide (ZnO) nanowires. Wax printing was used to implement the hydrophobic barriers

that delimit the reaction zones in paper, and electrodes patterned by stencil printing with conductive ink were drawn on top of these areas. Another paper layer that contains the carbon ink and the silver nanowires, where glucose oxidase is immobilized to enable the reaction that leads to the electric signal, is stacked, thus forming the complete device [85]. Similar strategy is common for glucose detection [86] or other metabolites such as creatinine, a chemical waste molecule resultant from muscle metabolism that can be found in the bloodstream, and is an indicator of good kidney function [87]. A very similar device using the same methodology has been developed for detection of biotin [88].

Another system was developed in the field of genetic science. The system allows to evaluate abnormalities in nucleotides present in a deoxyribonucleic acid (DNA) chain. In addition, this type of system has been shown to be capable of performing various laboratory functions, including DNA strand replication and strand separation simultaneously [59].

Cancer biomarker detection in PADs has also been developed. SU-8 photoresist was impregnated [89] into paper and cured, with electrodes added by screen-printing with carbon and silver (Ag) ink. Meticulously organized in layers and chambers, this device combined signal amplification strategies for the quantitative analysis of four different biomarkers.

PADs approaches for cell analysis have also received attention especially in biomedical research and clinical practice. A device capable of quantifying male fertility potential by evaluating live and motile sperm concentration and sperm motility was fabricated by wax-printing a well in two different layers on top of a laminate layer (figure 1.3) [90]. In the wells, 3-(4,5-dimethyl-2-thiazolyl)-2,5-diphenyl-tetrazolium bromide (MTT) assay was carried, generating a colorimetric signal; for the motility assay, another well contained a viscous buffer where the sperm must navigate in order to reach the reagent, generating a colorimetric signal [90].

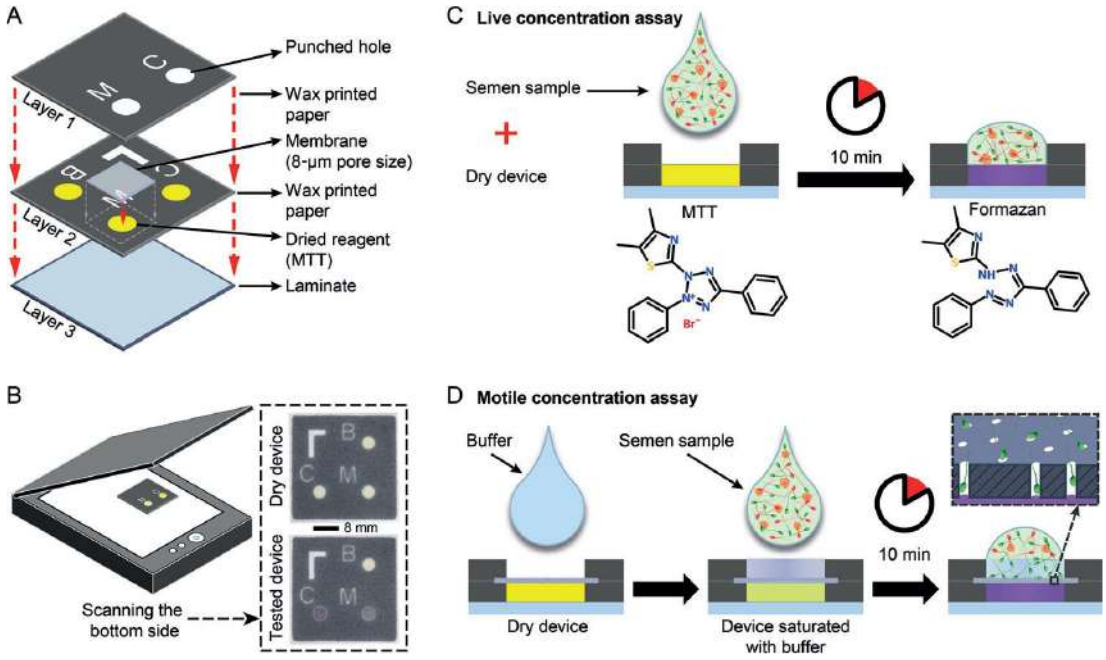

Figure 1.3. Schematic representation of a paper-based semen analysis device and protocol. (A) Exploded view of the 3D device. (B) Schematic view of the assembled device and images of devices before and 10 min after applying a semen sample. (C) In the concentration spot, the semen sample is pipetted directly on the dried MTT in paper to generate a colorimetric signal. (D) In the motility spot, sperm must swim through the highly viscous buffer and relatively narrow (8 µm) pores within the membrane filter (inset) to reach the reaction spot and generate a colorimetric signal [90].

Other biomedical area where PADs have been extensively applied is protein analysis. Tonello *et al.* [91] first developed a preliminary study for quantification of p53 protein, which has a conformational isoform that has been identified as a biomarker for Alzheimer's disease. The portable PADs testing system was developed based on screen-printed electrochemical sensors with conductive tracks composed of Ag, carbon and Ag/Ag chloride inks in a three-electrode anodic stripping voltammetry configuration. In a subsequent study [92], the authors further tested the screen-printed probes with different antibodies. As proof-of-concept, they tested the capabilities of the system by detecting the interleukin-8 protein. Moreover, they tuned the signal conditioning to enable more sensitive and accurate measurements and integrated the device into a Bluetooth system for wireless computer communication. These researchers pursued further studies using the same model protein, interleukin-8, but now by using aerosol jet printing for the fabrication of sensors similarly composed as the aforementioned ones with an additional layer of multi-walled carbon nanotubes (MWCNTs) over the carbon electrode to increase both the electronic performance and biofunctionalization, due to higher surface to volume ratio. These aerosol jet-printed electrodes showed several improvements in comparison to the previously screen-printed devices: a lower limit of detection, higher repeatability, and a decrease in relative standard deviation.

Besides, evaluating nucleic acids and obtaining a genetic sequence may provide relevant information on different health problems. For instance, PADs capable of detecting DNA may facilitate health care by personalizing pharmacological treatment or identifying agents responsible for infectious outbreaks. Electrochemical DNA sensors implemented in PADs have been developed by screen-printing carbon electrodes modified with an electro-deposited gold film. A conformational change occurs after the DNA strand binds with the electrode, which prompts a variation in the signal due to a change in efficiency in electron transfer [93]. In an effort to reuse and renew materials that would otherwise be disposed, researchers have developed a conductive ink based on graphene nanosheets synthetized by electrochemical exfoliation of biomass. This ink was used to print electrodes for analysis of calf thymus DNA, registering as an oxidative peak corresponding to the oxidation of an adenine base [94]. The fabrication process is illustrated in Figure 1.4.

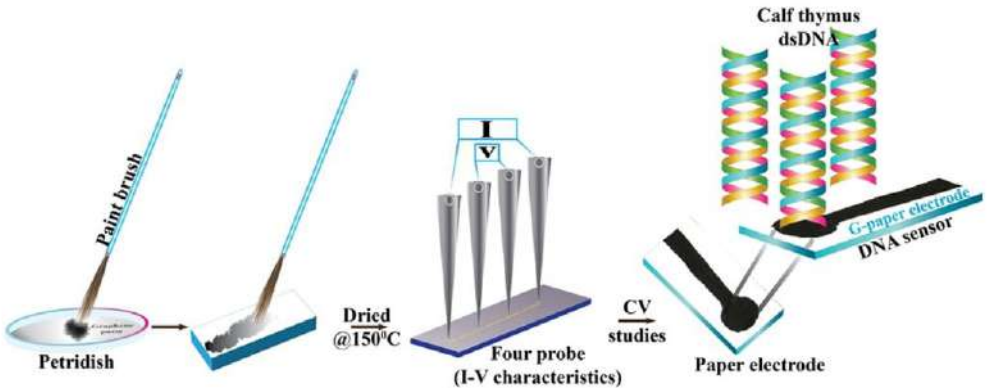

Figure 1.4. Schematic representation of the fabrication process of paper-based graphene electrodes using polyvinyl acetate solution mixed with graphene in a Petri dish, which is the graphene ink used to paint the paper substrate. After drying, the electrical conductivity of the painted graphene electrode was examined using a four probe method and further used as a DNA biosensor [94].

The WHO defined a biomarker as "any substance, structure, or process that can be measured in the body or its products and influence or predict the incidence of outcome or disease" [95]. Heavy presence of methyl groups in guanine and cytosine-rich DNA fragments has long been studied as a biomarker for tumorigenic activity, making it a good candidate for early cancer diagnosis [96]. Screen-printed gold electrodes have also been developed for detection of DNA methylation, in an assay also capable of carrying out polymerase chain reaction test for DNA amplification [97]. In another work, it has been developed a diagnostic device for the detection of DNA methylation. This device can extract, pre-concentrate, purify, amplify and detect nucleic acids from complex biological samples such as plasma and cerebral spinal fluid. These biological fluids may (respectively) carry *Plasmodium falciparum* (a protozoan parasite responsible for malaria), and *Neisseria meningitides* (a bacterium that causes

meningitis). Different techniques such as leak-proof polymerization and static coating were used to ensure optimal function and biocompatibility, capable of detecting these microorganisms within 50 min [98].

Worldwide outbreaks resulting from viral and infectious diseases such as the coronavirus 2019 (COVID-19), lead to enormous economic and social burdens. The genuine risk of more global outbreaks emphasizes the need for rapid, accurate, and sensitive detection techniques to speed up diagnostics and then allowing early intervention [99]. In viral infections where the rate of infection is extremely high and resources limited, it is important to simplify the process and reduce the use of external equipment. Mobile phones present themselves as an interesting auxiliary tool for viral detection on multiple printed μPADs. Kaarj *et al.* developed a wax-printed paper microfluidic chip to detect *Zika* virus, through reverse transcription loop-mediated isothermal amplification (RT-LAMP) reaction mixture and a smartphone. The results showed an amplification that could be quantified in real-time through statistically significant pixel intensities in 10 min [100]. These devices can be applied in several infectious diseases such as dengue [101], human immunodeficiency viruses [102], hepatitis C [103] or malaria [104] .

Food safety control is also essential for maintaining world health care levels, as there are several internal or external contaminants of bacterial or chemical origin that can be present in food. The United Nations (UN) estimates more than 1.8 million deaths from enteric diseases every year, near to 99 % belonging to developing countries [105]. Continuous exposure to these compounds may cause cancer, Alzheimer's and Parkinson's diseases, as well as fertility issues, allergies and hypersensitivity [105].

Detection, preferably early, is consequently an essential tool, and printed PADs have been widely used to this end. Nouanthavong *et al.* fabricated a portable device by screen-printing using a polystyrene solution to pattern the device, coated with nanoceria (cerium oxide) to detect organophosphates pesticides [78]. They can also be printed in the format of flexible paper devices made by screen-printing using silver nanoparticles and graphene oxide inks, to directly detect pesticide residues in fruits and vegetables through a simple swabbing approach and then analyzed by surface-enhanced raman scattering (SERS) as represented in Figure 1.4 [106].

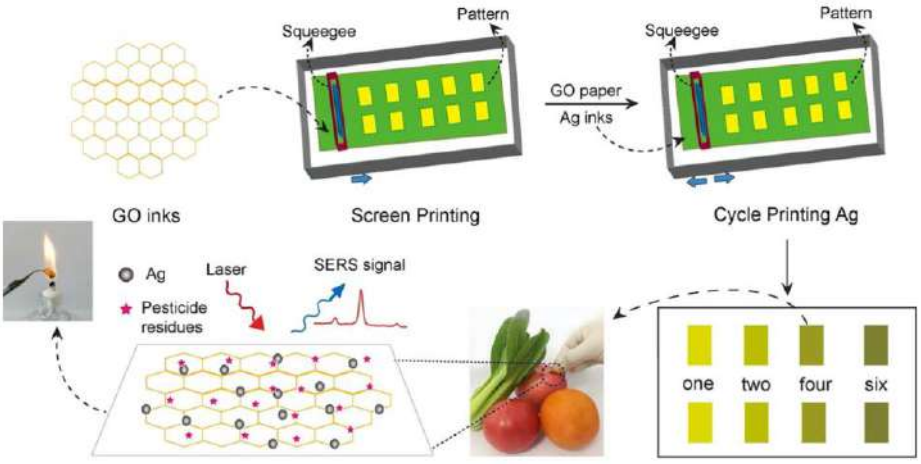

Figure 1.5. Schematic illustration of the fabrication process for SERS swabs by screen-printing and its application for the detection of pesticide residues in fruits and vegetables [106].

Another example is the study developed by Suaifan *et al.*, which proposed a printed PAD for detecting *Staphylococcus aureus*. The central sensing piece, a gold electrode, was fabricated by sputtering, and subsequently the magnetic nanobead-peptide probes were immobilized on the gold biosensor. The sensing mechanism was based on the application of *Staphylococcus aureus* proteases resulting in the dissociation of a magnetic nanobead-peptide complex. The developed colorimetric biosensor was successfully applied to detect *Staphylococcus aureus* in inoculated food and pure broth culture, presenting detection limits of 40 $CFU.mL^{-1}$ and 7 $CFU.mL^{-1}$, respectively [107].

Moreover, PADs developed for environmental safety, detecting water, soil or air contaminants, offer an alternative analytical technique to traditional methods, since they combine high sensitivity, selectivity and accuracy with low cost and so are suitable for *in-situ* analysis of environmental pollutants [108]. In resource-limited countries or after a natural disaster, an easy to use, low-cost device that provides information about drinking water quality, could be decisive in saving lives [108].

A wide variety of sensors for implementation in printed PAD for environmental applications have been developed, some of them combining wax and screen-printing technologies to create versatile and effective devices. Screen-printing inks of different physical and chemical constitutions such as carbon-based inks, Ag/AgCl or graphene oxide (GO), allow the development of screen-printed electrodes with increased and specific sensitivities. Furthermore, wax-printing allows the introduction of hydrophobic barriers that can be used to create delimited test areas and control the separation or possible mixture of chemical compounds and environmental samples in a very precise way [109]. In a similar approach, Chaiyo *et al.* presented a printed PAD with dual electrochemical and colorimetric detection of lead, cadmium and copper in water. The device was built by combining wax-printing to delimit the hydrophobic and hydrophilic

zones and screen-printing to create the electrodes for the active detection (carbon ink served as the counter electrode and Ag/Ag chloride ink served as the reference electrode). Samples tested showed minimum electrochemical detection limits of 0.1 $ng.L^{-1}$ for both lead and cadmium and about 4.12 $ng.mL^{-1}$ for copper by colorimetric detection [110].

While the research and development of functional prototypes in PADs and μPADs has undergone significant advances in recent years, a path is still needed in the introduction and/or optimization of (novel) materials and manufacturing techniques which can reduce costs and substantially increase the quantity of devices produced for full market implementation.

1.5. Printing techniques applied on portable analytical devices and microfluidic paper analytical devices

In the first half of the last century, Müller and Clegg produced the first paper-based assay, by using paraffin to pattern a fluidic channel on paper [111]. Since then, a massive flow on the improvement of fabrication techniques to build increasingly effective and reliable PADs and μPADs has been observed [112,113]. Among the most effective and efficient technologies for their fabrication are printing technologies.

Thus, this section provides an overview of the most representative printing techniques for fabrication of PADs and μPADs. Table 1.2 also summarizes the main advantages and limitations to be considered for mass production.

As one of the most accessible and inexpensive printing technique, screen printing is a compelling choice for the biomedical field and the fabrication of disposable PADs, showing advantages such as low cost, versatility and miniaturization. Since its introduction over 100 years ago, the technique has been continuously improved, becoming more specialized and tailorable for different applications. Renault *et al.* directly screen-printed 18 bipolar carbon electrodes on a cellulose substrate, using a single pair of driving electrodes [124]. Another study presented a polyester film as a multilayer device for the detection of metals, in which the reference electrode was screen-printed with carbon ink, and the working and counter electrodes were printed using a mixture of MWCNTs, graphite powder, and carbon ink [125]. Nyein *et al.* also adapted a screen printer to develop a sweat PAD sensor [126]. PET was selected as the substrate and a circular screen-printing system adapted to a roll-to-roll unit was used. With this method, different inks were printed to build the sensor, with underlying silver electrodes, carbon electrodes, dielectric polymer layers, and upper spiral silver electrodes. The patch allows sweat capture within a spiral

microfluidic for real-time measurement of sweat content including the concentration of Na^+, K^+ and glucose, as well as sweat rate in exercise and chemically induced sweat [126].

Table 1.2. Schematic overview of the most used printing techniques for PADs and μPADs fabrication.

Fabrication Technique	Equipment	Consumables	Advantages	Drawbacks	Refs
Wax dipping	Customized mask, heating device	Solid wax	Low cost and facile method	Inconsistency between batches due to the variation in dipping	[114, 115]
Screen printing	Customized mesh	Several inks and biokinks	Low cost; simple fabrication steps	Hard to obtain microfluidic channels; rough barriers; requires different printing screens for different patterns;	[116, 117]
Wax printing	Wax printer, hot plate	Solid wax	Produces massive devices with a simple and fast (5-10 min) process	Poor resolution when cured in highly porous substrates; requires an extra heating step after wax deposition	[118, 119]
Stamping	Polymer or stainless steel stamp	Commercial ink, paraffin or wax	Low cost, simple	Manual and inconsistent process; low resolution; preheating of the stamp and oxidization of the paper are needed when paraffin stamping with a metal stamp	[120, 121]

Inkjet printing	Computer software and inkjet printer	Different inks (Water based, Solvent based, UV or Hot melt)	High resolution; requires only a desktop printer to produce devices and print sensing reagents	Requires modified inkjet printers; different compositions for each printing; usually requires an extra heating step after deposition	[122, 123]

Inks and bioinks are one of the most important elements for the inkjet printing process, based on the limitation in ink characteristics in terms of viscosity and maximum particle size, among others, imposed by this technique. There are several examples of different inkjet inks used for printing portable analytical systems based on silver [127], gold [128], carbon nanotubes [129, 130], paper-sizing agent alkyl ketene dimer [131], poly-L-arginine ink [132], glycerol and Triton X-100 [132] or polyaniline (PANI) [133], among others. For instance, using inkjet printing, Maattanen *et al.* printed electrodes to work as glucose biosensors using Ag and Au inks. A commercial inkjet printer was used to pattern the electrodes on the substrate. Then, silver chloride (AgCl) was deposited over the silver lines to build the Ag/AgCl reference electrode. Finally, to obtain the glucose biosensor, the surface was modified with glucose oxidase [127]. Among the different techniques used to pattern hydrophilic/hydrophobic contrasts on microfluidic substrates, wax-based fabrication techniques are the most complete, as they are low-cost methods based on selective hydrophilization using non-toxic patterning reagents. Wax-based printing technologies feature several advantages, since the wax is inexpensive and usually readily available, as well as environmentally friendly. Moreover, printing can be accomplished without the use of a clean room, UV lamp, organic solvents, or sophisticated instrumentation. Another advantage over the previously mentioned methods is that it requires only a hot plate (or similar heated surface) making it ideal for the fabrication mainly for µPADs but also for PADs in developing countries. Wax printing was introduced by Lu et al. [134] in 2009. Despite being a three-step method encompassing paper design, printing and heating, it is suitable for mass production, once wax printers, are commercially available and relatively inexpensive [135]. The print head dispenses melted solid ink in the form of liquid droplets on a substrate, where they cool and solidify almost instantaneously. Common commercial solid inks used in this process are constituted of a mixture of hydrocarbons, carbamates and different dyes [10, 136]. Through this process, it is possible to obtain printing patterns with a resolution of up to 2400 x 2400 dpi before curing. However, to create

proper hydrophobic wax barriers, a second heating step is needed to ensure a correct impregnation of the wax into the substrate cross-section [43]. During this step, lateral spreading of the melted wax may occur depending on the substrate used, reducing the resolution of the printed pattern, which results in wider barriers [45, 137]. This behavior can lead to narrower channels than designed and thus to variations in the desired capillary flow rate. Therefore, depending on the intended application, this behavior must be considered when developing systems based on this technology. Nevertheless, wax printing features several positive characteristics, as it does not require specialized facilities, the process is fast (5-10 min), inexpensive (each wax cartridge can print a large number of devices) and environmentally friendly (no use of organic solvents throughout the fabrication process). Concerning the materials used as substrates, cellulose-based filter paper is presented as the gold standard [138]. Several applications have been developed in areas, such as energy storage [139], medical diagnostic [140], and environmental sensors [141], among others. The schematic representation of the wax printing process is presented in Figure 1.6.

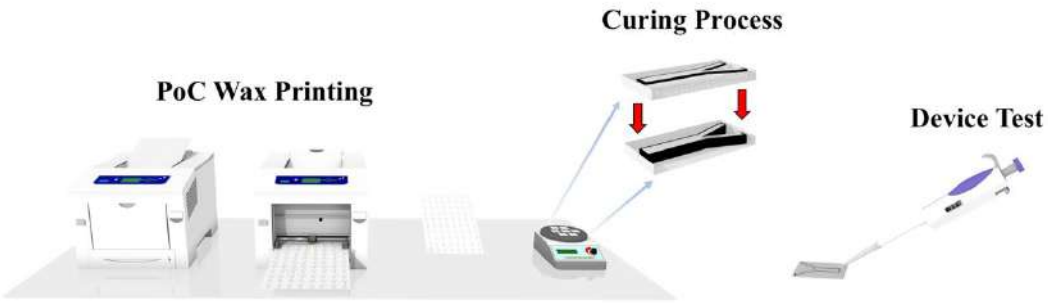

Figure 1.6. Schematic representation of the wax printing process.

However, as previously referred, wax printing uses exclusively commercial waxes that work as passive barriers to create hydrophilic/hydrophobic inert contrasts throughout the microfluidic substrate, i.e. without any action on the fluids [44].

The possibility of adding functional properties to these waxes is an exciting possibility combining commercial wax with the dispersion of different fillers such as iron-oxide magnetic nanoparticles, silver nanowires, graphene or barium titanate (BT). In fact, the conjugation of new active properties could lead to different microfluidic applications such as the detection of virus, cells infected with malaria [142] as well as bacteria detection [143], all responsive to magnetic and/or electric fields. Moreover, these active hydrophobic waxes can allow, through the printing of conductive or semi-conductive microchannels, to obtain temperature control and thus improve the hydrolysis reactions of DNA and ribonucleic acid (RNA)

directly in the PADs and μPADs. Other potential applications include the selective separation of pollutants according to their magnetic and/or electrical properties [144].

1.6. Objectives and methodology

The main objective of this thesis is to develop advanced materials for PADs and μPADs applications, addressing current shortcomings and aiming to reach real-world applications. This will be achieved by the development and validation of a new generation of advanced polymer-based substrates and new functional waxes.

This main objective will be achieved by applying the following methodology:

- Development of novel microfluidic substrates based on synthetic and bio-based polymers, including piezoelectric ones. Different morphologies and/or the introduction of fillers in the polymer matrices will be also tested to increase the potential of the new microfluidic substrates when compared to the commonly used passive paper substrates. The viability and performance of the developed substrates will also be assessed to combine both functional channels and smart substrates;
- Development of hydrophobic wax-based composites with functional properties, including magnetic, conductive and dielectric waxes using specific nanofillers that can be used to define functional channels within the substrate by using printing technologies. These composites will allow active manipulation of fluids and/or compounds that flow through the substrate;
- Evaluation and validation of the developed materials in magnetic and heating systems as proof-of-concept applications.

The ultimate purpose is to allow: i) precise control of morphology, hydrophilicity and sample capillary flow rate on the device in terms of direction and rate; Ii) higher storage stability and controllable degradation; iii) superior wet strength to increase the performance of PADs and their range of possible applications that require multiple and specific steps assays.

1.7. Structure of the thesis

The present thesis is divided into five chapters, three of them based on published or submitted scientific manuscripts. The sequence of these chapters provides a comprehensive and logical account of the progress achieved during the present research as well as further clarifies the used methodology. A summary of the work covered in each chapter is briefly described below.

Chapter 1 presents the motivation of the thesis with a general introduction to the work. The main objectives and the structure of the thesis are also presented. The state of the art on specific relevant issues for the development of the work is provided in each of the different chapters.

To better understand the importance of developing new alternatives to the existent PADs and μPADs, Chapter 2 is divided into four sub-chapters based on the four published works about the application of different polymer-based substrates as new platforms for as an alternative to existing devices. In the first subchapter, Chapter 2.1, microfluidic substrates based on electrospun PLLA membranes were fabricated and the influence of fibre orientation, addition of hydrophilic additives and plasma treatment on their morphology, physicochemical properties and capillary flow rate were evaluated and compared with paper-based Whatman substrates. In Chapter 2.2, polyvinylidene fluoride-co-trifluoroethylene (P(VDF-TrFE)) membranes with tailored morphological and physicochemical properties (electrospun oriented and randomly-oriented fibers, porous or spherulitic membranes) were processed, printed using wax-printing and evaluated as new platforms for colorimetric quantification of glucose. Chapter 2.3 introduces biodegradable membranes based on poly-DL-lactide-glycolide (PDLG) that were evaluated as an alternative to conventional paper substrates, revealing advantages in terms of controlled degradation and high colorimetric precision, proving suitability to a new generation of degradable PADs. Another polymer substrate is presented in Chapter 2.4, where multi-structural silk-based substrates were used as low-cost, environmentally friendly substrates for portable analytical systems by using Bombyx mori cocoons. Further, silk fibroin was extracted from these cocoons and electrospun into oriented and randomly-oriented fiber substrates. The developed materials were then used as substrates for the colorimetric quantification of three different clinical analytes. All four works are interconnected in the pursuit of developing a new generation of devices using polymers from different origins and functional characteristics, which bring unique advantages and characteristics for a next generation PADs and μPADs testing.

Chapter 3 is based on the development and functionalization of different hydrophobic inks based on wax. As in the previous chapter, it is divided into four different sub-chapters. Chapter 3.1 describes the development of a process for obtaining magnetic waxes with iron oxide (Fe_3O_4) NPs, and then printing

them on cellulose substrates using wax printing. In Chapter 3.2, the development of magnetic waxes is optimized, and a self-powered printed sensing device is presented, the piezoelectric/magnetic effect is explored via magneto-mechano-electric energy conversion. The dielectric properties of the wax reinforced with high-dielectric ceramic nanofillers such as barium titanate (BT) were studied in Chapter 3.3, and a functional hydrophobic ink suitable for paper-based microfluidics was developed, able to be combined with different ceramic materials to adapt its dielectric constant, an essential aspect in applications in printed electronics. Conductive hydrophobic inks, which can represent a critical step in the commercial expansion of PADs, are approached in Chapter 3.4, where carbon nanotube (CNT) and reduced graphene oxide (rGO)-filled wax composites were developed and proven to be suitable to be applied and printed for different PoC applications.

Chapter 4 integrates several of the developed technologies on new PADs platforms, evaluated in proof-of-concept applications. Chapter 4.1 describe the development of a fully functional magnetic POC printed device composed of two neodymium iron boron (NdFeB)/wax magnets capable of attracting and detecting magnetic nanoparticles with similar characteristics and concentrations compared to hemozoin present on malaria-infected red blood cells. Different analysis methods as energy-dispersive X-ray spectroscopy (EDX), vibrating sample magnetometry (VSM), Fourier-transformed infrared spectroscopy (FTIR-ATR); and mean grey scale evaluation on photographs taken by mobile phones, were presented as complementary analytical tools. Chapter 4.2 shows the development of multifunctional hydrophobic composites based on conductive graphene nanoplatelets (GNP) integrated into the wax matrix to allow a dual role of barrier and heater, relevant for a variety of temperature-sensitive reactions and applications in microfluidic technology.

Finally, Chapter 5 compiles the main conclusions of the work presented in this thesis and proposes some suggestions for future work and possible research directions.

1.8. References

1. Nations, U., Transforming our World: The 2030 Agenda for Sustainable Development. 2015.

2. Gong, M.M. and Sinton, D., Turning the Page: Advancing Paper-Based Microfluidics for Broad Diagnostic Application. Chemical Reviews, 2017. 117(12): 8447-8480.

3. Kankaanpää, M., et al., Use of point-of-care testing and early assessment model reduces length of stay for ambulatory patients in an emergency department. Scandinavian journal of trauma, resuscitation and emergency medicine, 2016. 24(1): 1-7.

4. Drain, P.K., et al., Diagnostic point-of-care tests in resource-limited settings. The Lancet infectious diseases, 2014. 14(3): 239-249.

5. Kosack, C.S., Page, A.-L. and Klatser, P.R., A guide to aid the selection of diagnostic tests. Bulletin of the World Health Organization, 2017. 95(9): p639.

6. Santhiago, M., et al., Microfluidic paper-based devices for bioanalytical applications. Bioanalysis, 2014. 6(1): 89-106.

7. Nge, P.N., Rogers, C.I. and Woolley, A.T., Advances in microfluidic materials, functions, integration, and applications. Chemical Reviews, 2013. 113(4): 2550-2583.

8. Mark, D., et al., Microfluidic lab-on-a-chip platforms: requirements, characteristics and applications, in Microfluidics based microsystems. 2010, Springer. p. 305-376.

9. Yamada, K., et al., Toward practical application of paper-based microfluidics for medical diagnostics: state-of-the-art and challenges. Lab on a Chip, 2017. 17(7): 1206-1249.

10. Akyazi, T., Basabe-Desmonts, L. and Benito-Lopez, F., Review on microfluidic paper-based analytical devices towards commercialisation. Analytica Chimica Acta, 2018. 1001: 1-17.

11. Jia, C., et al., Anisotropic, Mesoporous Microfluidic Frameworks with Scalable, Aligned Cellulose Nanofibers. ACS Applied Materials and Interfaces, 2018. 10(8): 7362-7370.

12. Ballerini, D.R., Li, X. and Shen, W., Patterned paper and alternative materials as substrates for low-cost microfluidic diagnostics. Microfluidics and Nanofluidics, 2012. 13(5): 769-787.

13. Abel, G., Current status and future prospects of point-of-care testing around the globe. Expert review of molecular diagnostics, 2015. 15(7): 853-855.

14. Barata, D., et al., Development of a microfluidic platform integrating high-resolution microstructured biomaterials to study cell–material interactions. Lab on a Chip, 2017. 17(23): 4134-4147.

15. Cardoso, V.F., et al., From superhydrophobic-to superhydrophilic-patterned poly (vinylidene fluoride-co-chlorotrifluoroethylene) architectures as a novel platform for biotechnological applications. Journal of Polymer Science Part B: Polymer Physics, 2016. 54(18): 1802-1810.

16. Whitesides, G.M., The origins and the future of microfluidics. Nature, 2006. 442: 368.

17. Terry, S.C., Jerman, J.H. and Angell, J.B., A gas chromatographic air analyzer fabricated on a silicon wafer. IEEE transactions on electron devices, 1979. 26(12): 1880-1886.

18. Auroux, P.-A., et al., Micro Total Analysis Systems. 2. Analytical Standard Operations and Applications. Analytical Chemistry, 2002. 74(12): 2637-2652.

19. Manz, A., et al., Planar chips technology for miniaturization and integration of separation techniques into monitoring systems: capillary electrophoresis on a chip. Journal of Chromatography A, 1992. 593(1-2): 253-258.

20. McDonald, J.C. and Whitesides, G.M., Poly(dimethylsiloxane) as a Material for Fabricating Microfluidic Devices. Accounts of Chemical Research, 2002. 35(7): 491-499.

21. Chiu, D.T., et al., Small but Perfectly Formed? Successes, Challenges, and Opportunities for Microfluidics in the Chemical and Biological Sciences. Chem, 2017. 2(2): 201-223.

22. Huh, D., Hamilton, G.A. and Ingber, D.E., From 3D cell culture to organs-on-chips. Trends in cell biology, 2011. 21(12): 745-754.

23. Sieben, V.J., et al., An integrated microfluidic chip for chromosome enumeration using fluorescence in situ hybridization. Lab on a Chip, 2008. 8(12): 2151-2156.

24. Huh, D., et al., Reconstituting organ-level lung functions on a chip. Science, 2010. 328(5986): 1662-1668.

25. Singh, R., et al., Recent advances for serial processes of hazardous chemicals in fully integrated microfluidic systems. Korean Journal of Chemical Engineering, 2016. 33(8): 2253-2267.

26. Ortseifen, V., et al., Microfluidics for biotechnology: bridging gaps to foster microfluidic applications. Frontiers in Bioengineering and Biotechnology, 2020. 8: 589074.

27. Wang, D.-S. and Fan, S.-K., Microfluidic surface plasmon resonance sensors: From principles to point-of-care applications. Sensors, 2016. 16(8): 1175.

28. Sia, S.K. and Whitesides, G.M., Microfluidic devices fabricated in poly (dimethylsiloxane) for biological studies. Electrophoresis, 2003. 24(21): 3563-3576.

29. Wang, A., Abdulla, A. and Ding, X., Microdroplets-on-chip: a review. Proceedings of the Institution of Mechanical Engineers, Part H: Journal of Engineering in Medicine, 2019. 233(7): 683-694.

30. Wang, H., et al., A portable microfluidic platform for rapid molecular diagnostic testing of patients with myeloproliferative neoplasms. Scientific reports, 2017. 7(1): 1-11.

31. Ng, J.M., et al., Components for integrated poly (dimethylsiloxane) microfluidic systems. Electrophoresis, 2002. 23(20): 3461-3473.

32. Lee, J.N., Park, C. and Whitesides, G.M., Solvent compatibility of poly (dimethylsiloxane)-based microfluidic devices. Analytical chemistry, 2003. 75(23): 6544-6554.

33. McDonald, J.C., et al., Fabrication of microfluidic systems in poly (dimethylsiloxane). Electrophoresis, 2000. 21(1): 27-40.

34. Tang, S.K. and Whitesides, G.M., Basic microfluidic and soft lithographic techniques, in Optofluidics: Fundamentals, Devices and Applications. 2010, McGraw-Hill. p. 7-32.

35. Anderson, J.R., et al., Fabrication of topologically complex three-dimensional microfluidic systems in PDMS by rapid prototyping. Analytical chemistry, 2000. 72(14): 3158-3164.

36. Fujii, T., PDMS-based microfluidic devices for biomedical applications. Microelectronic Engineering, 2002. 61: 907-914.

37. Kirikova, M.N., et al., Direct-write printing of reactive oligomeric alkoxysilanes as an affordable and highly efficient route for promoting local adhesion of silver inks on polymer substrates. Journal of Materials Chemistry C, 2016. 4(11): 2211-2218.

38. Eddings, M.A., Johnson, M.A. and Gale, B.K., Determining the optimal PDMS–PDMS bonding technique for microfluidic devices. Journal of Micromechanics and Microengineering, 2008. 18(6): 067001.

39. Tsao, C.-W. and DeVoe, D.L., Bonding of thermoplastic polymer microfluidics. Microfluidics and Nanofluidics, 2009. 6(1): 1-16.

40. Ren, K., et al., Whole-Teflon microfluidic chips. Proceedings of the National Academy of Sciences, 2011. 108(20): 8162-8166.

41. Mukhopadhyay, R., When PDMS isn't the best. Analytical Chemistry, 2007. 79(9): 3248-3253.

42. Carneiro, M.C., et al., Colorimetric paper-based sensors against cancer biomarkers. Sensors, 2022. 22(9): 3221.

43. Yetisen, A.K., Akram, M.S. and Lowe, C.R., Paper-based microfluidic point-of-care diagnostic devices. Lab on a Chip, 2013. 13(12): 2210-2251.

44. Yang, Y., et al., based microfluidic devices: Emerging themes and applications. Analytical chemistry, 2016. 89(1): 71-91.

45. Carrilho, E., Martinez, A.W. and Whitesides, G.M., Understanding wax printing: a simple micropatterning process for paper-based microfluidics. Analytical chemistry, 2009. 81(16): 7091-7095.

46. Sochol, R.D., et al., 3D printed microfluidics and microelectronics. Microelectronic Engineering, 2018. 189: 52-68.

47. Schonhorn, J.E., et al., A device architecture for three-dimensional, patterned paper immunoassays. Lab on a Chip, 2014. 14(24): 4653-4658.

48. Cai, L., et al., Fabrication of a microfluidic paper-based analytical device by silanization of filter cellulose using a paper mask for glucose assay. Analyst, 2014. 139(18): 4593-4598.

49. Murray, C.K., et al., Update on rapid diagnostic testing for malaria. Clinical microbiology reviews, 2008. 21(1): 97-110.

50. Rohrman, B.A., et al., A lateral flow assay for quantitative detection of amplified HIV-1 RNA. PLoS One, 2012. 7(9): e45611.

51. Kasetsirikul, S., Shiddiky, M.J. and Nguyen, N.-T., Challenges and perspectives in the development of paper-based lateral flow assays. Microfluidics and Nanofluidics, 2020. 24(2): 1-18.

52. Martins, P., Lopes, A. and Lanceros-Mendez, S., Electroactive phases of poly (vinylidene fluoride): determination, processing and applications. Progress in polymer science, 2014. 39(4): 683-706.

53. Bar-Cohen, Y., et al., Electroactive polymer materials. Smart Materials and Structures, 2007. 16(2), E01.

54. Ribeiro, C., et al., Electroactive poly (vinylidene fluoride)-based structures for advanced applications. Nature protocols, 2018. 13(4): 681.

55. Correia, D.M., et al., Influence of oxygen plasma treatment parameters on poly (vinylidene fluoride) electrospun fiber mats wettability. Progress in Organic Coatings, 2015. 85: 151-158.

56. Li, Q., et al., Preparation of Y-zeolite/CoCl2 doped PVDF composite nanofiber and its application in hydrogen production. Energy, 2012. 38(1): 144-150.

57. Bettinger, C.J., et al., Silk fibroin microfluidic devices. Advanced Materials, 2007. 19(19): 2847-2850.

58. Wei, X., et al., Target-responsive DNA hydrogel mediated “stop-flow” microfluidic paper-based analytic device for rapid, portable and visual detection of multiple targets. Analytical chemistry, 2015. 87(8): 4275-4282.

59. Zhu, J., et al., A microfluidic device for multiplex single-nucleotide polymorphism genotyping. RSC advances, 2014. 4(9): 4269-4277.

60. Wang, W., W.-Y. Wu, and J.-J. Zhu, Tree-shaped paper strip for semiquantitative colorimetric detection of protein with self-calibration. Journal of Chromatography A, 2010. 1217(24): 3896-3899.

61. Curto, V.F., et al., Fast prototyping of paper-based microfluidic devices by contact stamping using indelible ink. Rsc Advances, 2013. 3(41): 18811-18816.

62. Du, Y., et al., Dual-signal output paper sensor based on coordinative self-assembly biomimetic nanozyme for point-of-care detection of biomarker. Biosensors and Bioelectronics, 2022. 216: 114656.

63. Lu, J., et al., Electrochemical DNA sensor based on three-dimensional folding paper device for specific and sensitive point-of-care testing. Electrochimica Acta, 2012. 80: 334-341.

64. Rosa, A.M., et al., Capture and detection of DNA hybrids on paper via the anchoring of antibodies with fusions of carbohydrate binding modules and ZZ-domains. Analytical chemistry, 2014. 86(9): 4340-4347.

65. Augoff, K., A. Hryniewicz-Jankowska, and R. Tabola, Lactate dehydrogenase 5: an old friend and a new hope in the war on cancer. Cancer letters, 2015. 358(1): 1-7.

66. Lei, K.F., et al., based enzyme-free immunoassay for rapid detection and subtyping of influenza A H1N1 and H3N2 viruses. Analytica chimica acta, 2015. 883: 37-44.

67. Jaewjaroenwattana, J., et al., Electrochemical paper-based antigen sensing platform using plant-derived monoclonal antibody for detecting SARS-CoV-2. Talanta, 2023. 251: 123783.

68. Carneiro, M.C., et al., based ELISA for fast CA 15–3 detection in point-of-care. Microchemical Journal, 2022. 181: 107756.

69. Masumoto, M., et al., Colorimetric paper-based sarcosine assay with improved sensitivity. Analytical and bioanalytical chemistry, 2022. 414(1): 691-701.

70. Jarujamrus, P., et al., Mechanisms of red blood cells agglutination in antibody-treated paper. Analyst, 2012. 137(9): 2205-2210.

71. Yang, X., et al., Integrated separation of blood plasma from whole blood for microfluidic paper-based analytical devices. Lab on a Chip, 2012. 12(2): 274-280.

72. Luckham, R.E. and J.D. Brennan, Bioactive paper dipstick sensors for acetylcholinesterase inhibitors based on sol–gel/enzyme/gold nanoparticle composites. Analyst, 2010. 135(8): 2028-2035.

73. Zangheri, M., et al., A simple and compact smartphone accessory for quantitative chemiluminescence-based lateral flow immunoassay for salivary cortisol detection. Biosensors and Bioelectronics, 2015. 64: 63-68.

74. Nath, P., Arun, R.K., Chanda, N., Chanda, Smart gold nanosensor for easy sensing of lead and copper ions in solution and using paper strips. Rsc Advances, 2015. 5(84): 69024-69031.

75. Guo, J.-f., et al., Colorimetric detection of Cr (VI) based on the leaching of gold nanoparticles using a paper-based sensor. Talanta, 2016. 161: 819-825.

76. Wang, H., et al., Semiquantitative visual detection of lead ions with a smartphone via a colorimetric paper-based analytical device. Analytical chemistry, 2019. 91(14): 9292-9299.

77. Hossain, S.Z., et al., Development of a bioactive paper sensor for detection of neurotoxins using piezoelectric inkjet printing of sol– gel-derived bioinks. Analytical chemistry, 2009. 81(13): 5474-5483.

78. Nouanthavong, S., et al., Pesticide analysis using nanoceria-coated paper-based devices as a detection platform. Analyst, 2016. 141(5): 1837-1846.

79. Parolo, C., and Merkoçi, A., Paper-based nanobiosensors for diagnostics. Chemical Society Reviews, 2013. 42(2): 450-457.

80. Noiphung, J., et al., Electrochemical detection of glucose from whole blood using paper-based microfluidic devices. Analytica chimica acta, 2013. 788: 39-45.

81. Reboud, J., et al., based microfluidics for DNA diagnostics of malaria in low resource underserved rural communities. Proceedings of the National Academy of Sciences, 2019. 116(11): 4834-4842.

82. Rawson, F., et al., A microband lactate biosensor fabricated using a water-based screen-printed carbon ink. Talanta, 2009. 77(3): 1149-1154.

83. Hirst, N., et al., An amperometric lactate biosensor using H2O2 reduction via a Prussian Blue impregnated poly (ethyleneimine) surface on screen printed carbon electrodes to detect anastomotic leak and sepsis. Sensors and Actuators B: Chemical, 2013. 186: 674-680.

84. Delaney, J.L., et al., Electrogenerated Chemiluminescence Detection in Paper-Based Microfluidic Sensors. Analytical Chemistry, 2011. 83(4): 1300-1306.

85. Li, X., Zhao, C., Liu, X., A paper-based microfluidic biosensor integrating zinc oxide nanowires for electrochemical glucose detection. Microsystems & Nanoengineering, 2015. 1(1): 15014.

86. Zhu, X., et al., A dual enzyme–inorganic hybrid nanoflower incorporated microfluidic paper-based analytic device (μPAD) biosensor for sensitive visualized detection of glucose. Nanoscale, 2017. 9(17): 5658-5663.

87. Tseng, C.-C., et al., Microfluidic paper-based platform for whole blood creatinine detection. Chemical Engineering Journal, 2018. 348: 117-124.

88. Busa, L.S.A., et al., A competitive immunoassay system for microfluidic paper-based analytical detection of small size molecules. Analyst, 2016. 141(24): 6598-6603.

89. Wu, Y., et al., Paper-Based Microfluidic Electrochemical Immunodevice Integrated with Nanobioprobes onto Graphene Film for Ultrasensitive Multiplexed Detection of Cancer Biomarkers. Analytical Chemistry, 2013. 85(18): 8661-8668.

90. Nosrati, R., et al., Paper-Based Quantification of Male Fertility Potential. Clinical Chemistry, 2016. 62(3): 458-465.

91. Tonello, S., et al., Screen-Printed Biosensors for the Early Detection of Biomarkers Related to Alzheimer Disease: Preliminary Results. Procedia Engineering, 2016. 168: 147-150.

92. Tonello, S., et al., Wireless point-of-care platform with screen-printed sensors for biomarkers detection. IEEE Transactions on Instrumentation and Measurement, 2017. 66(9): 2448-2455.

93. Yang, W., Gerasimov, J.Y., Lai, R.Y., Folding-based electrochemical DNA sensor fabricated on a gold-plated screen-printed carbon electrode. Chemical communications, 2009(20): 2902-2904.

94. Tsaloglou, M.-N., et al., Handheld isothermal amplification and electrochemical detection of DNA in resource-limited settings. Analytical Biochemistry, 2018. 543: 116-121.

95. Strimbu, K. and J.A. Tavel, What are biomarkers? Current Opinion in HIV and AIDS, 2010. 5(6): 463.

96. Levenson, V.V., DNA methylation as a universal biomarker. Expert review of molecular diagnostics, 2010. 10(4): 481-488.

97. Koo, K.M., et al., eMethylsorb: rapid quantification of DNA methylation in cancer cells on screen-printed gold electrodes. Analyst, 2014. 139(23): 6178-6184.

98. Kadimisetty, K., et al., Fully 3D printed integrated reactor array for point-of-care molecular diagnostics. Biosensors and Bioelectronics, 2018. 109: 156-163.

99. Broadhurst, M.J., T.J. Brooks, and N.R. Pollock, Diagnosis of Ebola virus disease: past, present, and future. Clinical microbiology reviews, 2016. 29(4): 773-793.

100. Kaarj, K., Akarapipad, P., Yoon, J.-Y., Simpler, faster, and sensitive Zika virus assay using smartphone detection of loop-mediated isothermal amplification on paper microfluidic chips. Scientific reports, 2018. 8(1): 1-11.

101. Ganguli, A., et al., Hands-free smartphone-based diagnostics for simultaneous detection of Zika, Chikungunya, and Dengue at point-of-care. Biomedical microdevices, 2017. 19(4): 73.

102. Cheng, C.M., et al., Paper-based ELISA. Angewandte Chemie International Edition, 2010. 49(28): 4771-4774.

103. Mu, X., et al., Multiplex microfluidic paper-based immunoassay for the diagnosis of hepatitis C virus infection. Analytical chemistry, 2014. 86(11): 5338-5344.

104. Kolluri, N., Klapperich, C., and Cabodi, M., Towards lab-on-a-chip diagnostics for malaria elimination. Lab on a Chip, 2018. 18(1): 75-94.

105. Pérez-Fernández, B., Costa-García, A., and Muñiz, A.d.l.E., Electrochemical (Bio) Sensors for Pesticides Detection Using Screen-Printed Electrodes. Biosensors, 2020. 10(4): 32.

106. Ma, Y., et al., Rapid and sensitive on-site detection of pesticide residues in fruits and vegetables using screen-printed paper-based SERS swabs. Analytical methods, 2018. 10(38): 4655-4664.

107. Suaifan, G.A., Alhogail, S., and Zourob, M., Rapid and low-cost biosensor for the detection of Staphylococcus aureus. Biosensors and Bioelectronics, 2017. 90: 230-237.

108. Meredith, N.A., et al., based analytical devices for environmental analysis. Analyst, 2016. 141(6): 1874-1887.

109. Mani, V., et al., based electrochemiluminescent screening for genotoxic activity in the environment. Environmental science & technology, 2013. 47(4): 1937-1944.

110. Chaiyo, S., et al., High sensitivity and specificity simultaneous determination of lead, cadmium and copper using μPAD with dual electrochemical and colorimetric detection. Sensors and Actuators B: Chemical, 2016. 233: 540-549.

111. Müller, R.H. and Clegg, D.L., Automatic Paper Chromatography. Analytical Chemistry, 1949. 21(9): 1123-1125.

112. Spicar-Mihalic, P., et al., CO2 laser cutting and ablative etching for the fabrication of paper-based devices. Journal of Micromechanics and Microengineering, 2013. 23(6): 067003.

113. Cassano, C.L. and Fan, Z.H., Laminated paper-based analytical devices (LPAD): fabrication, characterization, and assays. Microfluidics and nanofluidics, 2013. 15(2): 173-181.

114. Songjaroen, T., et al., Blood separation on microfluidic paper-based analytical devices. Lab on a Chip, 2012. 12(18): 3392-3398.

115. Songjaroen, T., et al., Novel, simple and low-cost alternative method for fabrication of paper-based microfluidics by wax dipping. Talanta, 2011. 85(5): 2587-2593.

116. Dungchai, W., Chailapakul, O., Henry, C.S., A low-cost, simple, and rapid fabrication method for paper-based microfluidics using wax screen-printing. Analyst, 2011. 136(1): 77-82.

117. Sameenoi, Y., et al., One-step polymer screen-printing for microfluidic paper-based analytical device (μPAD) fabrication. Analyst, 2014. 139(24): 6580-6588.

118. Jeong, S.-G., et al., Toward instrument-free digital measurements: a three-dimensional microfluidic device fabricated in a single sheet of paper by double-sided printing and lamination. Lab on a Chip, 2015. 15(4): 1188-1194.

119. Camplisson, C.K., et al., Two-ply channels for faster wicking in paper-based microfluidic devices. Lab on a Chip, 2015. 15(23): 4461-4466.

120. de Tarso Garcia, P., et al., A handheld stamping process to fabricate microfluidic paper-based analytical devices with chemically modified surface for clinical assays. Rsc Advances, 2014. 4(71): 37637-37644.

121. Akyazi, T., et al., Fluidic flow delay by ionogel passive pumps in microfluidic paper-based analytical devices. Sensors and Actuators B: Chemical, 2016. 233: 402-408.

122. Kao, P.-K., and Hsu, C.-C., One-step rapid fabrication of paper-based microfluidic devices using fluorocarbon plasma polymerization. Microfluidics and nanofluidics, 2014. 16(5): 811-818.

123. Maejima, K., et al., Inkjet printing: an integrated and green chemical approach to microfluidic paper-based analytical devices. RSC advances, 2013. 3(24): p. 9258-9263.

124. Renault, C., et al., based bipolar electrochemistry. Journal of Electrochemical Science and Technology, 2013. 4(4): 146-152.

125. Rattanarat, P., et al., Multilayer paper-based device for colorimetric and electrochemical quantification of metals. Analytical chemistry, 2014. 86(7): 3555-3562.

126. Nyein, H.Y.Y., et al., Regional and correlative sweat analysis using high-throughput microfluidic sensing patches toward decoding sweat. Science advances, 2019. 5(8): eaaw9906.

127. Määttänen, A., et al., A low-cost paper-based inkjet-printed platform for electrochemical analyses. Sensors and Actuators B: Chemical, 2013. 177: 153-162.

128. Hu, C., et al., Inkjet printing of nanoporous gold electrode arrays on cellulose membranes for high-sensitive paper-like electrochemical oxygen sensors using ionic liquid electrolytes. Analytical chemistry, 2012. 84(8): 3745-3750.

129. da Costa, T.H., et al., A paper-based electrochemical sensor using inkjet-printed carbon nanotube electrodes. ECS Journal of Solid State Science and Technology, 2015. 4(10): S3044-S3047.

130. Shamkhalichenar, H. and Choi, J.-W., An inkjet-printed non-enzymatic hydrogen peroxide sensor on paper. Journal of The Electrochemical Society, 2017. 164(5): B3101-B3106.

131. Li, X., et al., Fabrication of paper-based microfluidic sensors by printing. Colloids and surfaces B: Biointerfaces, 2010. 76(2): 564-570.

132. Wang, J., et al., Morphology and entrapped enzyme performance in inkjet-printed sol–gel coatings on paper. Chemistry of Materials, 2014. 26(5): 1941-1947.

133. Kit-Anan, W., et al., Disposable paper-based electrochemical sensor utilizing inkjet-printed Polyaniline modified screen-printed carbon electrode for Ascorbic acid detection. Journal of Electroanalytical Chemistry, 2012. 685: 72-78.

134. Lu, Y., et al., Rapid prototyping of paper-based microfluidics with wax for low-cost, portable bioassay. Electrophoresis, 2009. 30(9): 1497-1500.

135. He, Y., et al., Fabrication of paper-based microfluidic analysis devices: a review. Rsc Advances, 2015. 5(95): 78109-78127.

136. Brito-Pereira, R., et al., Reconfigurable 3D-printable magnets with improved maximum energy product. Journal of Materials Chemistry C, 2020, 8(3): 952 - 958

137. Lu, Y., et al., Fabrication and characterization of paper-based microfluidics prepared in nitrocellulose membrane by wax printing. Analytical chemistry, 2010. 82(1): 329-335.

138. Phillips, E.A., et al., Thermally actuated wax valves for paper-fluidic diagnostics. Lab on a Chip, 2016. 16(21): 4230-4236.

139. Koo, Y., Sankar, J., and Yun, Y., High performance magnesium anode in paper-based microfluidic battery, powering on-chip fluorescence assay. Biomicrofluidics, 2014. 8(5): 054104.

140. Mace, C.R. and Deraney, R.N., Manufacturing prototypes for paper-based diagnostic devices. Microfluidics and nanofluidics, 2014. 16(5): 801-809.

141. Nguyen, T.-T.T., Huy, B.T., and Lee, Y.-I., Disposable Colorimetric Paper-Based Probe for the Detection of Amine-Containing Gases in Aquatic Sediments. ACS omega, 2019. 4(7): 12665-12670.

142. Martin, A.B., et al., Development of a high-throughput magnetic separation device for malaria-infected erythrocytes. Annals of biomedical engineering, 2017. 45(12): 2888-2898.

143. Carvalho, E.O., et al., Tailoring bacteria response by piezoelectric stimulation. ACS applied materials & interfaces, 2019. 11(30): 27297-27305.

144. Mariani, G., et al., High-gradient magnetic separation of pollutant from wastewaters using permanent magnets. Separation and Purification Technology, 2010. 72(2): 147-155.

Chapter 2.

Advanced polymer-based substrates for microfluidic applications

2.1. Tailoring electrospun poly(l-lactic acid) nanofibers as novel substrates portable analytical systems

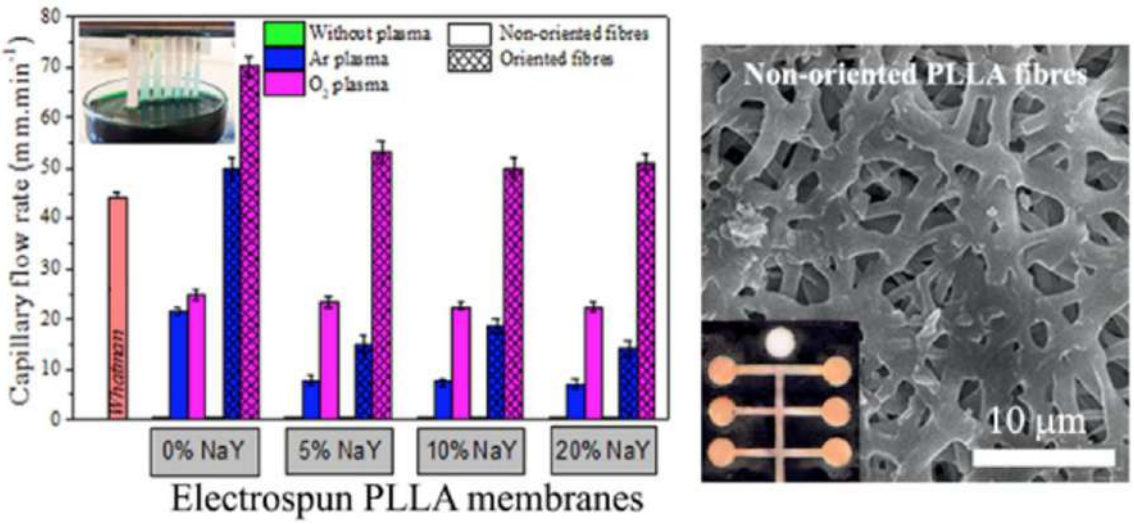

Novel microfluidic substrates based on electrospun poly(l-lactic acid) (PLLA) membranes were developed to increase the limited range of commercially available paper substrates, commonly used for the fabrication of microfluidic paper-based analytical devices (µPADs). PLLA advantageous properties include being biodegradable, biocompatible, easily processed in various tailored morphologies, and cost effective, among others. Oriented and non-oriented electrospun PLLA membranes were fabricated using electrospinning and the influence of fibre orientation, addition of hydrophilic additives and plasma treatments on the morphology, physicochemical properties and capillary flow rate were evaluated and compared with commercial Whatman paper. In addition, a proof-of-concept application based on the colorimetric detection of glucose in printed PLLA and paper-based microfluidic systems was also performed.

This chapter is based on the following publication: Ricardo Brito-Pereira, Eduardo S. Pimentel, Teresa Marques-Almeida, Clarisse Ribeiro, Filipe Vaz, Senentxu Lanceros-Mendez, Vanessa F. Cardoso, Tailoring electrospun poly(l-lactic acid) nanofibers as substrates for microfluidic applications, ACS applied materials & interfaces 12 (1), 60-69 (2019).

2.1.1. Introduction

Microfluidic paper-based analytical devices (μPADs) represent a promising platform for the development of fast, portable, disposable and cost-effective analytical tools in clinical diagnostic, environmental monitoring and food safety, among others [1]. This motivation is supported by the potential of μPADs to address the ASSURED (Affordable, Sensitive, Specific, User-friendly, Rapid and robust, Equipment-free and Deliverable to end-users) criteria for the development of portable analytical devices (PADs) defined by the World Health Organization (WHO), enabling local communities in developing regions to improve healthcare, environmental safety, animal health and food quality [2]. They were first introduced in 2007 as alternative to silicon, glass and PDMS materials, commonly used for prototyping and proof-of-concept studies [3]. Paper is typically made of cellulose fibres and shows the advantages of being inexpensive, ubiquitous, biocompatible and scalable [4]. In addition, cellulose's hydrophilicity, combined with patterned hydrophobic microfluidic barriers to create channels, generate sample flow via capillary action from an inlet to a defined reaction place for subsequent analysis [5]. Although with extensive academic developments, the entry of μPADs into real-life applications is still very limited [6]. This discrepancy may be related to the limited grade and properties of commercially available papers with low storage stability, poor wet strength, and limited control of fluid flow [7]. In this sense, various strategies have been developed for programmable and analyte manipulation (e.g. filtering, mixing, heating, separation, concentration) by the integration of functional components into μPADs, including diode valves, dissolvable sugar barriers and external electromagnets [8]. Moreover, there have been attempts to control the flow by tailoring the channels design, guiding the fluid to transport vertically and laterally through paper sheets and using materials such as threads and yarns [9]. However, the reported strategies have limitation for rapid and easy production.

Thus, as an attempt to address the limitations with the existing μPADs, alternative microfluidic substrates to complement paper have been developed in the present work. PLLA, a aliphatic semi-crystalline polyester, constitutes a promising candidate for this purpose. In fact, PLLA, which is a Food and Drug Administration (FDA) approved biomaterial, has attracted wide interests, from academic research to industry, due to its biocompatibility and biodegradability, as well as environmental friendliness and low-cost [10]. In addition, PLLA is also piezoelectric, allowing to convert mechanical energy into electrical and vice versa, which has been successfully used in tissue engineering and related biomedical applications [11]. A number of methods have been reported for the production of different types of PLLA structures such as films [12], membranes [13], fibres [14] and spheres [15], among others. Fibrous membranes are

particularly interesting for microfluidic applications based on the similar morphology with commercial Whatman cellulose filter paper grades, commonly used for the manufacture of μPADs [16]. They have been produced by a variety of methods such as template synthesis, self-assembly, phase separation, wet spinning, microfluidic spinning and electrospinning [17]. Within these techniques, electrospinning is currently the only one that allows the simple and reproducible fabrication of functional fibres to be applied in microfluidics [18] with diameters from few nanometres to several micrometres by applying a high electrical field to a droplet of polymer or composite solution from natural or synthetic polymers [18,19]. By properly controlling the composition of the polymer-based solution and processing parameters, a stable process can be achieved allowing to obtain structures ranging from single fibre to ordered arrangement of fibres with tailored fibre dimension and orientation [20]. The major drawback of PLLA-based electrospun membranes is associated to its inherent hydrophobicity, poor wettability and low surface energy that must be overcome so that it can be used as substrate, similar to paper, for the fabrication of microfluidic systems. Various strategies can be used to modify the surface properties and thus tailor the polymer wettability, such as chemical grafting, self-assembly and surface hydrolysis [21]. Another reported strategy involves the integration of specific fillers (such as polyethylene glycol [22], hydrophilic zeolites [23], superhydrophilic metal-organic frameworks [24], wet-chemistry treatment [25], among others) on the polymer matrix in order to reduce the hydrophobic behaviour of polymers [26].

Nevertheless, plasma treatment is one of the most extensively used methods to tailor surface adhesion and wetting properties, by the insertion of chemically reactive functional groups on the polymer surface, modifying its composition without affecting their bulk characteristics. A proper selection of plasma atmosphere (oxygen O_2, argon Ar, hydrogen H_2, or nitrogen N_2, among others), power and time is the key to ensure the success of the plasma treatment [27]. This approach has been used to promote surface modification in PLLA [28]. Thus, the surface modification of melt-extruded sheets of PLLA under O_2, H_2 and N_2 plasmas has been investigated, and the obtained results demonstrated a significant increase of the surface wetting, by the incorporation of polar groups composed of carboxylic (–COOH) and hydroxyl (–OH), along with a pronounced modification of its morphology, which depends much on the type of plasma [29]. Poly(glycolic acid) (PGA), poly(lactic-co-glycolic acid) (PLGA) and PLLA have been processed by electrospinning to obtain nanofibrous membranes, followed by a post-treatment by O_2 plasma and *in situ* grafting of hydrophilic acrylic acid (AA), which results in higher ratios of oxygen to carbon, lower contact angles and the presence of –COOH groups [30]. The influence of Ar-plasma treatments on flat rigid PLLA substrates, obtained by melting of PLLA powder on glass slide [31], shows that different times of this type of plasma treatment allows to achieve controlled water contact angles, down to the

superhydrophilic regime. Similarly, the suitability of carbon dioxide (CO_2) plasma treatment has been proved to decrease the hydrophobicity of PLLA surface, by the introduction of O_2-containing functional groups [32]. The hydrophobicity of PLLA has been also reduced by helium (He) atmospheric pressure plasma treatment, Ar and O_2 plasma treatments [33]. It is to notice that most of the aforementioned studies have been tested and applied, mostly on tissue engineering applications, in order to tailor cell-biomaterial interfaces. On the other hand, only few studies reports on the stability of plasma treatment over time. To the best of our knowledge, there is no work reporting on the processing of PLLA-based materials with stable superhydrophilic behavior, to be used as substrate, instead of paper, for the fabrication of microfluidic systems.

In this work, the effect of hydrophilic additives (NaY zeolites) and plasma treatments (using O_2 and Ar atmospheres) on the surface wettability and others relevant physicochemical properties of electrospun PLLA-based membranes are investigated. Randomly oriented electrospun PLLA-based membranes were first produced in an attempt to mimic the structure of commercial Whatman papers, commonly used in the fabrication of μPADs. Oriented electrospun PLLA membranes were also manufactured to study the effect of fibres orientation. Thus, microfluidic substrates based on biodegradable and biocompatible PLLA material with superhydrophilic behaviour, high storage stability, high wet strength and controlled fluid flow are obtained.

2.1.2. Experimental procedures

2.1.2.1. Materials

PLLA with an average molecular weight of 217.000-225.000 $g.mol^{-1}$ (*Purasorb PL18*) and NaY zeolites (CBV 100: SiO_2/Al_2O_3 mole ratio: 2.83; nominal cation form: sodium; Na_2O weight: 13 %; unit cell size: 24.65 Å; surface area: 900 $m^2.g^{-1}$) were supplied by Purac and Zeolyste International, respectively. N,N-dimethylformamide (DMF) and dichloromethane (DCM) were obtained from Merck and Sigma-Aldrich, respectively. Whatman filter paper, was purchased from Sigma-Aldrich. All chemicals and solvents were used as received.

2.1.2.2. Sample preparation

2.1.2.2.1. Randomly oriented electrospun substrates

Randomly oriented electrospun PLLA-based membranes were produced in an attempt to mimic the structure of commercial Whatman papers, commonly used in the fabrication of μPADs, whose microstructure consist of flat randomly oriented fibres. A 10 wt.% solution of PLLA in 3/7 vol/vol DMF/DMC mixture was prepared under magnetic stirring (IKA C-MAG HS7) at room temperature, until complete dissolution of the polymer. In the preparation of polymer solutions with zeolites, NaY was previously dispersed in the solvents under ultrasound bath for 1 h, followed by the addition and dissolution of PLLA by magnetic stirring. NaY percentages of 0, 5, 10 and 20 % relative to the polymer mass were studied. Then, the polymer solution was placed in a 10 mL plastic syringe fitted with a steel needle with an inner diameter of 500 μm and introduced into a syringe pump (Syringepump). The electrospinning procedure was conducted at 17 kV by means of a high voltage power supply (Glassman PS/FC30P04) at a solution feed rate of 0.5 $mL.h^{-1}$. Finally, randomly oriented electrospun membranes were collected on a grounded static plate collector with (20 cm x 15 cm) placed 15 cm away from the needle.

2.1.2.2.2. Oriented electrospun substrates

In addition, oriented electrospun PLLA-based membranes were processed to increase the range of microfluidic substrate structures, as well as to study the influence of fibre orientation on the capillary flow rate. The sample preparation is similar to the one described in section 2.2.1, except for the use of a rotating collector. Thus, oriented PLLA-based fibres were produced using a grounded rotating drum collector at a velocity of 1500 rpm. In this case, the addition of NaY zeolites was also performed.

2.1.2.3. Surface modification

As previously exposed, a limitation of PLLA comparatively to cellulose-based microfluidic substrates arises from their high hydrophobicity. Plasma treatments were performed, which is a technique commonly used to alter the hydrophobicity of polymers [31]. The success of a plasma treatment is associated with the selection of the plasma atmosphere (O_2, Ar, N_2, among others), treatment time and applied power. Oxygen is one of the most reactive elements and can generate carboxyl groups on the surface of polymers due to the incorporation of hydrophilic functional groups. Argon, in turn, tends to lead to relevant changes in surface morphology [21,27].

Surface treatments were conducted in a plasma chamber (Zepto, Diener Electronics), equipped with a 40 kHz radio frequency plasma generator. The base pressure, before plasma ignition, was 20 Pa. Plasma treatments were performed independently with O_2 and Ar as working gases, for 10 min. A plasma power of 100 W under a total pressure of 80 Pa was applied. This procedure was performed on both surfaces of the processed PLLA-based substrates.

2.1.2.4. Samples characterization

2.1.2.4.1. Physicochemical characterization

A scanning electron microscope (SEM) Quanta 650 FEG from FEI was employed to characterize the morphology of the electrospun PLLA-based membranes. The samples were previously coated with a thin gold layer using a sputter coater Polaron SC502. The mean fibre diameter and corresponding standard deviation were calculated measuring approximately 50 fibres by means of ImageJ software.

Surface wettability of the samples was evaluated by measuring the contact angle (CA) of 3 µL ultrapure water drop using a CA analyser Data-Physics OCA20. Six measurements were carried out in each membrane at different locations, the CA being reported as the average and standard deviation.

Fourier transformed infrared spectroscopy in attenuated total reflectance mode (FTIR-ATR) measurements were performed at room temperature using a Spectrum Two™ from Perkin-Elmer, with 64 scans in the range between 400 and 4000 cm^{-1} and a resolution of 4 cm^{-1}.

Differential scanning calorimetry (DSC) was performed with a DSC 6000 from Perkin-Elmer. Pieces of approximately 6 mg were cut and placed into 40 µL aluminium pans. The samples were heated between 30 and 200 °C at a scanning rate of 10 °C.min^{-1}. The degree of crystallinity (ΔX_C) was calculated using the following equation $\Delta X_C=(\Delta H/\Delta H_m^0) \times 100$, where ΔH is the area under the thermogram between 65 and 160 °C and ΔH_m^0 is the melting enthalpy for fully crystallized PLLA samples (93.1 $J.g^{-1}$) [35]. The mechanical properties were studied by means of a Shimadzu AD-IS with a load cell of 50 N. Samples with length and width of 15 and 10 mm, respectively, were prepared and stretched at a rate of 1 $mm.min^{-1}$. The oriented fibers were evaluated along the fiber direction. The thickness of the samples ranged between ~30 and ~100 µm. The essays were performed on dry and wet samples using in this last case 40 µL of water. Three tests were performed for each sample.

2.1.2.4.2. Cytotoxicity assay

Indirect cytotoxicity evaluation of the processed electrospun PLLA-based membranes was performed adapting the ISO 10993-5 standard test method. MC3T3-E1 pre-osteoblast cells (Riken cell bank, Japan) were cultured in 75 cm^2 cell culture flask at 37 °C, 5 % CO_2, in humidified environment using Dulbecco's modified Eagle's medium (DMEM, Gibco) containing 1 $g.L^{-1}$ glucose, 10 % fetal bovine serum (FBS, Biochrom) and 1 % (v/v) penicillin/streptomycin solution (P/S, Biochrom). Sterilization of the samples (13 mm diameter) were carried out by multiple immersion into 70 % ethanol for 30 min each, washing with sterile phosphate-buffered saline solution (PBS; 137 mM NaCl; 2.7 mM KCl, 10 mM Na_2HPO_4, 1.8 mM KH_2PO_4 at pH 7.4) for 5 min and exposition to ultraviolet radiation for 1 h each side. Thus, a suspension of 2×10^4 $cell.mL^{-1}$ was seeded in 96-well tissue culture polystyrene plates and incubated for 24 h at 37 °C with 5 % CO_2 in humidified environment to ensure cell attachment on the plate. Simultaneously, each sample was incubated for 24 h in 24-well tissue culture polystyrene plate under the conditions described above. After the incubation time, the cell culture medium in the 96-well plates was removed and 100 µL of culture medium that was in contact with the different samples was added to each well, individually. Cell viability was then evaluated after 72 h of incubation using the MTT proliferation assay according to the manufacturer's instructions (Sigma-Aldrich). Briefly, the medium of every well was removed and fresh medium containing MTT solution (5 $mg.mL^{-1}$ of MTT dissolved in DMEM in a 1:10 ratio) was added to the cells and incubated for 2 h at 37 °C in the dark. Thus, the MTT solution was removed and the precipitated formazan was dissolved with 100 µL dimethyl sulfoxide (DMSO)/well followed by measuring the optical density at 570 nm. Cells cultured in 20 % DMSO (Sigma-Aldrich) and standard culture medium were used as negative and positive controls, respectively. All quantitative results were obtained from four replicate samples and controls and presented as the average of viability ± standard deviation. The percentage of cell viability was calculated according to the following equation 2.1.1 [36].

$$\text{Cell viability } (\%) = \frac{\text{Absorbance of sample}}{\text{Absorbance of negative control}} \times 100 \qquad (2.1.1)$$

2.1.2.4.3. Capillary flow rate tests

Capillary flow rate represents the speed at which a liquid sample moves along a membrane strip in a diagnostic test strip or application. A proper control of this flow will enable to select the appropriate membrane for a specific application [37]. Thus, capillary tests were performed on all samples without

and with plasma treatments. Strips with dimensions of 2.5 cm length and 1 cm width were cut and placed vertically in contact with a water solution containing food colouring. The sample portion immersed in the solution was 0.5 cm and the time taken for the dye to travel across the sample in the "antigravity" direction was measured. These tests allow to evaluate the effect of the fibre orientation, presence of zeolites and plasma treatments with Ar and O_2, in the capillary flow rate and ultimately on the ability of the processed materials to generate passive flows.

2.1.2.5. Proof-of-concept

Glucose essays based on colorimetric detection were performed using a glucose kit from BioLabo Reagents™. During the reaction, glucose is oxidized by the enzyme glucose oxidase to gluconic and hydrogen peroxide, which in conjunction with peroxidase, reacts with chloro-4-phenol and 4-amino-antipyrine to form a red quinoneimine. The intensity of the coloured complex is proportional to the concentration of glucose. As a simple proof-of-concept, calibration curves were built using the following glucose concentrations: 10, 25, 75, 150 and 500 $mg.dL^{-1}$, for both commercial Whatman paper and non-oriented electrospun PLLA membranes with 10 % NaY (as representative example). A microfluidic system was designed using a computer aided design software and printed on both substrates using a Xerox ColorQube 8580 printer, as illustrated in Figure 2.1.1. After printing, the samples were placed on a heating plate at 90 °C during 10 min so that the wax penetrates the entire cross-section of the membrane and thus creating hydrophobic barriers that will contain the fluid. This temperature is slightly lower than the commonly used in paper (100 °C for 2 min) to maintain the integrity of the PLLA samples that undergo mechanical deformations when subjected to higher temperatures.

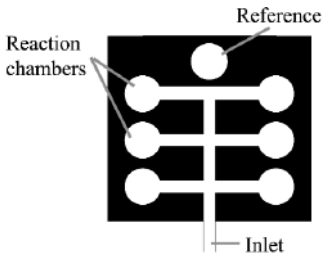

Figure 2.1.1. Microfluidic system design used for the quantification of glucose. Each reaction chambers and reference were first functionalized with reagent. The glucose oxidase flow by capillarity from the inlet to the reaction chamber to form a red colour with intensity proportional to the concentration of glucose. The reaction chamber features an area of ~80 mm^2 and the channels a width of 1.2 mm.

Each microfluidic system comprises six reaction chambers for the reproducibility of the study. A total of five microfluidic systems corresponding to the five studied glucose concentrations were printed in each substrate. The reagent chambers were first functionalized using 15 μL of reagent. After approximately 5 min, the inlet of the microfluidic system was introduced into the glucose solution under study, reaching the reaction chamber by capillarity. After 10 min of reaction, a red colour with intensity proportional to the concentration of the glucose was formed. Image analysis was performed by using ImageJ software in each microfluidic system. For each reaction chamber, the grey value and corresponding standard deviation were measured and the calibration curve was built.

2.1.3. Experimental Results and Discussion

Microfluidic substrates based on electrospun PLLA-based membranes were processed as an alternative to paper filters, such as the Whatman cellulose filter paper grades, commonly used for the fabrication of μPADs [16]. The effect of PLLA fibre orientation, introduction of NaY zeolites in the polymer matrix and plasma treatments with Ar and O_2 on the morphology, physicochemical properties and capillary flow rate were properly studied and compared with commercial Whatman.

2.1.3.1. Physicochemical characterization

Representative SEM images of commercial Whatman and non-oriented and oriented electrospun PLLA-based membranes are shown in Figure 2.1.2. The respective mean fibre diameter and standard deviation are presented in Figure 2.1.3.

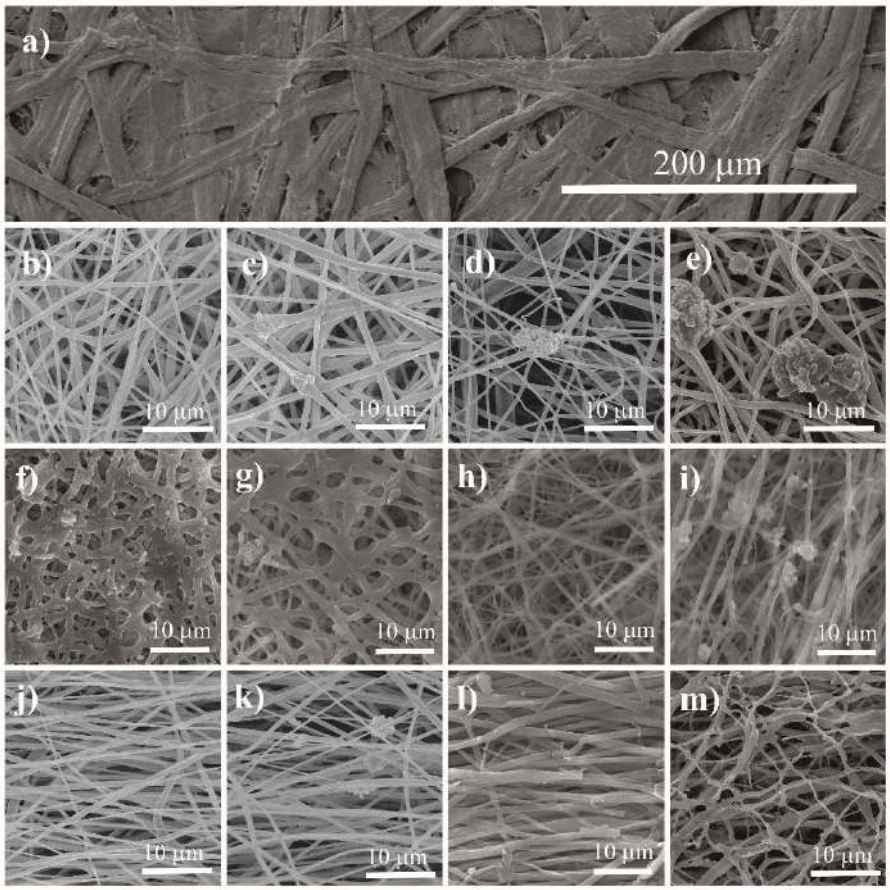

Figure 2.1.2. Representative SEM images of a) commercial Whatman; non-oriented PLLA fibres with NaY filler content of b) 0 %, c) 5 %, d) 10 %, e) 20 %, f) 0 % and Ar plasma treatment, g) 20 % and Ar plasma treatment, h) 0 % and O_2 plasma treatment, i) 20 % and O_2 plasma treatment; oriented PLLA fibres with NaY filler content of j) 0 %, k) 20 %, l) 0 % and Ar plasma treatment, m) 0 % and O_2 plasma treatment.

Whatman membranes consist of cellulose fibres with a flat microstructure associated with the pressing process generally employed in the manufacture of paper (Figure 2.1.2.). The fibres show sizes in the micrometre scale, with average width of ~16±7 µm. In turn, untreated electrospun PLLA-based membranes are characterized by finer and rounded fibres with smooth surface, spatially distributed both longitudinally and transversally (Figures 2.1.2b-e and Figures 2.1.2k). The dimension, orientation and distribution of the fibres are not affected by the introduction of zeolites, whose presence is confirmed by some clusters in the corresponding SEM images.

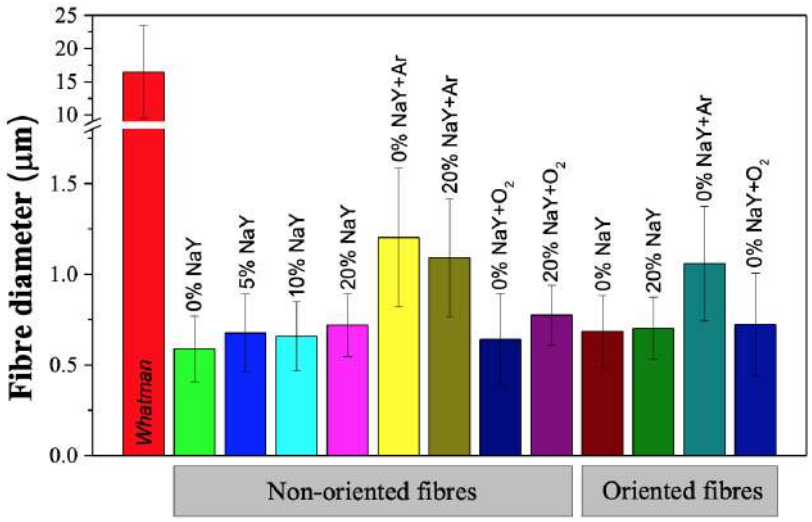

Figure 2.1.3. Fibre diameter of commercial Whatman and representative electrospun PLLA-based membranes.

Regardless the orientation of the fibres or presence of zeolites, fibres with average diameter of 650±200 nm are obtained. After plasma treatments, important fibre modifications were observed, being more evident using Ar as working gas. This result is consistent with the literature [21,33]. Surface modification by plasma treatment can cause the cleavage of polymer molecular chains promoting, therefore, the formation of free radicals that activate the surface [13]. While O_2 is one of the most reactive elements and can generate carboxyl group on the polymer surface due to the incorporation of hydrophilic functional groups, Ar typically leads to relevant changes in surface morphology [13,21]. Thus, it is observed that the diameter of the PLLA fibres remains approximately the same after O_2 plasma treatment, whereas an increase of this value occurs when Ar plasma treatment is performed, showing flat fibres with average surface width of 1.10±0.40 µm. In addition, Ar plasma treatment leads to the fusion of non-oriented fibres. On the other hand, Ar plasma treated PLLA oriented fibres also show significant morphological variations, but the fibres remain intact and with defined orientation. After O_2 plasma treatment, PLLA fibres show some fusion between them, and the orientation appears to be compromised in the case of initially oriented fibres. Surface polymer melting associated with the high power (100 W) and with the high exposure time (10 min) used during plasma treatment in electrospun PLLA-based membranes surfaces are at the origin of these behaviours. Although previous studies showed that shorter exposure times (lower than 1 min) can be used to generate superhydrophilic electrospun PLLA membranes, some alterations of the polymer fibrillar matrix were also observed [28,30,33]. More importantly, the stability of the superhydrophilic surface oven time, which is a key parameter in the scope

of the present work and applications, has not been demonstrated under the softer plasma treatment conditions used in these studies.

Figure 2.1.4 shows the CA measurement results of the commercial Whatman and non-oriented and oriented electrospun PLLA-based membranes, whose values remain stable for at least 1 month.

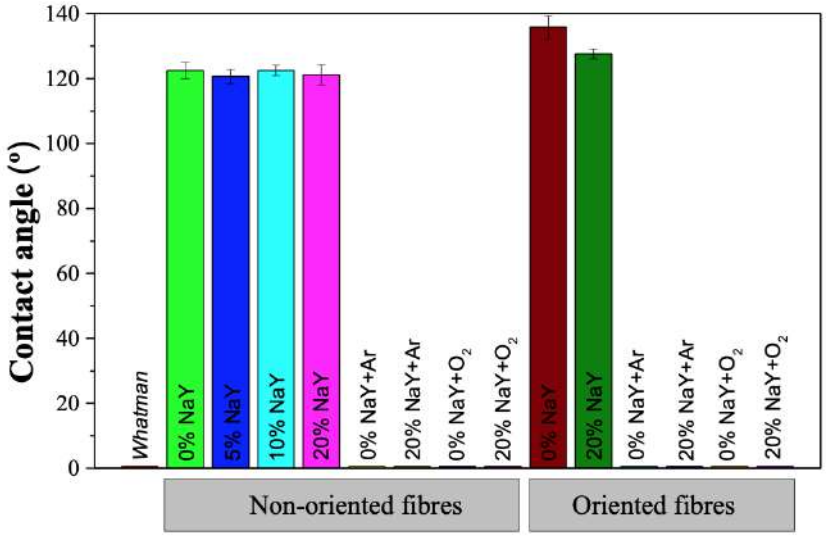

Figure 2.1.4. Contact angles of commercial Whatman and electrospun PLLA-based membranes, whose values remain stable for at least 1 month.

As previously stated, the major drawback of PLLA membranes comparatively to cellulose membranes for microfluidic applications is associated to their strong hydrophobicity that must be overcome to allow the generation of capillary flows, which cause the fluid to move through the membrane without the need for external actuation systems. Thus, the proper characterization of this parameter is of major relevance in the scope of this work. Surface wettability is governed by surface chemistry, surface energy and morphology [38] as well as by the properties of the liquid [39].

A simple and effective way to express wetting properties of a surface is by the CA of a droplet resting on a surface. A surface is generally called hydrophobic when its CA is higher than 90°, whereas a hydrophilic surface features a CA lower than 90°. Superhydrophobic and superhydrophilic are terms also used to characterize surfaces that present CA higher than 150° and lower than 10°, respectively [38,39]. While in flat and dense superhydrophilic surface it is expected that the water spreads completely as a flat film, in the case of porous films, i.e. membrane, it is expected that the water is absorbed through the material.

Figure 2.1.4 shows that Whatman membranes express a superhydrophilic behaviour with the water droplets being absorbed almost instantly, giving them suitable properties as substrate for microfluidic systems. In turn, the water surface CA of untreated electrospun PLLA-based membranes is 121.7±0.8° for non-oriented fibres and 131.7±4.1° for oriented fibres, demonstrating the strong hydrophobicity associated to PLLA [28]. The addition of zeolites between 0 and 20 % has no significant effect on the surface wettability of these samples, remaining hydrophobic. In this study, the Y zeolite (faujasite structure) on the sodium form (NaY) has been used because of its hydrophilic properties, related with its low Si/Al ratio [40]. Accordingly, a decrease in the CA with the addition of zeolites would be expected, which was not found, leading to the conclusion that the filler is wrapped by a polymer thin layer that does not allow the interaction between zeolite and water.

On the other hand, the post-treatment of electrospun PLLA-based membranes with both Ar and O_2 plasma gases leads to a strong reduction of the CA (Figure 2.1.4), preventing its measurement due to the immediate and total absorption of water droplets. This is justified by the increase of the surface energy after plasma treatment, resulting in a reduction of the CA. Thus, plasma treated electrospun membranes exhibit a paper-like superhydrophilic behaviour, suitable for microfluidic applications, with proven stability over 1 month, independently of the fibre orientation and presence of zeolites. This stability can be explained by the fact that after O_2 and Ar plasma treatments, stable physico-chemical fiber modifications are induced, as previously shown, and indicated, among others, by the slight decrease in the amount of carbon atoms and increase in the oxygen content [33]. The increase in oxygen content is more noticeable for PLLA fibers after O_2 exposure. Although the addition of zeolites has no significant effect on the wettability of the PLLA membranes, their presence will have a quantifiable effect on capillary flow tests, in the samples treated with plasma, as will be discussed in section 2.1.3.3.

FTIR-ATR measurements were carried out to study possible chemical variations in the PLLA polymer chain of the electrospun membranes. In addition, DSC measurements were conducted to evaluate possible changes on the thermal behaviour of the PLLA samples, in particular regarding the glass transition temperature that will set the higher temperature at which wax-based hydrophobic microfluidic channels can be printed and processed without deterioration of the structural properties of PLLA substrate. FTIR-ATR spectra and DSC curves of representative PLLA-based membranes are illustrated in Figure 2.1.5a and 2.1.5b.

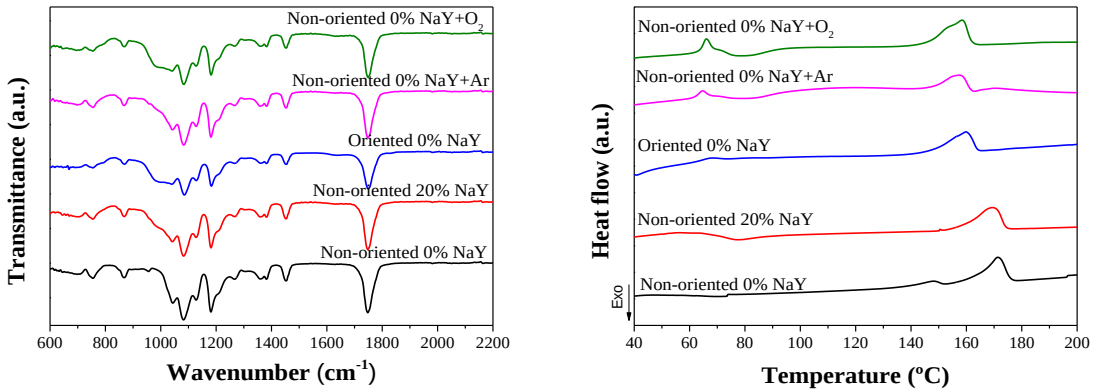

a) b)

Figure 2.1.5. a) FTIR-ATR spectra and b) DSC curves of representative electrospun PLLA-based membranes.

No noticeable variations are observed on the FTIR-ATR spectra of the electrospun PLLA-based membranes varying the processing conditions, namely in terms of orientation of the fibres, addition of zeolites, post-treatment with Ar or O_2 plasma, or combination of them. All spectra feature characteristic absorption bands at 755 and 870 cm^{-1}, related to CH_3 stretching and rocking, respectively [41]. The band at 1044 cm^{-1} is assigned to the stretching vibration of the C-CH_3 bond, while 1130, 1357 and 1450 cm^{-1} are attributed to $r_s(CH_3)$, $\delta(CH)$ and $\delta_{as}(CH)$ stretch, respectively. In turn, the absorption bands at 1083, 1185, 1271 and 1747 cm^{-1} are ascribed to ν_s(C-O-C), ν_{as}(C-O-C)+r_{as}(CH3), ν(CH)+ν(C-O-C) and ν(C=0), which is characteristic of the presence of O_2.

Regarding the thermal characterization, it is also shown that the processing conditions do not significantly influence the thermograms of the samples. All DSC curves are characterized by two endothermic peaks at 65 °C that correspond to the glass transition and a melting peak between 140 and 160 °C. A slight variation in the dynamic of the glass transition seems to occur in the PLLA samples treated with plasma, where the endothermic peak appears more evident. As previously stated, this temperature is relevant as it limits the temperature at which these substrates can be used without deterioration of their properties. This is not a concern for their use as microfluidic substrates for biomedical applications, where such high temperatures are hardly reached. However, the glass transition temperature should be considered during the fabrication of microfluidic systems when, for instance, wax printing is used. In this case, a post heating must be carried out to ensure a proper melting of the printed hydrophobic barriers to occupy the entire cross section of the microfluidic substrate, confining, therefore, the fluids. In addition, a broad exothermic

cold crystallization peak occurs approximately above the glass transition, at 85 °C. This behaviour is related to the formation of a well-defined crystal structure above the glass transition as a result of the ordering of the PLLA polymer chains in a regular array [35]. The electrospinning process leads to numerous crystal nuclei present in the polymer as a result of non-equilibrium chain conformations that crystallize in the heating process above the glass transition.

The degree of crystallinity of the PLLA samples remains approximately constant regardless of processing conditions, with a value of 30 %.

Membranes with proper mechanical properties are important for their use as microfluidic substrates, in particular when wetted, during functionalization and/or immersion in a solution containing the (bio)molecules to be quantified. Thus, strain-stress measurements were performed on dry and wet commercial Whatman and representative electrospun PLLA-based membranes. The characteristic stress-strain curves are presented in Figure 2.1.6a. From the linear regime of the curves, the Young's modulus was obtained by applying Hooke's law and presented in Figure 2.1.6b.

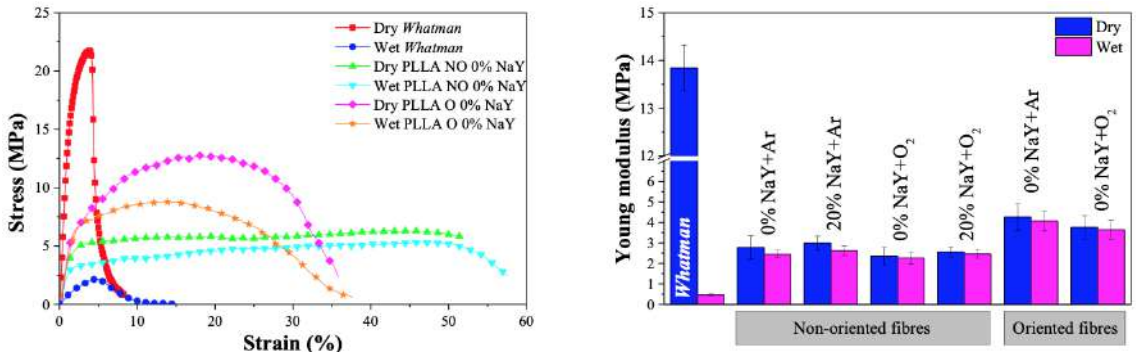

a) b)

Figure 2.1.6. a) Characteristic stress-strain curves and b) Young's modulus of commercial Whatman and representative electrospun PLLA-based membranes in dry and wet state.

Ductile materials are characterized by a linear elastic regime, followed by the yielding region, where the material enters in the plastic regime and suffers permanent deformation to any further increase in load or stress. By further stretching the samples, the rupture region is reached. In turn, brittle materials usually present little or no plastic deformation, fracturing near the end of the linear-elastic region of the curve. The mechanical response of the commercial Whatman paper features almost no plastic regime in both dry and wet state, contrary to the electrospun PLLA-based membranes. In all tested substrates, wet membranes show lower mechanical properties. In fact, less stress is required to deform wet membrane, being more significant for commercial Whatman papers. By analysing in more detail, the Young's modulus obtained from the linear regime, where materials are generally used, it is concluded that dry commercial

Whatman presents a more rigid behaviour with the highest Young's modulus of 13.8±0.5 MPa, decreasing significantly to 0.5±0.1 MPa when wet. In turn, electrospun PLLA-based membranes are more stable, nearly maintaining their elastic behaviour, with Young's modulus only undergoing a slight reduction when the membranes are wet. An average Young's modulus of 2.6±0.3 MPa was obtained for the non-oriented electrospun PLLA-based membranes, increasing to 3.9±0.5 MPa with the orientation of the PLLA fibres. No significant variation was observed with the addition of zeolites and plasma treatments.

2.1.3.2. Cytotoxicity essay

Cell viability of PLLA samples was assessed by indirect contact using MC3T3-E1 pre-osteoblast cell line. The results are presented in Figure 2.1.7.

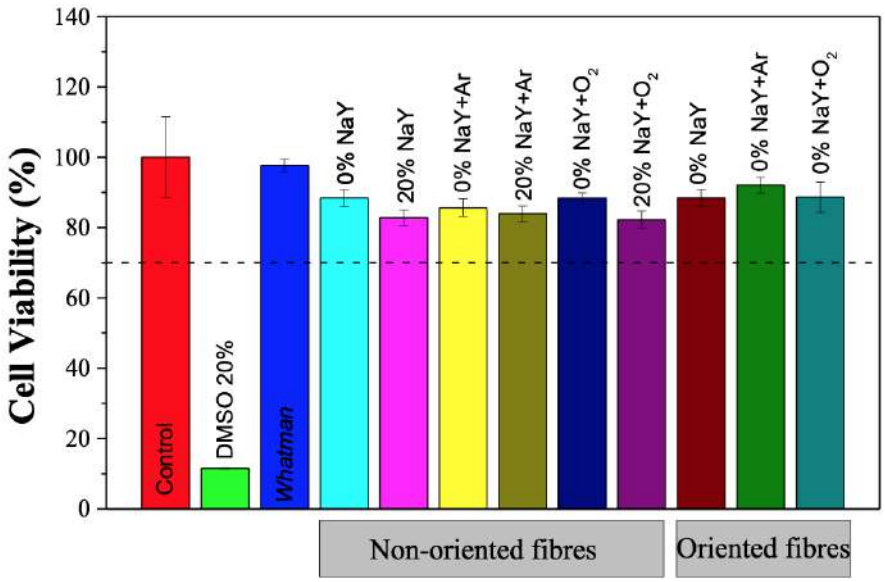

Figure 2.1.7. Cytotoxicity assay of MC3T3-E1 pre-osteoblast cells in contact with the as-prepared extraction media exposed to commercial Whatman and representative electrospun PLLA-based membranes for 72 h (relative cell viability was presented as the percentage of the negative control (n=4±SD)).

It is demonstrated that the processed samples do not show cytotoxic effect, with cell viability values higher than 70 %, which is the threshold accepted according to the ISO standard 10993-5. The addition of zeolites and plasma treatments with Ar and O_2 has no significant effect on the toxicity of the material. The same behaviour is presented by the commercial Whatman. Thus, it is proved that the processed samples can be used for biomedical applications.

2.1.3.3. Capillary flow rate tests

Capillary flow tests were performed in order to validate the possible use of the processed PLLA substrates in the development of microfluidic systems, where passive flows must be generated. As previously stated, thin strips of each sample were cut and dipped vertically and partially into a water solution containing food colouring. The results presented in Figure 2.1.8 were obtained calculating the time required for the dye to travel through the strip with a length of 2 cm (plus 0.5 cm dipped in solution).

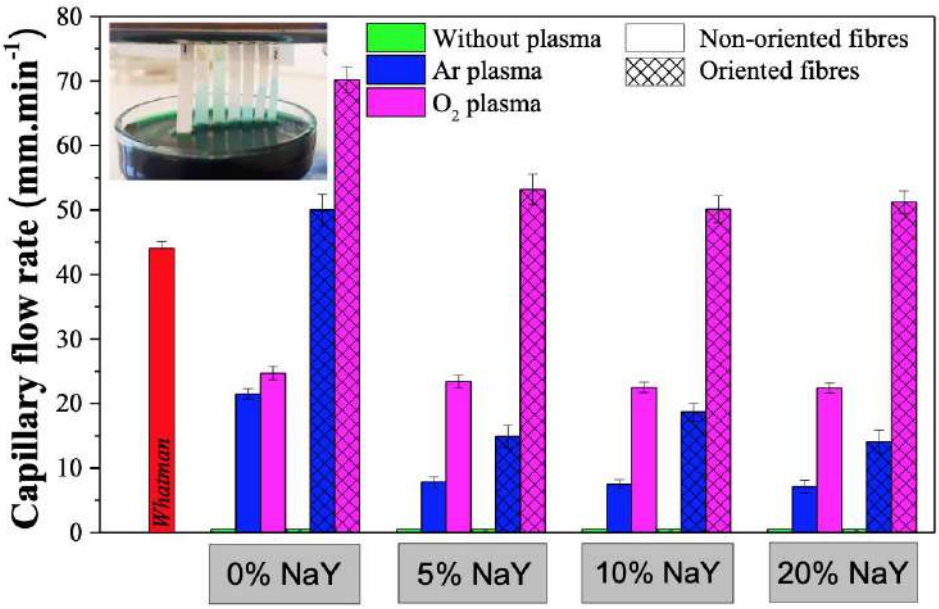

Figure 2.1.8. Capillary flow rates in the "antigravity" direction of dye solution in commercial Whatman and electrospun PLLA-based membranes strips.

The results demonstrate that the hydrophobic nature of the PLLA membranes, without plasma treatments, has a negative effect on the capillary flow rate, presenting no flow, regardless of zeolite concentration. In turn, because of its superhydrophilic behaviour, the plasma treated PLLA samples show capillary flow rates varying from 7.1±0.9 to 70.2±1.9 mm.min^{-1}, being the effect superior in samples treated with O_2 plasma. An interesting observation comes from the treated samples with zeolites, with capillary flow rates that tend to decrease with the presence of this additive, as demonstrated by comparing the samples with 0 % and 5 % filler content. Further, similar flow rates are observed for zeolite concentrations above 5 %, indicating that a saturation is reached with respect to the effect of the zeolite content in the flow rate. This result is justified by the high adsorption and the microporous structure of

NaY zeolites that will retain water molecules, leading to a consequent decrease in flow rate. Thus, although the presence of zeolites does not have the ability to change the surface hydrophobicity of the PLLA membranes by themselves, they demonstrate to have a relevant effect on the passively generated flow rate after plasma exposure. Another important conclusion is the capillary flow rate that increases significantly with the orientation of the fibres. Maximum values of 50±2.4 $mm.min^{-1}$ and 70.2±1.9 $mm.min^{-1}$ were obtained for the oriented PLLA fibres without zeolites and treated with Ar and O_2 plasma, respectively, comparatively to 21.5±0.8 $mm.min^{-1}$ and 24.7±1.0 $mm.min^{-1}$ obtained for the non-oriented PLLA fibres also without zeolites and treated with Ar and O_2 plasma, respectively. The higher fibre density and preferential orientation in the oriented PLLA samples compared to the non-oriented, as previously exposed in 2.1.2, can justify this result by allowing the dye to flow more easily, and consequently faster along the fibres of the PLLA strip. The lowest capillary flow rates were observed in the PLLA membranes constituted by non-oriented fibres with 20 % of zeolites and treated with Ar and O_2 plasma, with values of 7.1±0.9 $mm.min^{-1}$ and 22.4±0.8 $mm.min^{-1}$, respectively. In comparison, commercial Whatman features a capillary flow rate of 44±1.13 $mm.min^{-1}$. These results prove the ability of the processed PLLA substrates to generate passive flows. Controlling properly the processing parameters, namely in terms of PLLA fibres orientation, zeolites concentration and plasma treatment with Ar or O_2, it is possible to adjust the capillary flow rate according to a specific application that require controlled flow times and thus controllable reaction times, for example.

2.1.3.4. Proof-of-concept

Colorimetric assays based on the detection and quantification of glucose were evaluated on commercial Whatman and non-oriented PLLA membranes with 10 % NaY (as representative example) to demonstrate the viability and potential of the processed substrates for the fabrication of microfluidic systems in specific applications. Digital images of the glucose essays on the printed microfluidic systems are illustrated in Figure 2.1.9 and the corresponding calibration curves are presented in Figure 2.1.10. In this case, mean grey values are presented as a function of the logarithm of the glucose concentration ranging from 10 to 500 $mg.dL^{-1}$.

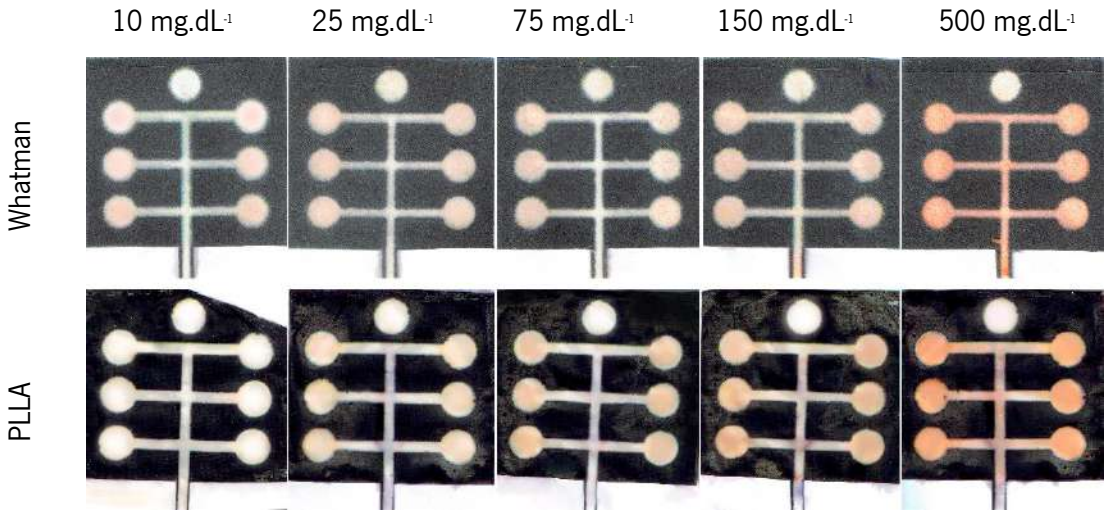

Figure 2.1.9. Digital images of microfluidic systems after glucose essays on commercial Whatman paper and non-oriented electrospun PLLA membranes with 10 % NaY (as representative example). From left to the right: glucose concentration of 10, 25, 75, 150 and 500 mg.dL^{-1}.

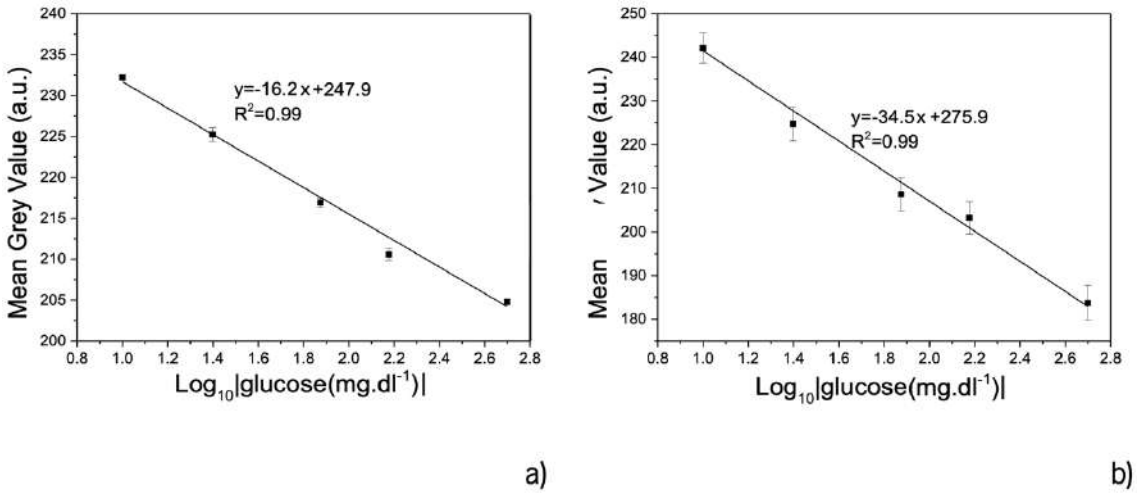

Figure 2.1.10. Calibration curves of glucose for a) commercial Whatman and b) non-oriented electrospun PLLA membranes with 10 % NaY (as representative example). The results are presented as mean grey value and corresponding standard deviation measured on the reaction chambers of the microfluidic substrates using ImageJ software according to the method described in [41].

Analysing first the print quality of the microfluidic systems on both substrates, it is concluded that the design loses some resolution in commercial Whatman paper, where the wax expands approximately

2 mm during the post-thermal treatment. Accordingly, this unavoidable effect must be taken into account when designing the microfluidic system since the width of the channels and, therefore, the dimensions of the entire system, is changed after the printing process, affecting not only the passive capillary flow rate but also the viability of the microfluidic system, depending on the application requirements. In turn, electrospun PLLA-based membranes feature the advantage of maintaining the dimension and definition of the microfluidic design. Regarding the colour of the reaction chambers, it is observed a gradual increase of the red colour intensity with increasing glucose concentration. The calibration curves, which present the correlations between the colour intensity, denoted as mean grey values, and the logarithm of glucose concentrations, demonstrate a good linearity with correlation coefficients R^2 of 0.99, in both substrates. It should be noted that the grey values were only analysed on the reaction chambers and the calibration curves built accordingly. Thus, the reddish colour observed on the channels of the microfluidic systems, which comes from colorimetric reaction between the reagent that flows passively outside the reaction chambers during functionalization and glucose, does not interfere with the measurements. In addition, the electrospun PLLA-based membranes demonstrate an improved sensibility with a curve slope of -34.5 comparatively to -16.2 obtained with the commercial Whatman. Thus, these results demonstrate the potential of the processed electrospun PLLA-based membranes as complementary or alternative substrates to the commonly used Whatman papers for the fabrication of microfluidic systems not just for colorimetric detection, as proven in this section, but also for other relevant (bio)technological applications that can take advantages of the demonstrated beneficial physicochemical properties of the processed substrates.

2.1.4. Conclusions

The present work reports on the processing and evaluation of electrospun PLLA membranes as innovative substrates for the fabrication of microfluidic systems, complementary or alternatives to the μPADs based on paper substrates. The influence of fibre orientation, addition of hydrophilic additives (NaY zeolites) and plasma treatments (Ar and O_2) on the morphology, physicochemical properties, biocompatibility and capillary flow rate were properly studied and compared with the commonly used paper substrates based on commercial Whatman. The results demonstrate that controlling properly the processing conditions, it is possible to tailor the morphology, surface hydrophilicity and capillary flow rate of the electrospun PLLA-based membranes, which is beneficial in order to reach specific applications requirements, which can be

difficult to obtain with the current commercially available paper substrates. Moreover, the developed materials are biocompatible, show good wet strength and appropriate thermal properties to be used as substrates for the fabrication of microfluidic substrates using wax printing technology. A proof-of-concept based on the colorimetric detection of glucose in printed microfluidic systems demonstrated the potential of PLLA substrates for the fabrication of portable analytical devices that benefit from the demonstrated controllable physicochemical and capillary flow rate properties. It is to notice that the smart properties of PLLA based on its piezoelectricity can be further explored to give rise to active multifunctional microfluidic substrates.

2.1.5. References

1. Martinez, A. W., et al., Patterned Paper as a Platform for Inexpensive, Low-volume, Portable Bioassays. Angew. Chemie - Int. Ed. 2007, 46(8), 1318-1320.

2. Yetisen, A. K., Akram, M. S., Lowe, C. R., Paper-based Microfluidic Point-of-Care Diagnostic Devices. Lab Chip 2013, 13(12), 2210-2251.

3. Nge, P. N., Rogers, C. I., Woolley, A. T., Advances in Microfluidic Materials, Functions, Integration, and Applications. Chem. Rev. 2013, 113(4), 2550-2583.

4. Yang, Y., et al., Paper-based Microfluidic Devices: Emerging Themes and Applications. Anal. Chem. 2017, 89(1), 71-91.

5. Wang, X., et al., Sensitive Colorimetric Assay for Uric Acid and Glucose Detection based on Multilayer-modified Paper with Smartphone as Signal Readout. Anal. Bioanal. Chem. 2018, 410(10), 2647-2655.

6. Yamada, K., et al., Toward Practical Application of Paper-based Microfluidics for Medical Diagnostics: State-of-the-art and Challenges. Lab Chip 2017, 17(7), 1206-1249.

7. Akyazi, T., Basabe-Desmonts, L., Benito-Lopez, F., Review on Microfluidic Paper-based Analytical Devices towards Commercialisation. Anal. Chim. Acta 2018, 1001, 1-17.

8. Jia, C., et al., Anisotropic, Mesoporous Microfluidic Frameworks with Scalable, Aligned Cellulose Nanofibers. ACS Appl. Mater. Interf. 2018, 10(8), 7362-7370.

9. Ballerini, D. R.; Li, X.; Shen, W., Patterned Paper and Alternative Materials as Substrates for Low-Cost Microfluidic Diagnostics. Microfluid. Nanofluidics 2012, 13(5), 769-787.

10. Kuang, T., et al., Facile Preparation of Open-Cellular Porous Poly(L-Lactic Acid) Scaffold by Supercritical Carbon Dioxide Foaming for Potential Tissue Engineering Applications. Chem. Eng. J. 2017, 307, 1017-1025.

11. Ribeiro, C., et al., Piezoelectric Polymers as Biomaterials for Tissue Engineering Applications. Colloids Surf. B: Biointerfaces 2015, 136, 46-55.

12. Carmagnola, I., et al., Tailored Functionalization of Poly(L-Lactic Acid) Substrates at the Nanoscale to Enhance Cell Response. J. Biomater. Sci., Polym. Ed. 2019, 30(7), 526-546.

13. Mattioli, S., Kenny, J. M., Armentano, I., Plasma Ssurface Modification of Porous PLLA Films: Analysis of Surface Properties and In Vitro Hydrolytic Degradation. J. Appl. Polym. Sci. 2012, 125 (SUPPL. 2), E239-E247.

14. Qiao, T., et al., Reinforced Electrospun PLLA Fiber Membrane via Chemical Crosslinking. Eur. Polym. J. 2016, 74, 101-108.

15. Hawari, A. A., Tham, C. Y., Hamid, Z. A. A., Effect of Synthesis Parameters on the Size of Biodegradable Poly(L-Lactide) (PLLA) Microspheres. Adv. Mat. Res., 2014, 858, 60-66.

16. Songjaroen, T., et al., Blood Separation on Microfluidic Paper-based Analytical Devices. Lab Chip 2012, 12(18), 3392-3398.

17. Huang, Z. M., et al., A Review on Polymer Nanofibers by Electrospinning and their Applications in Nanocomposites. Compos. Sci. Technol. 2003, 63(15), 2223-2253.

18. Reinholt, S., et al., Developing New Materials for Paper-based Diagnostics using Electrospun Nanofibers. Anal. Bioanal. Chem. 2014, 406(14), 3297-3304.

19. Bhardwaj, N., Kundu, S. C., Electrospinning: a Fascinating Fiber Fabrication Technique. Biotechnol. Adv. 2010, 28(3), 325-347.

20. Teo, W. E., Ramakrishna, S., A Review on Electrospinning Design and Nanofibre Assemblies. Nanotechnology 2006, 17(14), R89-R106.

21. Correia, D. M., et al., Influence of Oxygen Plasma Treatment Parameters on Poly(vinylidene fluoride) Electrospun Fiber Mats Wettability. Progr. Org. Coat. 2015, 85, 151-158.

22. Deng, F., et al., Microporous Polymer Electrolyte based on PVDF/PEO Star Polymer Blends for Lithium Ion Batteries. J. Memb. Sci. 2015, 491, 82-89.

23. Li, Q., et al., Preparation of Y-Zeolite/$CoCl_2$ Doped PVDF Composite Nanofiber and its Application in Hydrogen Production. Energy 2012, 38(1), 144-150.

24. Sun, H., Tang, B., Wu, P., Development of Hybrid Ultrafiltration Membranes with Improved Water Separation Properties Using Modified Superhydrophilic Metal-Organic Framework Nanoparticles. ACS Appl. Mater. Interf. 2017, 9(25), 21473-21484.

25. Ongaro, A. E., et al., Polylactic Acid, a Sustainable, Biocompatible, Transparent Substrate Material for Organ-On-Chip, and Microfluidic Applications. bioRxiv 2019, 647347.

26. González, E., et al., Surface Functional Poly(Lactic Acid) Electrospun Nanofibers for Biosensor Applications. Materials 2016, 9(1), 47.

27. Correia, D. M., et al., Surface Wettability Modification of Poly(Vinylidene Fluoride) and Copolymer Films and Membranes by Plasma Treatment. Polymer 2019, 169, 138-147.

28. Jin Seo, H., et al., Plasma Treatment Induces Internal Surface Modifications of Electrospun Poly(L-Lactic) Acid Scaffold to Enhance Protein Coating. J. Appl. Phys. 2013, 114(7), 073304.

29. Hirotsu, T., et al., Plasma Surface Treatments of Melt-Extruded Sheets of Poly(L-Lactic Acid). Polym. Eng. Sci. 2002, 42(2), 299-306.

30. Park, K., et al., Surface Modification of Biodegradable Electrospun Nanofiber Scaffolds and their Interaction with Fibroblasts. J. Biomater. Sci., Polym. Ed. 2007, 18(4), 369-382.

31. Song, W., et al., Bioinspired Degradable Substrates with Extreme Wettability Properties. Adv. Mater. 2009, 21(18), 1830-1834.

32. Khorasani, M. T., Mirzadeh, H., Irani, S., Plasma Surface Modification of Poly(L-Lactic Acid) and Poly(Lactic-Co-Glycolic Acid) Films for Improvement of Nerve Cells Adhesion. Radiat. Phys. Chem. 2008, 77(3), 280-287.

33. Correia, D. M., et al., Superhydrophilic Poly(L-Lactic Acid) Electrospun Membranes for Biomedical Applications obtained by Argon and Oxygen Plasma Treatment. Appl.Surf. Sci. 2016, 371, 74-82.

34. Cardoso, V. F., et al., From Superhydrophobic- to Superhydrophilic-Patterned Poly(Vinylidene Fluoride-co-Chlorotrifluoroethylene) Architectures as a Novel Platform for Biotechnological Applications. J. Polym. Sci. B: Polym. Phys. 2016, 54(18), 1802-1810.

35. Ribeiro, C., et al., Tailoring the Morphology and Crystallinity of Poly(L-Lactide Acid) Electrospun Membranes. Sci. Technol. Adva. Mater. 2011, 12(1), 015001.

36. Fischer, D., et al., In Vitro Cytotoxicity Testing of Polycations: Influence of Polymer Structure on Cell Viability and Hemolysis. Biomaterials 2003, 24(7), 1121-1131.

37. Otitoju, T. A., Ahmad, A. L., Ooi, B. S., Superhydrophilic (Superwetting) Surfaces: a Review on Fabrication and Application. J. Ind. Eng. Chem. 2017, 47, 19-40.

38. Simpson, J. T., Hunter, S. R., Aytug, T., Superhydrophobic Materials and Coatings: a Review. Rep. Prog. Phys. 2015, 78(8), 086501.

39. Kawai, T., Tsutsumi, K., Evaluation of Hydrophilic-Hydrophobic Character of Zeolites by Measurements of their Immersional Heats in Water. Colloid Polym. Sci. 1992, 270(7), 711-715.

40. Garlotta, D., A Literature Review of Poly(Lactic Acid). J. Polym. Environ. 2001, 9(2), 63-84.

41. Shangguan, J., et al., Paper Capillary Enables Effective Sampling for Microfluidic Paper Analytical Devices. ACS Sens. 2018, 3(7), 1416.

2.2. Fluorinated polymer membranes as advanced substrates for portable analytical systems

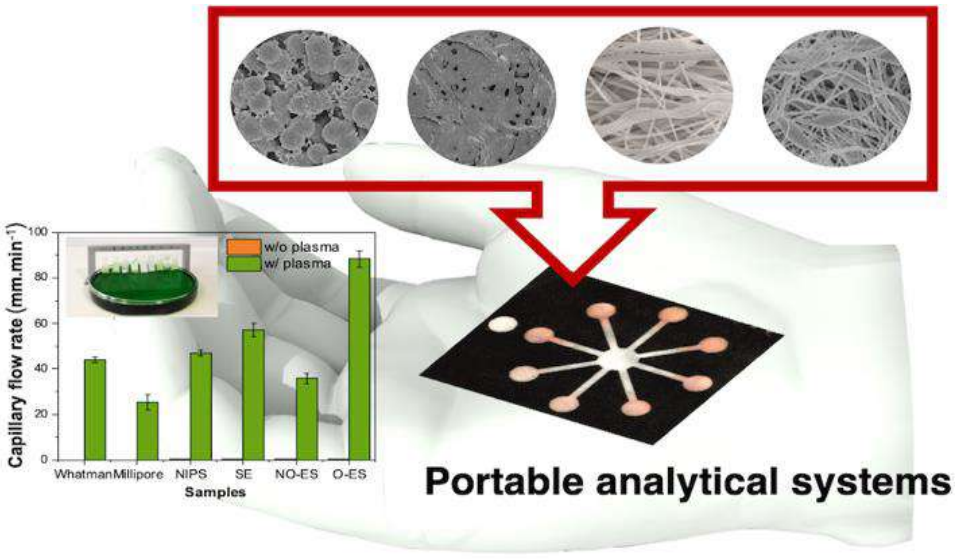

This chapter describes the processing of fluorinated poly(vinylidene-co-trifluorethylene), P(VDF-TrFE), membranes with tailored morphological and physicochemical properties to be used as microfluidic substrates for portable analytical systems, commonly called portable analytical devices (PADs) in the medical field. The morphology of the developed membranes includes spherulitic, porous, randomly oriented and oriented fibres. Microfluidic systems were then designed and printed by wax-printing for the colorimetric quantification of glucose.

This chapter is based on the following publication: Ricardo Brito-Pereira, AS Macedo, CR Tubio, Senentxu Lanceros-Mendez,Vanessa F. Cardoso, Fluorinated polymer membranes as advanced substrates for portable analytical systems and their proof-of-concept for colorimetric bioassays, ACS Applied Materials & Interfaces 13 (15), 18065-18076 (2021).

2.2.1. Introduction

Portable devices for expedite and easy medical diagnosis are increasingly demanded as a suitable tool to detect various diseases. Those devices allow early diagnosis *in situ* and can be accessible to a large number of people without the need for complex laboratory equipment. They are particularly valuable for preliminary analysis before further evaluation or to evaluate on-going processes, allowing to improve healthcare assistance [1]. Moreover, they have been also used in other research fields such as environmental safety [2], animal health [3] or food quality [4], among others.

In particular, in times of pandemic outbreaks, as the one we are experiencing nowadays, access to low-cost, easy to handle diagnostic methods that can be distributed quickly among the population is becoming essential to promote mass diagnosis and provide high quality control concerning the spread of a disease at an early stage [5].

It is particularly relevant that these tools address the ASSURED guidelines for the development of PADs, as defined by the WHO. Devices with low manufacturing cost, low sample volume and with minimal user manipulation are then best suited to satisfy these guidelines [6,7].

The μPADs, introduced by the Whitesides group in 2007 [8], are a relevant option for the development of such tools. Besides, microfluidic platforms have been fabricated from a wide array of materials such as silicon, glass or polymers that can be tailored into three-dimensional (3D) solid structures, as it is the case of PDMS and PMMA, which possess overall high mechanical strength [9]. Nonetheless, cellulose paper features economical, compact and lightweight properties for the fabrication of μPADs. Moreover, because of its superhydrophilic properties, passive capillary flow discards the need for an external pump [10]. Hydrophobic barriers can be printed to improve liquid flow through the substrate, allowing designs to guide solutions to different locations of the microfluidic platform for specific purposes. Several technologies may be used to implement these barriers, including wax and inkjet printing [9], photolithography [8], printed circuit technology [11] and screen-printing [12].

Nonetheless, commercial microfluidic substrates show disadvantages that include weak mechanical properties so the type of cellulosic paper has to be carefully selected: commercial inkjet printing paper is unsuitable due to its low porosity and surface tension; filter paper such as Whatman cellulose paper (the gold standard on point-of-care applications after its introduction [8] may possess pores that are too large, preventing proper capillary flow [6]. More recently, Hi-Flow Plus nitrocellulose substrates from Millipore have emerged as an interesting alternative for microfluidic applications, allowing controlled capillary flow rate and thus sensitivity, depending on the specific type of membrane. However, it is expensive, must be

handled very carefully to maintain the integrity the membrane and typically needs an external baking material to support the nitrocellulose structure. Thus, alternative microfluidic substrates are being explored, such as PLLA, an aliphatic semi-crystalline polyester known for its biocompatibility and biodegradability, in the form of electrospun membranes [13].

In this context, synthetic polymers, such as P(VDF-TrFE), a copolymer of poly(vinylidene fluoride) (PVDF), can be an interesting alternative to the commonly used microfluidic substrates. P(VDF-TrFE) presents excellent mechanical properties regardless of the processing method and resulting morphology, is characterized by high chemical and thermal resistance, as well as biocompatibility [14]. Furthermore, it has the highest dielectric constant among polymers and it is also an electroactive, including piezo-, pyro- and ferroelectricity, that crystallizes directly into the β phase, independently of the processing conditions, when the TrFE content is 20 % mol or higher. Its piezoelectric coefficient d_{33} is −38 $pC.N^{-1}$ [15]. Thus, P(VDF-TrFE) has been used in microfluidic applications for the development of piezoelectric micropumps [16], temperature sensors [17] as well as acoustic actuators [18].

P(VDF-TrFE)-based membranes can be manufactured with several microstructures using a variety of processing methods as described in a previous review [14]. One way to process this polymer is in the form of porous films. Techniques based on phase inversion allow porosity and pore size control, as well as industrial scalability. Two specific methods based on this principle were used in the present work: a) non-solvent induced phase separation (NIPS), where the liquid or vapour phase in the polymer solution is diffused by submerging it in a nonsolvent coagulation bath, giving rise to polymer-rich and poor zones which lead to pore formation, and b) thermally induced phase separation (TIPS), where the appearance of these structures is due to a polymer-solvent phase separation at a specific temperature, that occurs before solvent evaporation and polymer crystallization [19].

Electrospinning (ES) is another versatile and highly reproducible technique to produce polymer fibre membranes by applying a high electrical field to a droplet of polymer solution or melt. By controlling the characteristics of the polymer solution and processing conditions, a stable procedure can be achieved to obtain fibre mats with tailorable fibre diameter and orientation [20]. In the present work c) randomly oriented and d) oriented electrospun P(VDF-TrFE) membranes were thus also processed by ES.

P(VDF-TrFE) is a hydrophobic polymer, which prevents capillary flow through membranes or films. One way to overcome this limitation involves surface plasma treatments, which introduce morphological modifications and/or functional groups into the surface of the material by exposing it to plasma of a selected composition (Ar, O_2 and N_2 are some of the most used). Thus, hydrophobic membranes can be

converted into superhydrophilic ones [21], due to the cleavage of C-F and C-H bonds which are replaced by C=O, -OH and -COOH hydrophilic groups [22].

In order to provide novel and complementary microfluidic substrates to the limited commercially ones, this work evaluates the potential of P(VDF-TrFE) membranes processed in a variety of morphologies for manufacturing portable analytical devices. Thus, in the present work the suitability, advantages and limitations of P(VDF-TrFE) to be used as microfluidic substrates in the form of oriented and randomly oriented electrospun membranes, as well as in the form of porous membranes obtained by NIPS and TIPS techniques, has been addressed. The processed membranes were compared to the commonly used Whatman™ no. 1 cellulose filter paper and Hi-Flow Plus membranes HF090 from Millipore. Microfluidic platforms based on the P(VDF-TrFE) substrates were also designed and tested for the quantification of glucose. To our knowledge, this is the first time that superhydrophilic P(VDF-TrFE) substrates have been used for microfluidic applications.

2.2.2. Experimental section

2.2.2.1. Materials

P(VDF-TrFE) 70/30 powder (70 mol % vinylidene fluoride monomer and 30 mol % trifluoroethylene) was obtained from Piezotech (Pierre-Bénite, France). N,N-dimethylformamide (DMF) and absolute ethanol were obtained from Merck. Whatman qualitative chromatography paper grade 1 and Hi-Flow Plus HF090 (product number HF090MC100) were acquired from GE Healthcare and Millipore, respectively. Distilled water was prepared in our laboratory. All reagents and solvents were used as received.

2.2.2.2. Sample preparation

Several processing techniques and post-treatment protocols were employed to produce P(VDF-TrFE) membranes with tailored morphological and physicochemical properties suitable for microfluidic device development [14]. NIPS technique was used to produce P(VDF-TrFE) membranes using ethanol as a weak non-solvent in order to tune the liquid-liquid demixing process to produce samples with large spherical microstructures, similar to commercial Hi-Flow Plus substrates from Millipore [23]. On the other hand, TIPS technique was used to produce pore-based microstructures as an alternative morphology [23]. Further, ES has been used to obtain randomly oriented P(VDF-TrFE) fibre membranes, mimicking the morphology of commercial Whatman no.1 [24], and oriented electrospun membranes, in order to study the effect of fibre orientation.

As the hydrophobic nature of P(VDF-TrFE) membranes hinders their use as microfluidic substrates, the as-processed membranes were submitted to a post-treatment with oxygen plasma and its effect on the physicochemical properties of the membranes was evaluated.

2.2.2.2.1. *Poly(vinylidene-co-trifluorethylene)* solution preparation

A 20 wt.% solution of P(VDF-TrFE) powder dissolved in DMF was prepared under magnetic stirring. A slight heating at 40 °C was applied in the first 30 min of dissolution to speed up the process and the solution was then allowed to cool under magnetic stirring until a homogeneous (without air bubbles) and transparent solution was obtained, which took no longer than 3 h. The polymer concentration was defined in order to obtain a solution compatible with the processing techniques and conditions in order to obtain the membranes [14].

2.2.2.2.2. Non-solvent induced phase separation

The P(VDF-TrFE) solution was spread on clean and polished glass substrates (15 cm x 10 cm) by means of a hand-casting knife with a 450 µm gap. Then, the coated substrates were immersed in a coagulation bath composed by absolute ethanol for approximately 5 min at a temperature of 25 °C controlled by a hot-plate (Präzitherm PZ23-2) and a digital thermometer (Elitech WT-1), until complete crystallization, after which the films peeled off the glass substrates. It remained immersed for another 5 min in the coagulation bath before being transferred to a pure distilled water bath (also at 25 °C) to guarantee total removal of residual solvent. Finally, the membranes were left to dry at room temperature for 48 h [25]. The process is illustrated in Figure 2.2.1a. These membranes will be identified as NIPS membranes.

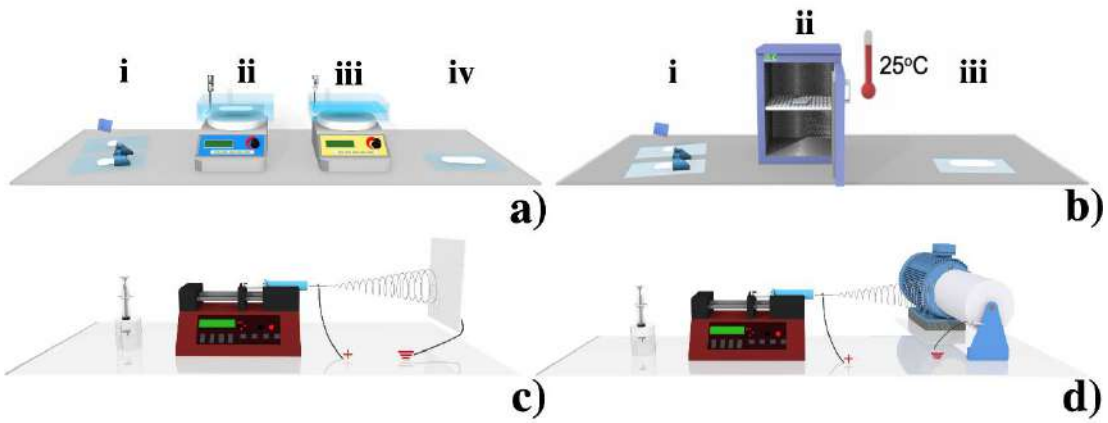

Figure 2.2.1. Schematic representation of the processing of a) P(VDF-TrFE) membranes by NIPS using ethanol as non-solvent: i. spreading of the polymer solution on a glass substrate by means of a hand-casting knife with a 450 µm gap; ii. immersion in a coagulation bath composed of ethanol at 25 °C; iii. transfer to a bath of pure distilled water at 25 °C; iv. drying at room temperature for 48 h. b) P(VDF-TrFE) membranes by TIPS: i. spreading of the polymer solution on a glass substrate by means of a hand-casting knife with a 450 µm gap; ii. placement within an oven at 25 °C for 48 h; iii. dry sample. c) Randomly oriented electrospun P(VDF-TrFE) membranes by ES: filling the syringe with the polymeric solution and collecting the electrospun fibres on a grounded static plate collector under a high voltage. d) Oriented electrospun P(VDF-TrFE) membranes by ES: filling the syringe with the polymer solution and collecting the electrospun fibres on a grounded rotating drum collector under a high voltage.

2.2.2.2.3. Thermally induced phase separation

The P(VDF-TrFE) solution was spread on clean and polished glass substrates (15 x 10 cm) by means of a hand-casting knife with a 450 µm gap, similarly to the NIPS process. Then, the coated substrates were placed into an oven (JP SELECTA Digitronic-TFT) to maintain a controlled temperature of 25 °C for 48 h until fully dried. In the TIPS method, the PVDF-based physicochemical and morphological characteristics can be anticipated by the phase diagram of the polymer and solvent binary systems, in which the regions of miscibility and phase separation are identified [26]. Lower drying temperatures are associated with lower evaporation rates of the solvent, leading to highly porous membranes [14]. The process is illustrated in Figure 2.2.1b and these processed membranes will be identified as TIPS membranes.

2.2.2.2.4. Randomly oriented electrospun fibre mats

The P(VDF-TrFE) solution was transferred to 10 mL disposable syringes fitted with a blunt steel needle with an inner diameter of 500 µm and placed in a syringe pump (New Era NE-1000). ES was conducted using a high voltage power supply (Glassman PS/FC30P04) set at 15 kV and the solution was pumped at a flow rate of 0.5 $mL.h^{-1}$. The resulting randomly oriented electrospun P(VDF-TrFE) membranes were collected on a grounded 20 cm x 15 cm static plate collector placed 15 cm away from the needle. The process is illustrated in Figure 2.2.1c and the processed membranes will be identified as RO-ES membranes.

2.2.2.2.5. Oriented electrospun fibre mats

Oriented electropun P(VDF-TrFE) membranes were obtained after a process similar to the one described in section 2.2.2.2.4 except for the use of a grounded rotating drum collector, which was set at a speed

of 1500 rpm. The process is illustrated in Figure 2.2.1d and the processed membranes will be identified as O-ES membranes.

2.2.2.3. Surface modification by plasma treatment

The inherent hydrophobic characteristics of P(VDF-TrFE) constitute a limitation for its use as microfluidic substrates in portable analytical systems, as previously mentioned. Thus, P(VDF-TrFE) membranes were subjected to plasma treatment in order to obtain superhydrophilic membranes [27]. The success of plasma treatment is associated with an adequate selection of the plasma atmosphere (O_2, Ar, N_2 or others), treatment duration and applied power. Oxygen is one of the most reactive elements and can generate hydrophilic carboxyl groups on the polymer surface [28]. Thus, surface treatments were conducted in a plasma chamber (Diener Electronics Zepto) equipped with a 40 kHz radio frequency plasma generator. The base pressure before the application of the plasma was 20 Pa. A plasma power of 100 W was then applied for 10 min using oxygen under a total pressure of 80 Pa. This procedure was performed on both surfaces of the P(VDF-TrFE) membranes. These parameters were defined according to previous studies and further optimization to guarantee non-significant morphological changes and superhydrophilic properties stable over time [13,29]. The processed P(VDF-TrFE) membranes with and without oxygen plasma treatment will be identified as w/ and w/o plasma, respectively.

2.2.2.4. Sample characterization

2.2.2.4.1. Physicochemical characterization

The morphology of the processed P(VDF-TrFE) membranes and commercial substrates were characterized by SEM (Hitachi S-4800). Samples were previously sputtered (Polaron SC502) with a thin gold layer. Mean fibre diameter was calculated from measuring approximately 50 fibres using ImageJ software.

The porosity of the P(VDF-TrFE) membranes was measured by liquid displacement method using a pycnometer [30,31]. The weight of the pycnometer filled with ethanol was measured and labelled as W_1. The P(VDF-TrFE) membranes, whose weight was W_s, were immersed in ethanol; after the sample was saturated by ethanol, additional ethanol was added to fill the volume of the pycnometer. Then, the pycnometer was weighted and labelled as W_2. The sample filled with ethanol was then taken out of the pycnometer and the residual weight of the ethanol and the pycnometer was labelled W_3. The porosity of

the membrane was calculated according to $\varepsilon p = (W_2 - W_3 - W_S)/(W_1 - W_3)$. The porosity of each membrane was obtained as the average of the values determined in three samples. Absolute ethanol, as a non-solvent of P(VDF-TrFE), was used as displacement liquid since it can penetrate in the pores of the membranes and the electrospinning fibres, not inducing shrinking or swelling. The assays were performed on hydrophobic P(VDF-TrFE) membranes before plasma treatment, since plasma treated membranes absorb the ethanol on the polymer matrix, which may lead to porosity measurement errors.

The DSC was performed with a Perkin-Elmer 6000. P(VDF-TrFE) samples weighing approximately 6 mg were placed into 40 µL aluminum pans and then heated from 30 to 200 °C at a rate of 10 °C.min^{-1}. The degree of crystallinity (X_C) was calculated after $\chi_C = (\Delta H_m/\Delta H_0) \times 100$, where ΔH_m corresponds to the melting enthalpy of the samples and ΔH_0 is the melting enthalpy for 100 % crystalline P(VDF-TrFE) (91.45 J.g^{-1}) [32].

Mechanical properties were evaluated in the tensile mode with a Shimadzu AD-IS universal testing set up with a load cell of 50 N. 15 mm long and 10 mm wide samples were stretched at a rate of 1 mm.min^{-1}. O-ES membranes were stretched along the direction of the fibres. Average sample thickness values are: 120 µm for Whatman no.1 and 110 µm, 103 µm, 92 µm and 81 µm for NIPS, TIPS, RO-ES and O-ES P(VDF-TrFE) membranes, respectively, measured using a Fischer Dualscope MPOR. The stress-strain measurements were performed in triplicate on dry and wet samples, using 40 µL of water in the latter. The assays were not performed on the Millipore HF090 substrates as it is a laminated membrane with backing material that prevents the determination of the Young modulus of the nitrocellulose membrane.

FTIR in attenuated total reflectance mode were performed at room temperature in all samples using a Jasco FT/IR-6100 set up, from 400 to 4000 cm^{-1} using 64 scans and a resolution of 4 cm^{-1}.

2.2.2.4.2. Contact angle and capillary flow rate assays

Surface wettability was evaluated using the sessile drop method (Data-Physics OCA20) by CA of 3 µL ultrapure water drops on the commercial and processed P(VDF-TrFE) samples. Six measurements were carried out in each sample at different locations and the average and standard deviation were calculated. The measurements were repeated every week during 2 months, storing the samples under environment conditions.

Capillary tests were also performed on all samples, including commercial ones. 2.5 cm long and 1 cm wide sample strips were cut and submerged vertically in a liquid coloured solution (green food dye) in order to visualize and determine the capillary flow. A segment of 0.5 cm was first submersed, and the

time taken for the dye to travel across the remaining 2 cm of the sample in the antigravitational direction was measured. These tests allow an evaluation of the effect of fibre orientation, film porosity and oxygen plasma treatment on capillary flow rate, and ultimately the evaluation of the ability of the different materials to generate passive flows. Three measurements were carried out in each sample and the average and standard deviation were calculated.

2.2.2.5. Proof-of-concept

Glucose assays based on colorimetric detection were performed using a glucose kit (Trinder – Endpoint, FAR Diagnostic). During the reaction, glucose is oxidised by glucose oxidase to gluconic acid and hydrogen peroxide. The latter reacts with phenol and 4-aminophenazone in the presence of peroxidase, producing a coloured complex whose colour intensity is directly proportional to the glucose concentration in the samples. Calibration curves were determined for all samples using glucose concentrations of 25, 50, 75, and 100 $mg.dL^{-1}$. This range of concentrations includes ranges of reference values for both new-born babies (20 to 80 $mg.dL^{-1}$) and adults (70 to 110 $mg.dL^{-1}$). A microfluidic system was designed using *SolidWorks 2020* and hydrophobic wax was printed using a Xerox ColorQube 8870 printer, as illustrated in Figure 2.2.2. Wax-Printing, when compared to other methods commonly used to produce μPADs presents several advantages such as not requiring specialized facilities, the process is rapid, inexpensive (each wax cartridge can print a large number of devices) and environmental friendly (no use of organic solvents throughout the fabrication process) [33-35].

After printing, the samples were placed on a hot plate at 100 °C for 10 min for the wax to penetrate the substrates all the way through to the opposing surface in order to fabricate the barriers able to properly contain the fluids.

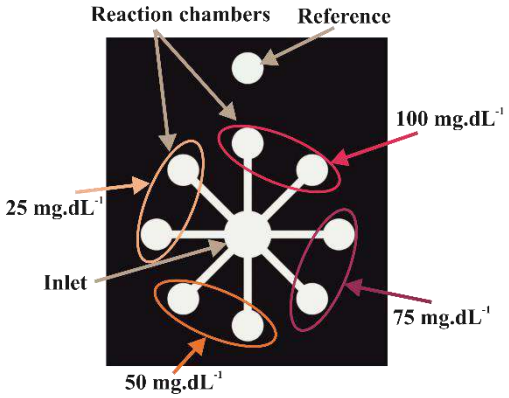

Figure 2.2.2. Design of the microfluidic system for the quantification of glucose. The glucose solution was placed in both reaction and reference chambers and the reagent in the inlet. The reagent flow by capillarity

from the inlet to the reaction chamber to form a red/orange colour with intensity proportional to the concentration of glucose. The reaction chamber features a diameter of 8 mm and the channels a width of 1.2 mm.

Each microfluidic system comprises eight reaction chambers, with each glucose concentration being carried out in two reaction chambers separately and at the same time, as indicated in Figure 2.2.2. Three microfluidic systems were printed for each membrane in order to assess the reproducibility of the system. The reaction chambers were first functionalized using 15 μL of the glucose solution under study. After approximately 5 min, the reagent was introduced in the inlet of the microfluidic system, reaching the reaction chambers by capillarity. After 10 min of reaction, a red/orange colour with intensity proportional to the glucose concentration was obtained. The substrates were then scanned (Brother DCP-1610W) and colour analysis was performed with the aid of ImageJ software by measuring mean grey values and the corresponding standard deviation on each reaction chamber of the microfluidic systems. These results were used to build the calibration curves [36].

2.2.3. Results and Discussion

P(VDF-TrFE) membranes with tailorable morphologies were processed by three distinct processing techniques. In the following sections, a complete physicochemical characterization of the processed P(VDF-TrFE) membranes will be presented, discussed and compared with commercial Whatman no.1 and Millipore HF090 membranes. The colorimetric quantification of glucose in the microfluidic systems printed on the membranes will also be presented.

2.2.3.1. Physicochemical characterization

The use of membranes as microfluidic substrates is dependent on proper porous morphology [37,38]. Representative SEM images of the processed and commercial membranes are presented in Figure 2.2.3.

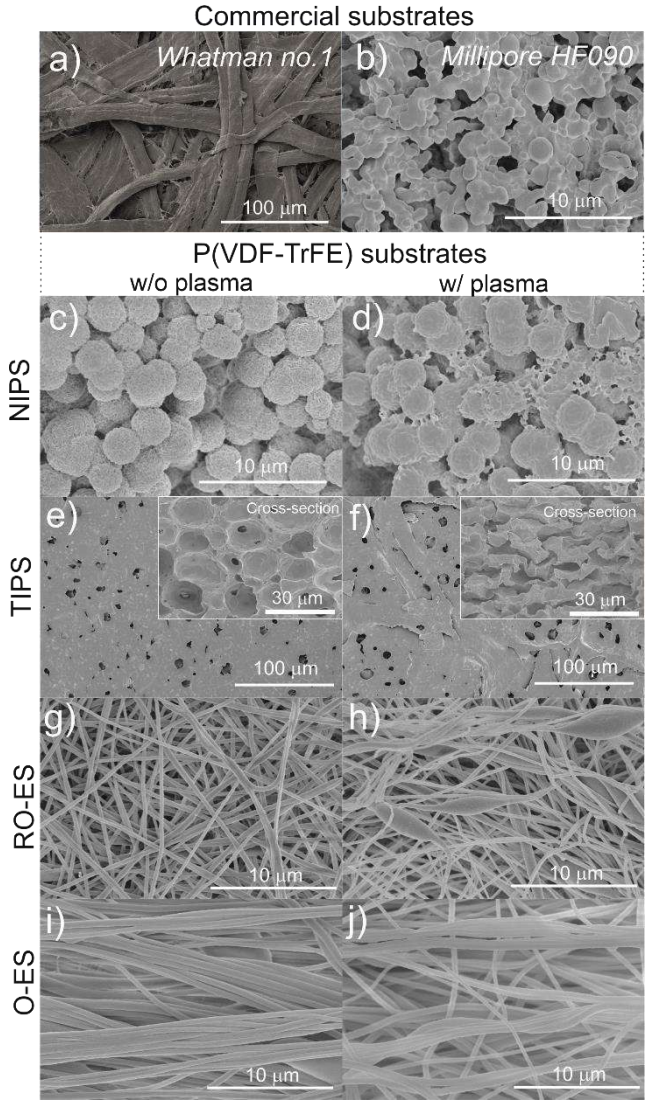

Figure 2.2.3. Representative SEM images of the processed P(VDF-TrFE) membranes before and after oxygen plasma treatment together with commercial Whatman no.1 and Millipore HF090 substrates, for comparison.

Commercial Whatman no.1 substrates (Figure 2.2.3a) are composed by randomly oriented cellulose microfibres with a flat structure (width in the order of tens of micrometer), which is associated with the manufacturing process of paper. On the other hand, Millipore HF090 substrates (Figure 2.2.3b) feature a spherulitic-like nitrocellulose porous structure laminated with a backing transparent material. Taking into account these microstructures, manufacturing techniques for P(VDF-TrFE)-based membranes were selected [14] in order to mimic the morphology of these commercial substrates and allowing to overcome some of their limitations, as will be discussed ahead. NIPS technique (Figure 2.2.3c) with ethanol as non-solvent was used to produce P(VDF-TrFE) membranes with morphology similar to Millipore HF090, however without the need for a support material. TIPS technique was also applied to obtain P(VDF-TrFE)

membranes with an alternative porous microstructure characterized by well-defined round shaped pores (Figure 2.2.3e). Randomly oriented P(VDF-TrFE) fibre membranes were produced by ES (RO-ES) in order to mimic the morphology of the Whatman no.1 substrates (Figure 2.2.3g). Finally, oriented electrospun P(VDF-TrFE) fibres (O-ES) were also processed in order to evaluate the influence of fibre orientation in the physicochemical properties and passive capillary flow rate of the P(VDF-TrFE) membranes (Figure 2.2.3i). As the processed samples are hydrophobic, the P(VDF-TrFE) membranes were subjected to oxygen plasma treatment in order to tailor the polymer's surface wettability and to allow capillary flow. Oxygen plasma treatment allows to generate carboxyl group on the polymer surface by the incorporation of hydrophilic functional groups [29]. SEM images of the plasma treated P(VDF-TrFE) membranes (Figure 2.2.3d, 2.2.3f, 2.2.3h and 2.2.3j) reveal a slight change in the morphology of the membranes compared to the untreated P(VDF-TrFE) membranes, which is attributed to local polymer melting associated with the high power (100 W) and high exposure time (10 min) [13]. For instance, the plasma-treated P(VDF-TrFE) membranes obtained by NIPS (Figure 2.2.3d) present some melted and recrystallized regions in the interfaces between the spherulites, whereas the cross-section images of the plasma-treated P(VDF-TrFE) membranes obtained by TIPS (Figure 2.2.3f, inset) reveal a change in pore spherical shape, presenting more deformed and flattened pores. In turn, the overall 3D fibre structure with smooth surfaces of the P(VDF-TrFE) membranes is maintained after plasma treatment, with average fibre diameter of 310 ±50 nm and 370±70 nm for the RO-ES (Figure 2.2.3g and 2.2.3h) and O-ES P(VDF-TrFE) (Figure 2.2.3i and 2.2.3j) membranes, respectively.

The porosity of the membranes is presented in Figure 2.2.4a.

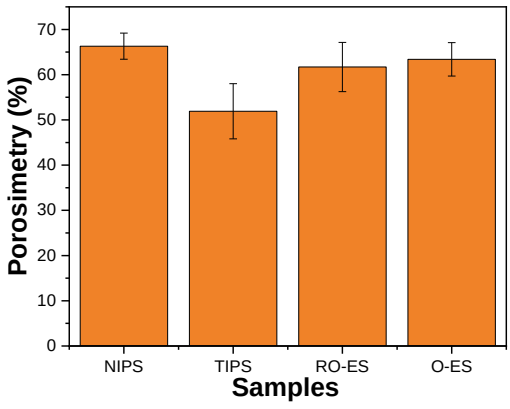

a)

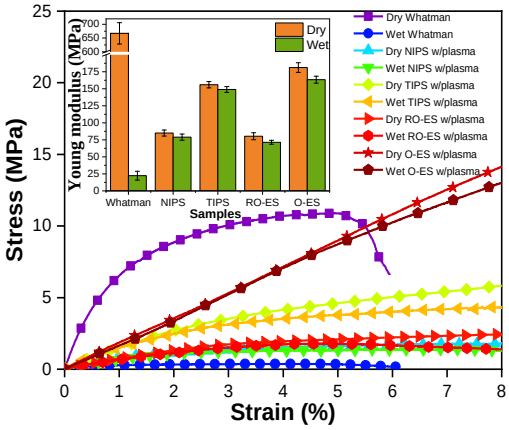

b)

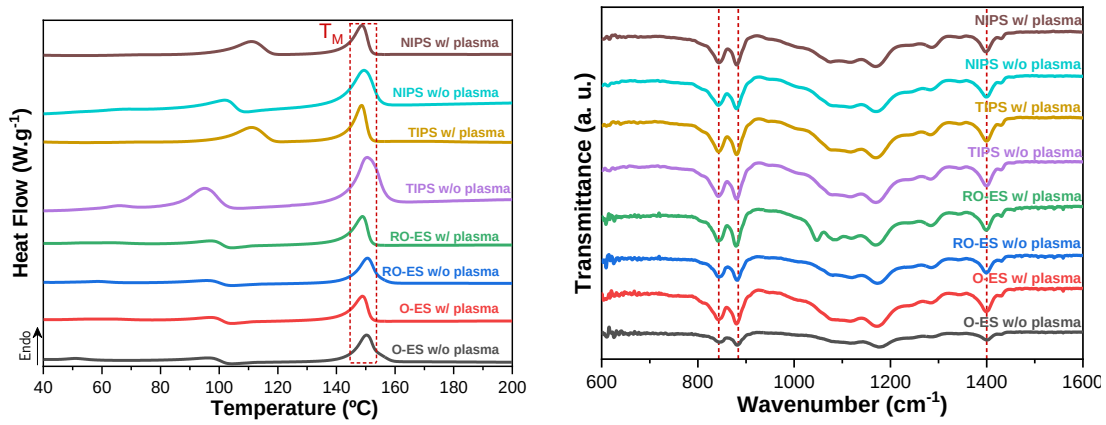

c) d)

Figure 2.2.4. a) Porosity of the P(VDF-TrFE) membranes before oxygen plasma treatment; b) Representative stress-strain curves up to 8 % of strain and corresponding Young modulus with mean and standard deviation (inset) of the plasma treated P(VDF-TrFE) membranes; c) Representative DSC curves and d) Representative FTIR-ATR spectra of the P(VDF-TrFE) membranes before and after oxygen plasma treatment.

Independently of the processing method, all samples show degrees of porosity above 50 %. No significant variations occur for the surface plasma treated samples (Figure 2.2.3).

In addition to the relevance of a porous morphology, membrane-based microfluidic substrates must keep adequate mechanical properties when wet during a functionalization process and/or after immersion in a solution containing the (bio)entity(ies) to be quantified. Stress-strain assays were conducted on dry and wet plasma treated P(VDF-TrFE) membranes and commercial Whatman no.1 microfluidic substrates. This experiment was not performed on Millipore HF090 substrates as they possess backing material, which provides improved mechanical stability but prevents the determination of the mechanical properties of the nitrocellulose membrane itself.

The stress-strain mechanical curves are characterized by a linear elastic regime followed by a plastic regime after yielding where the material suffers permanent deformation after any increase in load or stress. By further stretching the samples, the rupture stress-strain is reached. Brittle materials, contrarily to ductile materials, typically feature little or no plastic deformation, fracturing within the linear elastic region. From the linear regime of the stress-strain curves, where materials are generally used, the Young's modulus has been obtained for each sample by applying Hooke's law. The characteristic stress-strain curves up to 8 % of strain along with the Young's modulus of the samples under study are presented in Figure 2.2.4b. Commercial Whatman no.1 substrates show almost no plastic regime in both dry and wet state, contrarily to the plasma-treated P(VDF-TrFE) membranes. Dry commercial Whatman no.1

substrates feature a more rigid behaviour with the highest Young's modulus of 667.2 ± 38.8 MPa, strongly decreasing to 22.3 ± 6.5 MPa when wet. In turn, the P(VDF-TrFE) membranes are mechanically stable before and after wetting, with the wet samples nearly preserving the same elastic behaviour and mechanical characteristics as the dry ones. In fact, wet treated P(VDF-TrFE) membranes only suffered a slight decrease of the Young's modulus compared to dry treated P(VDF-TrFE) membranes, being the wet treated RO-ES P(VDF-TrFE) and the dry treated O-ES P(VDF-TrFE) membranes the ones with the lowest and highest Young's modulus of 71.4 ± 2.9 and 181.2 ± 7.1 MPa, respectively. This result shows that the orientation of the fibres directly influences the mechanical properties of the P(VDF-TrFE) membranes, where oriented fibre membranes lead to higher Young's modules, when stretched in the direction of the fibres [39]. Similar high Young's modules are also presented by the porous TIPS P(VDF-TrFE) membranes before and after wetted. On the other hand, comparing the RO-ES P(VDF-TrFE) membranes with the Whatman no.1 substrates, both featuring randomly oriented fibres, the former is characterized by a much higher Young's modulus, when wet, indicating that P(VDF-TrFE) membranes possess more suitable mechanical properties than cellulose for the present application. Moreover, although it was not possible to determine the Young's modulus of the Millipore HF090 substrates, it should be noted that besides needing a support material, the nitrocellulose membrane itself breaks up very easily when, for example, a finger is passed over and must therefore be handled very carefully, contrarily to the NIPS P(VDF-TrFE) membranes with similar spherulitic-like porous structure that present high Young's modulus, similar to the RO-ES P(VDF-TrFE) membranes, in both dry and wet state. Combined with these excellent mechanical properties, it should be noted that P(VDF-TrFE) membranes can be repeatedly wetted and dried without losing their physicomechanical properties, allowing, therefore, cleaning and reuse.

Molecular weight, degree of crystallinity and microstructure strongly influence the mechanical properties of polymer-based membranes. The degree of crystallinity, calculated (see Section 2.4.1) from the thermograms of the P(VDF-TrFE) membranes presented in Figure 2.2.4c, remains approximately constant, 26 ± 3 %, regardless of the processing conditions and plasma treatment, being within the typical range of values obtained for this copolymer [40]. Moreover, no significant variation is observed in the melting transition (T_M) which occurs at 149.7 ± 1.0 °C. Thus, the variations of the mechanical properties are attributed just to the different morphological features of the P(VDF-TrFE) membranes.

Finally, the crystalline phases of the P(VDF-TrFE) membranes are identified in the infrared spectra presented in Figure 2.2.4d. All membranes show the characteristic vibration modes at 839, 886 and 1402 cm^{-1}, which identify the polymer crystallization in the trans TTT' highly polar chain confirmation.

Because of its electroactive β-phase, these membranes can be further explored for active multifunctional microfluidic substrates, with added value compared to the passive commercial microfluidic ones [16-18].

2.2.3.2. Contact angle and capillary flow rate assays

The hydrophobic nature of P(VDF-TrFE) is a major drawback that must be overcome for its use as microfluidic substrates where capillary flow is essential. In this sense, various surface modification approaches can be applied to tailor the polymer surface wettability, such as plasma treatment, defluorination-sulfonation, surface coating/deposition, blending, and electron beam radiation, among others [41,42]. Plasma treatment stands out as the most suitable method, due to their high versatility and for maintaining the main physicochemical properties of the polymer [29]. In this context, a reactive oxygen atmosphere allows to promote a stable hydrophilicity through the generation of carboxyl groups on the polymer surface by the incorporation of hydrophilic functional groups [28]. Thus, contact angle measurements over time were performed on the different substrates as a simple and effective method to quantify the wetting properties of the surfaces. A surface is commonly named hydrophobic when its water contact angle is higher than 90°, whereas values lower that 90° are associated with hydrophilic surfaces. Superhydrophobic and superhydrophilic are terms also used to characterize surfaces that features contact angles higher that 150° and lower than 10°, respectively [43]. The water contact angle values of the processed P(VDF-TrFE) w/o and w/ plasma treatment, along with the ones for the commercial substrates, are presented in Figure 2.2.5a.

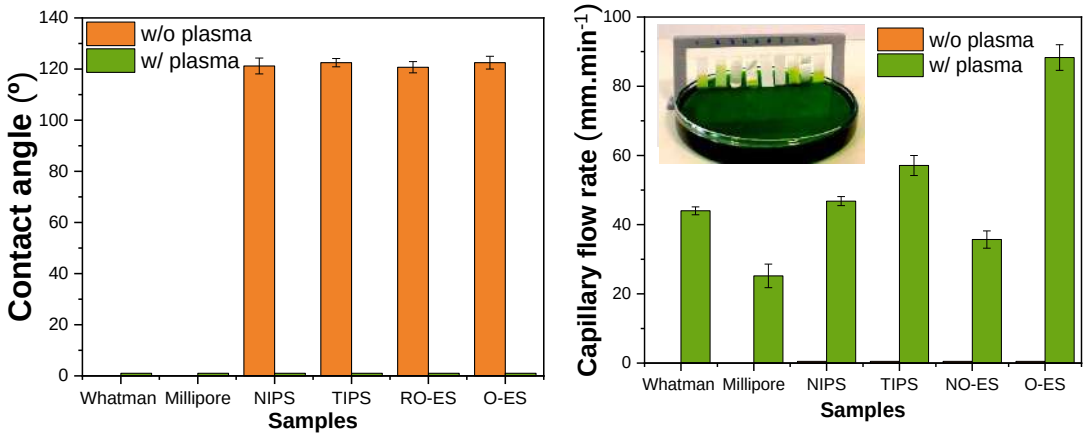

a) b)

Figure 2.2.5. a) Contact angle and b) capillary flow rates in the "antigravity" direction of a dye solution for the commercial substrates and P(VDF-TrFE) membranes before and after oxygen plasma treatment; inset: Representative photograph of an experimental assay.

Commercial Whatman™ no.1 and Millipore H090 substrates are superhydrophilic. In turn, the processed P(VDF-TrFE) membranes present hydrophobic properties with an average contact angle of 122±2°, independently of the morphology. After oxygen plasma treatment, the P(VDF-TrFE) membranes become superhydrophilic and are stable for at least 2 months.

Capillary flow rate assays were then performed. This experiment validates the ability of the membranes to be used as microfluidic substrates, where passive capillary flow must occur preventing the need of any external actuation systems. The results are presented in Figure 2.2.5b. As anticipated, no flow was observed in the as-processed hydrophobic P(VDF-TrFE) membranes. In turn, plasma treated P(VDF-TrFE) membranes feature capillary flow rates varying from 35.7 ± 2.5 $mm.min^{-1}$ to 88.3 ± 3.7 $mm.min^{-1}$, corresponding to the plasma treated RO-ES and plasma treated O-ES P(VDF-TrFE) membranes, respectively. This result demonstrates that, besides the type of porous morphology, the orientation of the fibres has a direct effect on the capillary flow rate, the highest value being obtained for the O-ES membranes due to the orientation of the fibres along the length of the strip. Comparing the plasma treated NO-ES P(VDF-TrFE) membranes and the commercial Whatman™ no.1 substrates, with similar randomly oriented fibre morphologies, the obtained capillary flow rates are slightly higher for the Whatman™ samples with values of 44.1 ± 1.1 $mm.min^{-1}$ compared to 35.7 ± 2.5 $mm.min^{-1}$ for the NO-ES P(VDF-TrFE) membranes, which can be attributed to the more compact structure of the Whatman™ membranes that allows higher flow rates. In turn, the spherulitic-like porous structure of the plasma treated NIPS P(VDF-TrFE) membranes present capillary flow rates of 46.8 ± 1.3 $mm.min^{-1}$, higher than the ones obtained for Millipore HF090 membranes with similar morphology (25.0 ± 3.4 $mm.min^{-1}$). This behaviour can be attributed to the polymer melted and recrystallized regions caused by the plasma treatment that increase the contact areas for the fluid to flow and thus allow faster flow rates. Finally, plasma treated porous TIPS P(VDF-TrFE) membranes feature capillary flow rates of 57.1 ± 2.9 $mm.min^{-1}$, an intermediate value between all measured samples. Thus, the capillary flow rate of the P(VDF-TrFE) membranes can be adapted and tailored by tuning their morphology and/or fibre orientation, which is relevant in order to match process requirements (such as collection, separation, pre-concentration or mixing, among others) in microfluidic substrates.

2.2.3.3. Colorimetric glucose determination

Colorimetric analysis allows to determine the presence or even concentration of a specific chemical entity in a solution based on a colour variation. This method is widely used in clinical analysis laboratories, for industrial purposes such as analysis of water contaminants and PADs. In the scope of this research, colorimetric assays based on the quantification of glucose were performed on commercial Whatman™ no.1 and Millipore HF090 substrates, as well as on the plasma treated P(VDF-TrFE) membranes with different morphologies to evaluate their performance as microfluidic substrates. First, an optimized microfluidic design was printed using a wax printer for the quantification of glucose in the range of 25 to 100 mg.dL^{-1}, as described. Scanned images of the microfluidic systems after the glucose assays are presented in Figure 2.2.6a and their corresponding calibration curves as well as the extrapolated linear fittings are shown in Figures 6b and 6c, respectively. For that, mean grey values are presented as a function of the logarithm of the glucose concentration.

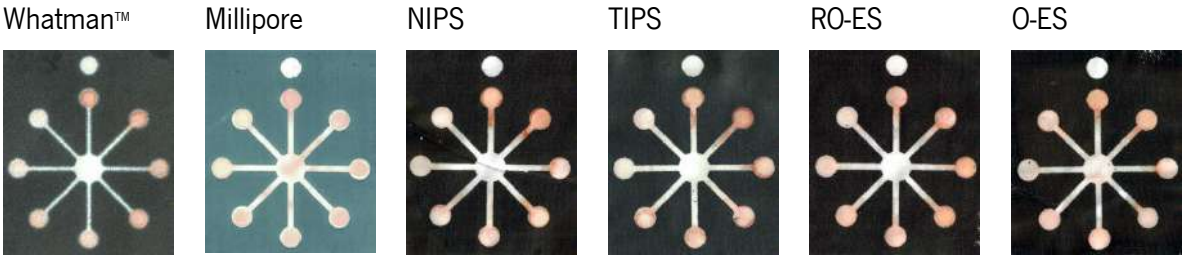

a)

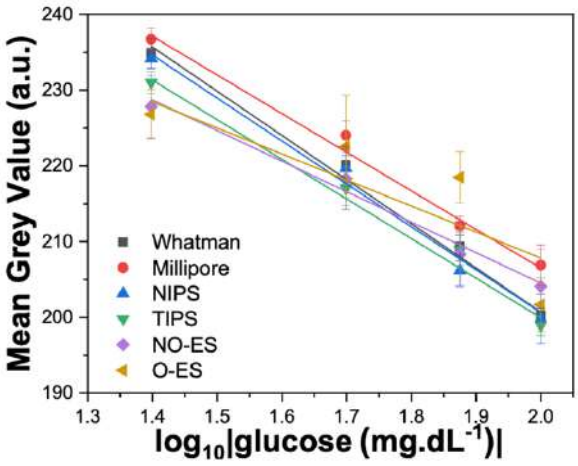

b)

	m	b	R^2
Whatman™ no.1	-58.4	317.5	0.994
Millipore HF090	-51.0	308.5	0.985
NIPS w/ plasma	-56.7	313.9	0.994
TIPS w/ plasma	-52.3	304.5	0.991
RO-ES w/ plasma	-40.3	285.1	0.989
O-ES w/ plasma	-34.4	276.6	0.746

c)

Figure 2.2.6. a) Representative scanned images of commercial substrates and plasma treated P(VDF-TrFE) membranes after glucose assays. Millipore HF090 substrates were evaluated on the baking side and the image horizontally inverted. For identification of glucose concentration see Figure 2.2.2. b) Calibration curves of glucose for commercial substrates and plasma treated P(VDF-TrFE) membranes. The results are presented as mean grey values and corresponding standard deviation measured on the

reaction chambers of the microfluidic substrates using ImageJ software according to the method described in ref [36]. c) Corresponding linear fitting.

With respect to the wax print quality, it is confirmed that all microfluidic substrates present good resolution, except for the Whatman no.1 substrates where the wax expands near to 1.2 mm during the thermal post-treatment. This behaviour may affect the capillary flow rate and thus attention must be paid when Whatman no.1 substrates are used in combination with wax printing, according to the applications requirements [38,44-46].

Regarding the colours generated after the colorimetric assays, they are only visible on the back side in the case of the Millipore HF090 substrates, remaining completely white on the front side. Thus, scanned images of the Millipore HF090 in Figure 2.2.6a represent the back side and the image was horizontally inverted to present colour intensities and thus glucose concentrations in the same reaction chambers as the other substrates. Figure 2.2.6a confirms that the plasma treated P(VDF-TrFE) substrates feature good wax printing resolution and colour formation on the front side. In all colorimetric assays, the grey intensity in the reaction chambers (corresponding to the red colour in Figure 2.2.6a, for proper identification) intensifies with increasing glucose concentration. However, the homogeneity of the colour generated in the reaction chambers varies depending on the substrate, which directly affects the quality of the obtained calibration curves (Figures 2.2.6b and 2.2.6c). Very good linear fittings were obtained with the Whatman no.1 substrates and plasma treated NIPS and TIPS P(VDF-TrFE) membranes with R^2 higher than 0.990, followed by the plasma treated RO-ES P(VDF-TrFE) and Millipore HF090 with R^2 of 0.989 and 0.985, respectively.

Higher slope associated with higher sensitivity was obtained with the Whatman no.1 substrates and plasma treated NIPS P(VDF-TrFE) membranes with values of -58.4 and -56.7, respectively. This small variation demonstrates that the expansion of the wax during the thermal post-treatment in the Whatman no.1 substrates did not affect significantly the colorimetric reaction, in this specific application.

The worst fitting was obtained with the plasma treated O-ES P(VDF-TrFE) membranes that may result from the orientation of the fibres were the unidirectional flow leads to the heterogeneous formation of the coloured solution in the reaction chamber that feature a circular shape. This behaviour along with the capillary flow rate presented in Figure 2.2.6b indicate that P(VDF-TrFE) membranes based on oriented fibres show high potential for unidirectional capillary flow of solutions/entities at higher rate but are not the most indicated for colorimetric quantification using more isotropic microfluidic design. Thus, except

for the orientation of the fibres and printing quality, the variation in the porous morphology of the microfluidic substrates does not appear to have a significant effect on the quality of colorimetric assays.

2.2.3.4. Comparative assessment and final remarks

According to the presented and discussed results, Table 2.2.1 summarizes the relevant properties of the developed P(VDF-TrFE) membranes and the commercial Whatman nº.1 and Millipore HF090 substrates for microfluidic applications.

Table 2.2.1. Comparative characteristics of commercial and P(VDF-TrFE) membranes as substrates for microfluidic applications.

	Whatman nº.1	Millipore HF090	P(VDF-TrFE) membranes			
Morphology	Randomly oriented cellulose microfibres	Spherulitic-like nitrocellulose porous structure (laminated membrane with backing material)	Spherulitic-like structure (by NIPS)	Porous structure (by TIPS)	Randomly oriented fibres structure (by ES)	Oriented fibres structure (by ES)
Wettability	Superhydrophilic	Superhydrophilic	Superhydrophilic after plasma treatment			
Capillary flow ($mm.min^{-1}$)	44.1 ± 1.13	25.0 ± 3.4 *	46.8 ± 1.3	57.1 ± 2.9	35.7 ± 2.5	88.3 ± 3.7
Wax print quality	Poor (expands 1.2 mm after curing)	High	High			
Colorimetric detection quality	Good	Good (only in the back side)	Good	Good	Good	Bad (heterogeneous)
Mechanical properties (dry/wet)	+/-	+/+**	+/+	+/+	+/+	+/+
Reusable	No	No	Yes (washable)			
Smart/active Properties	No	No	Electroactive (piezo-, pyro and ferroelectric)			

*tailorable according to Millipore type
**need backing material and scrapes easily

Although commercial Whatman no.1 and Millipore HF090 substrates are commonly used for the manufacture of PADs, some of their limitations were presented within the scope of this study and potential innovative solutions based on superhydrophilic P(VDF-TrFE) membranes were highlighted. In fact, the properties that most differentiate the processed P(VDF-TrFE) membranes when compared to the commercial ones evaluated in this work are related to their tailorable morphology, which has a direct effect on the capillary flow rate, the high wax print quality, the homogeneous generation of a colour reaction related to the concentration of the entities (except for the O-ES membranes) and the excellent mechanical properties both in dry and wet conditions. Moreover, the plasma treated P(VDF-TrFE) membranes can be washed and dried repeatedly without losing their physicochemical properties, allowing their reuse, which can be interesting for specific applications and with respect to circular economy and sustainability considerations (as an example, preventing waste and one time use by properly washing and reuse of the substrates). Finally, P(VDF-TrFE) membranes feature electroactive properties (piezo-, pyro- and ferroelectric) [47], which can be further explored in a future generation of microfluidic substrates with smart and/or (multi)functional properties.

2.2.4. Conclusions

P(VDF-TrFE) membranes with tailored morphologies, including spherulitic, porous, randomly oriented and oriented fibres were produced for microfluidic applications. Some of these morphologies were selected to mimic the commercial Whatman™ no. 1 cellulose filter paper with randomly oriented cellulose fibres and Hi-Flow Plus membranes HF090 from Millipore, with a spherulitic-like nitrocellulose porous structure, both commonly used as microfluidic substrates. The P(VDF-TrFE) membranes were characterized and compared to the commercial ones in terms of physicochemical properties, capillary flow rate and microfluidic systems for the colorimetric glucose quantification were fabricated and evaluated. The main limitations of commercial substrates are their poor mechanical properties when wet (Young's modulus of 0.5 ± 0.1 MPa), poor wax print quality (expansion of approximately 1.2 mm after curing) for the Whatman™ no.1 substrates and the need for a backing substrate in the case of Millipore HF090. Although hydrophobic by nature, the P(VDF-TrFE) membranes become superhydrophilic after oxygen plasma treatment. The suitability of the plasma-treated P(VDF-TrFE) membranes as alternative or complementary to the commercially available substrates for microfluidic applications is demonstrated based on their tailorable morphology, tailorable capillary flow rate (from 35.7 ± 2.5 $mm.min^{-1}$ to 88.3 $mm.min^{-1}$), high

wax print quality and excellent mechanical properties (Young's modulus from 71.4 ± 2.9 to 163.4 ± 5.1 MPa in the wet state), allowing to match process requirements of specific (bio)technological applications (such as collection, separation, pre-concentration or mixing, among others). Beyond those properties, P(VDF-TrFE) membranes can be re-used after a proper cleaning process, and their electroactive properties makes them suitable for the development of a new generation of eco-friendly and smart microfluidic substrates, as demonstrated in the present work by their use for the colorimetric quantification of glucose.

2.2.5. References

1. Nayak, S., et al., Point-of-Care Diagnostics: Recent Developments in a Connected Age. Analytical Chemistry. American Chemical Society 2017, 89, 102–123.

2. Chaiyo, S., et al., High Sensitivity and Specificity Simultaneous Determination of Lead, Cadmium and Copper Using MpAD with Dual Electrochemical and Colorimetric Detection. Sensors Actuators, B Chem. 2016, 233, 540–549.

3. Busin, V., et al., Opportunities and Challenges for the Application of Microfluidic Technologies in Point-of-Care Veterinary Diagnostics. Molecular and Cellular Probes. Academic Press October 2016, 331–341.

4. Cinti, S., et al., A Paper-Based Nanomodified Electrochemical Biosensor for Ethanol Detection in Beers. Anal. Chim. Acta 2017, 960, 123–130.

5. Zhu, H., et al., Recent Advances in Lab-on-a-Chip Technologies for Viral Diagnosis. Biosensors and Bioelectronics 2020, 153, 112041.

6. Yetisen, A. K., Akram, M. S., Lowe, C. R., Paper-Based Microfluidic Point-of-Care Diagnostic Devices. Lab on a Chip 2013, 13, 2210-2251.

7. Byrnes, S., Thiessen, G., Fu, E. Progress in the Development of Paper-Based Diagnostics for Low-Resource Point-of-Care Settings. Bioanalysis. 2013, 5, 2821–2836.

8. Martinez, A. W., et al., Patterned Paper as a Platform for Inexpensive, Low-Volume, Portable Bioassays. Angew. Chemie 2007, 119(8), 1340–1342.

9. Carrell, C., et al., Beyond the Lateral Flow Assay: A Review of Paper-Based Microfluidics. Microelectron. Eng. 2019, 206, 45–54.

10. Yang, Y., et al., Paper-Based Microfluidic Devices: Emerging Themes and Applications. ACS Publ. 2016, 89(1), 71–91.

11. Zhang, A. L., Zha, Y., Fabrication of Paper-Based Microfluidic Device Using Printed Circuit Technology. AIP Adv. 2012, 2(2), 022171.

12. Xia, Y., Si, J., Li, Z., Fabrication Techniques for Microfluidic Paper-Based Analytical Devices and Their Applications for Biological Testing: A Review. Biosensors and Bioelectronics 2016, 77, 774–789.

13. Pimentel, E. S., et al., Tailoring Electrospun Poly(l -Lactic Acid) Nanofibers as Substrates for Microfluidic Applications. ACS Appl. Mater. Interfaces 2020, 12(1), 60–69.

14. Ribeiro, C., et al., Electroactive Poly(Vinylidene Fluoride)-Based Structures for Advanced Applications. Nat. Protoc. 2018, 13(4), 681–704.

15. Gonçalves, R., et al., Evaluation of the Physicochemical Properties and Active Response of Piezoelectric Poly(Vinylidene Fluoride- Co-Trifluoroethylene) as a Function of Its Microstructure. J. Phys. Chem. C 2018, 122(21), 11433–11441.

16. Zhao, B., et al., A Controllable and Integrated Pump-Enabled Microfluidic Chip and Its Application in Droplets Generating. Sci. Rep. 2017, 7(1), 1–8.

17. Pullano, S., et al., PVDF Sensor Stimulated by Infrared Radiation for Temperature Monitoring in Microfluidic Devices. Sensors 2017, 17(4), 850.

18. Cardoso, V. F., et al., Polymer-Based Acoustic Streaming for Improving Mixing and Reaction Times in Microfluidic Applications. RSC Adv. 2014, 4(9), 4292 - 4300.

19. Cardoso, V. F., et al., S. Poly(Vinylidene Fluoride-Trifluoroethylene) Porous Films: Tailoring Microstructure and Physical Properties by Solvent Casting Strategies. Soft Mater. 2015, 13(4), 243–253.

20. Sun, B., et al., Advances in Three-Dimensional Nanofibrous Macrostructures via Electrospinning. Progress in Polymer Science. 2014, 39, 862–890.

21. Correia, D. M., et al., Strategies for the Development of Three Dimensional Scaffolds from Piezoelectric Poly(Vinylidene Fluoride). Mater. Des. 2016, 92, 674–681.

22. Pawde, S. M., Deshmukh, K., Surface Characterization of Air Plasma Treated Poly Vinylidene Fluoride and Poly Methyl Methacrylate Films. Polym. Eng. Sci. 2009, 49(4), 808–818.

23. Cardoso, V. F., et al., Piezoelectric β-PVDF Polymer Films as Fluid Acoustic Microagitator. In IEEE International Symposium on Industrial Electronics; 2008; 2028–2033.

24. Sencadas, V., et al., Fiber Average Size and Distribution Dependence on the Electrospinning Parameters of Poly(Vinylidene Fluoride-Trifluoroethylene) Membranes for Biomedical Applications. Appl. Phys. A Mater. Sci. Process. 2012, 109(3), 685–691.

25. California, A., et al., Tailoring Porous Structure of Ferroelectric Poly(Vinylidene Fluoride-Trifluoroethylene) by Controlling Solvent/Polymer Ratio and Solvent Evaporation Rate. Eur. Polym. J.

2011, 47(12), 2442–2450.

26. Ferreira, J. C. C., et al., Variation of the Physicochemical and Morphological Characteristics of Solvent Casted Poly(Vinylidene Fluoride) along Its Binary Phase Diagram with Dimethylformamide. J. Non. Cryst. Solids 2015, 412, 16–23.

27. Correia, D. M., et al., Superhydrophilic Poly(l-Lactic Acid) Electrospun Membranes for Biomedical Applications Obtained by Argon and Oxygen Plasma Treatment. Appl. Surf. Sci. 2016, 371, 74–82.

28. Correia, D. M., et al., Influence of Oxygen Plasma Treatment Parameters on Poly(Vinylidene Fluoride) Electrospun Fiber Mats Wettability. Prog. Org. Coatings 2015, 85, 151–158.

29. Correia, D. M., et al., Surface Wettability Modification of Poly(Vinylidene Fluoride) and Copolymer Films and Membranes by Plasma Treatment. Polymer (Guildf). 2019, 169, 138–147.

30. Costa, C. M., et al., Effect of Degree of Porosity on the Properties of Poly(Vinylidene Fluoride-Trifluorethylene) for Li-Ion Battery Separators. J. Memb. Sci. 2012, 407–408, 193–201.

31. Tan, Q., et al., Fabrication of Porous Scaffolds with a Controllable Microstructure and Mechanical Properties by Porogen Fusion Technique. Int. J. Mol. Sci. 2011, 12(2), 890–904.

32. Clements, J., Davies, G. R., Ward, I. M., A Broad-Line Nuclear Magnetic Resonance Study of a Vinylidene Fluoride/Trifluoroethylene Copolymer. Polymer (Guildf). 1992, 33(8), 1623–1629.

33. Lam, T., et al., Chemically Patterned Microfluidic Paper-Based Analytical Device (C-MPAD) for Point-of-Care Diagnostics. Sci. Rep. 2017, 7(1), 1188.

34. Abe, K., Suzuki, K., Citterio, D., Inkjet-Printed Microfluidic Multianalyte Chemical Sensing Paper. Anal. Chem. 2008, 80(18), 6928–6934.

35. Lu, Y., et al., Fabrication and Characterization of Paper-Based Microfluidics Prepared in Nitrocellulose Membrane by Wax Printing. Anal. Chem. 2010, 82(1), 329–335.

36. Shangguan, J.-W., et al., Paper Capillary Enables Effective Sampling for Microfluidic Paper Analytical Devices. ACS Sensors 2018, 3(7), 1416–1423.

37. Yamada, K., et al., Toward Practical Application of Paper-Based Microfluidics for Medical Diagnostics: State-of-the-Art and Challenges. Lab Chip 2017, 17(7), 1206–1249.

38. Akyazi, T., Basabe-Desmonts, L., Benito-Lopez, F., Review on Microfluidic Paper-Based Analytical Devices towards Commercialisation. Anal. Chim. Acta 2018, 1001, 1–17.

39. Maciel, M. M., et al., Relation between Fiber Orientation and Mechanical Properties of Nano-Engineered Poly(Vinylidene Fluoride) Electrospun Composite Fiber Mats. Compos. Part B Eng. 2018, 139, 146–154.

40. Costa, C. M., et al., Effect of the Microsctructure and Lithium-Ion Content in Poly[(Vinylidene

Fluoride)-Co-Trifluoroethylene]/Lithium Perchlorate Trihydrate Composite Membranes for Battery Applications. Solid State Ionics 2012, 217, 19–26.

41. Liu, F., et al., Progress in the Production and Modification of PVDF Membranes. J. Memb. Sci. 2011, 375(1–2), 1–27.

42. Kang, G.-D., Cao, Y.-M., Application and Modification of Poly(Vinylidene Fluoride) (PVDF) Membranes - A Review. J. Memb. Sci. 2014, 463, 145–165.

43. Otitoju, T. A., Ahmad, A. L., Ooi, B. S., Superhydrophilic (Superwetting) Surfaces: A Review on Fabrication and Application. J. Ind. Eng. Chem. 2017, 47, 19–40.

44. Carrilho, E., Martinez, A. W., Whitesides, G. M., Understanding Wax Printing: A Simple Micropatterning Process for Paper-Based Microfluidics. Anal. Chem. 2009, 81(16), 7091–7095.

45. Renault, C., et al., Three-Dimensional Wax Patterning of Paper Fluidic Devices. Langmuir 2014, 30(23), 7030–7036.

46. Younas, M., et al., Parametric Analysis of Wax Printing Technique for Fabricating Microfluidic Paper-Based Analytic Devices (MPAD) for Milk Adulteration Analysis. Microfluid. Nanofluidics 2019, 23(3), 38.

47. Cardoso, V. F., et al., Improving the Optical and Electroactive Response of Poly(Vinylidene Fluoride-Trifluoroethylene) Spin-Coated Films for Sensor and Actuator Applications. Smart Mater. Struct. 2012, 21(8), 085020.

2.3. Biodegradable polymer-based membranes for sustainable portable analytical devices applications

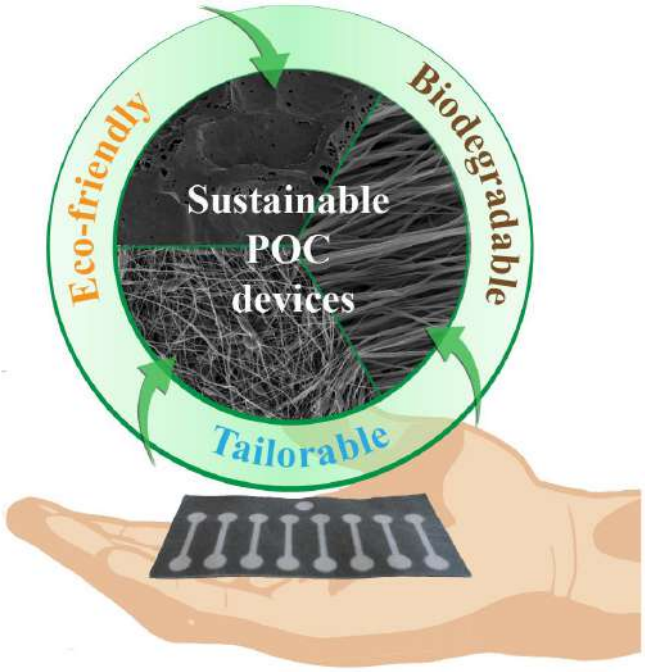

In this chapter, a biodegradable aliphatic polyester poly(D,L-lactide-co-glycolide acid) lactide:glycolide (50:50), PDLG, is used to produce pore- and fiber-based membranes, as alternative to conventional paper substrates. Two fabrication methods are used, with potential for industrial scale-up. These new substrates could presesent great importance for the design and manufacture of a new generation of sustainable portable analytical devices, compatible with circular economy paradigms, and a step forward to cross the challenging academia to industry barrier for their commercialization and widespread adoption.

This chapter is based on the following publication: Ricardo Brito-Pereira, Clarisse Ribeiro, Senentxu Lanceros-Méndez and Vanessa Fernandes Cardoso, Biodegradable polymer-based microfluidic membranes for sustainable point-of-care devices, Chemical Engineering Journal 448, 137639 (2022).

2.3.1. Introduction

Advances in biomedicine through near-patient follow-up continue to play an essential role in the improvement of healthcare services in the developed and developing world [1]. In fact, access to clinical analysis laboratory equipment cannot constitute a barrier against the performance of diagnostic tests, especially in resource-limited locations worldwide [2]. This led to the development of point-of-care (POC) devices that offer new possibilities for prevention, diagnosis and monitoring of medical conditions and/or disease [3]. This portable devices should addressed the ASSURED WHO [4]. Despite the relevant developments witnessed during the last decade, the field of POC devices using traditional microfluidic materials (e.g. silicon, glass and polymers such as polydimethylsiloxane) are still associated with high-cost, equipment-dependent and complicated fabrication process and environmental impact with respect to production and disposal, which has significantly limited their introduction to the market [5].

Since its introduction in 2007 by the Whitesides group, microfluidic paper-based analytical devices (μPADs) have attracted increasing attention as promising portable analytical tools not only in the medical field but also in the food industry, biodefence and environmental monitoring applications, owing to their advantages such as easy-to-use, portability, in situ measurement, minimal reagent consumption and disposability [6,7]. Moreover, the porous structure of paper composed of cellulose fibers with hydrophilic behavior allows fluid transport via capillary forces without the need for external pumping systems [8]. By properly tailoring the channels design using physical or chemical modification techniques such as wax, screen or inkjet printing, stamping, plasma treatment, photolithography or even cutting, fluids of a few microliters can be directed into specific detection zones for multiplexed assays [9]. Processing and surface treatments allow to modify specific zones of the paper substrate from hydrophilic to hydrophobic through specific hydrophobic barriers design creating channels that guide the liquid flow under the effects of capillary action [10]. The barrier type and characteristics are important and must be carefully selected considering the nature of substrate and solutions, in order to ensure compatibility. In addition, three-dimensional (3D) μPADs structures using origami technique have been also reported by folding or stacking the paper in an attempt to control sample and reagent flow rate and path [11]. Analytical detection can be accomplished by measuring the intensity of a colorimetric reaction or, for improved sensitivity, by using electrochemical, fluorescent, immunological or molecular detection methods [12–15].

Different types of paper may be employed in this scope, that depend on the processing method and the compound to be detect, such as filter paper, chromatography paper, nitrocellulose membrane paper, or

graphite paper, among others [16]. Within this range, Whatman cellulose filter paper, Advantec chromatography paper and Hi-Flow Plus nitrocellulose substrates from Millipore are among the most commonly used because of their good wicking performance and uniform thickness [16–18].

Although μPADS feature properties that make them a good choice for the fabrication of portable analytical devices, there are still at an early stage of development and significant research efforts are needed to improve their performance to reach comparable results than currently used technologies. A major challenge remains on reproducibility and sensitivity that are directly affected by the physicochemical properties of paper's porous membranes that offer limited control over sample flow speed and direction [4,19]. To overcome this fact, advanced processing and characterization on papers are needed, similarly to those performed in previous studies with Whatman n°1 cellulose filter paper and Hi-Flow Plus nitrocellulose substrates to properly understand their behaviour as microfluidic substrates [17,20]. Last but not least, paper usually required complex processes that include wood preparation, pulping, chemical recovery, bleaching and papermaking to convert wood to the final product [21]. These processes along with the paper composition that typically include additives such as starch, minerals and synthetic polymers, turn paper a multi-component materials with a complex and varied nature, wich in turn have a crucial role on paper aging and degradation, in most of the cases difficult to interpret or unknown [22].

On the other hand, little attention has been paid to the development of new materials with tailorable physicochemical properties as potential pathway to complement the range of available paper substrates. Recently, flexible polymer membranes based on poly(vinylidene-co-trifluorethylene) and PLLA have been explored as microfluidic substrates. They both demonstrated promising results including tailorable morphology, controlled capillary flow rate, suitable mechanical properties and biocompatibility [17,20].

In this work, a copolymer of poly(D,L-lactide-co-glycolide acid) (PLGA), an aliphatic polyester approved by the FDA has been explored for portable analytical platforms [23]. PLGA has been applied in drug-delivery, surgical implants and tissue engineering applications based on its adjustable biocompatibility and biodegradability, its degradation rate being controlled by varying the relative amount between D, L – lactic acid and glycolic acid monomers [19-21]. Other parameters that affect the degradation rate include molecular weights, size of the samples, integration of additives and environmental conditions [25,26]. During degradation, the copolymer undergoes hydrolysis to produce the original monomers, which are non-toxic for mammalian cells and are metabolized to water and carbon dioxide [27]. The primary role in using biodegradable polymers in medicine is typically to provide a mechanically robust temporary framework during a required time, from which it degrades rapidly and without unwanted side effects. In the case of microfluidic substrates for portable analytical devices, the same behavior is desired, that is,

to maintain the properties of the substrate until and during the assays and ensuring its subsequent quick degradation, turning then more sustainable materials, compatible with circular economy paradigms.

2.3.2. Material and methods

PDLG membranes with various morphologies were processed by two different processing techniques, temperature induced-phase separation (TIPS) and electrospinning (ES), and their potential to be used as substrates for microfluidic applications studied. For that, physicochemical characterization, along with wettability, cytotoxicity and degradation assays of the processed membranes were performed. To evaluate their applicability as microfluidic substrates for portable analytical devices, colorimetric quantification of glucose in printed plasma-treated PDLG substrates was carried out. The following nomenclature will be used to facilitate the identification of the membranes: TIPS, ES-RO, ES-O for pore-based, randomnly oriented and oriented fiber-based membranes, respetively. The samples without and with oxygen plasma treatment will be identified by w/o.P and w/.P, respectively.

2.3.2.1. Materials

PURASORB PDLG 5010, a copolymer of PLGA, with an inherent viscosity midpoint of 1.0 $dL.g^{-1}$ was acquired from Corbion Purac. N,N-dimethylformamide (DMF) and absolute ethanol were obtained from Merck, while chloroform (Chl) was acquired from Sigma-Aldrich. All chemicals and reagents were used as received.

2.3.2.1.1. Membranes processing

A 10 wt.% solution of PDLG was prepared dissolving the copolymer powder in a mixture of DMF/Chl 60/40 v/v solvent under magnetic stirring until a transparent, homogeneous and bubble free solution was obtained, which took no longer than 2 h. This protocol was previously optimized to guarantee a PDLG solution concentration compatible with the various processing techniques employed, described below. Accordingly, porous PDLG membranes were produced by TIPS. For that, PDLG solution was spread on clean glass substrates (10 cm × 15 cm) using a 450 µm gap hand-casting knife and placed in an oven (JP SELECTA Digitronic-TFT) at 25 °C during 72 h to ensure a controlled environment and full crystallization. Fibre-based PDLG membranes were produced by ES. A 10 mL disposable syringe with a

blunt steel needle with an inner diameter of 500 μm was filled with PDLG solution and placed in a syringe pump (New Era NE-1000). A high voltage power supply (Glassman PS/FC30P04) set at 17 kV was applied and the solution was pumped at a flow rate of 0.5 $mL.h^{-1}$. RO-ES PDLG membranes were collected on a grounded 20 cm × 15 cm static plate collector placed 15 cm away from the needle. O-ES PDLG membranes were collected on a grounded rotating drum collector set at a speed of 1500 rpm.

2.3.2.1.2. Membranes surface modification

PDLG membranes present a hydrophobic behaviour after their processing, avoiding the absorption of fluids and thus their ability to spontaneously generate passive flow along the membrane. Therefore, to overcome this limitation and allow their use in the development of portable analytical devices, oxygen plasma treatment was applied to the PDLG membranes to make them (super)hydrophilic [28]. This is an established technique to effectively change the hydrophobicity of polymers by the generation of carboxyl group due to the integration of hydrophilic functional groups on the surface of the copolymer [29,30]. Accordingly, the membranes were placed in a plasma chamber (Zepto, Diener Electronics), equipped with a 40 kHz radio frequency plasma generator. A plasma power of 50 W was used under a total pressure of 80 Pa. In order to overcome overheating and morphological variations, the procedure was optimized and thus plasma treatment was performed 10 times in periods of 30 s on both surfaces of the PDLG membranes.

2.3.2.2. Physicochemical characterization

The surface and transversal morphologies of the PDLG membranes were obtained using a scanning electron microscope (SEM) Quanta 650 FEG from FEI. The samples were previously sputtered (Polaron SC502) with a thin gold layer. From these images, the main pore size and fibre diameter distributions were determine using the software ImageJ. SEM images were obtained in just processed membranes and in membranes kept in vacuum for 6 months, to demonstrate their stability under this storage condition.

The porosity of the membranes was determined by liquid displacement technique using a pycnometer [31,32]. Ethanol was used to fill the pycnometer and the weight measured and labelled as W_1. Each membrane, whose weight was W_s, was individually immersed and saturated with ethanol and additional

ethanol was added to fill the volume of the pycnometer. The pycnometer was weighted and labelled as W_2. The sample filled with ethanol was then extracted from the pycnometer and the residual weight of the ethanol and the pycnometer was labelled as W_3. The following equation was used to calculate the porosity of the membrane $\varepsilon p = (W_2 - W_3 - W_S)/(W_1 - W_3)$. The data will be presented as the average of the values determined in three samples obtained after each processing technique. Absolute ethanol was employed for being a non-solvent of PDLG, penetrating the pores of the samples without inducing shrinking or swelling. The assays were performed on untreated plasma membranes, since hydrophilic membranes absorb ethanol, leading to porosity measurement errors.

Stress-stress mechanical measurements were performed to assess the mechanical properties of the processed plasma-treated PDLG membranes with hydrophilic properties for microfluidic substrates. For that, the assays were carried out in the tensile mode with a Shimadzu AD-IS universal testing set up with a load cell of 50 N. 15 mm long and 10 mm wide samples were stretched at a rate of 1 $mm.min^{-1}$ on dry and wet samples (to mimic the hydration that occurs in portable analytical systems), using 40 µL of PBS (pH 7.4) in the latter. The measurements were performed in triplicate and the plasma treated ES-O membranes were stretched along the direction of the fibres. The average sample thicknesses of the samples are ~108, ~87 and ~82 µm for the plasma treated TIPS, ES-RO and ES-O samples, respectively, as measured using a Fischer Dualscope MPOR.

Infrared measurements (FTIR), differential scanning calorimetry (DSC) and thermogravimetry (TGA) were also performed. FTIR was carried out using a Jasco FT/IR 4100 (Jasco, Easton, Maryland, USA) apparatus in attenuated total reflectance mode (ATR) from 4000 to 600 cm^{-1}. FTIR spectra were obtained after 64 scans with a resolution of 4 cm^{-1}. DSC analysis was performed in a Mettler Toledo DSC822e apparatus using a heating rate of 10 °C.min^{-1}. The samples were cut into small pieces and placed into 40 µL aluminium pans. Finally, TGA studies were performed with a thermal analyser TGA/SDTA 851e from Mettler Toledo. The samples were heated between 25 and 500 °C, at a heating rate of 10 °C.min^{-1}.

2.3.2.3. Contact angle and capillary flow rate assays

Water contact angle measurements were performed to study the effect of plasma treatment on the surface properties of the processed membranes, namely regarding their wettability. The assays were performed using a Data Physics OCA20 instrument by the static sessile drop method with ultrapure water. For that, water drops (3 µL and 15 µL) were dropped on the surface of the

sample and the contact angles were measured using the SCA20 software. The mean contact angle and standard deviation were calculated through the measurement at six different places of each sample. Two volumes were tested because of the different behaviour of the membranes according to the fluid volume.

Capillary assays were carried out to evaluate the ability of the different samples to generate spontaneously passive flows. For that, sample strips 2.5 cm long and 1 cm wide and a solution coloured with green food dye were used. A strip segment of 0.5 cm was vertically submersed and the time taken for the coloured solution to travel across the remaining 2 cm of the sample in the antigravitational direction was measured. Three measurements were performed in each sample and the average and standard deviation were calculated.

2.3.2.4. Cytotoxicity assays

Adapting the ISO 10993-5 standard test method, indirect cytotoxicity evaluation of the processed PLGA membranes (after processing or stored in vacuum for 6 months) was performed. For that, L929 cells were cultured in 75 cm^2 cell culture flask at 37 °C in a humidified environment and 5 % CO_2, using Dulbecco's modified Eagle's medium (DMEM, Biochrom, Berlin, Germany) containing 4.5 $g.L^{-1}$ glucose, 10 % fetal bovine serum (FBS, Biochrom, Berlin, Germany) and 1 % (v/v) penicillin/streptomycin solution (P/S, Biochrom).

The different samples were cut with approximately 1.5 cm^2. Then, their sterilization was carried out by exposition to ultraviolet radiation for 1 h each side of the samples and washing with sterile PBS at pH 7.4. Then, a suspension of 2 × 104 $cell.mL^{-1}$ was seeded in 96-well tissue culture polystyrene plates and incubated for 24 h at the same conditions described above to ensure cell attachment on the plate. Simultaneously, each sample was incubated for 24 h in a 24-well tissue culture polystyrene plate with DMEM. After this time, the cell culture medium in the 96-well plates was removed, and 100 µL of culture medium (that was in contact with the different samples) was added to each well and allowed to incubate for 72 h in standardized culture conditions as mentioned above. A solution of 20 % dimethyl sulfoxide (DMSO) was used for positive control. The metabolic activity was then evaluated after 72 h of incubation using the (3-(4,5-dimethylthiazol-2-yl)-5-(3-carboxymethoxyphenyl)-2-(4-sulfophenyl)-2H-tetrazolium) (MTS, Promega). Briefly, the medium of every well was removed, and fresh medium containing MTS solution (in a 1:5 ratio) was added to each well and incubated for 2 h. After this incubation time, the optical density was measured at 490 nm with a spectrophotometric plate reader (Biotech Synergy HT).

The results are presented as the average of viability ± standard deviation. The percentage of metabolic activity was calculated according to:

Metabolic activity (%) = (Absorbance of sample/Absorbance of negative control) × 100

2.3.2.5. Degradation assays

The degradation of the processed PDLG membranes was monitored by the weight loss in air and in PBS at pH 7.4. Samples from each morphology with an area of 1 cm^2 were cut and placed in 12-well tissue culture polystyrene plates, in contact with air or immersed in 3 mL of PBS at 37 °C. The PBS was replaced every week to avoid variations in pH and ion concentration. The samples were studied at week 1, 3 and 6. Each sample was weight at each time and compared with the initial weight using a Sartorius Cubis® II Micro Lab balance. The samples immersed in PBS were previously washed with distilled water and placed in an oven at 37 °C during 6 h for drying and subsequent weighting.

2.3.2.6. Colorimetric quantification of glucose

To validate the potential of the obtained microfluidic substrates, microfluidic platforms were designed (Figure 2.3.1) and set up using plasma-treated PDLG membranes for the colorimetric quantification of glucose. The microfluidic platforms were designed using a computer-aided design software and hydrophobic wax barriers were printed using a Xerox ColorQube 8870 printer. Before printing, the samples were fixed to a paper sheet with kapton tape. Thus, the hydrophobic barriers were printed, the samples fixed to a glass and then placed in a hot plate (Prazitherm PZ 28-1) and the temperature gradually increased until reaching 95 °C for 5 s, cooled down, and the process repeated 3 times. This temperature is required for the wax to melt and penetrate through the opposite surface of the substrates and thus to contain the fluids in the channels between the hydrophobic barriers. In the scope of the present study, wax-printing technique was used for allowing reproducibility assays, for being a rapid and inexpensive process and for being environmental friendly (lack of organic solvents), besides not requiring specialized facilities [33,34]. For the experiment, a glucose kit (Trinder – Endpoint, FAR Diagnostic) was used. Calibration curves were determined using glucose concentrations of 25, 50, 75, and 100 $mg.dL^{-1}$. This range of concentrations includes ranges of reference values for both new-born babies (20 to 80 $mg.dL^{-1}$) and adults (70 to 110 $mg.dL^{-1}$). Each microfluidic systems holds eight reaction chambers, with each

glucose concentration being quantified in two separate reaction chambers, as illustrated in Figure 2.3.1. Three microfluidic systems were printed for each plasma treated PDLG membranes in order to determine the reproducibility of the colorimetric reactions. 15 µL of glucose solution were used to functionalize the reaction chambers according to the glucose concentration. After 5 min, reagent was introduced in the inlets of the microfluidic system, flowing to the reaction chambers by capillarity. During the reaction, an orange/red colour with intensity proportional to the glucose concentration is produced, which take no more than 10 min. The substrates were then scanned (Brother DCP-1610 W) and colour analysis was performed using ImageJ software by measuring the mean grey values and the corresponding standard deviation on each reaction chambers of the microfluidic systems. Calibration curves were built according to the results obtained [35].

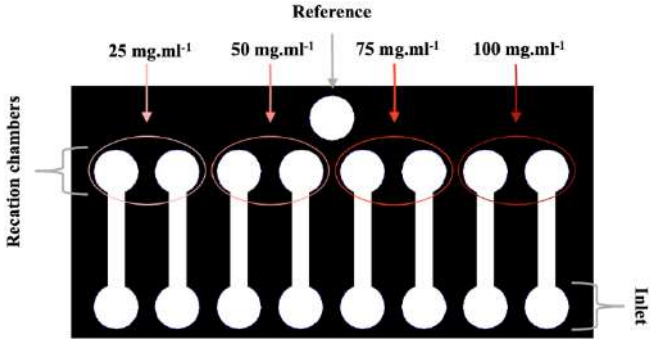

Figure 2.3.1. Schematic illustration of the microfluidic system for the colorimetric quantification of glucose. The glucose solution was placed in the reaction and reference chamber and the reagent was introduced in the inlet to flow by capillarity to the reaction chambers to form an orange/red color with intensity proportional to the concentration of glucose. The inlet, reaction and reference chambers present a diameter of 4 mm and the channels a width of 1.5 mm.

2.3.3. Results and Discussion

2.3.3.1. Physicochemical characterization

Characterization of the PDLG membranes morphology after processing is needed to confirm their morphology and to determine their porosity, which are key properties when applied as microfluidic substrates. Thus, representative SEM images of as processed PDLG membranes obtained by TIPS and ES are shown in Figure 2.3.2. Moreover, knowing the high degradability of PDLG, ES-RO.w/.P membranes were kept in vacuum for 6 months, as representative samples, to demonstrate their stability under vacuum.

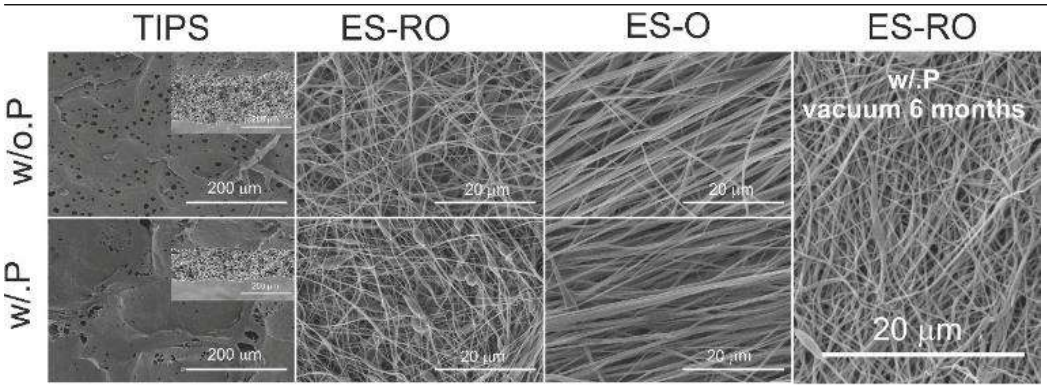

Figure 2.3.2. Representative SEM images of the processed PDLG membranes before and after oxygen plasma treatment and plasma treated randomly-oriented PDLG membrane stored in vacuum for 6 months.

The results demonstrate that the expected morphologies were obtained according to the corresponding processing technique. Pore-based PDLG membranes were produced by TIPS with well-defined pores all along the cross-section. The average diameter of the pores is 10.8 and 11.5 µm for untreated and plasma treated membranes, respectively. On the other hand, fibre-based PDLG membranes were obtained by ES with smooth fiber surface and controlled orientation. ES-RO membranes show average fiber widths of 239 and 153 nm for untreated and plasma treated membranes, whereas ES-O membranes present higher average fiber widths of 496 and 455 nm, respectively. Thus, oxygen plasma treatments lead to a reduction of fibre width and to the fusion of some fibers in the case of the ES-RO membranes. These results are consistent with the literature and are attributed to the high power used during the plasma treatment that lead to a surface heating and flowing of the polymer [29,36]. It is important to emphasize that the plasma treatment protocol was optimized to minimize overheating and significant morphological variations but also to ensure the stability of the hydrophilic surface over time, as will be discussed in the next section. Further, oxygen plasma treatment allows to integrate hydrophilic functional groups by the generation of carboxyl group on the polymer surface, which is a key issue to produce hydrophilic membranes for microfluidic applications [30,37]. Finally, the SEM image of the plasma treated ES-RO membrane stored in vacuum for 6 months shows no visible variations of the fiber morphology and orientation, contrary to the membranes exposed to air or immersed in PBS after processing.

The porosity of the untreated PDLG membranes was also studied and the results presented in Figure 2.3.3a. As indicated above, no experiments were performed on the plasma treated PDLG membranes since hydrophilic membranes absorb ethanol, leading to porosity measurement errors.

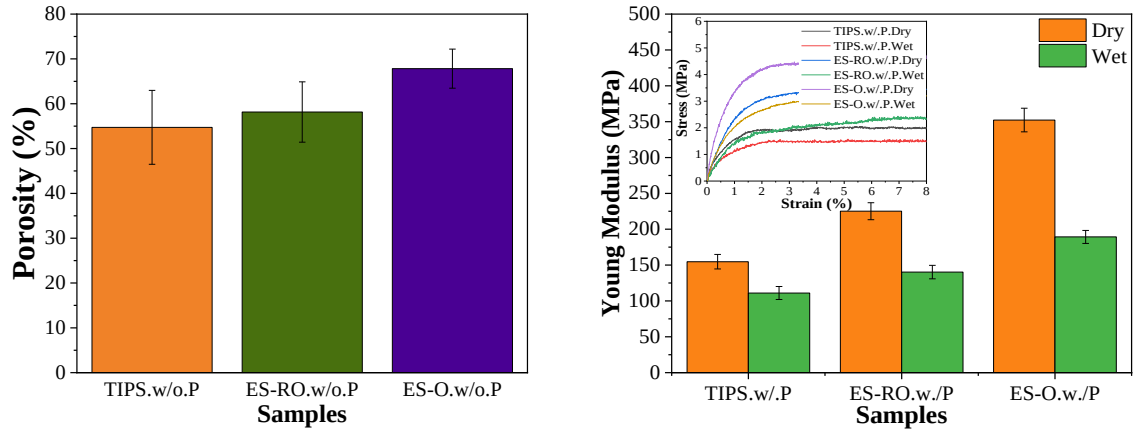

a) b)

Figure 2.3.3. a) Porosimetry results of the PDLG membranes before oxygen plasma treatment; b) Young's modulus with mean and standard deviation and corresponding stress-strain curves up to 8 % of strain for plasma treated dry and wet PDLG membranes.

All samples show mean degrees of porosity above 50 %, regardless the membrane processing method and morphology. The highest value of 67.8 ± 4.3 % is presented by the ES-O membranes and the lowest value of 54.7 ± 8.2 % is shown by the TIPS membranes. The degree of porosity of the ES-RO membranes is 58.1 ± 6.7 %. Thus, all samples show relatively similar porosities, which are also independently of the plasma treatment procedure (Figure 2.3.3a), taking into consideration the standard deviations and experimental error.

Mechanical stability of the plasma treated PDLG membranes are also important in the scope of microfluidic substrates, in particular when wetted, as it occurs during functionalization and/or assays with reagents/solutions containing (bio)molecules to be quantified. Therefore, stress-strain measurements were performed on dry and wet PDLG samples. Characteristic stress-strain mechanical curves feature a linear elastic regime followed by a plastic regime after yielding where the material suffers permanent deformation after any increase in strain or stress. By further stretching the sample, the rupture stress-strain is reached. This behaviour is typical of ductile materials, while brittle materials typically present little or no plastic deformation, fracturing within the linear elastic region of the stress-strain curve. From the linear regime of the curves, the Young's modulus is calculated by applying Hooke's law [38,39]. The results are presented in Figure 2.3.3b, along with the corresponding characteristic stress-strain curves up to 8 % of strain.

All plasma treated PDLG membranes feature stress-strain curves typical of a ductile material. Moreover, analysing the Young's modules, it is evidenced that the morphology and dry or wet state of the membrane

have a direct effect on the mechanical properties. The TIPS membranes feature the lowest Young's moduli of 154.7 ± 10.2 and 111.1 ± 9.9 MPa, for dry and wet membranes, respectively. Regarding the electrospun membranes, the orientation of the fiber lead to an increase of the Young moduli, from 225.1 ± 11.8 to 352.3 MPa in the dry state and from 140.2 ± 9.3 to 189.3 ± 9.0 MPa in the wet state for ES-RO and ES-O membranes, respectively. In all cases, the Young's modulus decrease in the wet state, is agreement with previous studies [17,20]. Comparing with commonly used commercial microfluidic substrates, such as the gold standard Whatman n°1 cellulose paper, or previous studies using PLLA or P(VDF-TrFE) substrates, the processed PDLG membranes feature similar or even higher Young's modules in the wet state [17,20].

2.3.3.2. Contact angle and capillary flow assays

The study of surface wettability and capillary flow rate are key issues for the development of materials to be used as microfluidic substrates, where (super)hydrophilic surfaces are typically required to absorb fluids and generate capillary flows. From several viable options to tailor the polymer surface wettability, such as coating/deposition, defluorination-sulfonation, or electron beam radiation, among others, plasma treatments stand out for its simplicity, versatility and for conserving the main physicochemical properties of the polymer [30-32]. In the scope of this work, a reactive oxygen atmosphere was used for allowing the integration of hydrophilic functional groups through the generation of carboxyl groups on the surface of the polymer, as previously stated [37,41]. To determine the efficiency of plasma treatment to turn the PDLG membranes (super)hydrophilic, contact angle measurements were performed. A surface is typically identified as hydrophobic when its water contact angle is higher than 90°, whereas values below 90° are related with hydrophilic surfaces. Superhydrophobic and superhydrophilic are used for surfaces characterized by water angles above 150° and below 10°, respectively [44]. Figure 2.3.4a shows the contact angles of the processed PDLG membranes without and with plasma treatment, using 3 and 15 µL water drops. Moreover, the plasma treated ES-RO PDLG membranes stored in vacuum for 6 months were also tested.

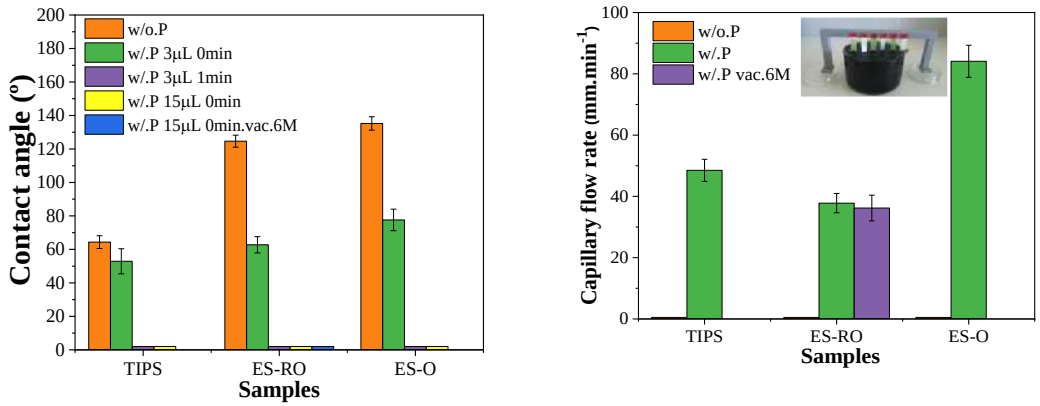

a) b)

Figure 2.3.4. a) Contact angle with water drops of 3 and 15 µm and b) capillary flow rate in the "antigravity" direction of a dye solution of the PDLG membranes before and after oxygen plasma treatment.

The results show that the morphology of the processed samples has a direct effect on the obtained contact angle and thus surface wettability. In fact, untreated TIPS membranes are characterized by contact angles of 64.4 ± 3.8 ° demonstrating a more hydrophilic behavior that the ES based membranes with contact angles of 124.6±3.6 ° and 135.2 ± 4.0 ° for the ES-RO and ES-O membranes, respectively. This result can be explained by the higher surface roughness of the ES membranes comparatively to the TIPS membranes, as shown in Figure 2.3.2, that are associated with superior hydrophobic behavior [30]. On the other hand, plasma-treated PDLG membranes feature values of 52.9 ± 7.5°, 62.8 ± 4.9° and 77.6 ± 6.4° for the TIPS, ES-RO and ES-O PDLG membranes, values lower than for the corresponding untreated-PDLG membranes, using in both cases 3 µL water drops. Thus, it is confirmed that more hydrophilic membranes are achieved using the oxygen plasma protocol. It is important to emphasize that the values with 3 µL water drops were obtained immediately after placing them in contact with the polymer surface but are totally absorbed after 1 min. Taking this result into account, the effect of the water drop volume was studied, especially because portable analytical systems commonly used higher liquid volumes [45]. Thus, contact angles using 15 µL water drops were also measured in plasma-treated PDLG membranes, showing all of them superhydrophilic properties with an instantaneous absorption of the water drops when brought into contact with the samples surfaces. Importantly, this superhydrophilic behavior was kept in the RO-PDLG membranes stored in vacuum for 6 months.

Capillary flow rate measurements were also performed in order to determine the capability of the PDLG membranes to generate passive flow, required property in the development of most portable analytical devices that integrate porous membranes (Figure 2.3.4b). The results were obtained determining the

time needed for a dye solution to travel across a sample strip dipped vertically and partially into a water solution containing green food coloring, as described in section 2.5. Only the plasma treated membranes show the ability to generate passive flows. Lower capillary flow rates were obtained using plasma treated ES-RO membranes with values of 37.5 ± 3.15 $mm.min^{-1}$, which remains unchanged when the sample is kept in vacuum for 6 months. This rate more than duplicates using plasma treated ES-O membranes reaching values of 84.1 ± 5.24 $mm.min^{-1}$, which proves that the orientation of the fiber is an important property to take into account if higher capillary flows are required. This result is explained by the preferential orientation of the fibers along the strip and flow. In turn, the plasma treated TIPS membranes present intermediate capillary flow rates of 48.5 ± 3.61 $mm.min^{-1}$. Thus, the capillary flow rate of plasma treated PDLG membranes can be tailored by tuning their morphology or fiber orientation, which is relevant according to the process to be carried out, such as pre-concentration, mixing, collection, separation, among other processes that may occur in portable analytical devices [46].

These results are consistent with previous studies and the capillary flow rates obtained are in the same order of magnitude as commercial or previously studied materials tested for microfluidic applications [17,20].

2.3.3.3. Cytotoxicity assays

Cell viability of the PDLG membranes, which is an important property of materials when applied in the biomedical field, is presented in Figure 2.3.5, as obtained by indirect contact using L929 cells. Cell viability values higher than 70 % is the threshold defined by the ISO standard 10993-5 to consider a material no cytotoxic.

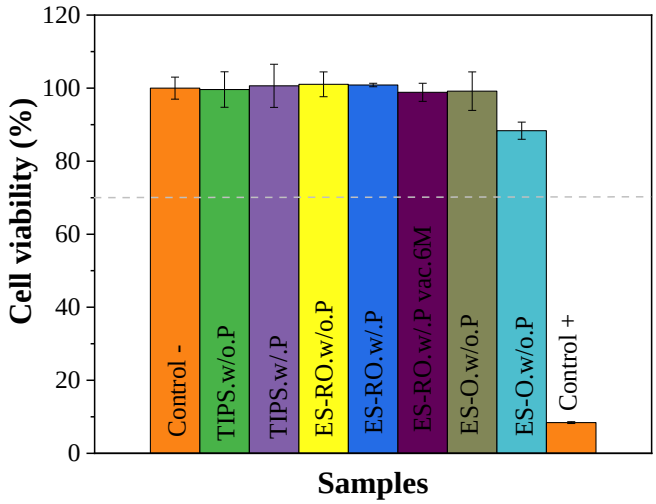

Figure 2.3.5. Cell viability of L929 cells in contact with the as-prepared extraction media exposed to the PDLG membranes for 72 h [relative cell viability is presented as the percentage of the negative control (n=4 ± standard deviation)].

The results show that no significant variations are observed in the citotoxicity of the materials regardless of the processing method, morphology or treated with oxygen plasma, with values higher that 70 % in all cases. Only the plasma-treated ES-RO membranes show a slight decrease, although not relevant, in cell viability. Thus, all membranes demonstrate the ability to be used for biomedical applications.

2.3.3.4. Degradation assays

PDLG is an aliphatic polyesther well known for its high degradation capabilities, which is a key benefit for the development of sustainable portable analytical devices [47]. Thus, the degradation of the PDLG membranes was determined by the weight loss under static conditions in air and in PBS (pH 7.4, 37 °C). The samples were weighed after 1, 3 and 6 weeks and compared with the initial weight. Further, the morphology of representative samples after 3 weeks of degradation is presented in the representative SEM images shown in Figure 2.3.6b. No SEM images of the samples after 6 weeks are shown as the samples were already degraded. ES-RO PDLG membranes are presented as representative of all electrospun membranes.

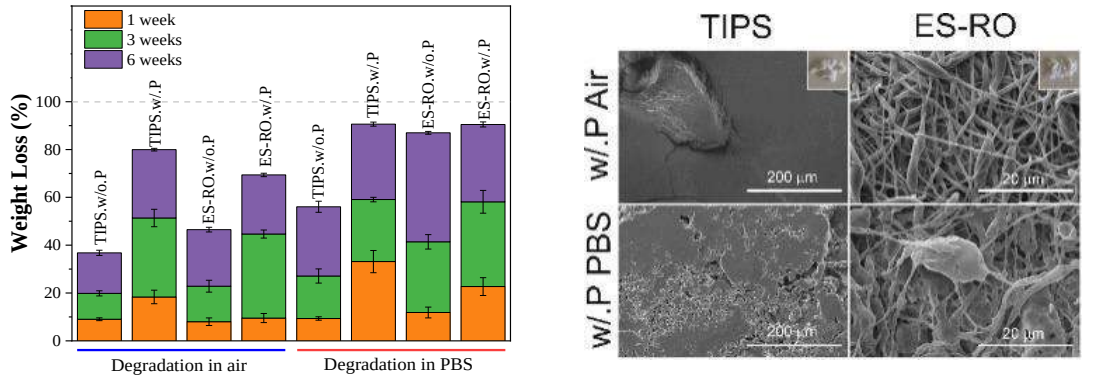

a) b)

Figure 2.3.6. a) Weight loss of untreated and plasma treated PDLG membranes after 1, 3 and 6 weeks in contact with air and immersed in PBS, relative to the initial weight after processing; b) Representative SEM images of PDLG membranes after 3 weeks.

After 3 weeks, all samples lost more than 20 % of their initial weight. The half-time degradation varies according to the morphology and plasma treatments. Moreover, higher weight loss of the PDLG membranes is observed after 6 weeks when immersed in PBS when compared to the corresponding morphology exposed to air. This result is explained by the hydrolytic degradation (whose values depend on factors such as monomers ratio, molecular weights, size of the sample, integration of additives and environmental conditions), through which the polymer degrades into lactic and glycolic acids [20- 22]. When used in vivo, these two monomers are broken in the body without toxic effect [48,49]. Plasma treated PDLG membranes show higher weight loss after 6 weeks than the corresponding untreated membranes with the same morphology, reaching values around 90 % for the plasma treated TIPS, ES-RO and ES-O PDLG membranes immersed in PBS. The SEM images presented in Figure 2.3.6b corroborate the obtained results where it is possible to observe the variation of the morphology after 3 weeks of degradation compared to the initial SEM images presented in Figure 2.3.2. The surface of the plasma treated TIPS membranes clearly lose their surface porous morphology and the plasma treated ES-RO membranes are characterized by heterogeneous fiber diameters and roughness, showing also the formation of polymer aggregates, more visible in the samples immersed in PBS.

This results further support the potential of these membranes to be used as microfluidic substrates to manufacture portable analytical devices where their physicochemical properties remain unchanged when stored in vacuum (for at least 6 months) and degrade quickly after their use.

2.3.3.5. Proof-of-concept

Colorimetric analyses are qualitative or quantitative methods commonly used in medical laboratories and for industrial purposes to determine the presence and/or concentration of a chemical compound in a solution with the aid of a specific reagent, in such a way as to produce a colour intensity proportional to the concentration of the compound being tested. This technique has been adapted for the development of portable analytical devices for the detection and/or quantification in situ of glucose, uric acid, nitrite, creatinine, drugs, HIV, SARS-CoV-2 (Covid-19), drugs, contaminants in water samples, among others [50].

In the scope of this work, the plasma-treated PDLG membranes were evaluated for the colorimetric quantification of glucose, to validate their use as microfluidic substrates for the manufacture of portable analytical devices, taking into account their tailorable physicochemical properties, superhydrophilicity, biocompatibility, biodegradability and portability. To do so, hydrophobic microfluidic channels were printed to fabricate a system composed of a geometry allowing the quantification in the same system of several glucose concentrations, as described in section 2.3.2.6. For the experiments, the samples kept in vacuum for 6 months after processing were used. The results obtained for the ES-RO and ES-O membranes are presented in Figure 2.3.7 and illustrated the mean grey values as a function of the logarithm of the glucose concentration ranging from 25 to 100 mg.dL^{-1}, from which the calibration curves were produced. Moreover, scanned images of the microfluidic systems after the experiments are also presented as inset. The assays were not performed in the pore-based PDLG membranes, as they change to a viscous state and do not promote a proper wax adhesion during the wax printing process. Nevertheless, it is to notice that the pore-based PDLG membranes are compatible with other manufacturing processes conventionally used for the fabrication of portable analytical devices such as cutting process or screen printing, among other.

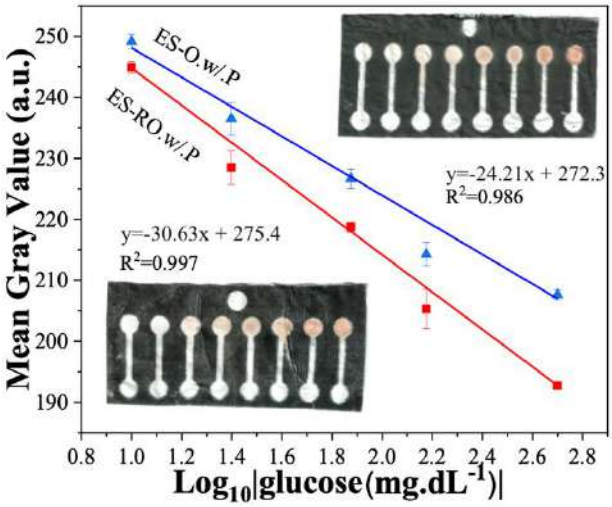

Figure 2.3.7. Calibration curves of glucose for plasma-treated ES-RO and ES-O PDLG membranes. The results are presented as mean gray values and corresponding standard deviations, which were measured on the reaction chambers of the printed PDLG microfluidic substrates using ImageJ software according to the methods described in [35]. Inset: PDLG membranes after the colorimetric reaction.

Both electrospun membranes present good printing quality, as observed in the inset of the Figure 2.3.7. On the other hand, the homogeneity of the colour generated in the reaction chambers is lower in the case of the ES-O membranes, which is related to the orientation of the fiber [2]. However, this behaviour does not have a significant impact on the quality of the calibration curves that feature very good determination coefficient R^2 of 0.997 and 0.986, for the ES-RO and ES-O membranes, respectively. Nevertheless, the ES-RO membranes present a higher sensitivity with a calibration curve slope of 30.63 slightly superior to the 24.21 value obtained for the ES-O membranes. Comparing with previous studies carried out with P(VDF-TrFE) and PLLA membranes, the sensitivity of the samples for the colorimetric quantification of glucose with the same fiber-based morphologies are quite similar, being only slightly inferior to commercial paper substrates [17,20]. Nonetheless, as previously stated and demonstrated, the PDLG membranes can be degraded very quickly after their use, which is a key point for the development of sustainable portable analytical devices. Therefore, this property along with the biocompatibility, tailorable morphology and capillary flow rate, good wax printing quality and excellent mechanical properties (including in the wet state) make this material as an excellent alternative to the commonly used paper substrates, not just for colorimetric assays but also for related (bio)technological applications that can take advantages of the characteristics of PDLG [51].

2.3.4. Conclusions

This work demonstrates the suitability of PDLG membranes for sustainable next generation portable analytical devices. Biodegradable aliphatic polyester PDLG was processed by TIPS and ES followed by oxygen plasma treatment to produce hydrophilic pore- and fiber-based membranes. The processed samples were characterized in terms of physicochemical properties along with contact angle, capillary flow, biocompatibility and degradation assays. The results demonstrate the potential of PDLG membranes to be used as microfluidic substrates, by virtue of their tailorable morphologies, i.e. pore, randomly and oriented fiber-based membranes, surface hydrophilic adaptation to generate spontaneously passive flows and controllable capillary flow rates from 36.2 ± 4.2 to 84.1 ± 5.2 $mm.min^{-1}$. Moreover, the membranes

show good mechanical properties even in wet state and are biocompatible. Engineered wax-based hydrophobic patterns were printed on the membranes to fabricate portable analytical platforms suitable for the colorimetric quantification of glucose. The ES-based membranes were successful in determining the glucose concentration in the ranges of clinical reference values with results comparable to commercial microfluidic substrates. Last but not least, it was proven the physicochemical stability of the plasma-treated PDLG membranes over time when kept in vacuum for at least 6 months and showing a subsequent quick degradation after use, reaching values higher than 90 % after 6 weeks when wet. All these features make PDLG membranes suitable microfluidic substrates for the development of sustainable portable analytical devices and proves that more efforts should be carried out in the development of alternative substrates to the commercially available conventional ones in order to meet the ASSURED criteria defined by the WHO and increase their commercialization and adoption worldwide.

2.3.5. References

1. Samiei, E., Tabrizian, M., Hoorfar, M., A review of digital microfluidics as portable platform f for lab-on a-chip applications, Lab Chip. 2016, 16, 2376–2396.

2. Morbioli, G.G., et al., Technical aspects and challenges of colorimetric detection with microfluidic paper-based analytical devices (μPADs) - A review, Anal. Chim. Acta. 2017, 970, 1–22.

3. Luppa, P.B., et al., Clinically relevant analytical techniques, organizational concepts for application and future perspectives of point-of-care testing, Biotechnol. Adv. 2016, 34, 139–160.

4. Jiang, X., Fan, Z.H., Fabrication and Operation of Paper-Based Analytical Devices, Annu. Rev. Anal. Chem. 2016, 9, 203-222.

5. Tang, R.H., et al., Advances in paper-based sample pretreatment for point-of-care testing, Crit. Rev. Biotechnol. 2017, 37, 411–428.

6. Martinez, A.W., et al., Patterned Paper as a Platform for Inexpensive, Low-Volume, Portable Bioassays, Angew. Chemie. 2007, 119, 1340–1342.

7. C. Li, M., et al., Paper-Based Surfaces with Extreme Wettabilities for Novel, Open-Channel Microfluidic Devices, Adv. Funct. Mater. 2016, 26, 6121–6131.

8. L. Sun, Y., et al., A novel, simple and low cost paper-based analytical device for colorimetric detection of Cronobacter spp., Anal. Chim. Acta. 2018, 1036, 80–88.

9. Dixon, C., Lamanna, J., Wheeler, A.R., Printed Microfluidics, Adv. Funct. Mater. 2017, 27, 1604824.

10. Arduini, F., et al., Paper-Based Electrochemical Devices in Biomedical Field: Recent Advances and Perspectives, Compr. Anal. Chem. 2017, 77, 385-413.

11. Ozer, T., McMahon, C., Henry, C.S., Advances in Paper-Based Analytical Devices, Annu. Rev. Anal. Chem. 2020, 13, 85-109.

12. López-Marzo, A.M., Merkoçi, A., Paper-based sensors and assays: A success of the engineering design and the convergence of knowledge areas, Lab Chip. 2016, 16, 3150–3176.

13. Pardee, K., et al., Rapid, Low-Cost Detection of Zika Virus Using Programmable Biomolecular Components, Cell. 2016, 165, 1255–1266.

14. Ge, S., et al., Nanomaterials-modified cellulose paper as a platform for biosensing applications, Nanoscale. 2017, 9, 4366–4382.

15. Zheng, X.-J., et al., One-step, stabilizer-free and green synthesis of Cu nanoclusters as fluorescent probes for sensitive and selective detection of nitrite ions, Sensors Actuators, B Chem. 2016, 230, 314–319.

16. Kung, C.-T., et al., Microfluidic paper-based analytical devices for environmental analysis of soil, air, ecology and river water, Sensors Actuators, B Chem. 2019, 301, 126855.

17. Brito-Pereira, R., et al., Fluorinated Polymer Membranes as Advanced Substrates for Portable Analytical Systems and Their Proof of Concept for Colorimetric Bioassays, ACS Appl. Mater. Interfaces. 2021, 13, 18065–18076.

18. Lang, A.W., A.M. Österholm., J.R. Reynolds., Paper-Based Electrochromic Devices Enabled by Nanocellulose-Coated Substrates, Adv. Funct. Mater. 2019, 29, 1903487.

19. Cate, D.M., et al., Recent developments in paper-based microfluidic devices, Anal. Chem. 2015, 87, 19–41.

20. Pimentel, E.S., et al., Tailoring Electrospun Poly(l -lactic acid) Nanofibers as Substrates for Microfluidic Applications, ACS Appl. Mater. Interfaces. 2020, 12, 60–69.

21. Bajpai, P., Green chemistry and sustainability in pulp and paper industry, in Pulp and Paper Industry, 2015, 1 - 258.

22. Area, M.C., Cheradame, H., Paper aging and degradation: Recent findings and research methods, BioResources. 2011, 6, 5307 - 5337.

23. Ji, W., et al., Biocompatibility and degradation characteristics of PLGA-based electrospun nanofibrous scaffolds with nanoapatite incorporation, Biomaterials. 2012, 33, 6604–6614.

24. Fouad, H., et al., Preparation and in vitro thermo mechanical characterization of electrospun PLGA nanofibers for soft and hard tissue replacement, Int. J. Electrochem. Sci. 2013, 8, 2293–2304.

25. Heljak, M.K., et al., Micro and nanoscale characterization of poly(DL-lactic-co-glycolic acid) films subjected to the L929 cells and the cyclic mechanical load, Micron. 2018, 115, 64-72.

26. Choinska, E., et al., Influence of macromolecular structure of novel 2- and 4-armed polylactides on their physicochemical properties and in vitro degradation process, J. Polym. Res. 2016, 23, 132.

27. Choinska, C., et al., PLGA with less than 1 month of half-life time: Tensile properties in dry and wet states and hydrolytic degradation, Int. J. Polym. Mater. Polym. Biomater. 2018, 67, 509–516.

28. Chi, J., et al., Bio-inspired wettability patterns for biomedical applications, Mater. Horizons. 2021, 8, 124–144.

29. Correia, D.M., et al., Superhydrophilic poly(l-lactic acid) electrospun membranes for biomedical applications obtained by argon and oxygen plasma treatment, Appl. Surf. Sci. 2016, 371, 74–82.

30. Cardoso, V.F., et al., From superhydrophobic- to superhydrophilic-patterned poly(vinylidene fluoride-co chlorotrifluoroethylene) architectures as a novel platform for biotechnological applications, J. Polym. Sci. Part B Polym. Phys. 2016, 54, 1802 - 1810.

31. Costa, C.M., et al., Effect of degree of porosity on the properties of poly(vinylidene fluoride-trifluorethylene) for Li-ion battery separators, J. Memb. Sci. 2012, 407–408, 193–201.

32. Tan, Q., et al., Fabrication of porous scaffolds with a controllable microstructure and mechanical properties by porogen fusion technique, Int. J. Mol. Sci. 2011, 12, 890–904.

33. Lu, Y., et al., Fabrication and characterization of paper-based microfluidics prepared in nitrocellulose membrane by Wax printing, Anal. Chem. 2010, 82, 329–335.

34. Lam, T., et al., A Chemically Patterned Microfluidic Paper based Analytical Device (C-μPAD) for Point-of-Care Diagnostics, Sci. Rep. 2017, 7, 1188.

35. Shangguan, J.-W., et al., Paper Capillary Enables Effective Sampling for Microfluidic Paper Analytical Devices, ACS Sensors. 2018, 3, 1416-1423.

36. Mattioli, S., Kenny, J.M., Armentano, I., Plasma surface modification of porous PLLA films: Analysis of surface properties and in vitro hydrolytic degradation, J. Appl. Polym. Sci. 2012, 125, E239-E247.

37. Correia, D.M., et al., Influence of oxygen plasma treatment parameters on poly(vinylidene fluoride) electrospun fiber mats wettability, Prog. Org. Coatings. 2015, 85, 151–158.

38. Cardoso, V.F., et al., Poly(vinylidene fluoride-trifluoroethylene) porous films: Tailoring microstructure and physical properties by solvent casting strategies, Soft Mater. 2015, 13, 243–253.

39. S. Jain, T., et al., Printability and Critical Insight into Polymer Properties during Direct-Extrusion Based 3D Printing of Medical Grade Polylactide and Copolyesters, Biomacromolecules. 2020, 21, 388–

396.

40. Hodge, I.M., Enthalpy relaxation and recovery in amorphous materials, J. Non. Cryst. Solids. 1994, 169, 211–266.

41. Malhotra, S., et al., Mesenchymal Stromal Cells as Cell-Based Therapeutics for Wound Healing, Stem Cells Int. 2016, 2016, 4157934.

42. Liu, F., et al., Progress in the production and modification of PVDF membranes, J. Memb. Sci. 2011, 375, 1–27.

43. Kang, G.-D., Cao, Y.-M., Application and modification of poly(vinylidene fluoride) (PVDF) membranes - A review, J. Memb. Sci. 2014, 463, 145–165.

44. Otitoju, T.A., Ahmad, A.L., Oo.i, B.S., Superhydrophilic (superwetting) surfaces: A review on fabrication and application, J. Ind. Eng. Chem. 2017, 47, 19–40.

45. Yuan, H., Chiu, P.-Y., Chen, C.-F., Paper-based analytical devices for point-of-care blood tests, Biomicrofluidics. 2021, 15, 041303.

46. Boobphahom, S., et al., Recent advances in microfluidic paper-based analytical devices toward high-throughput screening, Molecules. 2020, 25, 2970.

47. Elkaseer, A., et al., Replication of overmolded orthopedic implants with a functionalized thin layer of biodegradable polymer, Polymers (Basel). 2018, 10, 707.

48. Anderson, J.M., Shive, M.S., Biodegradation and biocompatibility of PLA and PLGA microspheres, Adv. Drug Deliv. Rev. 1997, 28, 5–24.

49. Sélley, T.L., Kertész, A., Bognár, E., Observed phenomena during the development of an adhesion test for coated medical devices, 2015, 812, 381 - 386.

50. Akyazi, T., Basabe-Desmonts, L., Benito-Lopez, F., Review on microfluidic paper-based analytical devices towards commercialisation, Anal. Chim. Acta. 2018, 1001, 1–17.

51. Brito-Pereira, R., et al., Electroactive polymer membranes as substrates for point-of-care devices, in: MicroTAS 2020 - 24th Int. Conf. Miniaturized Syst. Chem. Life Sci., 2020, 410–411.

2.4. Natural silk based reusable materials for portable analytical devices

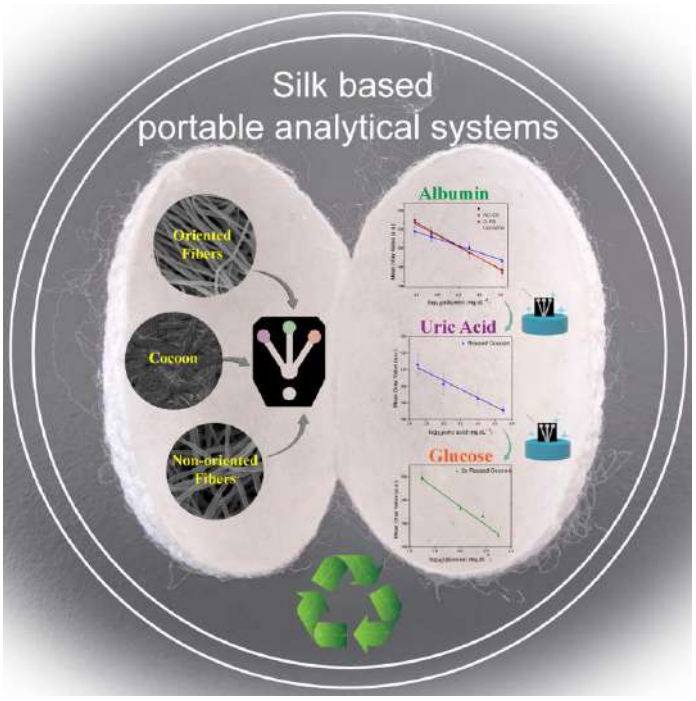

This chapter contributes to the increasing demand for low-cost, environmentally friendly substrates for portable analytical systems by using *Bombyx mori* cocoons. Further, silk fibroin was extracted from these cocoons and electrospun into oriented and randomly-oriented fiber substrates. The developed materials can be used as substrates for multiple colorimetric quantification of three commonly scrutinized clinical analytes: albumin, uric acid, and glucose.

This chapter is based on following publication: Ricardo Brito-Pereira, André S. Macedo, Clarisse Ribeiro, Vanessa F. Cardoso, Senentxu Lanceros-Méndez, Natural based reusable materials for microfluidic substrates: The silk road towards sustainable portable analytical systems, Applied Materials Today 28, 101507 (2022).

2.4.1. Introduction

Prevalence of diseases often associated with bad nutritional habits or poor lifestyles in regions that suffer from inequality of income and a lack of access to medical supervision has been rising. In Germany, by 2040, an increase ranging from 54 % to 77 % of the incidence of type 2 diabetes has been projected [1]. High serum uric acid levels have been linked to prediabetes [2], as well as an increased risk of cardiovascular diseases [3], gout and renal calculi [4]. Low blood albumin levels can be caused by liver diseases such as cirrhosis or hepatitis [5], infections, general inflammation, as well as malnutrition and malabsorption [6]. The populace of third-world countries, where resources are scarcer, especially struggle with the latter. This data demonstrates there is a strong need for low-cost, easy to use, fast and portable devices capable of not only early medical diagnosis and low-cost periodic monitoring of specific health conditions, but also for other applications such as detection of water contaminants [7] or food safety [8]. PADs are diagnostic tools suitable to assist in solving of those issues, allowing *in situ* preliminary evaluation that can be followed up accordingly. Microfluidic paper-based analytical devices (μPADs), first introduced by Martinez et al. [9], who created hydrophobic channel walls using photolithography on Whatman chromatography paper, are particularly appealing due to their portability, versatility, ease of use and low-cost to manufacture. Hydrophobic channels for the development of μPADs have been also implemented by plotting [10], inkjet [11], screen [12] or wax printing [13]. The latter has been used, among others, to develop μPADs able to carry out colorimetric assays, where a reaction between one or more reagents and an analyte generates a color change that may correspond to either the simple presence or a more exact quantification of the specific analyte [14]. Research is being developed to overcome the limitations of paper based substrates, such as unsuitable porosity and weak mechanical properties [15], by exploring alternative polymer-based microfluidic substrates such as PLLA [16] or P(VDF-TrFE) [17].

In the present day, together with the improving the performance of devices, one of the most urgent needs is increasing sustainability of materials and processes, in particular in the area of disposable devices [18]. In fact, the amount of waste produced per hospital patient per year varies greatly worldwide, from 0.44 kg in Mauritius to 8.4 kg in the United States of America (USA) [19], here with an additional 50000 tons generated from home healthcare annually [20]. This waste is a danger to global health and the environment, and thus the search for natural, reusable, and renewable materials, as well as the use of sustainable processing techniques and general circular economy concerns has been met with investment [21]. The development of reusable PADs based on sustainable materials represent one way to address this problem.

Silk fibroin (SF), a biocompatible and biodegradable [22] fibrous protein with mechanical strength and thermal resistance [23], can be extracted from a number of arthropods including spiders and silkworms [24], most typically from Bombyx mori cocoons, as is the case of the present work. The silk filament is composed of sericin (the outer coating) and fibroin (the inner brins) [25]. Silk fibroin can be processed into a variety of formats and has been extensively used in applications as diverse as scaffolds for tissue engineering and *in vitro* disease models or drug delivery in the form of hydrogels, microspheres or films [27, 28], combined with polyethylene oxide to create air filtration systems [29], substrates for wearable displays [30], and often joined with graphene in electronic applications such as bio-integrated electrode systems [31], pressure sensors [32], or enzymatic biosensor transistors [33].

Electrospinning is a technique that allows the development of fiber matts by applying a high voltage electrical field to a droplet of polymeric solution, typically fed through a syringe with a metallic needle by a pump, giving rise to a jet that is collected in a metallic platform. The intensity of the electrical field, solution concentration, pumping rate and distance to the collector regulate fiber shape and size. Oriented fibers can be obtained by using a rotating collector [34]. ES silk fibroin mats have been prepared by tailoring diameter and thickness for controlled drug release [35], modified with graphene oxide to improve antibacterial activity and biocompatibility [36], or carbon nanotube composites for enhancing cardiomyocyte functionalities [37].

Further, the surface characteristics and hydrophilicity of silk fibroin fiber matts can be modified by plasma treatment, where functional groups are introduced to the surface of the exposed material changing its composition, improving the bonding of water molecules by integrating C=O bonds [38, 39].

Herein we report on silk cocoon and ES SF substrates for reusable portable analytical systems. Together with their processing and characterization, their suitability to carry out colorimetric assays for the detection and quantification of albumin, uric acid, and glucose as proofs of concept is demonstrated.

2.4.2. Materials and Methods

2.4.2.1. Materials

Bombyx mori silkworm cocoons were supplied by APPACDM from Castelo Branco (Portugal). Sodium carbonate (Na_2CO_3), formic acid (FA, $CH2O_2$), calcium chloride ($CaCl_2$), absolute ethanol (C_2H_5OH) and Hach pH 4.01 buffer solution were obtained from Sigma-Aldrich. Distilled water was prepared in the laboratory. All reagents and solvents were used as received.

2.4.2.2. Sample preparation

2.4.2.2.1. Preparation of Bombyx mori silkworm cocoon-based substrates

The cocoons were first cleaned and cut in 30 mm^2 pieces and then subjected to a mechanical press (Model 4350.L Bench Top, Carver, Inc., USA) at a pressure of 5 tons for 3 h, reducing their thickness and making them flat and suitable for printing. Raw cocoons will be addressed as R-cocoons, whereas pressed cocoons will be identified as P-cocoons.

2.4.2.2.2. Silk Fibroin extraction and purification

The extraction of SF from Bombyx mori silkworm cocoons was carried out by a soap degumming method. Cocoons were cleaned, cut in 1 cm^2 pieces and boiled in a 0.05 wt.% Na_2CO_3 solution for 30 min in a silk to water solution ratio (w/v) of 1:40. The resultant fibers of SF were thoroughly washed with distilled water and dried at room temperature for 24 h. These fibers were then dissolved in a 0.17 M solution of FA/$CaCl_2$ with a ratio of 12:1 v/w (FA:SF). To remove impurities, this solution was centrifuged at 6000 rpm for 10 min and the supernatant SF/FA/$CaCl_2$ solution was cast on a Petri dish and left to dry at room temperature for 24 h to allow the FA to evaporate. The resultant transparent and plastic material was once again washed in a distilled water bath to remove $CaCl_2$ and dried at room temperature, leading to brittle, whitish solid SF.

2.4.2.2.3. Randomly oriented and oriented electrospun fiber mats

SF was dissolved in FA (8:1 v/w FA:SF) to obtain a solution suitable for ES. The SF/FA solution was transferred to a 10 mL disposable syringe fitted with a blunt steel needle, with an inner diameter of 0.41 mm, and placed in a syringe pump (New Era NE-1000). ES was conducted using a high voltage power supply (Glassman PS/FC30P04) set at 20 kV and the solution was pumped at a flow rate of 0.5 $mL.h^{-1}$. The resulting randomly oriented ES SF samples were collected on a grounded 20 cm x 15 cm static plate collector placed 15 cm away from the tip of the needle. These will be referred to as RO-ES samples and substrates. Oriented ES SF samples were obtained using the same process as the one described before except for the use of a grounded rotating drum collector set at a speed of 1500 rpm. These will be referred to as O-ES samples and substrates.

2.4.2.2.4. Surface modification by plasma treatment

Pressed Bombyx mori silkworm cocoons, O-ES and RO-ES SF samples were subjected to plasma treatment in order to obtain superhydrophilic substrates [28]. The surface treatments were conducted in a plasma chamber (Diener Electronics Zepto) equipped with a 40 kHz radio frequency plasma generator using oxygen. Base pressure before plasma irradiation was 20 Pa. 50 W of power were applied for 100 seconds under a total pressure of 80 Pa. This procedure was performed on both surfaces of the samples. The samples and substrates with and without oxygen plasma treatment will be identified as w/ and w/o plasma, respectively.

2.4.2.3. Sample characterization

2.4.2.3.1. Physicochemical characterization

A scanning electron microscopy (SEM, FEI Nova 200) was employed for the characterization of the morphology and fiber size of all samples, which were previously sputtered with a thin gold layer (Polaron SC502). Mean fiber diameter was calculated from measuring approximately 50 fibers using the ImageJ software.

The porosity of the samples was measured by liquid displacement using a pycnometer. The weight of the pycnometer filled with ethanol was measured and labelled as W_1. The samples, whose weight was W_s, were immersed in ethanol. After the sample was saturated, additional ethanol was added to completely fill the volume of the pycnometer, and the device was weighed (W_2). The sample was then taken out of the pycnometer and the weight of the system with ethanol was labelled W_3. The porosity of the sample was obtained as the average of three values according to equation 2.4.1:

$$\varepsilon p = \frac{W_2 - W_3 - W_S}{W_1 - W_3} \qquad (2.4.1)$$

Absolute ethanol, as a non-solvent for Bombyx mori cocoons and SF, was used as displacement liquid since it can penetrate the pores without inducing either shrinking or swelling. The assays were performed on hydrophobic samples before plasma treatment, since plasma treated samples absorb the ethanol into the matrix which would lead to porosity measurement errors.

Mechanical properties were evaluated in the tensile mode with a Shimadzu AD-IS universal testing set up using a load cell of 50 N for ES samples and 500 N for cocoon samples. 15 mm long and 10 mm wide

samples were stretched at a rate of 1 mm.min^{-1}. O-ES SF samples were stretched along the direction of the fibers. Sample thickness averaged 110, 103 and 81 µm for P-cocoons, RO-ES and O-ES SF samples, respectively, as measured using a Fischer Dualscope MPOR. The stress-strain measurements were performed in triplicate on dry and wet samples, using 40 µL of water in the latter.

Fourier-transformed infrared spectroscopy measurements in attenuated total reflectance mode (FTIR-ATR) were performed at room temperature in all samples with a Bruker Alpha II, from 1000 to 2000 cm^{-1} using 64 scans and a resolution of 4 cm^{-1}.

The degree of crystallinity of the Bombyx mori cocoons and ES SF samples with and without plasma treatment was calculated according to Equation 2, comparing the absorption bands intensity ratio at approximately 1263 cm^{-1} and 1230 cm^{-1} assigned to amide III associated to β-pleated-sheet conformation and random-coil conformation, respectively, from the FTIR-ATR spectra.

$$X_C = \frac{A_{1263}}{(A_{1230} + A_{1263})} \times 100 \qquad (2.4.2)$$

Thermal characteristics of the samples was evaluated by Differential scanning calorimetry (DSC) in a PerkinElmer 6000. Samples weighing approximately 6 mg were placed into 40 µL aluminum pans and then heated from 30 to 400 °C at a rate of 10 °C.min^{-1} after a rapid heating and cooling from 30 to 100 °C at a rate of 20 °C.min^{-1}. This first cycle was carried to promote the evaporation of the solvent and the water molecules that could be included in the polymer structure.

2.4.2.4. Contact angle and capillary flow rate assays

Surface wettability was evaluated using the sessile drop method with a Data-Physics OCA20, by measuring the CA of 3 µL ultrapure water drops on all samples. Six measurements were carried out for each sample in different zones of the samples to obtain the mean contact angle and standard deviation.

2.4.2.5. Colorimetric assays

The preparation of the PADs is illustrated in Figure 2.4.1. The design was created using computer-aided design software Solidworks 2020 and printed with a Xerox ColorQube 8880 printer. After printing, the samples were placed on a hot plate at 100 °C for 2 min for the wax to penetrate the samples all the way

through to the opposing surface, so the barriers can fully contain the fluids. Each system comprises three reaction chambers that act as replicas, an inlet, and a control chamber. The diameters of the reaction and control chambers are 4 mm, the diameter of the inlet is 4.5 mm and the channels connecting the inlet to the reaction chambers are 9 mm long and 2 mm wide. These dimensions shrunk around 15 % during the curing process due to wax expansion. A total of four systems corresponding to four different measurement concentrations were printed for each sample.

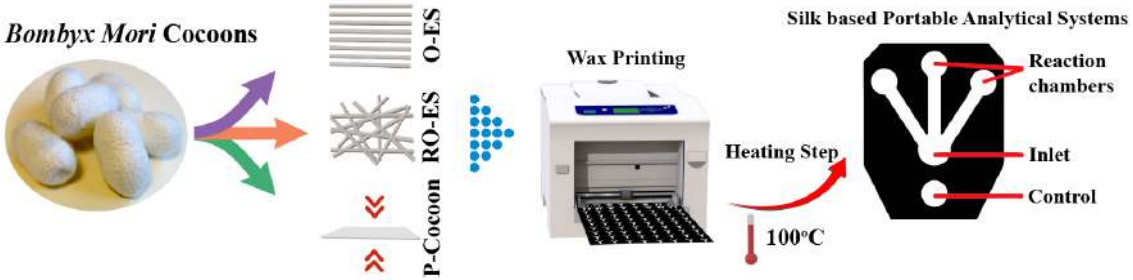

Figure 2.4.1. Procedure for fabrication of the portable analytical system involving wax printing on the developed substrates.

The reaction chambers were first functionalized using 15 µL of the analyte solution under study (albumin, uric acid and glucose) and left to dry for approximately 5 min. For the albumin assay, as correct color complex formation depends on the acidity/basicity, a buffer solution of pH 4.01 was previously added to uniform the pH of the different substrates. The reagent was pipetted into the inlet of the microfluidic system, reaching the reaction chambers by capillarity. After an appropriate time with depends on the analyte being used, the corresponding color variation occurred. The substrates were then scanned (Brother DCP-1610W) and color analysis was performed with ImageJ software by measuring the mean grey values of each reaction chamber. These results were used to obtain the calibration curves.

Colorimetric detection assays for albumin, uric acid and glucose were performed using commercial kits (Trinder – Endpoint, FAR Diagnostic). Reaction time for glucose and uric acid is around 10 min, while for albumin it is immediate.

Albumin reacts with bromocresol green at a pH of 3.8, inducing a change to green color. Calibration curves were determined for all types of substrates using albumin concentrations of 100, 200, 1000, and 4000 $mg.dL^{-1}$. As the cocoons were perfectly viable for carrying the colorimetric tests, their unprocessed natural quality makes them more interesting candidates for PADs substrates. As such, only P-cocoons were used for subsequent tests, which required a washing step in between uses. The substrates were

placed under subtle agitation at a temperature of 60 °C, in a solution with a small amount of dissolved biodegradable pink soap, rinsed in water, and left to dry before carrying out another assay. Uric acid is transformed into allantoin in the presence of uricase, with formation of hydrogen peroxide which, in presence of peroxidase, reacts with ethyl-sulphopropyl-toluidine and 4-aminophenazone to produce a violet/purple complex whose color intensity is directly proportional to the concentration of uric acid in the samples. Concentrations of 0.5, 1, 2 and 5 $mg.dL^{-1}$ were used. The substrates were once again washed, and the glucose assay was carried out. Glucose is oxidized into gluconic acid and hydrogen peroxide by glucose oxidase. Hydrogen peroxide reacts with phenol and 4-aminophenazone in the presence of peroxidase, producing a red/orange complex whose color intensity is directly proportional to the glucose concentration in the samples. These tests were carried at concentrations of 50, 100, 150 and 200 $mg.mL^{-1}$.

2.4.3. Results and discussion

2.4.3.1. Physicochemical characterization

The morphology of the ES SF samples and pressed *B. mori* cocoons, before and after plasma treatment, are shown in Figure 2.4.2a. R-cocoons were also analyzed to evaluate any change of their micromorphology that could arise from the pressing process. Fiber diameter influences the structural and physical properties of the samples, including mechanical strength or capillary flow [32]. The values for each sample are represented in Figure 2.4.2b, and the porosity of the samples in Figure 2.4.2c.

ES samples present cylindrical randomly oriented and oriented fibers according to the processing conditions. The *B. Mori* cocoons exhibit a relatively smooth surface even before pressing, but more so when pressed. After plasma treatment, there appears to be no evidence of removal of the silk sericin layer in the P-cocoon samples. Overall, the characteristic fiber distribution and multilayered structure, as well as their interconnectivity, high porosity, and diameter were reasonably preserved in all samples, independently of the processing conditions. Very slight differences in terms of fiber surface texture can be observed when comparing pre and post plasma treatment, as has been previously reported [40]. This confirms that the O_2 plasma treatment did not significantly modify the morphology of the samples at the microscale, as the treatment protocol was previously optimized [41] not only to minimize overheating or significant morphological changes, but also to ensure the stability of the hydrophilic surface over time, as the samples were tested and remained hydrophilic after 3 months.

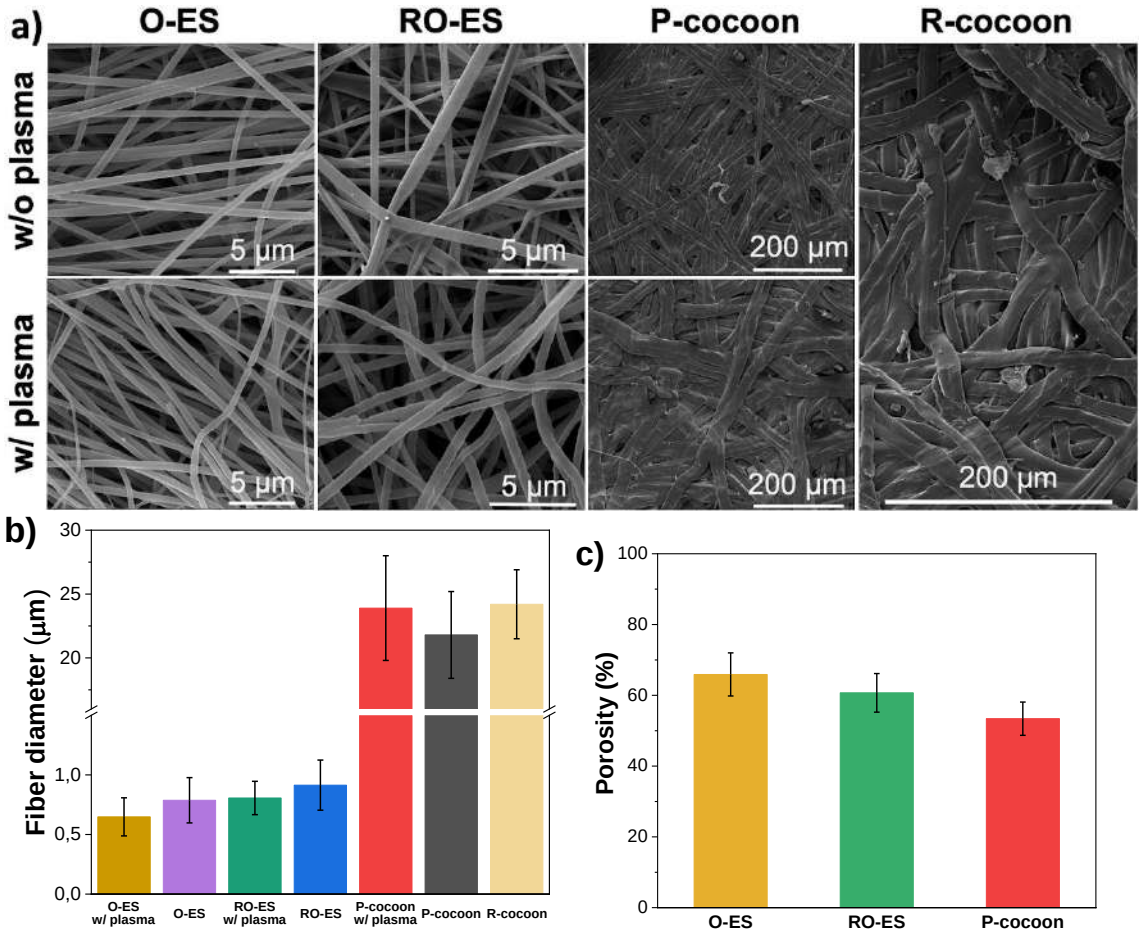

Figure 2.4.2. a) Representative SEM images of the randomly-oriented (RO-ES), oriented (O-ES) electrospun Bombyx mori silk fibroin substrates and pressed cocoons (P-cocoons) before and after oxygen plasma treatment. Images of the raw cocoons (R-cocoons) are also presented. b) Fiber diameters of and c) porosity of the samples before oxygen plasma treatment.

RO-ES samples are characterized by mean fiber diameters of 914 ± 21 nm and 806 ± 14 nm, for non-treated and plasma treated samples, respectively, while O-ES samples present slightly lower diameters of 787 ± 19 nm and 648±20 nm, respectively. The smaller size of the oriented fibers results from stretching during their collection in the rotating drum [42]. A slight decrease in average fiber diameter after plasma exposure is observed and also in agreement with the literature [43]. This can be attributed to the applied atmosphere pressure and heating during the treatment which promotes evaporation of the solvent remnants. *B. mori* cocoons' average fiber widths are significantly larger than for ES SF samples, both as R-cocoons and P-cocoons, and either without or with plasma treatment. These sizes are at the micrometer scale, with values of 24.2 ± 2.7 µm for R-cocoons and 21.8 ± 3.4 µm and 23.9 ± 4.1 µm for P-cocoons, without and with plasma treatment, respectively. The increase of the average fiber size after plasma treatment can be attributed to the local heating of sericin and leading to fiber dilatation by

releasing the effect of the applied pressure. Further, differences can also be expected due to the natural variations between samples produced by *B. mori* [44].

Porosity is one of the main factors that affects how solutions behave when interacting with a sample, which is essential to evaluate for printable materials and their applications PADs and μPADs. Porosimetry results (Figure 2.4.2c) show that O-ES samples are characterized by a porosity of 65.9 ± 6.1 %, followed by the RO-ES samples with 60.7 ± 5.45 %. As the fibers in these samples are similar in size, the more the fibers are randomly deposited one above the other, the tighter the spaces between them, explaining the lower value in the RO-ES samples. Cocoons, with similar non-oriented fiber morphology, present a degree of porosity of 53.4 ± 4.7 %. *B. mori* fibers are flatter than the cylindrical ES fibers, which promotes a lower porosity due to their ability to be deposited in a more compact way.

Stress-strain mechanical curves and the corresponding Young's modulus, FTIR-ATR spectra, and DSC thermograms for the different samples are presented in Figure 2.4.3.

Mechanical stability is essential in materials for PADs, as samples must be able to withstand wear and tear that may come from simple user manipulation or repeated washing and reutilization.

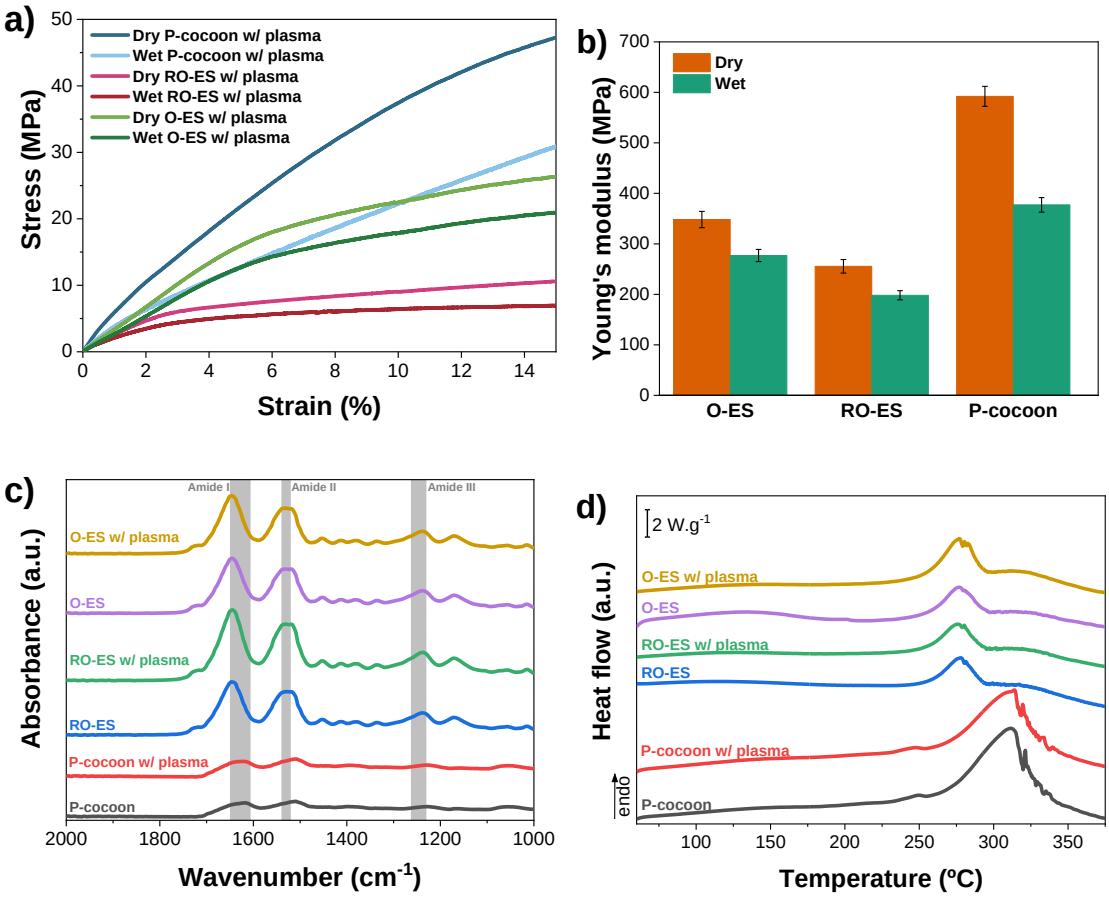

Figure 2.4.3. a) Stress–strain curves up to 15 % of strain; b) Elastic modulus; c) FTIR-ATR spectra and d) DSC thermograms of the oriented (O-ES), randomly-oriented (RO-ES) electrospun Bombyx mori silk fibroin samples and pressed cocoons (P-cocoons).

Stress-strain curves up to 15 % reveal highly deformable structures at low forces, with the mechanical characteristics being determined by a deformation of the network structure and not of the material itself [45]. P-cocoons possess a much higher resistance to deformation when compared with the electrospun samples, due to their larger fiber diameter. The electrospun samples reveal an earlier plastic regime, with the O-ES samples possessing higher resistance than RO-ES, as the aligned fibers allow the sample to withstand higher forces. O-ES samples in dry state reach 348.23 ± 16.16 MPa (276.96 ± 12.09 MPa when wet), a value close to, but still inferior to the wet P-cocoons. The lowest values correspond to the RO-ES fibers (255.54 ± 13.46 and 198.18 ± 9.04 MPa dry and wet, respectively), concurrently revealing they possess the lowest linear regime capacity, quickly giving way to plastic regime. The fact that the stress-strain measurements were taken in the direction the fibers were spun (not perpendicularly) explain the higher resistance of O-ES samples when compared to the RO-ES sample [45]. The cocoons' superior strength can be attributed to greater fiber-size, as well as the presence of sericin which has been shown to enhance the tensile properties of regenerated silk filament [46]. As is later proven by the proofs of

concept, these values show the samples are more than able to withstand the conditions necessary for carrying aqueous assays. Figure 2.4.3b shows that all samples are consistently more resistant to mechanical deformation when dry. Cocoons present the highest Young's modulus, with values of 592.13 ± 19.83 MPa in a dry state and 377.2 ± 14.39 MPa when wetted, the highest values of the three samples. This data, in association with knowing the deformation occurs at a network structure level, shows the samples possess an ability to recuperate their initial structure.

FTIR spectra (Figure 2.4.3c) of samples exposed and unexposed to plasma treatment show no relevant differences among them, indicating that the use of O_2 plasma does not induce any significant chemical change. amide I (which corresponds to C=O stretching) and II (N-H in-plane bending) bands with peaks at 1616 and 1508 cm^{-1} are evident in the cocoons' spectra, with a clear shift to higher wavenumbers for all RO-ES and O-ES samples, peaking at 1648 and 1527 cm^{-1} respectively. The bands corresponding to amide III (–N and N–H functionalities) at around 1263 and 1230 cm^{-1} are less apparent but may also be correlated with an alteration of the secondary structure, an increase of the relative proportion between the random coils and β-sheet conformations [44,47]. This alteration can be attributed to the slow solvent evaporation during the electrospinning process, which leads to improved polymer chain organization and consequentially a highly crystallized structure [48]. The lower peaks in the P-cocoon samples for Amide I, II and III may be due the presence of sericin which seems to have an effect of masking the fibroin and of attenuating the vibrational peaks, as sericin is present as a sheath over the fibroin core of the fiber [49].

The degree of crystallinity of the different samples was calculated from the FTIR-ATR spectra, and the results are shown in Table 2.4.1.

Table 2.4.1. Crystallinity degree of the Bombyx mori cocoons and electrospun SF samples.

Sample	X_c (%)
P-cocoon	47.6 ± 1.9
P-cocoon w/ plasma	47.3 ± 1.9
RO-ES	43.2 ± 1.7
RO-ES w/ plasma	42.9 ± 1.7
O-ES	43.1 ± 1.7
O-ES w/ plasma	42.9 ± 1.7

Crystallinity degrees of approximately 47 % and 43 % were obtained for the Bombyx mori cocoons and electrospun SF samples, respectively. This difference is within experimental margin considering the natural origin of the cocoon and the typical variations between samples [50]. No variations in the degree of crystallinity of the samples are observed due to the plasma treatment, as its effect is restricted to the fiber surface [41].

Figure 2.4.3d shows the DSC thermograms of the different samples for a heating scan from 60 to 375 °C. Cocoons show the endothermic peak at 310 °C associated with the heat-protective sericin layer [51]. Silk I conformation, an organized, crystalline form of fibroin, transforms into the β-sheet structure of silk II with the application of mechanical strain or other energy inputs. The presence of silk II or both I and II is correlated with the endothermic peaks at higher temperatures [52], and a larger presence of silk II crystalline domain may have been induced by the pressing of the cocoons. O-ES and RO-ES samples show the characteristic endothermic peak around 280 °C due to the degradation of highly crystalline SF structures, specifically the side chains groups amino acid residues and the cleavage of peptide bonds [48, 53]. This lower temperature peak is ascribed to the sole presence of fibroin in the electrospun samples, as opposed to fibroin and sericin in the P-cocoons. There are no significant changes between the plasma-exposed and untreated samples, as the treatment only acts at the surface level.

2.4.3.2. Contact angle and capillary flow rate assays

Contact angle and capillary flow rate results are presented in Figure 2.4.4.

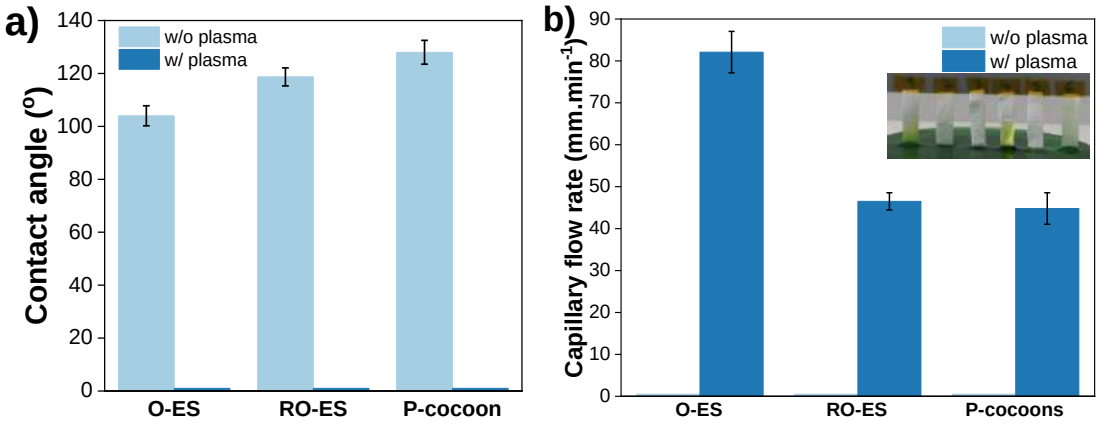

Figure 2.4.4. a) Contact angle and b) capillary flow rates in the antigravity direction of a dye solution for the oriented (O-ES), randomly-oriented (RO-ES) electrospun *Bombyx mori* silk fibroin samples and pressed cocoons (P-cocoons).

The hydrophobic nature of *B. mori* and ES samples is a key issue that must be overcome for their use as microfluidic substrates, where capillary flow is essential. Surface wettability is governed by surface chemistry, surface energy and morphology as well as by the properties of the solution [54]. CA is the most used method to measure these properties and provides accurate results about the wettability of materials and was used in both *B. mori* cocoons and SF electrospun samples [39, 44].

Morphology and plasma treatment have a direct effect on water CA values and therefore on surface wettability (Figure 2.4.4a). Pressed B. mori samples have a CA value of 130 ± 4.5°, representing a slightly hydrophobic behavior when compared to the ES samples which have lower CA values of 117.7 ± 3.4 ° and 104.1 ± 3.8 ° for the RO-ES and O-ES SF samples, respectively. This difference can be explained by the higher surface roughness of the P-cocoons samples when compared to the ES samples, as well as differences in terms of compactness, crystallinity, and composition as cocoons still possess sericin, while the electrospun samples are only composed of fibroin [55]. The CA of all O_2 plasma-treated samples, P-cocoons, O-ES and RO-ES fibers decreased to 0 °, with the water drop being completely absorbed after a 30 s exposure. The reduction of the CA value is a clear indication of the increase in wettability, based on the introduction of C-O and C=O groups [41].

Capillary flow rate evaluation ascertains the ability of the samples to generate passive capillary flow. The results for the different samples can be found in Figure 2.4.4b. The samples that were not exposed to plasma treatment show no visible capillary flow, as expected due to their hydrophobic nature. Treated cocoons and RO-ES samples are characterized by similar flow rates: 44.8 ± 3.75 and 46.5 ± 2.05 $mm.min^{-1}$, respectively. The closeness of these results is related to the similar microstructural features governed by the non-oriented fibers, with the differences in fiber diameter seemingly having no effect on capillary flow. Oriented fibers allow solutions to follow a specific direction without obstruction from transversal fibers, as is verified by the higher mean value of capillary flow, 82.1 ± 4.95 $mm.min^{-1}$, obtained for the O-ES samples.

2.4.3.3. Albumin, uric acid and glucose colorimetric assays on silk substrates

After wax-printing the pattern for the portable analytical system, colorimetric analysis for albumin was first carried out for all the silk-based substrates under study. These tests are depicted in Figure 2.4.5a.

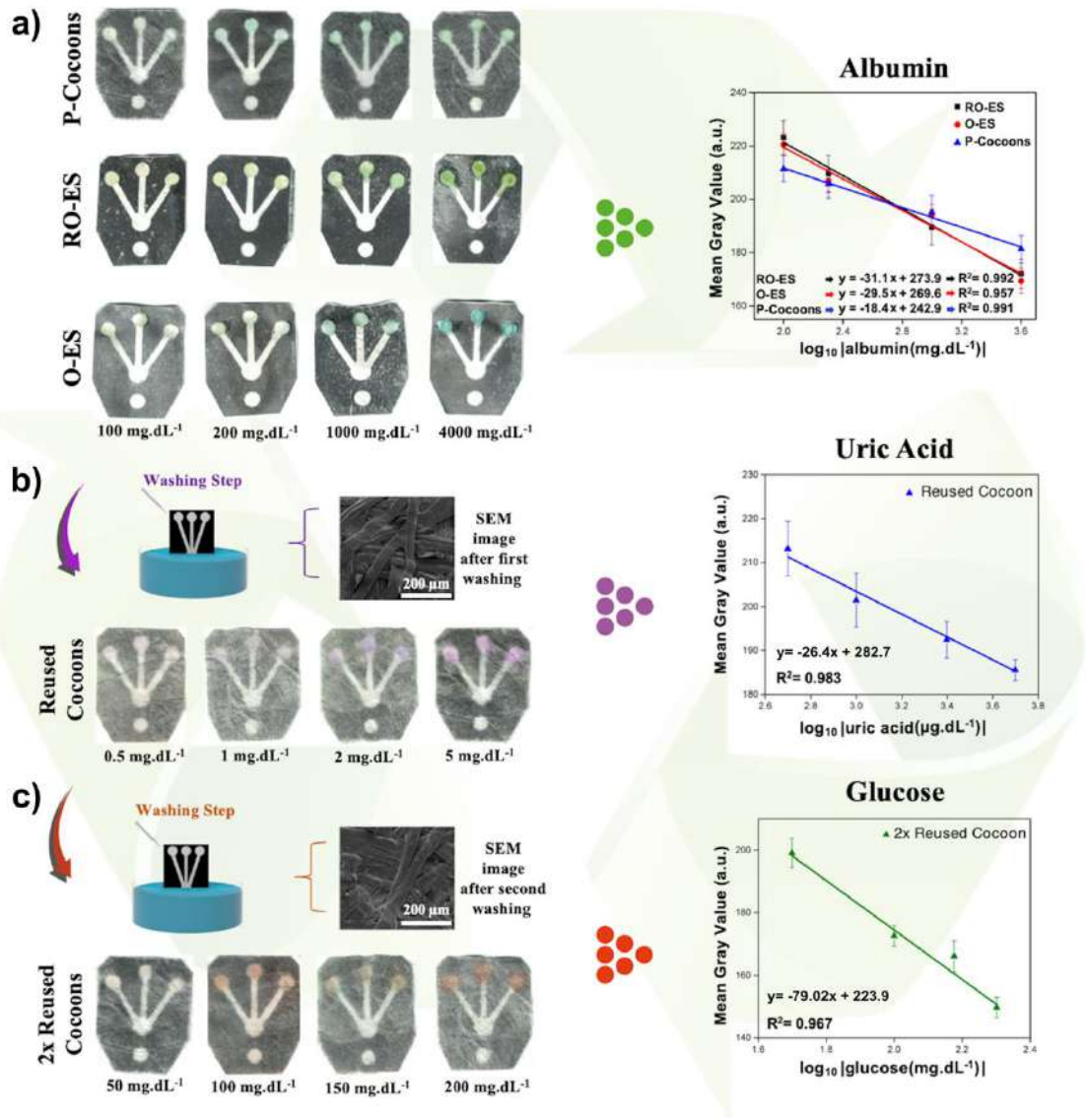

Figure 2.4.5. Colorimetric albumin bioassay proofs of concept on silk-based substrates and the corresponding calibration curves using a) pressed *Bombyx mori* cocoons (P-cocoons), oriented (O-ES) and randomly-oriented (RO-ES) electrospun plasma-treated. b) Colorimetric uric acid assays in reused cocoons, corresponding calibration curves and SEM image of cocoon microstructure after the washing process. c) Colorimetric glucose assays on two times reused cocoons, corresponding calibration curves and SEM image of cocoon microstructure after the second washing process.

Overall, print quality and wax adhesion varies for each substrate. The plasma treated SF substrates show more defined borders in comparison to the cocoon substrates, as expected given the cocoons' more irregular surface even after pressed. On the other hand, wax adhesion is improved in the cocoons. Electrospinning produces thinner fibers than those of the P-cocoons, which are also deposited in a much more compact manner, leading to smaller interstices. This may explain the absence of wax at certain spots in the electrospun substrates, which nevertheless did not hinder the applicability of the materials. The same principle applies to the cocoons: as the interstitial spaces between fibers are wider, vestigial

spaces that were not filled with wax during the thermal curing process may allow small leakages of fluid beyond the printed frontiers, as is observed in Figure 2.4.5a. This did not affect the assays in any of the cases, immediately apparent by the color formation which gradually grows in intensity as concentrations increase, and also confirmed by mean gray value evaluation. The calibration curves for the albumin assay show that colorimetric assays on all substrates show linear fittings, with R^2 values of 0.992, 0.957 and 0.991 for RO-ES, O-ES, and P- cocoons respectively, demonstrating the strong correlation between variation in color intensity and concentration. The somewhat lower R^2 value for the O-ES substrate may be due to the more heterogeneous color formation within the reaction chamber due to fiber orientation. Aligned fiber orientation may prevent less homogeneous reagent and sample mixing than occurs in the other substrates. Nonetheless, with a value of 0.957, the correlation is still evident. The cocoons exhibit a lower slope value, which is associated with a lower sensitivity to the color gradient, which may be associated with how the color tone is produced when contrasting with the substrate's own color. This is not detrimental for the assay, as the correlation is still very strong (R^2 0.991).

After the assay, P-cocoons were then cleaned according to the indicated protocol (see experimental section) and uric acid colorimetric assays were performed, as illustrated in Figure 2.4.5b. In addition to the reagent and sample used to carry the albumin colorimetric assay, the cleaning process removed some of the wax from the printed zone of the cocoons, as indicated by the lighter areas observed in some samples (figure 2.4.5b). In this sense, the cleaning process can be further optimized to better preserve the wax patterns. Nevertheless, the fluids are still mostly contained within the reaction chambers and color complex formation is clear, which is confirmed by the corresponding fitting. R^2 value decreased only slightly (from 0.991 to 0.983), showing that a strong correlation between concentration and color intensity is maintained. The slope value is closer to those observed in the ES substrates, higher than the albumin assay and hence an improvement towards the previous assay in the same cocoons. This may be due to a better contrast of the pigment when interacting with the substrate.

Substrates were once again cleaned and the glucose assays were carried, as shown in Figure 2.4.5c. The cleaning process did not remove wax any further than in the previous assay, which suggests the amount of wax previously washed away was mostly excess from the surface. The leakage from the channels and chambers is slightly higher but the hydrophobic barriers still fulfill their role in containing the fluids. The R^2 value again decreases in a very small amount from 0.983 to 0.967, showing that a strong correlation is still present for the glucose assay. The slope value is considerably higher than the result from the uric acid assay (79.02 compared to 26.4), suggesting the pigment may be even more adequate for this substrate.

2.4.4. Conclusions

Bombyx mori cocoons and ES silk fibroin were used to manufacture substrates for a next generation of sustainable portable analytical devices. The substrates consist of pressed cocoons and both oriented and randomly-oriented ES fibers prepared from purified silk fibroin extracted from the same type of cocoon. Oxygen plasma treatment was applied to these samples to make them superhydrophilic, and a thorough characterization of their physicochemical properties and overall behavior when interacting with aqueous solutions was carried out, showing mechanical stability, thermal resistance, and ability for capillary flow. Plasma treated Bombyx mori cocoons in particular show superhydrophilicity, capillary flow rates of 44.8 ± 3.75 $mm.min^{-1}$, and mechanical resistance, with Young's modulus values of 592.13 ± 19.83 MPa (dry conditions) and 377.2 ± 14.39 MPa (wet conditions). Proofs of concept were produced by wax-printing hydrophobic barriers according to a pattern composed of insertion and reaction chambers joined by channels. Although ES samples allow higher printing quality, an albumin colorimetric assay showed that all substrates performed well and a suitable quantity of fluid was contained inside the chambers, allowing formation of the colored complexes. As P-cocoons require no further processing besides pressing and plasma treatment, they were selected for subsequent cleaning and further colorimetric testing. Uric acid and glucose tests were successfully carried out after in between cleaning procedures, showing that reutilization is possible without compromising substrate and printed microstructure and, therefore, system functionality.

B. mori P-cocoons as well as silk fibroin ES mats are demonstrated to be suitable substrates for the development of portable analytical devices. Natural-based materials as reusable substrates are thus proposed for a next generation of PADs with reduced environmental impact, not only for colorimetric assays, but also for other methods of detection in areas such as biomedicine, environmental monitoring, or food quality control, among others.

2.4.5. References

1. Tönnies, T., et al., Projected number of people with diagnosed Type 2 diabetes in Germany in 2040. Diabetic Medicine. 2019; 36(10): 1217-25.

2. Van der Schaft, N., et al., The association between serum uric acid and the incidence of prediabetes and type 2 diabetes mellitus: The Rotterdam Study. PLOS ONE. 2017; 12(6): e0179482.

3. Virdis, A., et al., Identification of the Uric Acid Thresholds Predicting an Increased Total and Cardiovascular Mortality Over 20 Years. Hypertension. 2020; 75(2): 302-308.

4. De Oliveira, EP., Burini, RC., High plasma uric acid concentration: causes and consequences. Diabetol Metab Syndr. 2012; 4: 12.

5. Gatta, A., Verardo, A., Bolognesi M., Hypoalbuminemia. Internal and emergency medicine. 2012; 7(3): 193-199.

6. Soeters, PB., Wolfe, RR., Shenkin, A., Hypoalbuminemia: Pathogenesis and Clinical Significance. JPEN J Parenter Enteral Nutr. 2019; 43(2): 181-193.

7. Zhao, C., et al., A portable analytical system for rapid on-site determination of total nitrogen in water. Water Research. 2021; 202: 117410.

8. Weng, X., Neethirajan, S., Ensuring food safety: Quality monitoring using microfluidics. Trends in Food Science & Technology. 2017; 65: 10-22.

9. Martinez, AW., et al., Patterned Paper as a Platform for Inexpensive, Low-Volume, Portable Bioassays. Angewandte Chemie International Edition. 2007; 46(8): 1318-1320.

10. Bruzewicz, DA., Reches M., Whitesides GM., Low-Cost Printing of Poly(dimethylsiloxane) Barriers To Define Microchannels in Paper. Analytical Chemistry. 2008; 80(9): 3387-3392.

11. Li, X., et al., Fabrication of paper-based microfluidic sensors by printing. Colloids Surf B Biointerfaces. 2010; 76(2): 564-570.

12. Dungchai, W., Chailapakul, O., Henry, CS., A low-cost, simple, and rapid fabrication method for paper-based microfluidics using wax screen-printing. Analyst. 2011; 136(1): 77-82.

13. Preechakasedkit, P., et al., Development of an automated wax-printed paper-based lateral flow device for alpha-fetoprotein enzyme-linked immunosorbent assay. Biosensors and Bioelectronics. 2018 ;102: 27-32.

14. Benhabib, M., Li, XJ., Low-cost assays in paper-based microfluidic biomedical devices. IMicrofluidic Devices for Biomedical Applications. Woodhead Publishing; 2013. p. 492- 528e.

15. Yetisen, AK., Akram, MS., Lowe, CR., Paper-based microfluidic point-of-care diagnostic devices. Lab Chip. 2013; 13(12) :2210-2251.

16. Pimentel, ES., et al., Tailoring Electrospun Poly(l -lactic acid) Nanofibers as Substrates for Microfluidic Applications. ACS Applied Materials and Interfaces. 2020; 12(1): 60-69.

17. Brito-Pereira, R., et al., Fluorinated Polymer Membranes as Advanced Substrates for Portable Analytical Systems and Their Proof of Concept for Colorimetric Bioassays. ACS Applied Materials and Interfaces. 2021; 13(15): 18065-18076.

18. Olivetti, EA., Cullen, JM., Toward a sustainable materials system. Science. 2018; 360(6396): 1396-1398.

19. Minoglou, M., Gerassimidou, S., Komilis, D., Healthcare waste generation worldwide and its dependence on socio-economic and environmental factors. Sustainability. 2017; 9(2): 220.

20. Kaiser, B., Eagan, PD., Shaner, H., Solutions to health care waste: life-cycle thinking and" green" purchasing. Environmental Health Perspectives. 2001; 109(3): 205-207.

21. Stahel, WR., The circular economy. Nature. 2016; 531(7595): 435-438.

22. Seo, J-W., et al., Calcium-Modified Silk as a Biocompatible and Strong Adhesive for Epidermal Electronics. Advanced Functional Materials. 2018; 28(36): 1800802.

23. Um, Ic., et al., Structural characteristics and properties of the regenerated silk fibroin prepared from formic acid. International journal of biological macromolecules. 2001; 29(2): 91-97.

24. Liu, Z., et al., "Print-to-pattern": Silk-Based Water Lithography. Small. 2018; 14(47): 1802953.

25. Motta, A., Fambri, L., Migliaresi, C., Regenerated silk fibroin films: thermal and dynamic mechanical analysis. Macromolecular Chemistry and Physics. 2002; 203(10-11): 1658-1665.

26. Tien, LW., et al., Silk as a Multifunctional Biomaterial Substrate for Reduced Glial Scarring around Brain-Penetrating Electrodes. Advanced Functional Materials. 2013; 23(25): 3185-3193.

27. Rockwood, DN., et al., Materials fabrication from Bombyx mori silk fibroin. Nature Protocols. 2011; 6(10): 1612-1631.

28. Kundu, B., et al., Silk fibroin biomaterials for tissue regenerations. Advanced Drug Delivery Reviews. 2013; 65(4): 457-470.

29. Gao, X., et al., A silk fibroin based green nano-filter for air filtration. RSC advances. 2018; 8(15): 8181-8189.

30. Liu, Y., et al., Flexible Efficient Top-Emitting Organic Light-Emitting Devices on a Silk Substrate. IEEE Photonics Journal. 2017; 9(5): 1-6.

31. Kim, D-H., et al., Dissolvable films of silk fibroin for ultrathin conformal bio-integrated electronics. Nature Materials. 2010; 9(6) :511-517.

32. Liu, Y., et al., Flexible, highly sensitive pressure sensor with a wide range based on graphene-silk network structure. Applied Physics Letters. 2017; 110(12): 123508.

33. You, X., Pak JJ., Graphene-based field effect transistor enzymatic glucose biosensor using silk protein for enzyme immobilization and device substrate. Sensors and Actuators B: Chemical. 2014; 202: 1357-1365.

34. Doshi, J., Reneker DH., Electrospinning process and applications of electrospun fibers. Journal of Electrostatics. 1995; 35(2): 151-160.

35. Farokhi, M., et al., Functionalized silk fibroin nanofibers as drug carriers: Advantages and challenges. Journal of Controlled Release. 2020 ;321: 324-347.

36. Wang, S-D., et al., Improving Antibacterial Activity and Biocompatibility of Bioinspired Electrospinning Silk Fibroin Nanofibers Modified by Graphene Oxide. ACS Omega. 2018; 3(1): 406-413.

37. Zhao, G., et al., Solvent-Free Fabrication of Carbon Nanotube/Silk Fibroin Electrospun Matrices for Enhancing Cardiomyocyte Functionalities. ACS Biomaterials Science & Engineering. 2020; 6(3): 1630-1640.

38. Lai, J., et al., Study on hydrophilicity of polymer surfaces improved by plasma treatment. Applied Surface Science. 2006; 252(10): 3375-3379.

39. Jeong, L., et al., Plasma-treated silk fibroin nanofibers for skin regeneration. International Journal of Biological Macromolecules. 2009; 44(3): 222-228.

40. Jeong, L., et al., Plasma-treated silk fibroin nanofibers for skin regeneration. International journal of biological macromolecules. 2009; 44(3): 222-228.

41. Correia, DM., et al., Influence of oxygen plasma treatment parameters on poly(vinylidene fluoride) electrospun fiber mats wettability. Progress in Organic Coatings. 2015; 85: 151-158.

42. Ishii, Y., et al., A new electrospinning method to control the number and a diameter of uniaxially aligned polymer fibers. Materials Letters. 2008; 62(19): 3370-3372.

43. Unalan, I., et al., Biocompatibility of plasma-treated poly (3-hydroxybutyrate-co-3-hydroxyvalerate) nanofiber mats modified by silk fibroin for bone tissue regeneration. Materials Science and Engineering: C. 2016; 68: 842-850.

44. Pereira, RFP., et al., Plasma-treated Bombyx mori cocoon separators for high-performance and sustainable lithium-ion batteries. Materials Today Sustainability. 2020; 9: 100041.

45. Maciel, MM., et al., Relation between fiber orientation and mechanical properties of nano-engineered poly(vinylidene fluoride) electrospun composite fiber mats. Composites Part B: Engineering. 2018; 139: 146-154.

46. Ki, CS., et al., The effect of residual silk sericin on the structure and mechanical property of regenerated silk filament. International Journal of Biological Macromolecules. 2007; 41(3): 346-353.

47. Gupta, D., Agrawal A., Rangi A. ,Extraction and characterization of silk sericin. Indian Journal of Fibre & Textile Research (IJFTR). 2014; 39(4): 364-372.

48. Reizabal, A., et al., Silk fibroin magnetoactive nanocomposite films and membranes for dynamic bone tissue engineering strategies. Materialia. 2020; 12: 100709.

49. Deveoglu, O., et al., Examination of Dyeing Properties on Silk of Some Flavonoids by Spectroscopic Techniques. Journal of Natural Fibers. 2021; 18(2): 238-249.

50. Iizuka, E., Size dependency of the physical properties of Bombyx silk. The Journal of Sericultural Science of Japan. 1996; 65(2): 102-108.

51. Mazzi, S., et al., Comparative thermal analysis of Eri, Mori, Muga, and Tussar silk cocoons and fibroin fibers. Journal of Thermal Analysis and Calorimetry. 2014; 116(3): 1337-1343.

52. Cebe, P., et al., Silk I and Silk II studied by fast scanning calorimetry. Acta Biomaterialia. 2017; 55: 323-332.

53. Agarwal, N., Hoagland, DA., Farris, RJ., Effect of moisture absorption on the thermal properties of Bombyx mori silk fibroin films. Journal of Applied Polymer Science. 1997; 63(3): 401-410.

54. Tian, D., Song, Y., Jiang, L., Patterning of controllable surface wettability for printing techniques. Chemical society reviews. 2013; 42(12): 5184-5209.

55. Szewczyk, PK., et al., Roughness and fiber fraction dominated wetting of electrospun fiber-based porous meshes. Polymers. 2019; 11(1): 34.

Chapter 3. Processing multifunctional hydrophobic waxes

3.1. Wax printing magnetic paper-based sensors and actuators

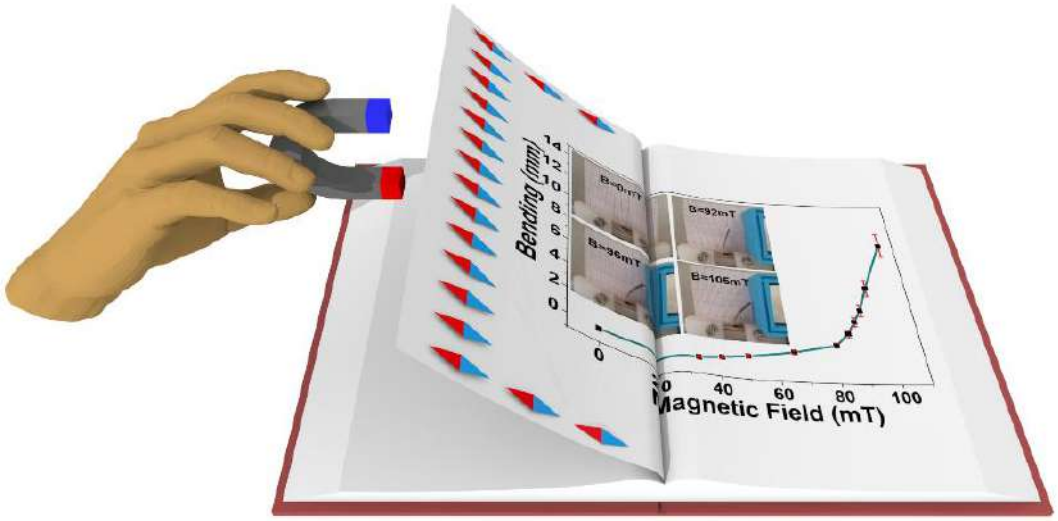

Paper-based advanced functional materials have become the focus of intense research in recent years. Particularly, magnetic papers show strong potential for applications in a wide range of 4.0 technologies including communication, magnetic sensing, electromagnetic filtering, magnetic-based health care tools, point-of-care microfluidic devices. *In situ* and lumen-loading, the main methods to prepare magnetoactive papers, have problems such as the rigorous reaction conditions, hard control of deposition location, decreased tensile strength, poor retention of magnetic nanoparticles or the obligation to perform the magnetic impregnation during papermaking process, that hinder their applicability. In this work, a new concept and methodology are proposed for the fabrication of magnetic paper based on printing technologies and in an impregnation process. For that, a magnetic Fe_3O_4/wax cartridge was developed and the magnetic wax printed on a cellulose paper and incorporated into the paper matrix through a thermal process.

This chapter is based on following publication: R. Brito-Pereira, C. Rial Tubio, S. Lanceros-Mendez, and P.Martins , A Facile Nano-Impregnation Method for Preparing Paper-Based Sensors and Actuators. Advanced Materials Technologies 6 (9), 2100476 (2021).

3.1.1. Introduction

Cellulose is a widespread sustainable resource on an industrial scale [1-3]. The use of fillers together with a cellulosic paper network can result in unique features which are not available in its pristine cellulose, such as magnetic response [4-7]. Such magnetic paper will exhibit the inherent properties of paper fibers and the magnetic properties of nanoparticles, allowing the obtention of valuable documents such as banknotes, bank checks, identity cards and passports with improved security requirements [8, 9]. In addition to these examples related to security papers, magnetic papers are also of interest due to their potential applications in electromagnetic shielding, information storage, magnetic filtering, magnetographic printing, textronic, loudspeaker membranes, flexible data storage, toxic waste remediation, membrane filtration/purification, PADs and magnetomechanical actuators [10-13]. In comparison to other magnetic materials, magnetic paper exhibits some superior properties, such as softness, renewable use, and higher folding resistance[14].

The established methods for the preparation of magnetic papers can be divided in two main groups: *in situ* synthesis and lumen loading [10, 15-17]. *In situ* synthesis relies on the chemical formation of magnetic nanoparticles in the presence of fibers and allows a better distribution of particles on the surface of fibers and a great control of magnetic properties. It has some disadvantages such as rigorous reaction conditions, limited control of deposition location, unstable composition of particles, and low tensile strength of paper [8, 18].

In contrast, lumen loading is a physical deposition process that allows the possibility of magnetic nanoparticles to be introduced into the lumen of fibers, leaving the external surface of the filler free. Additionally, lumen loading ensures protection of nanoparticles, by the cell wall, from the fluid shearing force during the papermaking process [8, 19]. Nevertheless, the lumen-loading approach exhibits some limitations such as the poor retention of magnetic particles and the loss of mechanical strength of the paper[19].

For the magnetic impregnation process, a wide range of magnetic fillers have been considered to provide magnetic properties to paper: bare nanoparticles, organic capped nanoparticles, single core-(oxide) shell particles, multicore-(oxide)shell particles, and fibers [20-22].

Despite the low price, low toxicity, good mechanical properties and high magnetization saturation of cobalt ferrite[1, 23] - $CoFe_2O_4$ (≈60 $emu.g^{-1}$), its high coercivity (higher than > 200 Oe) is an important restrictive factor in certain applications like electromagnetic shielding, magnetic filtering, actuators or security papers [20, 24]. Fe_3O_4 can be a solution for a successful magnetic impregnation process due to

its biocompatibility, low toxicity in human body, and stable room-temperature superparamagnetic response [25-29].

In a new approach, paper can be functionalized with magnetic materials in the form of inks that impart their magnetic properties to the substrate while maintaining its flexibility [30, 31]. The use of printing technologies to obtain magnetic paper allows the production of magnetoactive papers with adequate mechanical and thermal properties, with no limitation in shape and dimensions, which are highly desired to overcome design and manufacturing restrictions [32-35]. Most importantly, this approach enables efficient production of paper-based magnetic elements with lightweight and after papermaking procedures with obvious advantages [20].

Among the different inks and printing technologies, wax printing method [24, 36] is very promising for the development of magnetic waxes to be printed on paper due to its high throughput production and modest technological requirements to fabricate complex two or three-dimensional structures for multipurpose systems.

The possibility to produce papers with their magnetic properties added after paper production with no shape restriction and by printing technologies allows to change the present design and manufacturing model, which is based on *in situ* synthesis or on lumen loading [10].

Thus, in the present work, a new concept and methodology are proposed for the fabrication of magnetic paper, based on printing technologies and in an impregnation process. For that, a home-made magnetic Fe_3O_4/wax cartridge was developed, being the magnetic wax printed on a cellulose paper, and later incorporated into the paper matrix through a thermal process.

3.1.2. Material and methods

3.1.2.1. Materials

Ferric chloride hexahydrate ($FeCl_3 \cdot 6H_2O$ (99 %)), ferrous chloride tetrahydratate ($FeCl_2 \cdot 4H_2O$) (99 %), sodium oleate (82 %), aqueous NH_4OH solution (28-30 %), and cyclohexane (99.8 %) were purchased from Sigma-Aldrich (Missouri, USA); ethanol (96 %) was purchased from Carlo Erba (Barcelona, Spain). Pure ethanol (99 %) was obtained from Sigma-Aldrich (Missouri, USA). The Wax cartridge (S-9511) was purchased from Xerox Corporation (Connecticut, USA). Ultrapure water was obtained by using a Milli-Q Advantage A10 system (Millipore). Whatman n°1 paper was purchased from Merck (Darmstadt, Germany).

3.1.2.2. Synthesis of ferrite nanoparticles

The Fe_3O_4 nanoparticles were synthesized using a hydrothermal method as reported elsewhere [38]. Briefly, 14 mmol of Fe^{3+} precursor and 8 mmol of Fe^{2+} precursor were dissolved in 10 mL of Milli-Q water. A solution containing 0.5 g of sodium oleate dissolved in 10 mL of water was gradually added, followed by a fast addition of 15 mL of concentrated ammonia solution. The hydrothermal treatment was performed at 200 °C for 1 day. The product of the treatment was collected by decantation, methodically washed with water and dried during 12 h at room-temperature under reduced pressure (≈0.08 MPa). The obtained dry powder was once again dispersed in cyclohexane and centrifuged (10 min at 3000 rpm) being precipitated Fe_3O_4 nanoparticles. The centrifuged precipitate was dried at room temperature under reduced pressure and, finally, homogenized in an agate mortar using a pestle.

3.1.2.3. Ink preparation

For the preparation of the Fe_3O_4/wax ink, the Fe_3O_4 nanoparticles were firstly added to pure ethanol (5 mL) and the mixture was putted into an ultrasonic bath for 3 h to ensure high dispersibility and to avoid agglomeration between nanoparticles (Figure 3.1.1i-ii).

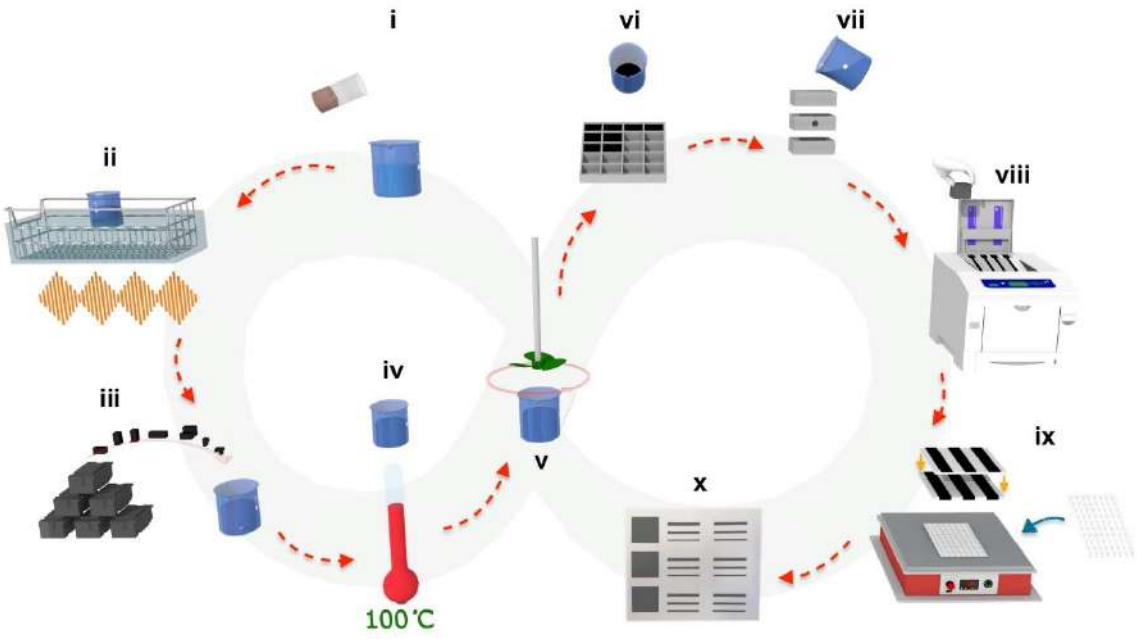

Figure 3.1.1. Graphical representation of the preparation procedure of the Fe_3O_4/wax cartridges and the posterior printing process.

Afterwards, the previously cut Xerox wax (1.5 g) was added to the mixture (to obtain final weight percentages of 1 wt.%, 5 wt.% and 10 wt.% of Fe_3O_4) and placed inside an oven (JP Selecta, Model 2000208) for 30 min at a temperature of 120 °C for polymer melting and complete removal of the solvent (Figure 3.1.1iii-iv).

Then, the mixture was removed from the oven, placed on a hot plate with a temperature of ≈100 °C and mixed for 1 h with the help of a mechanical Teflon stirrer to ensure the homogeneity of the Fe_3O_4/wax mixture (Figure 3.1.1v). Finally, the melt mixture was poured into a 3D printed polyethylene terephthalate (PET-G) mold (1x1x1 cm) to obtain small solid samples of Fe_3O_4/wax blocks (Figure 3.1.1vi), that were used for further characterization.

The nomenclature of the samples in this work will be Paper@Fe_3O_4/wax_A/B, where A is the wt.% of Fe_3O_4 in the wax cartridge and B the width of the printed parallelepiped on the paper matrix.

3.1.2.4. Magnetic cartridge development

The magnetic cartridge was prepared by slowly pouring the molten Fe_3O_4/wax ink into a homemade aluminum mold, specifically shaped and manufactured to be highly compatible with a commercial wax printer (Xerox Colorqube 8880). The system could cool at room temperature (≈10 min) to solidify in the required shape. Then, the mold was disassembled, being the developed magnetoactive cartridge ready to be introduced into the printer.

3.1.2.5. Printing process

Subsequently, after the functional magnetic cartridge fabrication (Figure 3.1.1vii), the cartridge was placed into the printer (Figure 3.1.1viii) and printed patterns with 15 mm length and 30 μm thick (with 1, 2 and 3 mm width) were prepared using a commercial Whatman n°1 paper as substrate (Figure 3.1.1x). To magnetically impregnate the paper, the samples were heated at 120 °C in a in a high-resolution hot plate (Prazitherm P272) for 2 min to ensure the complete distribution of wax and magnetic nanoparticles (Figure 3.1.1ix).

3.1.2.6. Physicochemical characterization

Transmission electron microscopy (TEM) studies were performed using a probe aberration corrected Titan ChemiSTEM (FEI) electron microscope, operated at 200 kV. The average size of the nanoparticles was obtained using the Image J software by counting ≈300 nanoparticles.

Powder X-ray diffraction (XRD) data were collected on a X'Pert PRO diffractometer (PANalytical) set at 45 kV and 40 mA, and equipped with Cu Kα radiation (λ=1.541874 Å) and a PIXcel detector.

Fe_3O_4/wax sample's morphology was evaluated by SEM. The images were obtained from the surface and cross section of the samples using a Hitachi S-4800 scanning electron microscope at an accelerating voltage of 5.0 kV with magnifications from 150x to 20,000x. The wax composites were previously coated with a 40 nm gold layer by a Quorum Q150T S sputter coater.

For the scanning electron microscopy (SEM) of the wax printed patterns on paper, the analyses were performed using a Carl Zeiss EVO 40 (Oberkochen, Germany) SEM equipped with an energy-dispersive X-ray detector EDS Oxford Instrument X-Max (Abingdon, UK). The samples were sputtered with 10 nm thin gold–palladium layer before imaging.

Magnetization M(H) curves were measured up to 1.85 T at room-temperature, using a MicroSense EZ7 vibrating sample magnetometer (VSM). From these loops, saturation magnetization and coercive field of the composites were obtained.

The thermal properties of the Fe_3O_4/wax composites were determined using differential scanning calorimetry (DSC, Perkin Elmer, PYRIS Diamond). The melting enthalpy of the composite samples was determined by numerical integration of the area under the peaks. DSC measurements were conducted at 5 °C.min^{-1} heating and cooling rate in the temperature range of 0–120 °C.

In-plane Young's modulus values E_Y were obtained from the initial slope of strain–stress curves measured for 15 mm length and 30 μm thick (with 1, 2 and 3 mm width) specimens using a TST350 Linkam Scientific Instruments universal testing machine in tensile mode, with a 20 μ.s^{-1} strain rate.

The actuation performance was obtained in a home-made set-up by measuring the displacement of the samples after magnetic actuation with a commercial magnet (KJ Magnetics, Pipersville, PA, USA) that applied a magnetic field in the sample ranging from 0 mT (when the magnet was at 30 mm away from the magnetic paper) to 105 mT (when the magnet was at 1 mm from the magnetic paper).

3.1.3. Results and discussion

3.1.3.1. Nanoparticles

To study the morphology and average size of the produced nanoparticles, TEM images were obtained. The XRD patterns used to determine the structure of the Fe_3O_4 nanoparticles are shown in Figure 3.1.2.

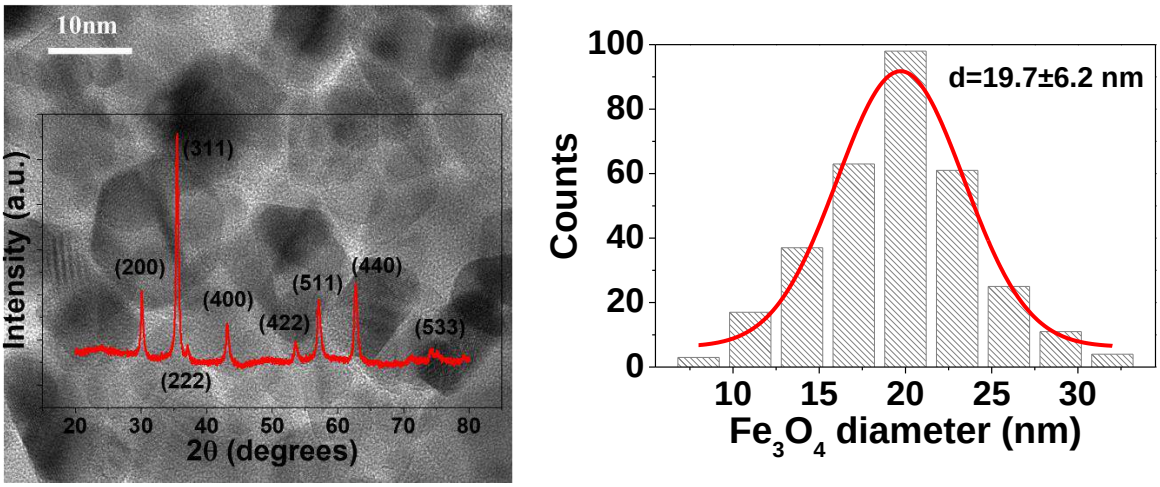

a) b)

Figure 3.1.2. a) TEM image of the Fe_3O_4 nanoparticles. Insets: Representative X-ray diffraction pattern. b) Size distribution of the Fe_3O_4 nanoparticles obtained from TEM.

TEM images show (a representative image is presented in Figure 3.1.2a) a spherical shape for the synthesized Fe_3O_4 nanoparticles with average diameters of 19.7 ± 6.2 nm (Figure 3.1.2b). Since the size of the magnetic nanoparticles is below the superparamagnetic limit (≈25 nm [37]) a superparamagnetic behaviour should be observed in the corresponding polymer composites [38]. In the XRD patterns (inset in Figure 3.1.2a) no peaks corresponding to impurities are detected, being observed an inverse cubic spinel structure with space group Fd-3m [39, 40]. The narrow sharp peaks reveal the high purity of the synthesized Fe_3O_4 nanoparticles [38, 40]. After this initial characterization the magnetic nanoparticles haven been introduced into a previously cut Xerox wax matrix leading to composite blocks with weight percentages of 1 wt.%, 5 wt.% and 10 wt.% (see experimental section).

3.1.3.2. Magnetic composite blocks

Figure 3.1.3 shows representative SEM surface (a-c) and cross section (d-f) images of Fe_3O_4/wax composites. The neat wax surface (Figure 3.1.3a) is slightly rough while the cross section is completely irregular showing lumps and ridges.

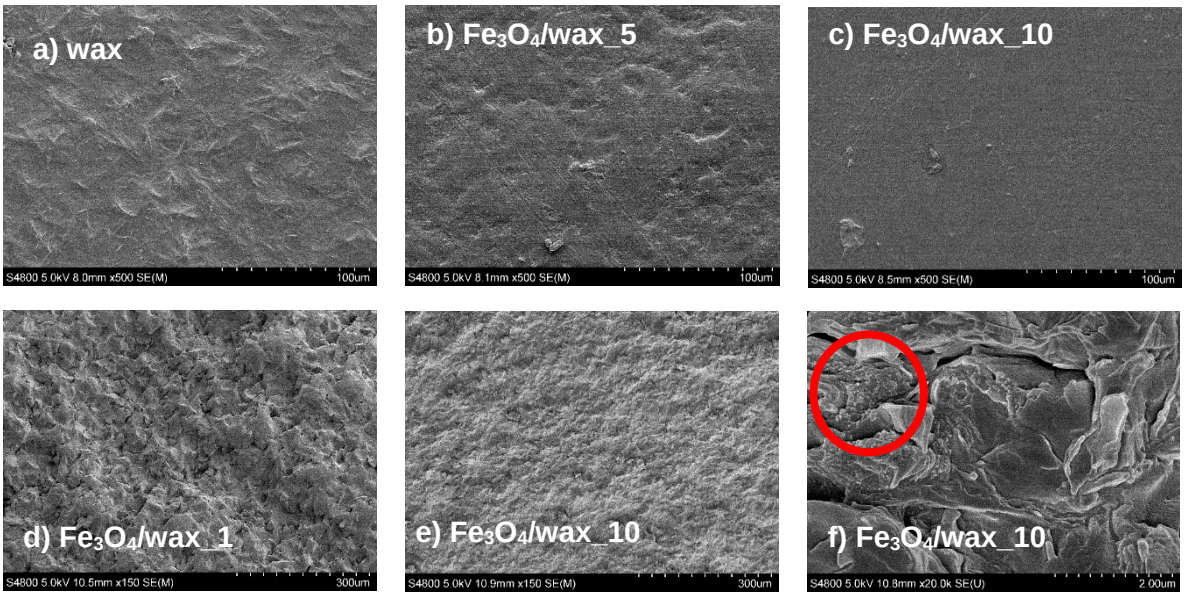

Figure 3.1.3. Surface (500x) SEM images of Fe_3O_4/wax composites with different wt.% of Fe_3O_4: a) 0; b) 5; and c) 10. Cross section (150x) SEM images of Fe_3O_4/wax composites with different wt.% of Fe_3O_4: d) 1; and e) 10. f) Cross section SEM image (20000x) of the Fe_3O_4/wax composite cartridges with 10 wt.% Fe_3O_4 content.

Figure 3.1.3 shows that increasing Fe_3O_4 content within the composite leads to a smoother surface and cross section, being more noteworthy the differences between cross section images. This fact is attributed to the covering of the nanoparticles by the wax, leading to more homogenous and smaller bulks/defects of wax than those formed with neat wax. Further, higher magnification images of the Fe_3O_4/wax composites at 20000x (Figure 3.1.3f) don't show significant differences on the surface topographies.

Meanwhile, in cross section images, agglomerates corresponding to Fe_3O_4 coated with wax can be observed for the 10 wt.% composites (Figure 3.1.3f, marked with red circles). Such agglomerates should not affect the magnetic properties of the composites [41].

Preceding the printing process, the room-temperature magnetic properties of the Fe_3O_4/wax composites have been accessed by VSM measurements (Figure 3.1.4).

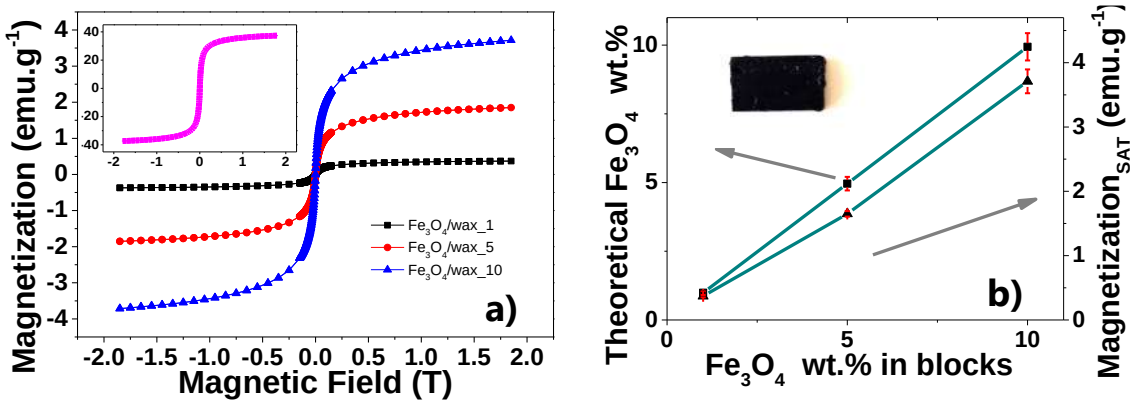

Figure 3.1.4. a) Room-temperature magnetization of the Fe_3O_4/wax cartridges. The inset reveals the room-temperature magnetization of the neat Fe_3O_4 powder. b) Relation between Fe_3O_4 wt.% in the composite blocks: left, the Fe_3O_4 theoretical wt.% (in melt state) and, right, the corresponding magnetization saturation values ($Magnetization_{SAT}$) The inset shows a photograph of the Fe_3O_4/wax composite block with 10 wt.% of nanoparticle content.

Fe_3O_4/wax composites show almost a complete absence of hysteresis, remanence and coercivity consistent with the superparamagnetic behaviour, once room temperature (≈25 °C) is above the blocking temperature and the magnetic moment of the particle is free to rotate in response to the applied magnetic field [42]. Data from Figure 3.1.4a allows also to determine the effective content of Fe_3O_4 nanoparticles in the composite using equation 3.1.1 (method proposed in [43]).

$$Fe_3O_4\ wt.\%_{cartridge} = \frac{Saturation\ Magnetization_{sample} \times 100}{38} \qquad (3.1.1)$$

By comparing the saturation magnetization value of pure Fe_3O_4 nanoparticles (≈38 $emu.g^{-1}$) with the value obtained for the Fe_3O_4/wax composite, it was possible to verify that the difference between the theoretical contents in ink molten solution (1 wt.%, 5 wt.% and 10 wt.%) and the ones calculated on the printed magnets (0.99 wt.%, 4.96 wt.% and 9.92 wt.%) increases with increasing content of Fe_3O_4. This fact is attributed to the higher density of the Fe_3O_4 nanoparticles when compared to the wax matrix that causes the settling of some nanoparticles on the bottom of the composite block. It is to notice that those differences are below 1 % in the worst case.

Additionally, the magnetic remanence values increase almost linearly with increasing ferrite content (Figure 3.1.4b). The shape and magnetization maximum values of the measured magnetic loops demonstrate that Fe_3O_4 nanoparticles are randomly oriented within the wax matrix, being the magnetic saturation maximized (3.71 $emu.g^{-1}$) in the cartridge with higher Fe_3O_4 content (10 wt.%). It is to notice

that this procedure could be also applied to obtain blocks with higher magnetic particle content (50 wt.%) with good printability.

The Fe_3O_4/wax composites were further characterized by DSC to determine the phase transition and the melting enthalpy (Figure 3.1.5).

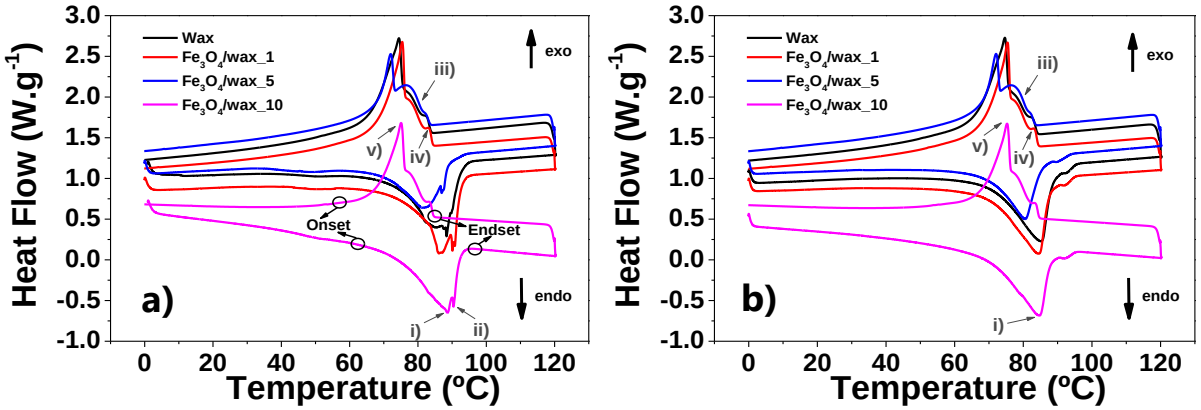

Figure 3.1.5. a) First DSC scans of Fe_3O_4/wax composites at heating and cooling rates of 5 °C.min^{-1} between 0 and 120 °C and; b) DSC second scans of Fe_3O_4/wax composites at heating and cooling rates of 5 °C.min^{-1} between 0 and 120 °C. Heat flow indicates exothermic phase transitions up.

On the heating scans, a wide endothermic peak at 86-88 °C reveals the melting process (i) and the small peak at 88-90 °C indicates the presence of impurities/defects (ii) within the wax matrix that also appears in the neat wax thermogram, disappearing in a second scan (Figure 3.1.5b). In the cooling process three different phase transitions can be observed. The first one (iii) is represented by a small peak at 82-83 °C. Then, the slope changes, resembling a half peak shape (iv) that finish at the beginning of a pronounced peak at ≈74 °C (v). The upward main peaks are attributed to the solid–liquid phase transition, and the small peaks are attributed to a solid–solid phase transition [44]. Additionally the three different peaks are related with the composition of the Xerox wax (paraffin wax, epoxy resin and dye) [45, 46]. The obtained melting and crystallization temperatures are presented in Table 3.1.1.

Table 3.1.1. Melting and crystallization temperatures, obtained from DSC, of the Fe_3O_4/wax composites.

	Heating (± 2 °C)	Cooling (± 2 °C)		
wt. %		1	2	3
0	85-88 °C	82 °C	77 °C	74 °C
5	84-86 °C	83 °C	77 °C	75 °C

10	80-81 °C	82 °C	76 °C	72 °C
20	85-88 °C	83 °C	77 °C	75 °C

From Table 3.1.1 is possible to conclude that, considering the measurement error, no relevant differences are obtained (less than 7 %) on the melting and crystallization temperatures of pristine wax and composites, revealing that the incorporation of magnetic nanoparticles has no significant effect on the thermal properties of wax composites.

The latent heat of fusion and crystallization, obtained by integrating the areas under the peaks of the first DSC scans, are presented in Table 3.1.2.

Table 3.1.2. Latent heat of fusion and crystallization of the Fe_3O_4/wax composites.

	Heating (± 3 °C)			**cooling (± 3 °C)**		
%	Onset (°C)	Endset (°C)	ΔH ($J.g^{-1}$)	Onset (°C)	Endset (°C)	ΔH ($J.g^{-1}$)
0	59.7	96.2	11.20	56.6	84.8	10.03
1	61.5	95.1	11.02	57.8	85.7	9.76
5	57.3	94.6	8.50	56.7	84.3	7.75
10	62.6	95.2	9.58	57.2	85.1	9.16

Results from Table 3.1.2, with similar values on the onset/endset temperatures and latent heats, mean that the thermal energy storage capacity of the wax is maintained with the addition of magnetic nanoparticles. DSC results also reveal that the magnetic impregnation of the paper should be performed at temperatures higher than ≈90 °C (melting temperature of the Fe_3O_4/wax composites).

3.1.3.3. Magnetic paper

After the structural, magnetic and thermal characteristics of the Fe_3O_4/wax composites have been obtained, a Fe_3O_4/wax cartridge with the highest Fe_3O_4 nanoparticle content (Fe_3O_4/wax_10) has been developed and an impregnation process was used to print on paper substrates with a parallelepiped geometry (15 mm length, 30 μm thick and with 1, 2 and 3 mm width) resulting on Paper@Fe_3O_4/wax_10/1, Paper@Fe_3O_4/wax_10/2 and Paper@Fe_3O_4/wax_10/3 samples (see experimental section).

To evaluate the extent of the impregnation process and to ensure that the width of the printed material has not any influence on filler distribution, SEM/EDX images have been used (Figure 3.1.6).

	SEM	O	Fe	C

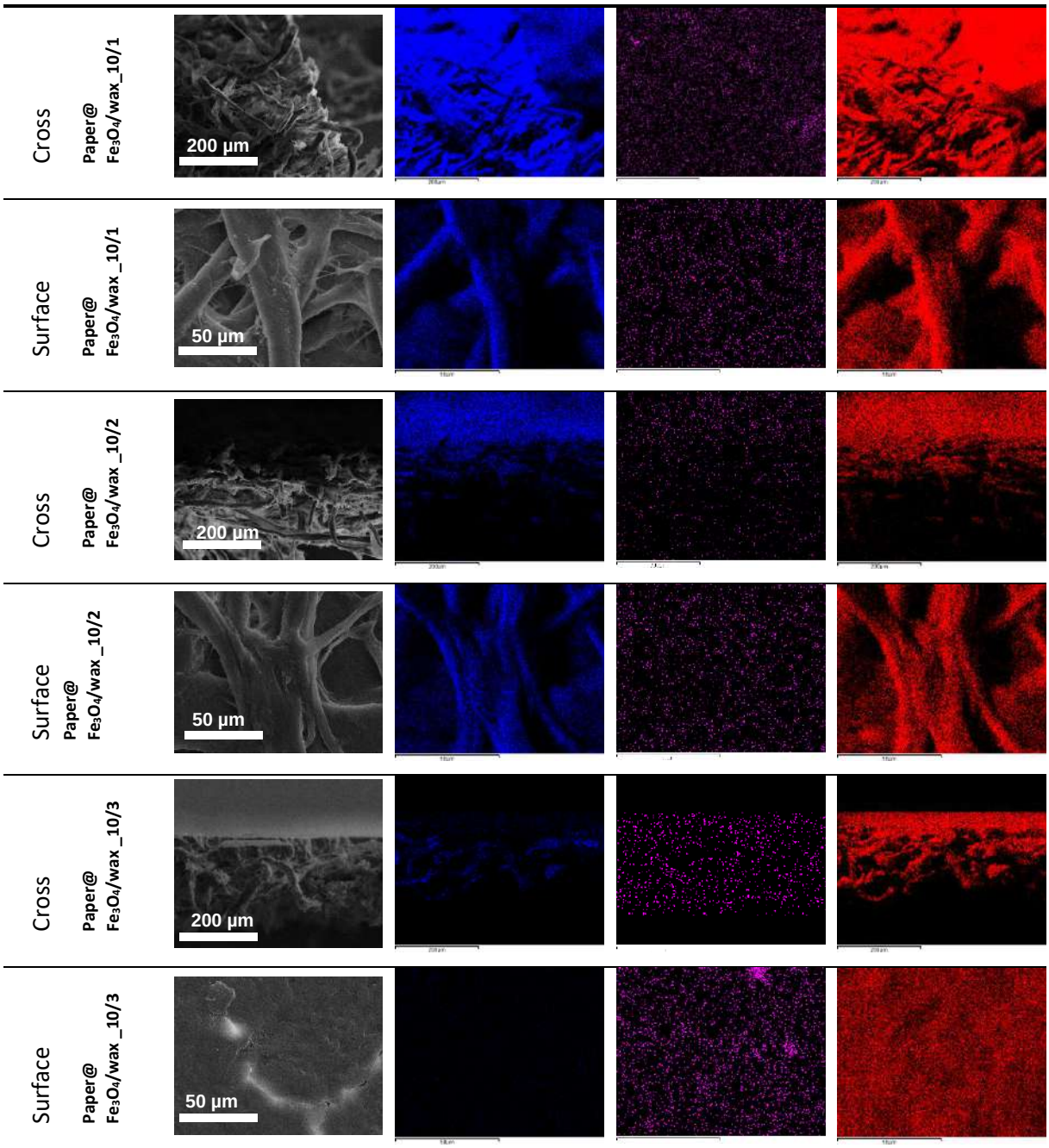

Figure 3.1.6. - Surface and cross-section SEM/EDX elemental mapping images of the magnetic paper samples. On the first column are placed the SEM images and in the other three columns are shown the different chemical elements (oxygen, iron and carbon). The lines correspond to the different paper samples.

The elemental mapping analysis confirmed that Fe_3O_4 nanoparticles are present in all magnetic paper samples. Additionally, Figure 3.1.6 makes it evident that the impregnation process similarly occurs in all samples. Particularly, the ones that reveal the Fe locations on the magnetic paper (indicating the sites where Fe_3O_4 nanoparticles can be found) show that such process ensures a uniform distribution, both in depth, length and width. Finally, no significant differences are detected on the Fe_3O_4 distribution (both

surface and cross-section) among samples with different widths of the printed material. The average wt.% of Fe in all Paper@Fe_3O_4/wax_10 samples obtained from EDX images was 4.79 ± 0.37.

To verify how the printing process and corresponding thermal treatment affects the mechanical properties of the paper, stress-strain measurements were performed in tensile mode (Figure 3.1.7).

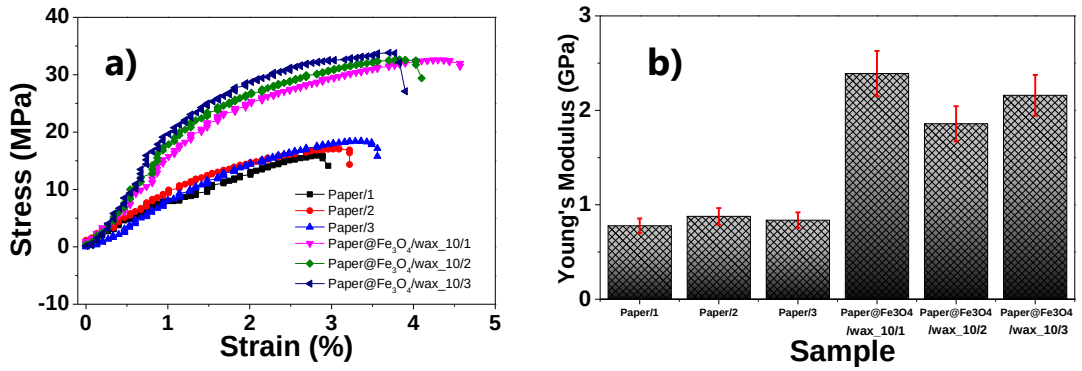

Figure 3.1.7. a) Characteristic room-temperature stress-strain curves on both paper and magnetic paper samples. b) Young's Modulus values obtained from Figure 3.1.7a.

From the linear regime of the curves, the Young's modulus was obtained by applying Hooke's law. The obtained values are presented in Figure 3.1.7b. In traditional paper it is usually observed just a small or even no plastic deformation, being detected a fracture near the end of the linear elastic region of the curve. Such typical response is observed in the three samples from commercial Whatman no. 1 paper with the three different widths (1, 2 and 3 mm), featuring almost no plastic regime (Paper/1, Paper/2 and Paper/3). The Paper@Fe_3O_4/wax_10 samples exhibit both higher stress and strain at the breaking strain giving a clear indication of the improvement of the mechanical properties of the paper. Such indication is reinforced with the duplication of the Young's modulus (from less than 1 GPa to ≈2 GPa) of the paper after the impregnation process. No differences are detected on samples (both in magnetic paper and traditional paper) with different widths (Paper/1, Paper/2, Paper/3 and Paper@Fe_3O_4/wax_10/1, Paper@Fe_3O_4/wax_10/2 and Paper@Fe_3O_4/wax_10/3).

With the aim of evaluating the effect of the width on the magnetic properties of the Paper@Fe_3O_4/wax_10 samples, VSM measurements and magnetic actuation studies were performed (Figure 3.1.8.a).

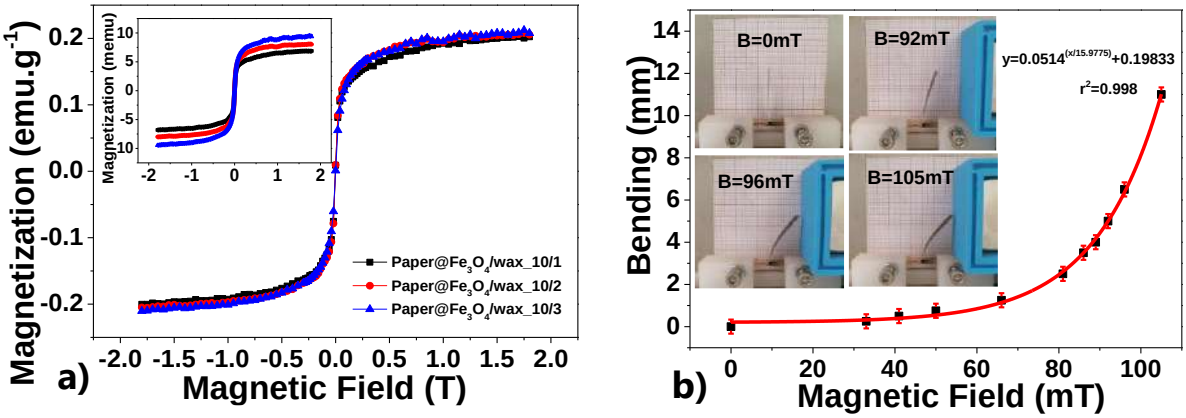

Figure 3.1.8. Room-temperature magnetization of the Paper@Fe_3O_4/wax_10 samples with three printed widths (1, 2, 3). The inset shows the neat magnetization for each sample. b) Magnetic actuation ability of the Paper@Fe_3O_4/wax_10/3 sample.

The magnetic saturation of the samples (inset of Figure 3.1.8a) increases with increasing width of Paper@Fe_3O_4/wax_10 samples due to the proportional increase of the number of magnetic nanoparticles. This fact shows that the net magnetic moment exhibited by the magnetic paper samples turns out to be directly the vector sum of the individual contributions of the Fe_3O_4 grains inside the wax/paper matrix. This is also a clear indication of the good dispersibility of magnetic nanoparticles in the material [42].When the magnetic saturation of each sample is divided by the respective weight (Figure 3.1.8.b), no differences are detected on their maximum magnetic saturation value once the Fe_3O_4 wt.% is the same in all samples. To validate the proposed magnetic paper as an actuator, the displacement (Δl) of the samples after magnetic actuation with a commercial magnet (KJ Magnetics, Pipersville, PA, USA) was monitored (Figure 3.1.9a).

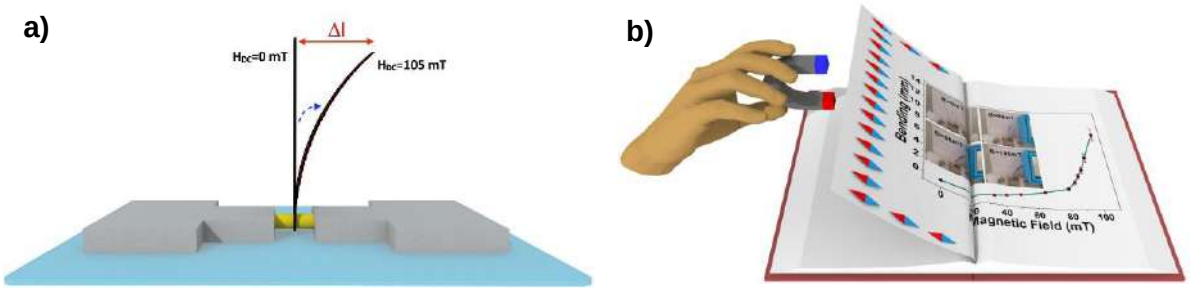

Figure 3.1.9. a) Scheme of the displacement calculation on the magnetic paper. b) An interactive/smart book, one of the potential applications of the developed materials.

The application of a magnetic field in the sample ranging from 0 mT (when the magnet was at 30 mm away from the magnetic paper) to 105 mT (when the magnet was at 1mm from the magnetic paper) leads to a magnetic force on the paper and, as a consequence, a bending movement. It was observed that the displacement increases exponentially with increasing magnetic field reaching a maximum value of ≈12 mm at 105 mT.

Due to the high correlation coefficient (R^2=0.998) between bending and magnetic field, such magnetoactive properties can be used to provide interactive/sensing capabilities and magnetic-responsiveness to traditional paper-based materials (Figure 3.1.9b). If it is intended to induce ferromagnetic properties in the paper matrix this approach can be used with related magnetic nanoparticles such as $CoFe_2O_4$. In a similar way, the proposed impregnation process can endow other properties to paper, namely conductivity (with the addition of conductive fillers: carbon nanotubes, graphene and silver), improved dielectric response, with the addition of dielectric materials ($BaTiO_3$, $CaCu_3Ti_4O_{12}$ or lead zirconate titanate) and photoluminescence (with the addition of photoluminescent particles). This type of paper-based magnetic composites can be also used on electromagnetic wave absorption [47-49].

3.1.4. Conclusions

Magnetic Paper@Fe_3O_4/wax materials have been obtained through a new wax-based nano-impregnation method.

The thermal energy storage capacity of the wax was not hindered with the addition of magnetic nanoparticles. Further, the mechanical properties of the resulting paper (stress at rupture, strain at rupture and Young's modulus: 15 MPa, 3.5 % and less than 1 GPa, respectively) have been improved (30 MPa, 4.5 % and 2 GPa, respectively) after such the impregnation process. The success of the impregnation process has been also proven by SEM/EDX, with a good distribution of the fillers along the thickness of the paper, and by the magnetoactive properties of the paper-based material: 0.2 emu.g^{-1} magnetic saturation and 12 mm bending actuation when submitted to an external magnetic field of 105 mT.

Such materials and optimized magnetic and mechanical features will enable applications in magnetic printing, sensing, actuation, magnetic health care materials, PADs and μPADs, security papers and interactive/smart books, among others.

3.1.5. References

1. Qin, L., et al., Confined Transformation of Organometal-Encapsulated MOFs into Spinel $CoFe_2O_4$/C Nanocubes for Low-Temperature Catalytic Oxidation. Advanced Functional Materials, 2020, 30: 1910257.

2. Zhang, J., et al., Hierarchical Interface Engineering for Advanced Nanocellulosic Hybrid Aerogels with High Compressibility and Multifunctionality. Advanced Functional Materials, 2021, 31: 2009349.

3. Liu, X., et al., Dual Physically Cross-Linked Hydrogels Incorporating Hydrophobic Interactions with Promising Repairability and Ultrahigh Elongation. Advanced Functional Materials, 2021, 31(3): 2008187.

4. Sriplai, N., et al., White magnetic paper based on a bacterial cellulose nanocomposite. Journal of Materials Chemistry C, 2018, 6(42): 11427-11435.

5. Peng, J., et al., Synthesis of interfacially active and magnetically responsive nanoparticles for multiphase separation applications. Advanced Functional Materials, 2012, 22(8): 1732-1740.

6. Shen, Y., et al., Engineering Oxygen-Irrelevant Radical Nanogenerator for Hypoxia-Independent Magnetothermodynamic Tumor Nanotherapy. Small Methods, 2021, 5: 2001087.

7. Liu, X., et al., Coupling of Silk Fibroin Nanofibrils Enzymatic Membrane with Ultra-Thin PtNPs/Graphene Film to Acquire Long and Stable On-Skin Sweat Glucose and Lactate Sensing. Small Methods, 2021, 5: 2000926.

8. Piñeres, O.H., et al., Magnetic paper from sugarcane bagasse fibers modified with cobalt ferrite nanoparticles. Cellulose, 2020, 27(7): 3903-3918.

9. Liang, J., et al., Electromechanical actuators based on graphene and graphene/Fe_3O_4 hybrid paper. Advanced Functional Materials, 2011, 21(19): 3778-3784.

10. Lim, G.H., et al., Mechanically Robust Magnetic Carbon Nanotube Papers Prepared with $CoFe_2O_4$ Nanoparticles for Electromagnetic Interference Shielding and Magnetomechanical Actuation. ACS Applied Materials and Interfaces, 2017, 9(46): 40628-40637.

11. Barud, H.S., et al., Biocellulose-based flexible magnetic paper. Journal of Applied Physics, 2015, 117(17): 17B734.

12. Lin, B., et al., Microfluidic-Based Exosome Analysis for Liquid Biopsy. Small Methods, 2021, 5: 2001131.

13. Hong, J.S., et al., Nickel-Doping Effect on Mn3O4 Nanoparticles for Electrochemical Water Oxidation under Neutral Condition. Small Methods, 2020, 4(3): 1900733.

14. Gao, D., et al., Preparation and characterization of a new white magnetic paper. Materials Letters, 2014, 137: 487-490.

15. Shen, J., et al., A review on use of fillers in cellulosic paper for functional applications. Industrial and Engineering Chemistry Research, 2011, 50(2): 661-666.

16. Eskilson, O., et al., Self-Assembly of Mechanoplasmonic Bacterial Cellulose–Metal Nanoparticle Composites. Advanced Functional Materials, 2020, 30(40): 2004766.

17. Wang, J., et al., Enhancement of proton conduction at low humidity by incorporating imidazole microcapsules into polymer electrolyte membranes. Advanced Functional Materials, 2012, 22(21): 4539-4546.

18. Calvo, S., et al., Thermal and magnetic behavior of Angustifolia Kunth bamboo fibers covered with Fe_3O_4 particles. Physica B: Condensed Matter, 2012, 407(16): 3267-3270.

19. Wu, W.B., et al., Preparation and properties of magnetic cellulose fiber composites. BioResources, 2011, 6(3): 3396-3409.

20. Papaparaskeva, G., et al., White magnetic paper with zero remanence based on electrospun cellulose microfibers doped with iron oxide nanoparticles. Nanomaterials, 2020, 10(3): 517.

21. Wang, Y., et al., Transparent, stimuli-responsive films from cellulose-based organogel nanoparticles. Advanced Functional Materials, 2015, 25(9): 1434-1441.

22. Nguyen, T.D., et al., Black Titania with Nanoscale Helicity. Advanced Functional Materials, 2019, 29(40): 1904639.

23. Testa-Anta, M., Rivas-Murias, B., and Salgueiriño, V., Spin Frustration Drives Exchange Bias Sign Crossover in $CoFe_2O_4$–Cr_2O_3 Nanocomposites. Advanced Functional Materials, 2019, 29(36): 1900030.

24. Brito-Pereira, R., et al., Reconfigurable 3D-printable magnets with improved maximum energy product. Journal of Materials Chemistry C, 2020, 8(3): 952-958.

25. Ghazanfari, M.R., et al., Perspective of Fe_3O_4 Nanoparticles Role in Biomedical Applications. Biochemistry Research International, 2016, 2016: 7840161.

26. Gawande, M.B., Branco, P.S., and Varma, R.S., Nano-magnetite (Fe_3O_4) as a support for recyclable catalysts in the development of sustainable methodologies. Chemical Society Reviews, 2013, 42(8): 3371-3393.

27. Nicolas-Boluda, A., et al., Self-Assemblies of Fe_3O_4 Nanocrystals: Toward Nanoscale Precision of Photothermal Effects in the Tumor Microenvironment. Advanced Functional Materials, 2020, 31: 2006824.

28. Chen, X., et al., Electrospinning Multilayered Scaffolds Loaded with Melatonin and Fe_3O_4 Magnetic Nanoparticles for Peripheral Nerve Regeneration. Advanced Functional Materials, 2020, 30(38): 2004537.

29. McCoey, J.M., et al., Quantum Magnetic Imaging of Iron Biomineralization in Teeth of the Chiton Acanthopleura hirtosa. Small Methods, 2020, 4(3): 1900754.

30. Rincón-Iglesias, M., et al., Water-based 2D printing of magnetically active cellulose derivative nanocomposites. Carbohydrate Polymers, 2020, 233: 115855.

31. Rincón-Iglesias., M., Lizundia, E., and Lanceros-Méndez, S., Water-Soluble Cellulose Derivatives as Suitable Matrices for Multifunctional Materials. Biomacromolecules, 2019, 20(7): 2786-2795.

32. Oliveira, J., et al., Polymer-based smart materials by printing technologies: Improving application and integration. Additive Manufacturing, 2018, 21: 269-283.

33. Zhao, T.H., et al., Printing of Responsive Photonic Cellulose Nanocrystal Microfilm Arrays. Advanced Functional Materials, 2019, 29(21): 1804531.

34. Siqueira, G., et al., Cellulose Nanocrystal Inks for 3D Printing of Textured Cellular Architectures. Advanced Functional Materials, 2017, 27(12): 1604619.

35. Yu, C., et al., Recent Advances in Design of Flexible Electrodes for Miniaturized Supercapacitors. Small Methods, 2020, 4(6): 1900824.

36. Dixon, C., J. Lamanna, and A.R. Wheeler, Printed Microfluidics. Advanced Functional Materials, 2017, 27(11): 1604824.

37. Krishnan, K.M., et al., Nanomagnetism and spin electronics: materials, microstructure and novel properties. Journal of Materials Science, 2006, 41(3): 793-815.

38. Martins, P., et al., Tailored Magnetic and Magnetoelectric Responses of Polymer-Based Composites. ACS Applied Materials and Interfaces, 2015, 7(27): 15017-15022.

39. Liu, X.D., et al., Hydrothermal synthesis of superparamagnetic Fe_3O_4 nanoparticles with ionic liquids as stabilizer. Materials Research Bulletin, 2015, 62: 217-221.

40. Houshiar., M., et al., Synthesis of cobalt ferrite $CoFe_2O_4$ nanoparticles using combustion, coprecipitation, and precipitation methods: A comparison study of size, structural, and magnetic properties. Journal of Magnetism and Magnetic Materials, 2014, 371: 43-48.

41. Martins, P., et al., Effect of filler dispersion and dispersion method on the piezoelectric and magnetoelectric response of $CoFe_2O_4$/P(VDF-TrFE) nanocomposites. Applied Surface Science, 2014, 313: 215-219.

42. Martins, P., et al., Dielectric and magnetic properties of ferrite/poly(vinylidene fluoride) nanocomposites. Materials Chemistry and Physics, 2012, 131(3): 698-705.

43. Gonçalves, R., et al., Development of magnetoelectric $CoFe_2O_4$ /poly(vinylidene fluoride) microspheres. RSC Advances, 2015, 5(45): 35852-35857.

44. Qi, H., et al., Paraffin/chitosan composite phase change materials fabricated by piercing-solidifying method for thermal energy storage. AIP Advances, 2020, 10(3): 035218.

45. Chen, K., et al., Preparation and characterization of form-stable paraffin/polyurethane composites as phase change materials for thermal energy storage. Energy Conversion and Management, 2014, 77: 13-21.

46. Xerox Corporation, O.G., https://www.xerox.com/download/ehs/msds/S-9511.en-us.pdf.

47. Lou, Z., et al., In-situ formation of low-dimensional, magnetic core-shell nanocrystal for electromagnetic dissipation. Composites Part B: Engineering, 2021, 214: 108744.

48. Lou, Z., et al., Phenolic foam-derived magnetic carbon foams (MCFs) with tunable electromagnetic wave absorption behavior. Chemical Engineering Journal, 2020, 391: 123571.

49. Lou, Z., et al., Fabrication of Magnetic Conjugation Clusters via Intermolecular Assembling for Ultrasensitive Surface Plasmon Resonance (SPR) Detection in a Wide Range of Concentrations. Analytical Chemistry, 2017, 89(24): 13472-13479.

3.2. Printed multifunctional magnetically activated energy harvester with sensing capabilities

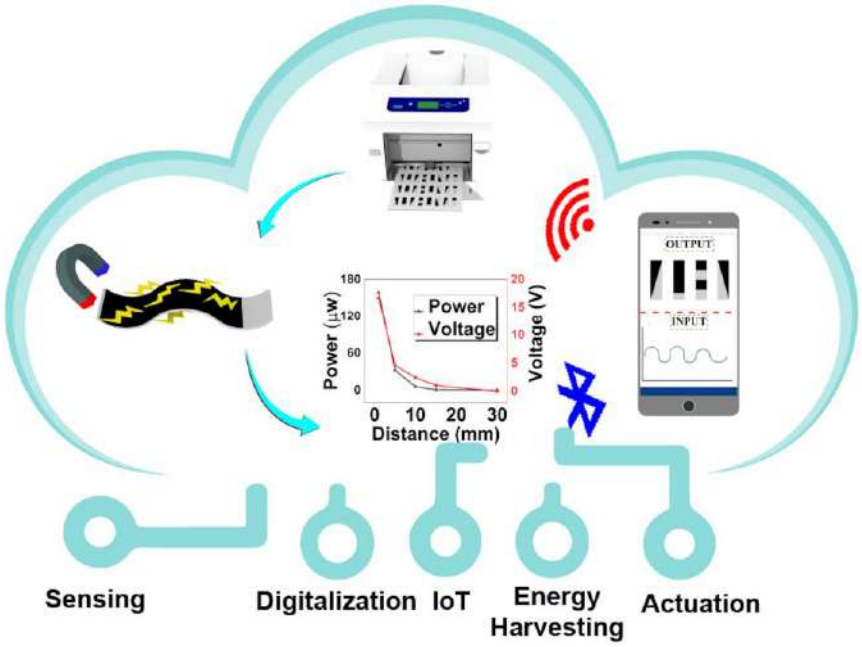

The exponential growth and ubiquitous use of mobile electronics supported by the Internet of Things (IoT) is leading to an increasing need of self-powered wearable electronic devices. In particular, converting electrical energy from magnetic fields is very appealing for the development of a sustainable power sources/sensing tools. Magneto-mechano-electric energy conversion is an effective way to convert magnetic fields into electricity for low power applications. The successful printing of such materials allows the design of customized structures, improved integration into devices and reduced materials waste. Here, a self-powered printed sensing device is presented, by exploiting piezoelectric/magnetic composites in response to magnetic stimuli via magneto-mechano-electric energy conversion.

This chapter is based on following publication: R. Brito-Pereira, C. Ribeiro, N. Pereira, S. Lanceros-Mendez and P Martins, Printed multifunctional magnetically energy harvester with sensing capabilities, Nano Energy 94, 106885 (2022).

3.2.1. Introduction

Fifteen years ago, the International Telecommunications Union (ITU) published its first report on the Internet of Things (IoT), introducing a new dimension on information and communication Technologies linked to the premises of connecting anyone, anything, anytime and anywhere [1-3].

IoT is defined as the information technology that interconnects objects and users [4], making possible the perception, recognition and management of both objects and processes. This will transform everyday tools into components of an "intelligent" network [4]. In this way, more aspects of our daily life will involve interactive processes [5], and as a result smart materials will be placed everywhere (on fabrics, machines, furniture, technological devices and everyday objects) to monitor in real-time a variety of physical quantities including temperature, position, deformations or magnetic fields, among others. Such connectivity introduced the need of producing smart materials through more adaptable techniques [2, 6, 7].

Additive manufacturing, and particularly printing technologies offer not only the possibility to fulfil such needs but also to integrate those smart materials faster, easier, and more cost-effective [8-10]. Additionally, printing technologies are more versatile and environmentally-friendly, also allowing the design of customized structures (micro-, nano-, asymmetric, flexible, or stretchable) that are essential for an effective IoT environment [11, 12].

With the increasing demand of portable smart electronic devices enhancers of the IoT connectivity, the smarter/more environmentally friendly production of those materials, as well as their energy supply are two of the major IoT-based problems/challenges [8, 11, 13]. Urgently needed is the substitution of the more traditional sources of energy for these devices (batteries) by alternatives that are cheaper, greener, and do not need to be periodically replaced [14-16], once wired power is impractical for most wearable applications, and batteries suffer from current leakage, limited energy capacity problems and security issues [15]. Moreover, the breaks of the batteries attributed to the extreme weather conditions may lead to a chemical leakage that is harmful to the environment [15, 17]. As a result of this situation, more efforts are being centered on the development of innovative sensing tools and energy harvesting solutions that can replace the conventional batteries/cables, leading to self-powered systems through harvesting energy from ambient sources such as human biomechanical energy, blue energy, solar energy, magnetic fields energy and wind energy [18, 19]. Among these energy sources, magnetic energy harvesting has been reported as one of the most effective ways to provide energy to applications in terms of power density and stability [9, 20]. Another advantage of this type of energy is that magnetic fields are ubiquitous in our living environment [21-23] and can be found around any wire carrying current such as wires connected to lights, heating/cooling appliances, refrigeration units, displays, and also in the vicinity of permanent magnets (hard disc drives, audio equipment, magnetic resonance imaging scanners, or electric motors). Moreover, magnetoactive materials are attracting uninterrupted increasing interest because of their fast response, distance-dependent sensing, cost-effective approach, and environmentally friendly procedures [24].

Magnetic field sensing is so important in the IoT context (related to position/proximity, velocity or electric current sensing), that advanced magnetoactive smart material are continuously being developed and optimized for magnetic sensing/harvesting applications [25]. However, traditional methods for capturing/sensing this magnetic energy, based on Faraday's law of induction, do not fully meet the most challenging/disruptive IoT-related demands, such as flexibility and printability [25, 26].

Piezoelectric energy harvesting from magnetically coupled vibrational sources can be an effective way not only to harvest magnetic energy [27] but also to promote magnetic sensing with self-power capabilities [28]. However, such self-power feature is difficult to achieve due to the rigid feature of magnets that traditionally are used on harvesting devices [29]. To solve this limitation, some studies have reported the utilization of magnetic fields to actuate piezoelectric devices at the macroscale in combination with magnetic components [30-32]. However, to the best of our knowledge, no report has yet presented a unique printed system, capable of both magnetic sensing and energy harvesting, and fully-demonstrated the magnetoelectrical energy conversion by utilizing the movement of the printed magnets coupled to a piezoelectric element.

Herein, a novel printed magnetic sensor/harvester based on a piezoelectric polymer and $CoFe_2O_4$ nanoparticles/wax composite is designed and fabricated by printing technologies. The proposed energy harvesting device exhibits mechano-magneto-electric energy conversion with an observed output power of ≈160 μW. When mechanical energy was added to the magnetic stimulus the output power increased to ≈350 μW. It was also demonstrated that the multifunctional module can serve as magnetic sensing element with an R^2 of 0.9991 and sensitivity of 30 $V.T^{-1}$.

3.2.2. Materials and methods

3.2.2.1. Printing of the poly(vinylidene-co-trifluorethylene) layer

P(VDF–TrFE) ink suitable for screen printing was developed by adding 4 g of the polymer powder (70/30 composition - Solvay West Deptford, NJ, USA) to the desired content of DMF (Fluka Milwaukee, WI, USA). The mixture was magnetically stirred for 2 hours at room temperature (≈25 °C) until complete dissolution of the polymer. The P(VDF–TrFE) ink was printed on a clean glass substrate (Figure 3.2.1i) by doctor blade technique [33, 34]. The polymer was then placed in an oven (JP Selecta, Model 2000208) at 210 °C for 10 minutes and allowed to cool down to room-temperature. The transversal poling of the P(VDF-TrFE) layer was achieved after an optimization procedure by 2 hours of corona poling at 120 °C in a home-made chamber and cooling down to room temperature under the applied electric field.

3.2.2.2. Printing of the silver electrodes

Novacentrix HPS-021LV – Silver ink was screen-printed on both sides of the previous ≈30 μm P(VDF–TrFE) film using a polyester mesh with 64 wires (Figure 3.2.1ii), leading to a ≈7 μm layer of silver with a resistivity of 15 $m\Omega.sq^{-1}.mil.^{-1}$. The resulting 3-layer laminate was placed in an oven at 80 °C for 1 hour and allowed to cool down to room-temperature.

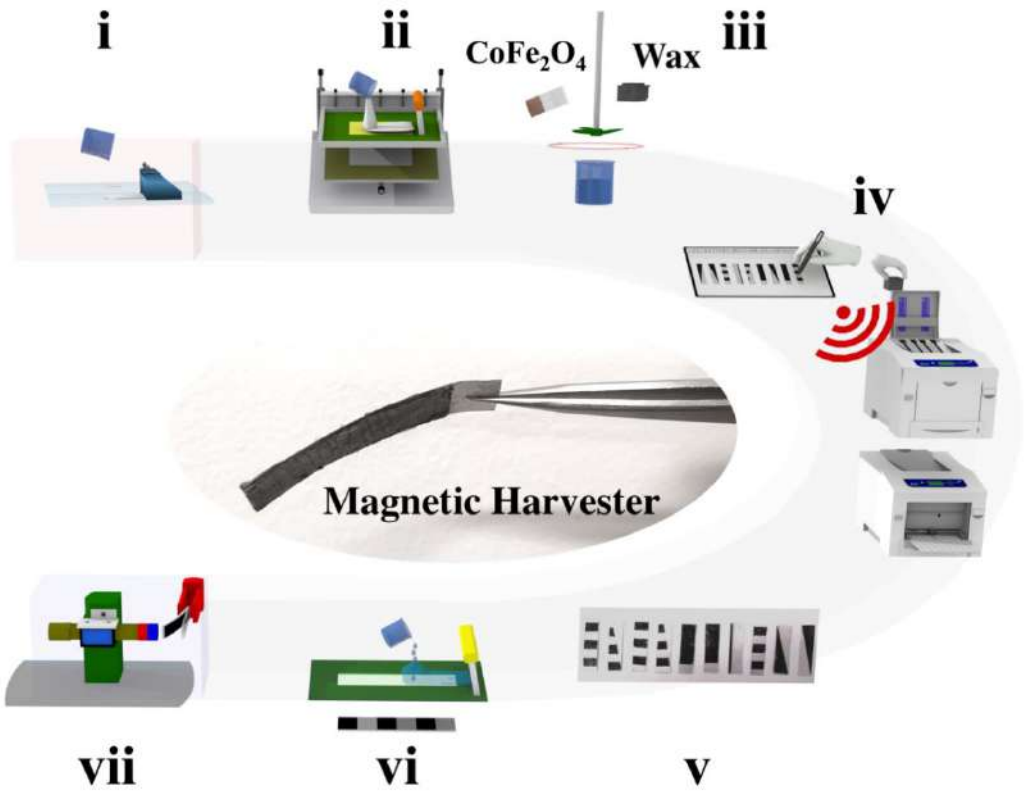

Figure 3.2.1. Printing procedure of the proposed sensing/harvesting platform.

3.2.2.3. Printing of the magnetoactive wax/$CoFe_2O_4$ layers

For the preparation of the wax/$CoFe_2O_4$ ink, $CoFe_2O_4$ nanoparticles (with 35-55 nm particle size range, Nanoamor, Texas, USA) were initially added (in 3 weight percentages – (40wt.%, 60 wt.% and 80 wt.%) to 5 mL pure ethanol (99 %, Sigma-Aldrich, Missouri, USA) – Figure 3.2.1iii, and the solution was dispersed in an ultrasound bath for 4 hours to ensure good dispersion and to prevent nanoparticle agglomeration (such volume of ethanol has been used since it is the minimum quantity of solvent that ensures a good dispersion of $CoFe_2O_4$ magnetic nanoparticles). Afterwards, the previously cut wax (5 g, Xerox Corporation, Connecticut, USA) was added to the solution and placed inside an oven (JP Selecta, Model 2000208) for 30 min at a temperature of 120 °C for polymer melting and complete removal of the ethanol. Then, the solution was removed from the oven, placed on a hot plate with a

temperature of ≈120 °C and mixed for 1 hour with the help of a mechanical Teflon stirrer to ensure complete dissolution of the polymer and homogeneity of the mixture, and finally placed in a mold. Thereafter, each concentration was poured into an aluminum mold designed and machined with the same dimensions of the Xerox cartridge (Xerox Colorqube 8870 wax printer). After the insertion of the liquid wax, it was allowed to cool at room temperature for 10 min to solidify. Then, the mold was disassembled, and the magnetic cartridge was placed into the Xerox Colorqube 8870 printer. Different printing designs were projected using the Sketchup 2017 (Trimble Inc - California, USA) - (Figure 3.2.1iv) and printed on the P(VDF-TrFE) + electrodes substrate. In some samples the magnetoactive layer was magnetized along the length direction for 60 minutes at 3 T direct current (DC) magnetic field.

3.2.2.4. Printing of the protective resin layer

To provide a protective layer to the printed magnetoactive layer (Figure 3.2.1v), an epoxy-resin (Nitofill, EPLV with Nitofill EPLV hardener from Fosroc Company, Dubai, UAE: Young's modulus = 1.6 GPa) layer was screen printed (DSTAR, model DX-305D) over the surface with a final thickness of ≈ 60 μm (Figure 3.2.1vi), being the resulting harvester ready for the functional characterization (Figure 3.2.1vii).

3.2.2.5. Physicochemical characterization

The morphology of the sample was evaluated by SEM with a NanoSEM - FEI Nova 200 (FEG/SEM) scanning electron microscope at 10 kV. Before SEM, samples were gold coated by magnetron sputtering using a Polaron SC502 sputter coater. The thickness of the layers was calculated from 5 images with 10 measurements by using an ImageJ software. In-plane Young's modulus were obtained from the initial slope of the stress-strain curves measured in 4mmx15mm specimens using a Shimadzu AG-IS universal test set-up, in tensile mode with a 2 $mm.min^{-1}$ deformation rate.

CA measurements of the different samples were performed using a Data Physics OCA20 instrument by the static sessile drop method. Ink drops (3 μL, 6 μL and 9 μL) were deposited on the surface of the P(VDF-TrFE)/silver substrates and the SCA20 software was used to evaluate the measurements. The mean contact angle and standard deviation were obtained through the measurement at six different places of each sample.

Magnetic hysteresis loops were accessed at room temperature using an ADE Technologies 3473-70 VSM from -2 T to 2 T. The piezoelectric response (d_{33}) of the poled samples was obtained with a wide range d_{33}-meter (model 8000, APC Int. Ltd).

3.2.2.6. Magnetic sensing/harvesting characterization

The sensing/harvesting characterization setup was composed by a permanent magnet (342-358 kJ.m^{-3} energy density, 8 mm of diameter and 3 mm thickness, neodymium, N45 from Supermagnete, Gottmadingen Germany) that activates the composite material by approaching/moving away from it (Figure 3.2.2a-b). This movement was triggered by an Keithley 2400 source with a frequency ranging from 0.1 Hz to 13.2 Hz. The composite film was connected to an oscilloscope (Rigol DS1074) with a load resistance in parallel. The load resistance was changed from 10 kΩ to 5 MΩ to acquire both the short-circuit current and the open-circuit voltage.

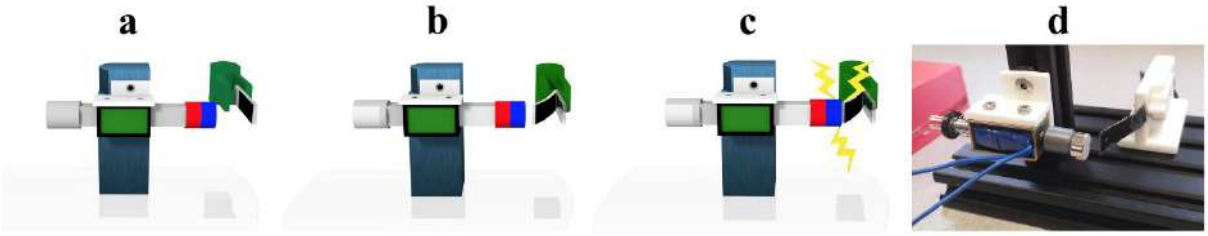

Figure 3.2.2. Working principle of the proposed sensing/harvesting platform.

The sensing/harvesting performance of the platform was evaluated in conditions where the magnet did not touch the piezoelectric/magnetic laminate (Figure 3.2.2b) staying 1 mm away (sample's maximum displacement of 9 mm), and in conditions where the magnet could touch the piezoelectric/magnetic laminate (Figure 3.2.2c) where the sample's maximum displacement is 12 mm, the impact force is 0.2 N (measured with a Vernier DFS-BTA dual-range Force sensor), the impact area 0.6 mm^{2} and the impact time 33 ms. Figure 3.2.2d shows a photograph of the experimental setup used to characterize the sensing/harvesting platform composed of a mechanical actuator, a permanent magnet and the printed magnetoactive composite.

3.2.2.7. Internet of Things connectivity

The interconnected harvester/sensor was developed by connecting the composite material to a charge amplifier (MCP6V01-E/SN, capacitors, and resistors Figure 3.2.3). Then the charge amplifier filtered and amplified the piezoelectric charge, and through a connection to an Analog to digital converter (ADC) sent the converted voltage to a microcontroller. After, the microcontroller (ESP32- WROOM-32U from Espressif) dispatched the received data from the ADC via Bluetooth to the smartphone application previously created. (Figure 3.2.3).

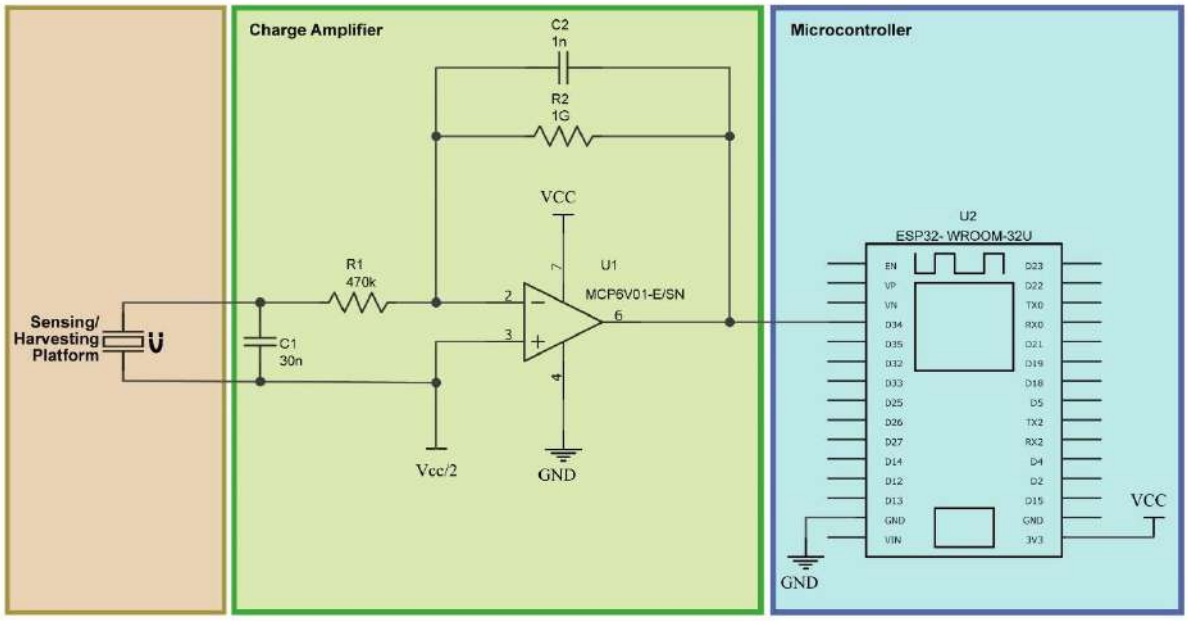

Figure 3.2.3. Schematic representation of the electronic circuit that ensures IoT connectivity.

3.2.3. Results and Discussion

3.2.3.1. Piezoelectric, magnetic, and mechanical evaluation

P(VDF-TrFE) was doctor blade-printed on a glass substrate with three distinct polymer/solvent weight ratios (10 wt.%/90 wt.%, 20 wt.%/80 wt.%, and 30 wt.%/70 wt.%) and corona poled to optimize the d_{33} piezoelectric response (Figure 3.2.4a).

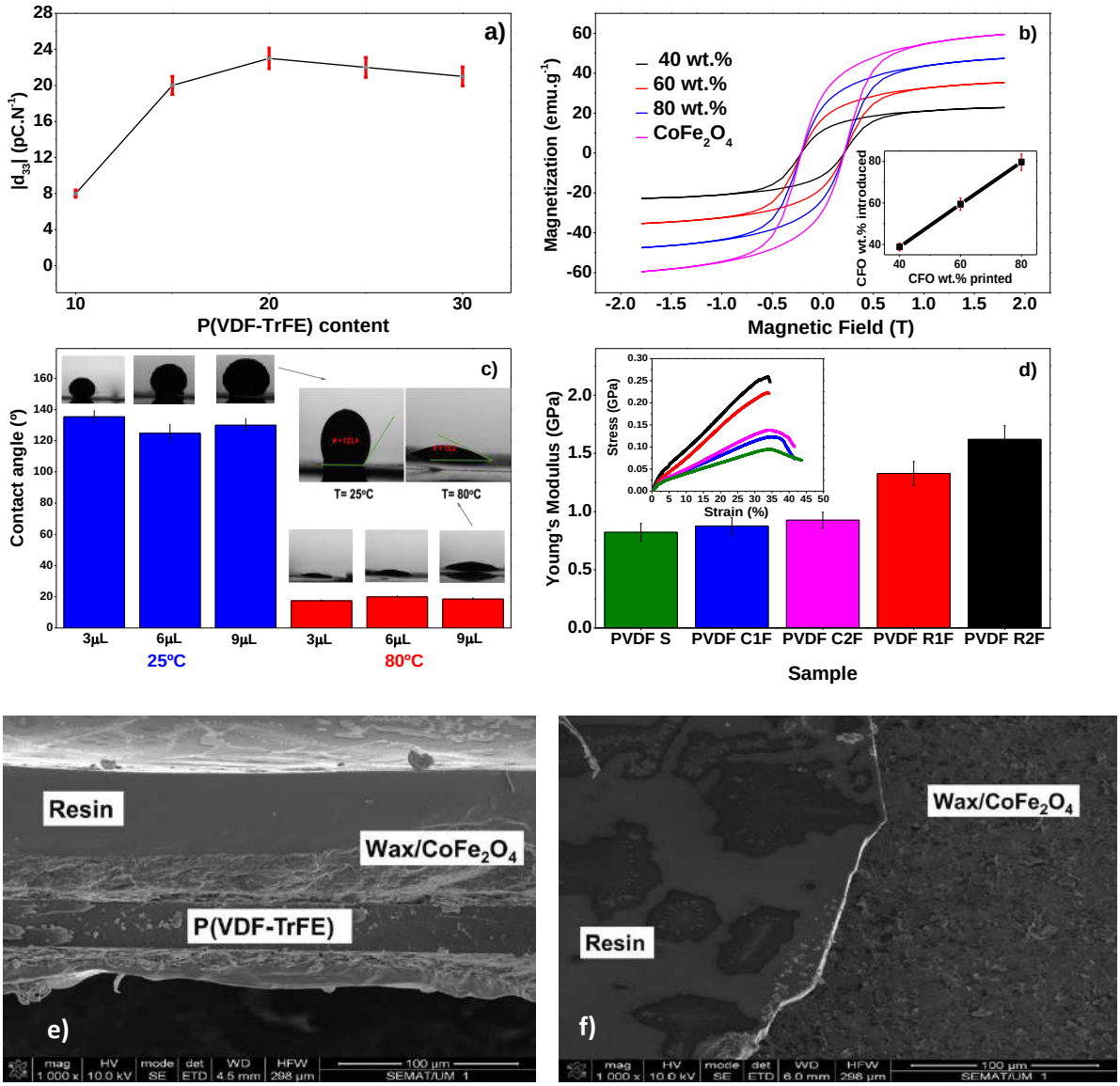

Figure 3.2.4. a) Relation between the $|d_{33}|$ piezoelectric coefficient and the P(VDF-TrFE) weight content in the printed polymer prepared with different P(VDF-TrFE)/ DMF ratios. b) Room-temperature magnetic hysteresis cycles for the printed wax-$CoFe_2O_4$ compositions with different $CoFe_2O_4$ wt.% content. The inset reveals the relation between the $CoFe_2O_4$ wt.% in solution and the CFO wt.% in the corresponding printed layers. c) Contact angle at room-temperature and at 80 °C of different wax- $CoFe_2O_4$ (80 wt.% of $CoFe_2O_4$) drops on printed P(VDF-TrFE) with silver electrodes. d) Young's Modulus of the different samples. The inset shows a representative stress-strain curve for each sample. Representative e)-cross section and f)-surface SEM images of the P(VDF-TrFE)/silver//Wax-CFO/Resin 3-layered composite.

Figure 3.2.4a shows that the sample prepared with 10 wt.% P(VDF-TrFE) content in solution is characterized by a much lower piezoelectric response (≈60 %) when compared to the other four concentrations. This may be due to the high concentration of DMF on the piezoelectric ink which can lead to a lower polymer density after printing. Once the ink composition with 20 wt.% of P(VDF-TrFE)) achieved the highest piezoelectric response ($|d_{33}|$≈23 $pC.N^{-1}$) it was selected to print the piezoelectric layer of the device.

The room-temperature magnetic response of the magnetoactive wax/$CoFe_2O_4$ layers has been studied as a function of the applied DC magnetic field and $CoFe_2O_4$ wt.%. The hysteresis loops presented in Figure 3.2.4b confirm the usual ferromagnetic behaviour with a coercivity of 2450 Oe and blocked magnetic moment in both $CoFe_2O_4$ nanopowder and wax/$CoFe_2O_4$ nanocomposites. Such ferromagnetic behaviour, that ensures a magnetization when the imposed magnetizing field is removed, will allow the magnetization of samples in directions that will increase their functional response, demonstrating also that the printing process did not affect the magnetic properties of $CoFe_2O_4$.

The magnetic saturation values increase with increasing $CoFe_2O_4$ wt.%, being the maximum value (47.4 emu.g^{-1}) obtained for the composite with the highest (80 wt.%) filler content. Such magnetic saturation (M_{SAT})values at 1.8 T were used to determine the effective $CoFe_2O_4$ wt.% on the printed samples by using Equation 3.2.1 and the method introduced in[35].

$$Effective\ CoFe_2O_4\ wt.\% = \frac{Printed\ Composite\ M_{SAT}}{CoFe_2O_4\ M_{SAT}} \quad (3.2.1)$$

Small differences, lower than 1 %, were observed between the printable and the printed wax/$CoFe_2O_4$ composites (inset of Figure 3.2.4b) meaning that the whole sample preparation and printing procedures did not cause the settling of nanoparticles.

Aiming to optimize the magnetic ink spreading on the P(VDF-TrFE)/Ag substrate, essential for a successful printing [36, 37], the printing procedure has been tested with the substrate at temperatures ranging from 25 °C to 80 °C, being found that a higher spreading (contact angle ≈ 19.2 °) was obtained at the highest processing temperature (Figure 3.2.4c), independently of the drop volume (3 µL, 6 µL or 9 µL). This is explained by the high surface energy of the substrate that led to a stronger wetting, promoting a better drop spreading and printing quality [36, 38]. In all the inset photographs (with a quadrangular shape) each square side size corresponds to 6 mm in real size of the drops. Smaller contact angles result in overspilling and overspreading of the ink, while larger contact angles could lead to the formation of mechanical instabilities and poor spreading [38].

The mechanical characteristics of representative prints (PVDF S: PVDF-Ag layer; PVDF C1F: PVDF-Ag layer with $CoFe_2O_4$-based magnetic layer printed in one side; PVDF C2F: PVDF-Ag layer with $CoFe_2O_4$-based magnetic layer printed in both sides; PVDF R1F: PVDF-Ag layer with $CoFe_2O_4$-based magnetic layer and the protective resin layer printed in the same side; PVDF R2F: PVDF-Ag layer with $CoFe_2O_4$-based magnetic layer and the protective resin layer printed in both sides) were obtained after room-temperature stress-strain measurements (inset of Figure 3.2.4d). The Young's modulus values of all samples, determined in the linear zone of elasticity (between 0 and 1 % of strain), evidenced the increase of the mechanical stiffness with the increasing number of printed layers: The Young's modulus of the PVDF S (≈0.8 GPa) increases to ≈0.9 GPa with the addition of 1-2 layers of magnetic layers (PVDF C1F and PVDF C2F) and to ≈1.4 GPa with the additional introduction of 1-2 resin layers (PVDF R1F and

PVDF R2F), being this last increase explained by the higher Young's Modulus value (≈1.5 GPa) of the thicker layer of the laminated composite: the epoxy resin. No substantial effect (difference less than 3 %) was found by the printing of the silver electrodes on the Young's modulus of the PVDF layer. SEM images (Figure 3.2.4 e-f) reveal that the different layers have ≈32 µm (P(VDF-TrFE)/Ag substrate), ≈30 µm (wax/$CoFe_2O_4$) and ≈60µm (epoxy-resin layer).

3.2.3.2. Device optimization

After the piezoelectric, magnetic, and mechanical evaluation, the voltage output of the sensor/harvester has been evaluated in terms of $CoFe_2O_4$ content on the magnetoactive layer (Figure 3.2.5a), thickness of the magnetoactive layer (Figure 3.2.5b), minimum distance to the magnet (Figure 3.2.5c), frequency of the magnetic stimulus (Figure 3.2.5d), cycling solicitation (Figure 3.2.5e) and design of the magnetic prints (Figure 3.2.5f).

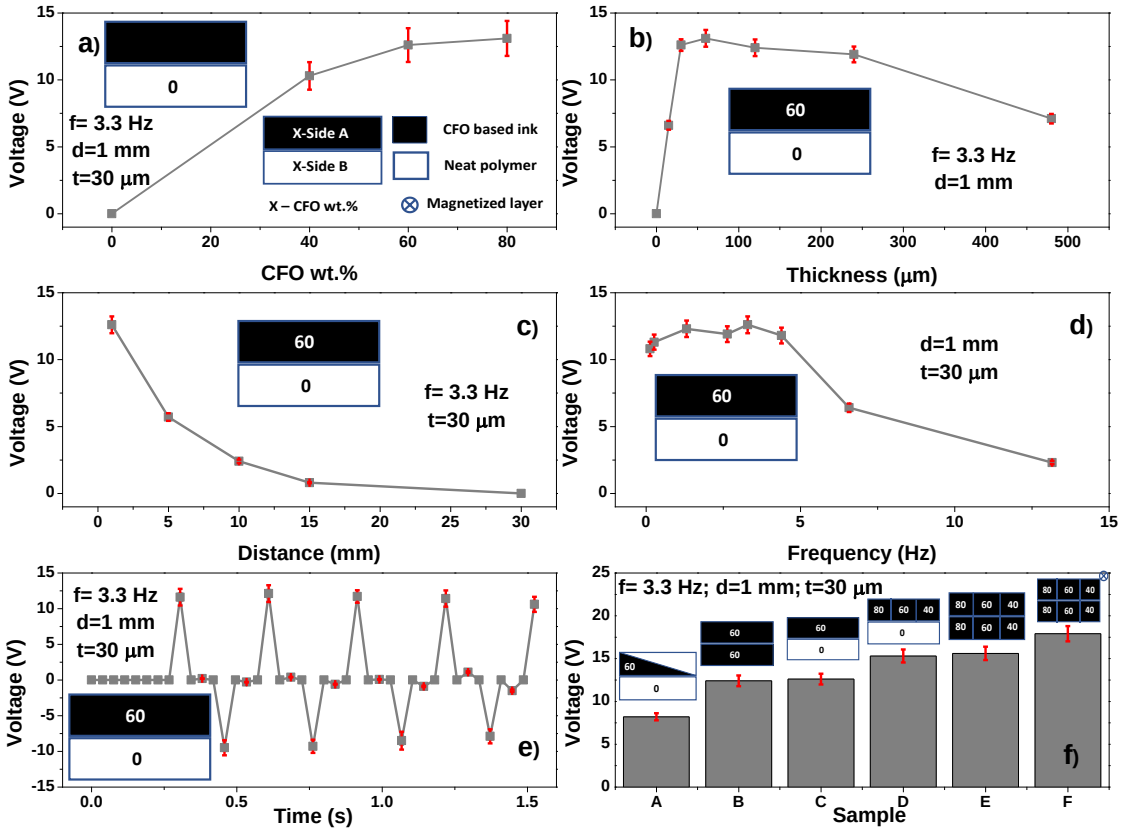

Figure 3.2.5. Output voltage of a PVDF R1F sample as a function of: a) CFO wt.%; b) magnetoactive layer thickness; c) minimum distance to the magnet; d) frequency of the magnetic stimulus; e) cycling solicitation; and f) magnetic prints design.

By increasing the $CoFe_2O_4$ wt.% from 40 to 80, the magnetic force that acted on the magnetic layer of the device increased leading to a larger mechanical stimulation on the piezoelectric layer and consequently to a higher

generated voltage (Figure 3.2.5a). On the studies summarized in Figure 3.2.5b-d PVDF R1F samples were used (60 wt.% of $CoFe_2O_4$ in the magnetoactive layer). A higher magnetic force is also the explanation for the detected increase of the output voltage (from 6.6 V to 12.6 V) with increasing thickness of the magnetoactive layer (from 15 μm to 30 μm) – Figure 3.2.5b. Although the magnetic force also increases with increasing thickness of the magnetoactive layer, from 30 μm to 480 μm, the greater mechanical stiffness resulting from the greater thickness leads the output voltage to remain almost constant, decreasing even for the thickest sample. Due to the existence of a higher magnetic field at 1 mm from the magnet (440 mT) and an almost negligible magnetic field (0.003 mT) at 30 mm of the sample, it is observed and exponential decrease of the output voltage from 12.6 V to 0 V with increasing distance (Figure 3.2.5c). Regarding the frequency evaluation no substantial differences on the output voltage are detected on the (0.1 Hz - 4.4 Hz) range. When the frequency is further increased up to 13.2 Hz the output voltage was found to decrease because of the smaller range of motion caused by the delay (Figure 3.2.5d). The higher the frequency, the greater is the delay. At very high frequencies (higher than 13.2 Hz) the sample will not be able to move, and the output power comes to naught. When the output voltage response is studied to f= 3.3 Hz as a function of time it is observed an almost sinusoidal behaviour being the maximums and minimums explained by the mechanical stimulus resulting from the movement induced by the magnetic attraction and by the movement back to the equilibrium position, respectively (Figure 3.2.5e). Finally, several geometries have been tested to optimize the output voltage of the sensor/harvester (Figure 3.2.5f). In a general way no significant differences are detected on samples with only one or both sides printed with the same type of magnetic ink. Although two layers of magnetic material led to a greater magnetic force induced in the device (when compared to the only one magnetic layer structure), the mechanical confinement is also greater. On the contrary, the existence of a $CoFe_2O_4$ wt.% gradient on the printed magnetic layers increases the output voltage in ≈30 % (from 12.1 V to 15.6 V) due to the existence of different intensities of mechanical stimuli along the piezoelectric layer. This gradient led to the appearance of an additional strain in the thickness direction, as a result of the different magnetic force induced along the laminate sample, leading to an increase in the output voltage value.

A significant increase is also observed (from sample E - 15.6 V to sample F - 17.9 V) when one magnetic layer of the device is previously magnetized against the direction of the magnetic field applied with the permanent magnet of the measurement setup. Such additional magnetizing process leads to the appearance of an additional mechanical stimulus resulting from the interaction between the piezoelectric layer and the magnetized magnetic layer: the piezoelectric layer tends to follow the movement promoted by the non-magnetized magnetic layer (that is attracted to the magnet), while the magnetized magnetic layer (that is repelled by the magnet), on the other side, suffers a force in the opposite direction.

3.2.3.3. Magnetic sensing and harvesting evaluation

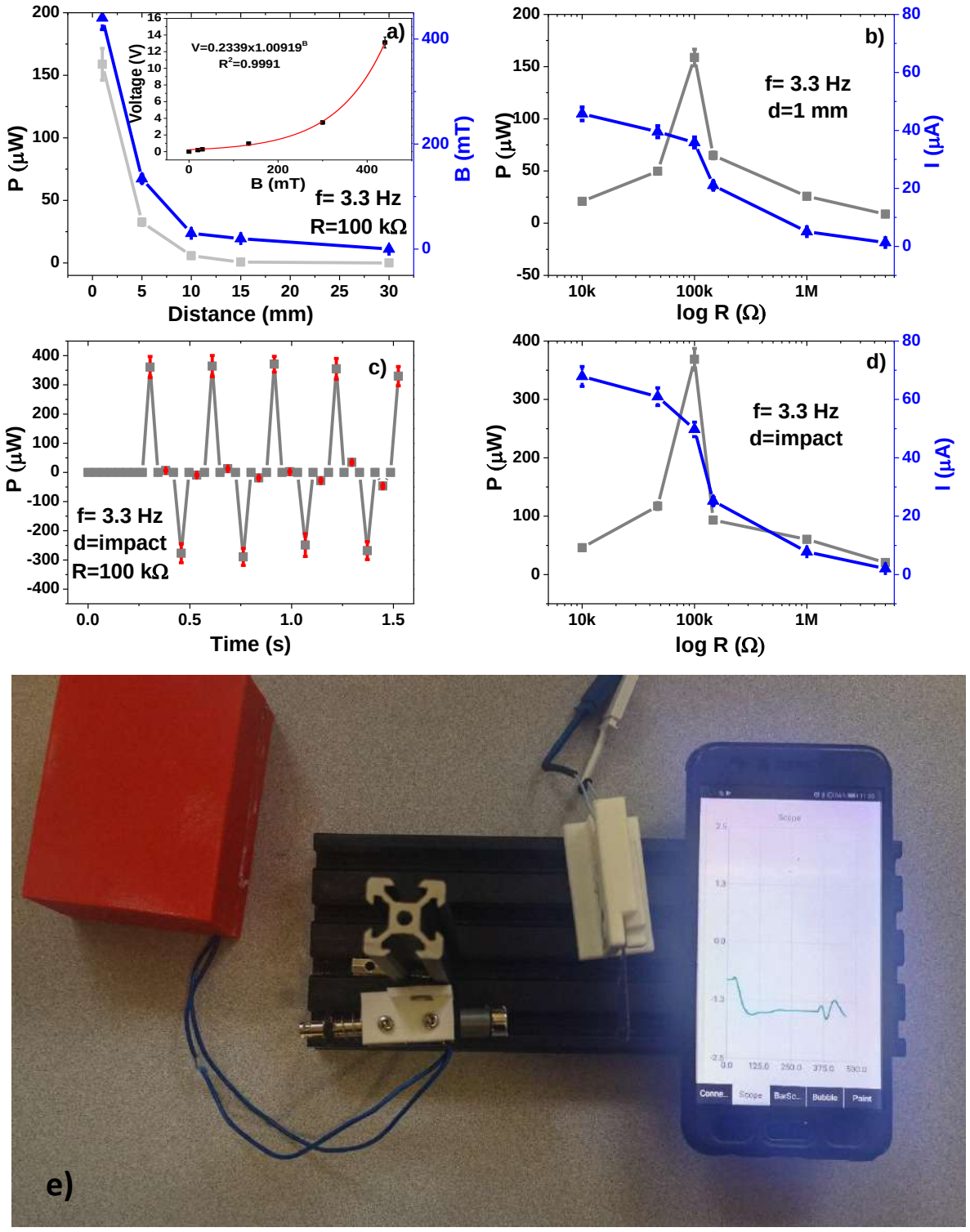

Figure 3.2.6. a) Harvested power (Po) and magnetic field (Bm) as a function of the distance to the magnet without the mechanical deformation resulting from the impact between the magnet and the printed composite. b) Relation between the measured power, load resistance (R) and current (I) without the mechanical impact between the magnet and the printed composite. c) Harvested power (Po) as a function of the cycling solicitation (f=3.3 Hz). d) Relation between the measured power, load resistance (Rl) and current (I) with mechanical impact between the magnet and the printed composite. e) Data sent (through Bluetooth) by the microcontroller and received by a smartphone.

Once magnetic fields decay with the distance from the source, the magnetic force that is induced in the device also decreases leading to a decrease on the harvested power (Figure 3.2.6a). At a distance from the magnet ≈3 mm the harvested energy is negligible. In order to prove the self-power sensing capability of this material, the inset of Figure 3.2.6a reveals a strong correlation coefficient (R^2=0.9991) between the generated voltage and the magnetic field value, opening up good possibilities for this material to be used as a magnetic sensor once it is superior than the ones recently reported on magnetic devices based in similar effects [39]. Figure 3.2.6b shows that the power across the load resistance increases with increasing electrical resistance until reaching a maximum of 7 mW at the load resistance of 100 kΩ. This maximum power emerges when the resistive value of the load resistance is equal to that of the laminate sample internal resistance. An additional increase in the load resistance leads to a decrease of the electric power. Additionally, the current flowing through the load decreases with increasing electrical resistance from 45 μA to 1 μA.

Aiming to take advantage of the synergistic effect between magnetic and mechanical stimulation, the harvesting device was approached for a d≈ 0 mm in a such way that the magnetic stimulation also caused the impact (Figure 3.2.2c) between the permanent magnet and the lateral surface of the sample (f=3.3 Hz). To avoid possible electric interactions between the magnet and the sample, the magnet has been previously coated with an isolator epoxy layer. In such conformation the output power (with a load resistance of 100 kΩ) was increased to 370 μW (Figure 3.2.6c). After hundreds of period rotations, the maximum output power decreases to ≈330 μW (which is about 90 % of original device), probably due to the deformation of the device structure or possible alterations on the surface morphology[40]. The electric current decreased from ≈67 μA to ≈2 μA with increasing load resistance from 10 kΩ to 5 MΩ. (Figure 3.2.6d).

The reported power outputs (both magnetic-based or combined: magnetic+mechanical) of the proposed energy harvester, higher than the previously reported in analogues systems (magneto-mechano-electric) and among the highest reported on other magnetic-based harvesting systems (Table 3.2.1), are suitable for self-powered devices such as actuators, antennas, magnetic sensors and biomedical implantable devices [29, 41-44], such as the one shown on Figure 3.2.6e. Additionally, and with power densities higher than the ones previously reported on other magneto-mechano-electric energy harvesters coupled to the high-linearity magnetic field sensing capability (R^2=0.9991), the proposed printed multifunctional magnetically activated energy harvester can be seen as a viable harvesting source for temperature and humidity sensors, Bluetooth gadgets and LED indicators, with high application potential in sustainable personal electronics and in the IoT/4.0 revolution scenarios [44].

Table 3.2.1. Power densities of energy harvesting technologies.

Type	Power density ($mW.cm^{-3}$)	Information source
Magnetic (nanocrystalline alloy core)	7.828	[45]
Magnetic (ferrite core)	1.978	

Magnetic (helical core)	0.002	[46]
Magneto-mechano-electric	Magnetic (0.0035) Combined (0.02)	[47]
	Combined (7.8)	[44]
	Magnetic (4.2) Combined (9.7)	This work
Compression/bending (piezoelectric)	287	[48]
Vibrations (piezoelectric)	0.1-0.2	[49]
Monocrystalline solar cells	15	[50]
Microbial fuel cell	300	[51]
Thermoelectric (10 % gradient)	0.04	[52]
Combined (vibration+magnetic+solar)	18.67	[53]

The interfacial/mechanical stability over time was guaranteed after the device being working in extreme conditions (uninterruptedly for 24 hours and retested after a week) with no significant change in the output power (less than 5 %).

3.2.4. Conclusions

A self-powered magneto-mechano-electric printed device has been fabricated, which not only provides excellent harvesting capability, but also suitable self-powered magnetic sensing performance. The printed device can harvest magnetic energy with maximum output power densities of 4 and 10 $mW.cm^{-3}$, on magnetic and magnetic+mechanical solicitation conditions, respectively. Additionally, the device reveals a sensing performance characterized by R^2 of 0.9991 and a sensitivity of 30 $V.T^{-1}$. The presented sensing/harvesting principle, as well as the simple and cost-effective fabrication technology, will allow advances in self-powered wearable sensors and devices compatible with IoT-related systems.

3.2.5. References

1. ITU Internet Reports 2005: The Internet of Things ITU Publications, 2015.

2. Sanislav, T., et al., Energy Harvesting Techniques for Internet of Things (IoT). IEEE Access, 2021, 39530-3954.

3. Liu, D., et al., Wind-driven self-powered wireless environmental sensors for Internet of Things at long distance. Nano Energy, 2020, 73: 104819.

4. Wen, F., et al., Advances in chemical sensing technology for enabling the next-generation self-sustainable integrated wearable system in the IoT era. Nano Energy, 2020, 78: 105155.

5. Zhao, Z., et al., Flexible nanogenerators for wearable electronic applications based on piezoelectric materials. Materials Today Energy, 2021, 20: 100690.

6. Duan, S., et al., Screen Printing of Flexible Electronic Devices. Progress in Chemistry, 2018, 30(4): 429-438.

7. Yuan, F., et al., Smart touchless triboelectric nanogenerator towards safeguard and 3D morphological awareness. Nano Energy, 2021, 86: 106071.

8. Borghetti, M., et al., Future sensors for smart objects by printing technologies in Industry 4.0 scenario. Energies, 2020, 13(22): 5916.

9. Maharjan, P., Toyabur, R.M., and Park, J.Y., A human locomotion inspired hybrid nanogenerator for wrist-wearable electronic device and sensor applications. Nano Energy, 2018, 46: 383-395.

10. Chen, Y., et al., 3D printed stretchable smart fibers and textiles for self-powered e-skin. Nano Energy, 2021, 84: 105866.

11. Zhang, Y.Z., et al., Printed supercapacitors: Materials, printing and applications. Chemical Society Reviews, 2019, 48(12): 3229-3264.

12. Bissannagari, M., et al., All inkjet-printed flexible wireless power transfer module: PI/Ag hybrid spiral coil built into 3D NiZn-ferrite trench structure with a resonance capacitor. Nano Energy, 2019, 62: 645-652.

13. Brito-Pereira, R., et al., Reconfigurable 3D-printable magnets with improved maximum energy product. Journal of Materials Chemistry C, 2020, 8(3): 952-958.

14. Hussein, H.M.E., et al., A chip-less and battery-less subharmonic tag for wireless sensing with parametrically enhanced sensitivity and dynamic range. Scientific Reports, 2021, 11(1): 3782.

15. Li, P., Long, Z., and Yang, Z., RF Energy Harvesting for Batteryless and Maintenance-Free Condition Monitoring of Railway Tracks. IEEE Internet of Things Journal, 2021, 8(5): 3512-3523.

16. Liang, X., et al., Spherical triboelectric nanogenerator based on spring-assisted swing structure for effective water wave energy harvesting. Nano Energy, 2021, 83: 105836.

17. Narita, F., Fox, M., A Review on Piezoelectric, Magnetostrictive, and Magnetoelectric Materials and Device Technologies for Energy Harvesting Applications. Advanced Engineering Materials, 2018, 20(5): 1700743.

18. Maharjan, P., et al., A Fully Functional Universal Self-Chargeable Power Module for Portable/Wearable Electronics and Self-Powered IoT Applications. Advanced Energy Materials, 2020, 10(48): 2002782.

19. Lee, D., Kim., Kim, D, Hybrid tribo-thermoelectric generator for effectively harvesting thermal energy activated by the shape memory alloy. Nano Energy, 2021, 82: 105696.

20. He, P., et al., Screen-Printing of a Highly Conductive Graphene Ink for Flexible Printed Electronics. ACS Applied Materials and Interfaces, 2019, 11(35): 32225-32234.

21. Jain, A., Bhatia, D., Spiral Spring Shaped Cantilever Magnetic Energy Harvesters for IOT. in Proceedings of the International Conference on Inventive Research in Computing Applications, ICIRCA 2018. 2018.

22. He, W., et al., Magneto-Electric Hybrid Generator for Simultaneously Harvesting Vibration and Stray Magnetic Field Energy. IEEE Magnetics Letters, 2019. 10.

23. Islam, E., et al., Electromagnetic-triboelectric-hybrid energy tile for biomechanical green energy harvesting. Nano Energy, 2020, 77: 2105004.

24. Zhou, Q., et al., Tilted magnetic micropillars enabled dual-mode sensor for tactile/touchless perceptions. Nano Energy, 2020, 78: 105382.

25. Xu, Y., et al., Ultrathin All-in-One Spin Hall Magnetic Sensor with Built-In AC Excitation Enabled by Spin Current. Advanced Materials Technologies, 2018, 3(8): 1800073.

26. Kang, M.G., et al., High Power Magnetic Field Energy Harvesting through Amplified Magneto-Mechanical Vibration. Advanced Energy Materials, 2018, 8(16): 1703313.

27. Deepak, P., George, B., Piezoelectric Energy Harvesting from a Magnetically Coupled Vibrational Source. IEEE Sensors Journal, 2021, 21(3): 3831-3838.

28. Reis, S., et al., Electronic optimization for an energy harvesting system based on magnetoelectric Metglas/poly(vinylidene fluoride)/Metglas composites. Smart Materials and Structures, 2016, 25(8): 085028.

29. Qi, H., et al., Paraffin/chitosan composite phase change materials fabricated by piercing-solidifying method for thermal energy storage. AIP Advances, 2020, 10(3): 035218.

30. Cui, N., et al., Magnetic force driven nanogenerators as a noncontact energy harvester and sensor. Nano Letters, 2012, 12(7): 3701-3705.

31. Wu, W.-H., et al., Non-contact magnetic cantilever-type piezoelectric energy harvester for rotational mechanism. Microelectronic Engineering, 2018, 191: 16-19.

32. Kim, S., et al., Utilization of a magnetic field-driven microscopic motion for piezoelectric energy harvesting. Nanoscale, 2019, 11(43): 20527-20533.

33. Yamada, N., Shiratori, A., Murasawa, G., A poly(vinylidene fluoride) film printing system using solution droplet casting. Smart Materials and Structures, 2019, 28(4): 044003.

34. Ribeiro, C., et al., Electroactive poly(vinylidene fluoride)-based structures for advanced applications. Nature Protocols, 2018, 13(4): 681-704.

35. Gonçalves, R., et al., Development of magnetoelectric $CoFe_2O_4$/poly(vinylidene fluoride) microspheres. RSC Advances, 2015, 5(45): 35852-35857.

36. Krainer, S., Smit, C., Hirn, U., The effect of viscosity and surface tension on inkjet printed picoliter dots. RSC Advances, 2019, 9(54): 31708-31719.

37. He, B., et al., The roles of wettability and surface tension in droplet formation during inkjet printing. Scientific Reports, 2017, 7(1): 11841.

38. Matavž, A., Bobnar, V., Malič, B., Tailoring Ink-Substrate Interactions via Thin Polymeric Layers for High-Resolution Printing. Langmuir, 2017, 33(43): 11893-11900.

39. Castro, N., et al., Development of a contactless DC current sensor with high linearity and sensitivity based on the magnetoelectric effect. Smart Materials and Structures, 2018, 27(6): 065012.

40. Huang, L.-B., et al., 4D-printed self-recovered triboelectric nanogenerator for energy harvesting and self-powered sensor. Nano Energy, 2021, 84: 105873.

41. Wu, H., et al., A multiferroic module for biomechanical energy harvesting. Nano Energy, 2021, 83: 105777.

42. Wu, Z., et al., A ball-in-ball type self-powered magnetoelectric inertial sensor for 3D multi-angle motion monitoring of humanoid robots. Nano Energy, 2021, 85: 106016.

43. Singh, J., Kaur, R., Singh, D., Energy harvesting in wireless sensor networks: A taxonomic survey. International Journal of Energy Research, 2021, 45(1): 118-140.

44. Kumar, A., et al., Effect of aspect ratio of piezoelectric constituents on the energy harvesting performance of magneto-mechano-electric generators. Energy, 2022, 239: 122078.

45. Dos Santos, M.P., et al. Energy harvesting using magnetic induction considering different core materials. in Conference Record - IEEE Instrumentation and Measurement Technology Conference. 2014.

46. Yuan, S., et al., A high-efficiency helical core for magnetic field energy harvesting. IEEE Transactions on Power Electronics, 2017, 32(7): 5365-5376.

47. Chu, Z., et al., Dual-stimulus magnetoelectric energy harvesting. MRS Bulletin, 2018, 43(3): 199-205.

48. Stassi, S., et al., Flexible piezoelectric energy nanogenerator based on ZnO nanotubes hosted in a polycarbonate membrane. Nano Energy, 2015, 13: 474-481.

49. Hande, A., Bridgelall, R., and Zoghi, B., Vibration energy harvesting for disaster asset monitoring using active RFID Tags. Proceedings of the IEEE, 2010, 98(9): 1620-1628.

50. Hande, A., et al., Indoor solar energy harvesting for sensor network router nodes. Microprocessors and Microsystems, 2007, 31(6): 420-432.

51. Ringeisen, B.R., et al., High power density from a miniature microbial fuel cell using Shewanella oneidensis DSP10. Environmental Science and Technology, 2006, 40(8): 2629-2634.

52. Raghunathan, V., et al. Design considerations for solar energy harvesting wireless embedded systems. in 2005 4th International Symposium on Information Processing in Sensor Networks, IPSN 2005. 2005.

53. Sriramdas, R., et al., Universal Multienergy Harvester Architecture. ACS Applied Materials and Interfaces, 2021, 13(1): 324-331.

3.3. High-dielectric mouldable and printable wax reinforced with ceramic nanofillers and its suitability for capacitive sensing

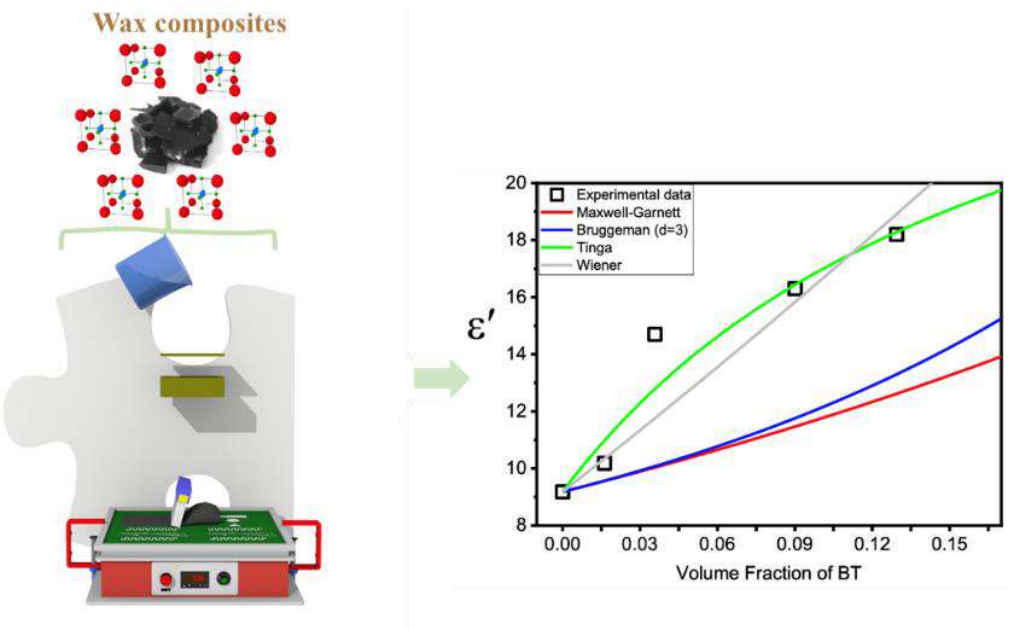

Functional polymer composites are being increasingly developed to improve performance and integration into devices. Wax, as a material suitable for paper-based microfluidics, can be combined with ceramic materials to adapt its dielectric constant, an essential property for many applications, such as printed electronics. Wax reinforced with high-dielectric ceramic nanofillers such as barium titanate (BT) has been developed with varying filler content up to 50 wt.% and processed by moulding and screen-printing techniques, without the use of solvents.

This chapter is based on following publication: R. Brito-Pereira, T.Rodrigues-Marinho, C.R Tubio, P.Costa, S. Lanceros-Mendez, High-dielectric mouldable and printable wax reinforced with ceramic nanofillers and its suitability for capacitive sensing, Flexible and Printed Electronics 6 (3), 035005, (2021)

3.3.1. Introduction

Ceramic nanofillers reinforced polymer composites to improve dielectric properties is an area of increasing interest [1,2] due to the wide area of applications in electronic equipment's and telecommunications [3], high-density capacitors [3], the electromagnetic wave absorbing materials [4], microwave antenna [5, 6], biomedical applications [6], and sensors [7,8], among others. The development of advanced high-performance materials for electronic applications is essential for the full implementation of the IoT 4.0 paradigms [9], in particular, when the materials are compatible with additive manufacturing technologies [9,10].

For the proper development of applications-oriented materials, the fillers must be carefully selected to improve the dielectric properties of the composite, without degradation of other relevant properties, such as mechanical or thermal ones. High-dielectric composites have achieved using two main types of fillers: conductive and dielectric [3]. Conductive fillers (such as nanocarbonaceous [3]) lead to composites with a large dielectric constant but their electronic properties change abruptly near the percolation threshold [3]. Concerning dielectric fillers, the most used ones are high-dielectric ceramics, such as barium or strontium titanate due to their intrinsic properties that allow fine tailoring of the dielectric response of the composites [3,11,12]. Thus, the concentration, size and shape of the fillers are parameters that affect the overall properties of the composites and the dielectric response. BT has a high-dielectric constant with low losses and can be chemically or structurally tailored for improving the performance of the composites [11].

High-dielectric composites have been studied with different polymeric matrices, including resins, thermoplastics or elastomers [3,13]. The selection of the polymeric matrix depends on the application and processability requirements [3]. Often, polymers with an intrinsic large dielectric response, such as PVDF or its copolymer, are among the most used matrix [3, 14] based on their dielectric constant ranging from 6 to 18 [15]. Stretchable elastomers with a dielectric constant between 8 and 12 have been also used, such as polyurethane and fluoroelastomer materials [16], as well as polyimide matrices for high-temperature applications, despite the lower dielectric constant (about 3.5) [17]. Nowadays, novel host matrices are being developed and implemented with functional properties, solvent-free processing and/or compatible with circular economy requirements [18-20].

Synthetic wax is a petroleum-based material being paraffin the most common in applications such as candles, paper coatings and crayons [10, 18], being microcrystalline waxes also used for applications [18]. Paraffin wax has been gained attention due to its hydrophobicity for food packing applications in

various fields such as anti-adhesion of liquid foods, fruit preservation and anti-bioadhesion [21]. Furthermore, paraffin is an insulator with nontoxic and noncorrosive properties [11]. Functional materials based on paraffin composites include energy storage materials, thermoelectric devices and microfluidic devices [20], one of the main advantages being the thermal properties with a low melting temperature that favours simple processability without the need of using solvents [20].

The low melting temperature of the wax allows expanding the applicability of the materials by the use of additive manufacturing technologies, such as by printing techniques, mainly by spray [22] or screen-printing technique [23]. Microfluidic devices applied in the biomedical area (e.g. detection of biomarkers) which use a filament thread have a large potential for the development of low-cost devices [23]. Further, printable PADs substrates allows liquid flow within the devices without external stimulus, a principle increasingly being used in a variety of microfluidic devices [23].

The multifunctionality of wax-based materials makes these composites suitable for microwave absorption applications, where dielectric and electromagnetic properties play a relevant role [24-26]. Thus, dielectric composites using wax have been developed in order to tune the electrical response. Literature reports, that paraffin can be reinforced BT, carbon microsphere, graphene or nanotubes, where the dielectric properties increases from about 2 for pristine paraffin wax [25] to near to $\varepsilon' \approx 6.5$ reinforced with carbon microspheres [27], $\varepsilon' \approx 17$ with graphene [25], $\varepsilon' \approx 18$ with carbon nanotubes [28] and $\varepsilon' \approx 18$ with BT coated $BaFe_{12}O_{19}$ [29] or $\varepsilon' \approx 35$ with BT coated by PANI [30]. All these composites have large filler contents up to above 50 %.

The material's dielectric constant is one of the most relevant properties to determine the applicability of the composite and to better understand the nature of the interactions between the fillers and the matrix, several theoretical models have been developed [31] considering, in a different way, the most relevant interactions determining the dielectric response, including matrix-filler and filler-filler interactions [31, 32].

In this work, paraffin wax reinforced with BT was developed for moulding and screen-printing processing methods. Theoretical and experimental data support the suitability of the wax composites for mouldable and printable dielectric applications.

3.3.2. Materials and Methods

3.3.2.1. Materials

Commercial black dye wax (W) cartridges were purchased from Xerox Corporation (Connecticut, USA). The solid ink wax composition is about 60 % of paraffin wax, 20 % of polyethylene resin, and about 10 % of black dye. Barium titanate (BT) nanopowder with an average diameter of 100 nm, with a purity of 99.9 % and a density of 6.08 $g.cm^{-3}$ (at 25 °C), was provided by Sigma-Aldrich (Munich, Germany). Pure ethanol (99 %) was also purchased from Sigma-Aldrich (Munich, Germany). All materials were used as received from the providers.

3.3.2.2. Preparation of the wax and composites

To prepare barium titanate/wax (BT/W) composites, the filler was first added in the precise filler contents (0, 10, 20, 40, 50 wt.%) to 5 mL of pure ethanol (Figure 3.3.1a-i). An ultrasound bath (ATU, model ATM40-3LCD) (ii) was used to disperse the filler/ethanol solution during 3 h to ensure good dispersion and to prevent filler agglomeration.

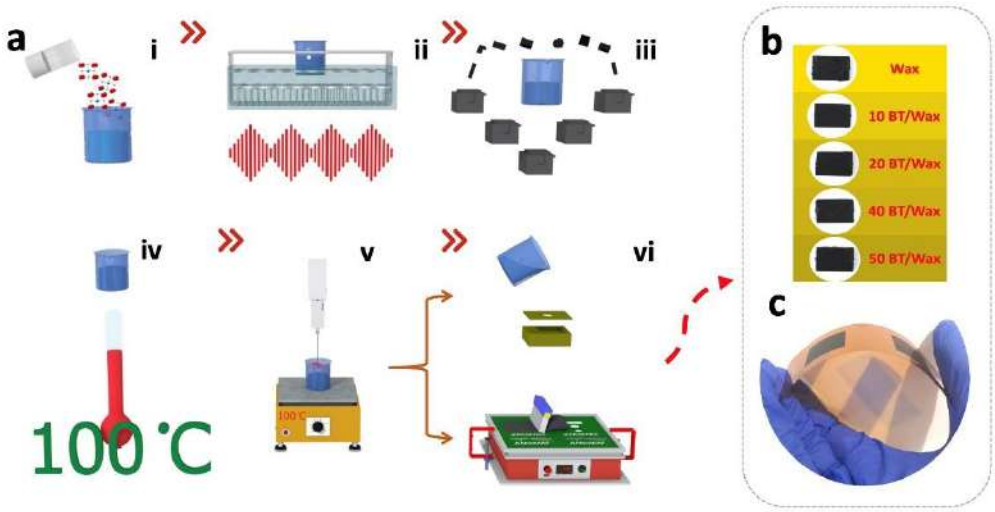

Figure 3.3.1. Experimental procedure for the preparation of the wax and wax composites for the different barium titanate contents a). Moulded b) and screen-printed c) samples illustrating the materials processability.

Subsequently, a previously weighed wax block (1.5 g) was added (iii) to the filler/ethanol solution and placed inside an oven (JP Selecta, Model 2000208) for 30 min (iv) at a temperature of 100 °C for wax melting embedding the fillers and, at the same time, for the complete removal of the ethanol.

The filler/wax solution was removed from the oven and placed in a hot plate at the same temperature (100 °C) and mixed for 1 h at 100 rpm with the help of a mechanical Teflon stirrer (v) to ensure the homogeneity of the melt for the different composites. The nomenclature of the samples along the paper will be the following: filler content/matrix as, for example, 10 BT/W or 50 BT/W.

The different wax and composite solutions were then processed using two processing techniques (vi): moulding and screen-printing.

Moulding was carried out in shaped 3D format (15 mm × 10 mm × 2 mm) acrylonitrile-butadiene-styrene (ABS) moulds previously printed with a 3D printer (Prusa MK3). Screen-printing was carried out at 100 °C on Kapton film substrates fixed in a hot plate (Prazitherm P272), also at 100 °C during the printing process.

For the screen-printing process, the screen (200 mesh of nylon on an aluminum frame) was placed at 1 mm distance from a hot plate surface and the previously melted wax was rubbed through the screen stencil, forcing it to pass through the mesh and thus to form wax patterns (10 mm x 8 mm) on the Kapton surface. Finally, the patterned Kapton film was ready for use after removing it from the hot plate and allowing it to cool at room temperature.

Wax and wax composites with 10, 20, 40 and 50 wt.% of BT were processed by both methods. Low thermal and no solvents were used in the processing´s techniques.

3.3.2.3. Physicochemical characterization

SEM was used to evaluate the morphology of the samples and the dispersion of the BT fillers within the wax host matrix. The images were obtained in the surface and cross-section modes using a Carl Zeiss EVO 40 (Oberkochen, Germany) SEM equipped with an energy-dispersive X-ray detector EDS Oxford Instrument X-Max (Abingdon, UK) at magnifications of 1 000× and 5000×. The samples were sputtered with a 10 nm thin gold layer before imaging, using a Polaron SC502 sputter coater.

The chemical evaluation was carried out by Fourier transformed infrared (FTIR) spectroscopy using a Jasco FT/IR-4100 equipment in the attenuated total reflectance (ATR) mode. FTIR-ATR spectra were obtained in the spectral range from 600 to 4000 cm^{-1}, with 64 scans at 4 cm^{-1} of resolution.

The thermal evaluation was performed by differential scanning calorimetry (DSC) from 25 to 160 °C at a rate of 20 °C.min^{-1} under a nitrogen atmosphere using a DSC200 F3 Maia (NETZSCH).

Mechanical measurements wax and BT/W composite samples were obtained in moulded samples and bending mode for screen-printed ones. Mechanical measurements were performed using a Shimadzu AG-IS with a load cell of 500 N at 5 mm/min for both tests: compression (up to 400 N) and bending (for 2, 4 and 6 mm) in the corresponding samples.

Electrical and dielectric measurements were performed in samples with 2 mm of thickness and diameter of 5 mm painted with conductive silver ink as electrodes (Agar scientific, AGG3790, having 0.02 - 0.05 Ω/sq). The DC conductivity of the materials was obtained from the characteristic I-V curves applying voltage steps of 1 V from -10 to +10 V and measuring the electrical current with an automated picoammeter/voltage source Keithley 487. The dielectric measurements were performed using a Quadtech 1929 Precision LCR meter. Electrical conductivity and dielectric constant were determined by equations 3.3.1 and 3.3.2, respectively:

$$\sigma = {}^{1}/_{\rho} = {}^{d}/_{R \times A} \qquad (3.3.1)$$

$$C = \varepsilon \times \varepsilon_0 \, {}^{A}/_{d} \qquad (3.3.2)$$

where σ is the electrical conductivity, ρ the resistivity and R is the sample resistance, d is the thickness of the sample, and A is the area of the electrodes (5 mm of diameter). The capacitance is C, ε and ε_0 is the dielectric constant of the material and the vacuum (8.854×10^{-12} C.V^{-1}.m^{-1}), respectively.

3.3.3. Results and Discussion

3.3.3.1. Morphological Features

The morphology of the wax and wax composites was evaluated after the SEM images shown in Figure 3.3.2. Cross-section images of the wax (Figure 3.3.2A and B) and composites with 10 wt.% (Figure 3.3.2C and D) and 50 wt.% (Figure 3.3.2E and F) show wax composites without voids and with a uniform microstructure. This behaviour is representative of all composites. The barium titanate shows agglomeration in small size clusters that increase in size with increasing BT content in the composite. Thus, the 10BT/W composites present smaller clusters with less than 10 μm of diameter, whereas the 50BT/W composites show a larger number of clusters with sizes between 10 and 20 μm of diameter

(Figure 3.3.2C and D). Thus, a homogeneous dispersion of the BT fillers within the polymeric matrix was achieved, the number and size of the BT clusters increasing with increasing filler content.

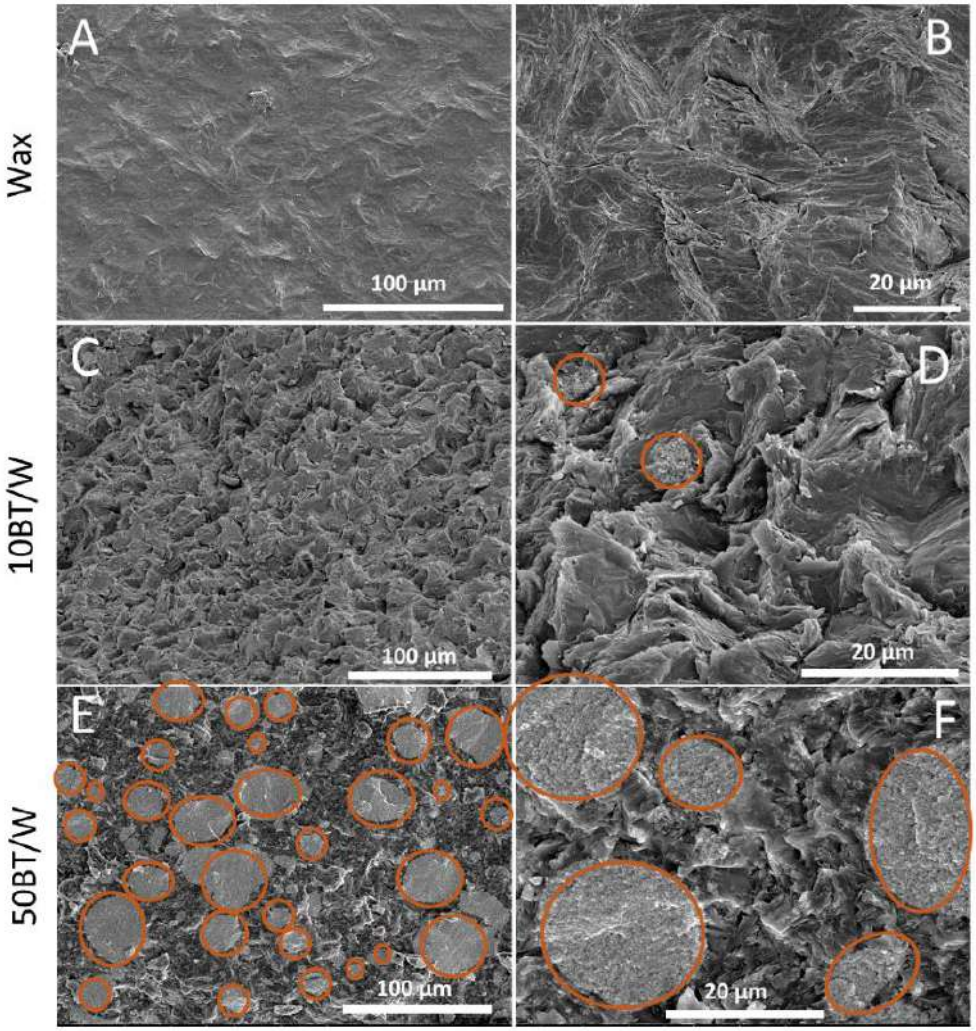

Figure 3.3.2. SEM images of the wax (A and B) and wax composites with the lower and higher BT content, 10 (C and D) and 50 wt.% (E and F) respectively. The orange circles show the barium titanate agglomerates in the composite. The magnifications are 1 000× and 5 000× for both composites.

The EDX analysis of the composites is presented in Figure 3.3.3, identifying the barium and titanium contents in the composites.

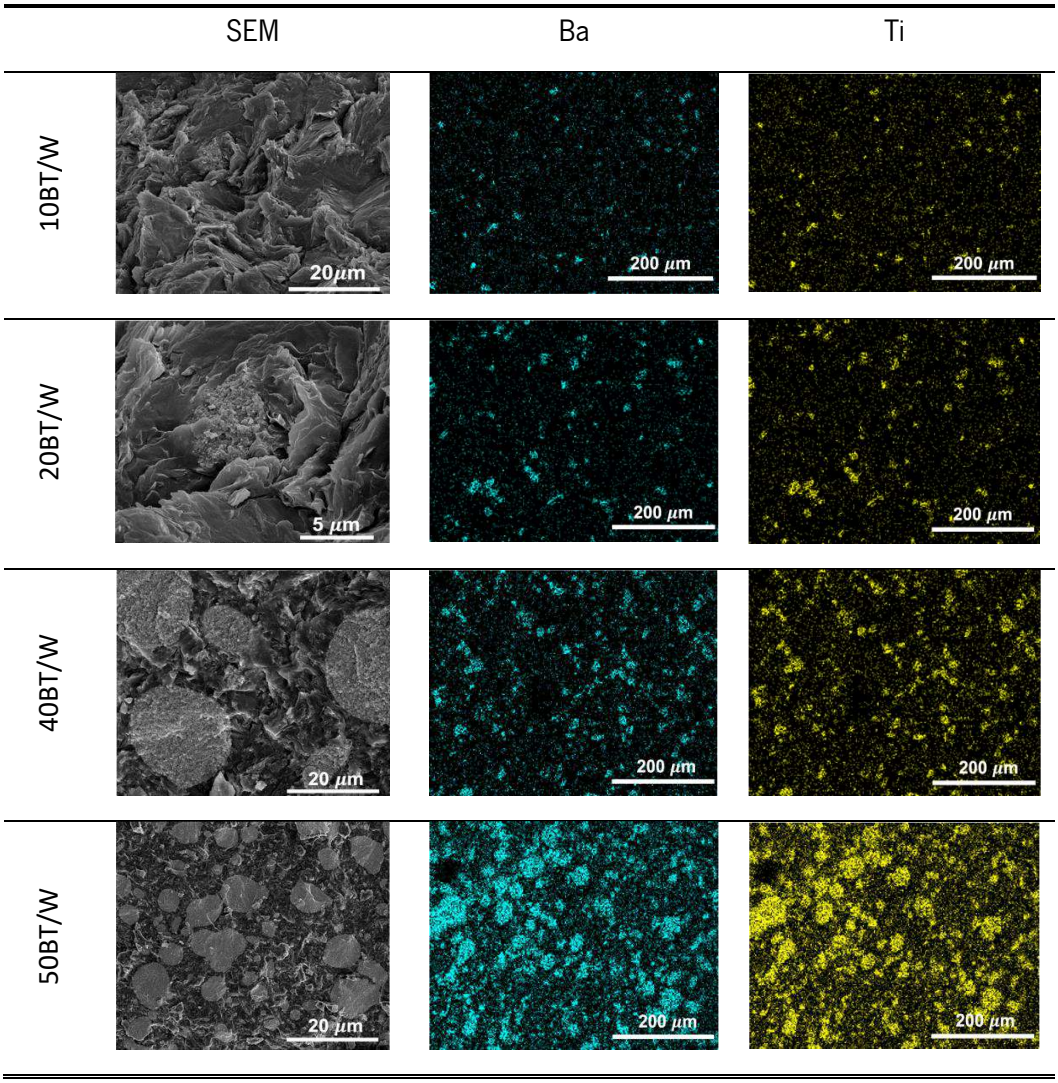

Figure 3.3.3. SEM and EDX analysis of the composites where are represented the barium (Ba) and titanium (Ti) contents of representative composites.

It is observed that barium and titanium content increase with increasing filler content in the composites, the EDX data also corroborating the good dispersion of the BT into a wax matrix, with smaller clusters homogeneously distributed into the wax matrix, the cluster being larger for the larger filler contents.

3.3.3.2. Chemical, thermal dielectric and mechanical properties

The chemical characteristics and thermal behaviour of the wax and composites are represented in Figure 3.3.4. The FTIR-ATR spectra show the typical absorption bands of the paraffin wax [33, 34] (Figure 3.3.4A and B). These characteristic peaks do not change with the inclusion of the fillers or thermal aging [34].

The peak at 720 cm^{-1} represents rocking of -CH_2, 1379 and 1460 cm^{-1} represent the deformation of -CH_3 and -CH_2 and the peaks at 2847 and 2915 cm^{-1} represent the symmetric stretching vibration of -CH_3 and -CH_2 groups [34]. The barium titanate characteristic band at 540 cm^{-1} which corresponds to Ti-O stretching vibration (along with spontaneous polarization in barium titanate) [35], is not shown in spectra for any filler content. No chemical bonding between the wax matrix and the filler is identified by the presence of new bands in the spectra of the composite samples.

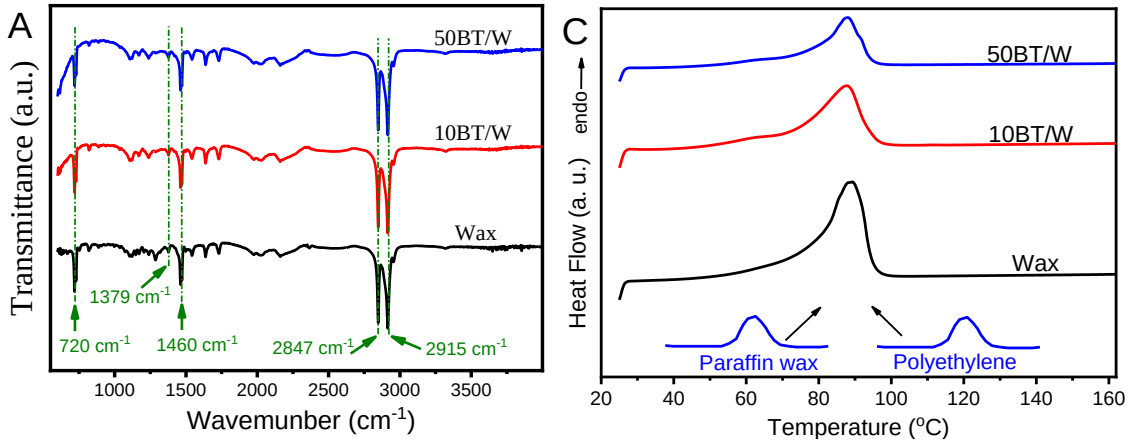

B	deformation / stretching		D		PE	Wax	BT/ W
Vibrational mode	CH_2	CH_3 - CH_2 / CH_3 - CH_2	Material	Paraffin Wax			
Wavenumber (cm^{-1})	720	1375-1460 / 2850-2920	T_m (°C)	≈60	≈120	89	89

Figure 3.3.4. Chemical characteristics and thermal properties of the wax and BT/W composites with 10 and 50 wt.% of BT. A and B) FTIR specta of the materials with representatinve abspoption bands and C and D) DSC analysis with melting temperature (T_m) of the materials.

Paraffin and polyethylene materials present a melting temperature of about 60 and 120 °C [36]. The wax used in this work contains about 40 % of polyethylene and the melting temperature is found at about 89 °C. Independently of the ceramic filler content, the melting temperature of the composites remains constant, up to 50 wt.% of BT content. This is due to the similar thermal conductivity of the paraffin wax and barium titanate, about 0.2 and 3 $W.m^{-1}.K^{-1}$ for wax and barium titanate, respectively [37, 38] and the absence of chemical interactions.

Compression and bending mechanical measurements (Figure 3.3.5) were carried out in the moulded and screen-printed samples, respectively, to evaluate the mechanical properties of the wax and composite with 20 % of BT (sample that presents one of the higher dielectric constants but with lower

filler content, as shown in Figure 3.3.6). The compression measurements (Figure 3.3.5A to D) were carried out up to forces of 400 N and the bending measurements (Figure 3.3.5E) for 2, 4 and 6 mm of deformation.

The compression measurements were carried out up to 400 N (0⟶ 400⟶ 0 N) for 5 cycles for wax and the 20BT/W composite (Figure 3.3.5A and B). The performance of both samples is similar over cycling, being that the deformation under compression is larger for pristine wax than for the composite. Under the force of 400 N, the pristine wax compression is near 18.5 % (0.52 mm) for the first cycle, increasing every cycle up to 22.6 % of strain at the fifth cycle (Figure 3.3.5A). Similarly, for the 20BT/W composite, the strain increases under compression with increasing cycling, from 14.3 % for the first cycle to 17.4 % for the fifth cycle (Figure 3.3.5B). The Young modulus was obtained using the first cycle under the compression testing, the linear region being up to 4 %. The determined value is 7.9 and 7.8 MPa for pristine wax and 20BT/W composite, respectively. Thus, the Young modulus of the wax and composite are similar, despite the BT content and its intrinsic mechanical properties, as the Young modulus value of BT ranges between 50 and 100 GPa [39], when compared to paraffin wax, which is in the order of few MPa [40, 41], being about 5 MPa in paraffin wax-graphite foams [42] in compression mode. Thus, the mechanical properties are determined by the wax matrix.

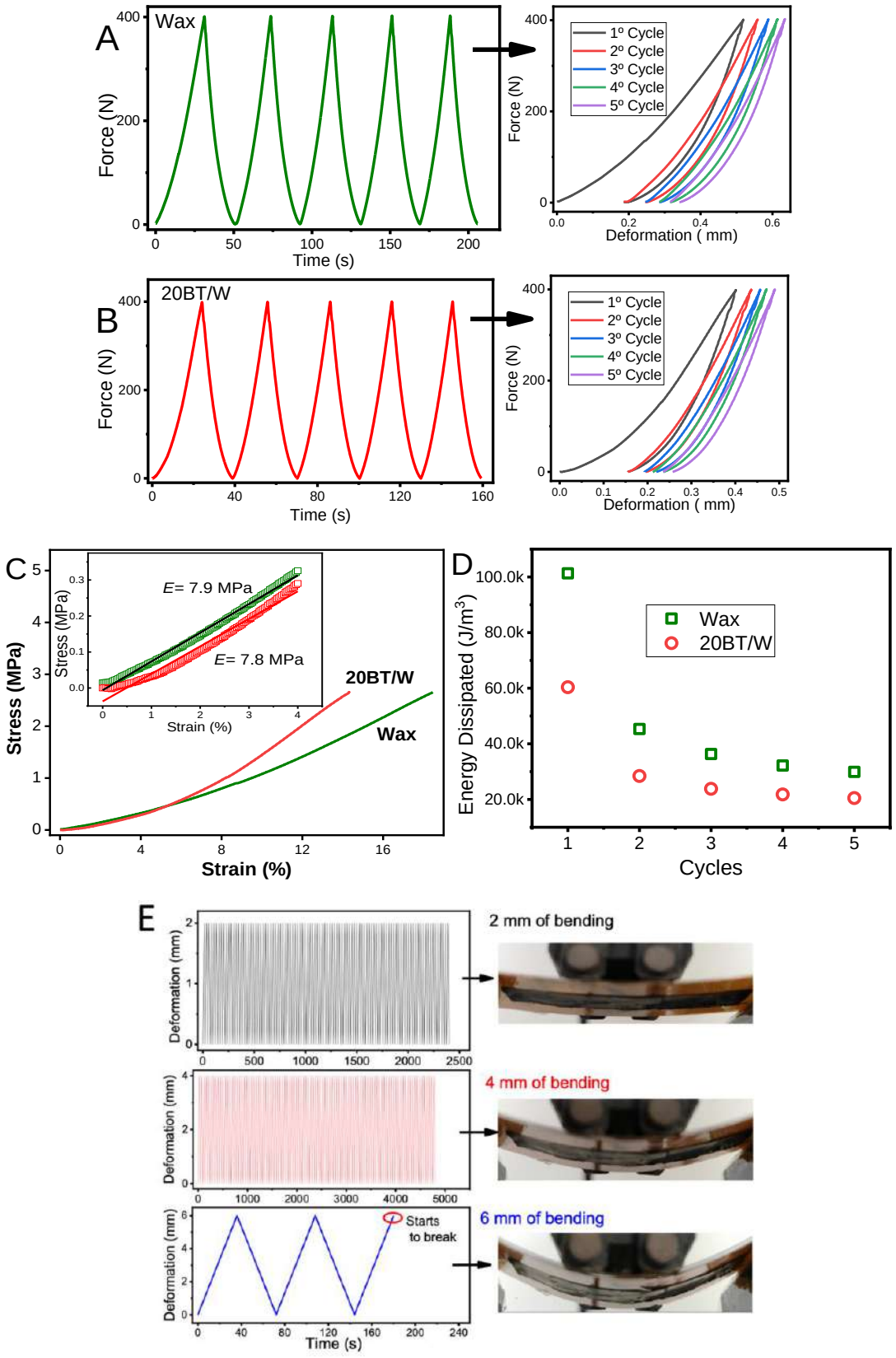

Figure 3.3.5. - Mechanical compression measurements of the wax and 20BT/W molded samples A-D) and bending evaluation E) of the screen-printed 20BT/W composite.

Figure 3.3.5 shows the mechanical response of moulded wax under compression up to 400 N with good cycling endurance. The Young modulus is in agreement with the values reported in the literature for compression testing, but depends on the paraffin content and crystallinity, among other parameters [43]. The compression strain decreases from about 23 % to 17 %, for wax and 20BT/W composite, respectively, after 5 cycles. By the area of individual cycles, the mechanical hysteresis and the energy dissipated by the samples is calculated (Figure 3.3.5D). The dissipated energy is larger for pristine wax than for the composite with 20 wt.% of BT, with 100 and 60 $kJ.m^{-3}$, respectively, presenting similar behaviour with increasing cycling. The dissipated energy decreases with repeated cycles, being near 30 and 20 $kJ.m^{-3}$ for the samples in the fifth cycle. Both samples also show a rapid stabilization of the dissipated energy per cycle, demonstrating suitability to work as a functional device.

The screen-printed composite (20BT/W) shows good flexible properties, capable of bending cycles up to 4 mm (Figure 3.3.5E), being its limit, where cracks and displacements begin to appear in the sample at 6 mm of bending, soon in the tests. For bending up to 4 mm, cycling endurance was performed (100 cycles) without cracks or detachment on the screen-printed film. At 6 mm of bending the film after few cycles start to break. As observed in the images of Figure 3.3.5E, the adhesion of the wax to Kapton (high-thermal stable polymer) without any pre-treatment was achieved, being suitable for bending measurements and applications.

3.3.3.3. Dielectric response

The dielectric response of wax and BT/W composites up to 50 wt.% BT content was measured as a function of frequency, from 100 Hz to 1 MHz (Figure 3.3.6A). The dielectric constant is constant as a function of frequency and increases with increasing ceramic filler content in the composites due to the larger dielectric constant of the filler, $\varepsilon_{BT} = 150$ (Figure 3.3.6.B). The dielectric constant of paraffin wax at 1 kHz is near $\varepsilon \approx 9$, increasing up to $\varepsilon \approx 18$ for the highest filled composite with 50%wt BT content. Literature reports that polymeric composites reinforced with barium titanate start to decrease the dielectric properties after 50 wt.% BT embedded into polymer matrix [44] due to particle agglomeration and increased ionic conductivity due to interfacial effects. In addition, the composite becomes brittle.

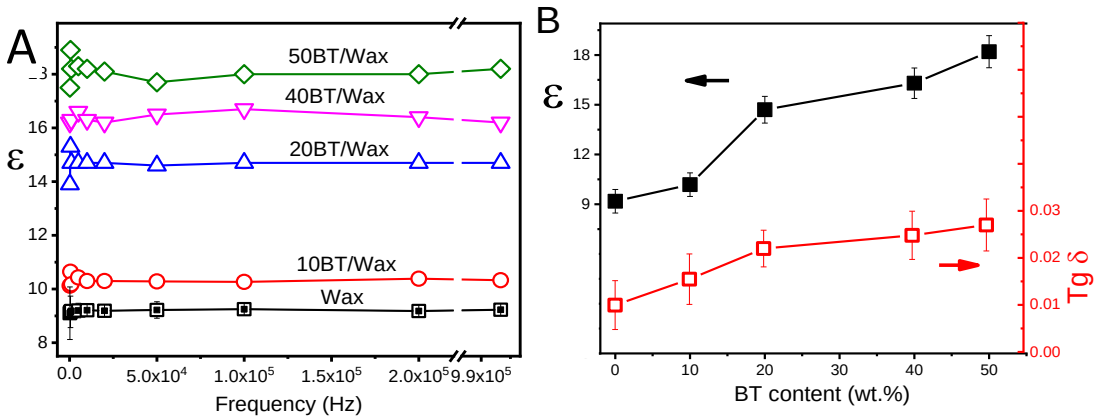

Figure 3.3.6. - Dielectric response of wax and corresponding composites up to 50 wt.% BT as a function of frequency (A) and ceramic content at a frequency of 1 kHz (B).

Similarly, the dielectric losses also increase with increasing BT content in the wax matrix, from tg δ ≈0.01 for wax and tg δ ≈0.027 for the composite with 50 wt.% of BT, remaining a low loss material and thus demonstrating a suitable wettability of the filler by the wax and low contribution of the interfaces to the dielectric losses.

3.3.3.3.1. Theoretical modelling of the dielectric response of the composites

The dielectric response of the composites was analysed considering the size of the nanoparticles (diameter, Φ=100 nm) and the BT content (10, 20, 40 and 50 wt.% corresponding to a volume fraction of 0.016, 0.036, 0.090 and 0.129, respectively) [45]. Different models were used that vary among them depending on the considerations of the relevance of the effect of volume fraction as well as on the different considerations of the most relevant interactions: matrix-filler and filler-filler [32, 45].

The theoretical models consider the polarization of the materials with the applied electric field, the filler-local field and filler-applied field interactions and the local field variation is taken into account spherical dielectric inclusions [45]. The models that consider these effects are Bruggeman [46] and Maxwell-Garnett [47]. The dielectric particles are considered as an electric dipole (as a reasonable approximation [45, 48]) and when an electric field is applied to the composite material, an electric field oscillation is creating in its surrounding, which depends on the filler content [48]. More complex and precise models also consider the shape and relative filler orientation, most of the models considering an ellipsoids shape for the fillers. On the theoretical models, these parameters as expressed as depolarization factor (n) (influenced by the principal axe's length of the fillers and the relative orientation to the applied field [49])

or shape parameter (n'). The models of Tinga [50] and Wiener [51] consider n and n' respectively to better predict the dielectric behaviour of the composites. The used models are summarized in Table 3.3.1, as representative of the several ones existing in the literature, as being those that best predict the dielectric behaviour of the samples under consideration.

Table 3.3.1 – Summary of the theoretical models considered in this work, where ν and ε values represent the volume fraction and dielectric constant, respectively. The subscripts 1 and 2 represent the matrix and filler, respectively and d is the system dimensionality.

Model	Equation
Bruggeman [46]	$\nu_1 \frac{\varepsilon_1 - \varepsilon}{\varepsilon_1 + (d-1)\varepsilon} + \nu_2 \frac{\varepsilon_2 - \varepsilon}{\varepsilon_2 + (d-1)\varepsilon} = 0$
Maxwell-Garnett [47]	$\varepsilon = \varepsilon_1 \left[1 + \frac{3\nu_2\gamma}{1-\nu_2\gamma-\frac{2}{3}\nu_2\gamma \ln\left(\frac{8+\gamma}{8-2\gamma}\right)}\right]$, where $\gamma = \frac{\varepsilon_2-\varepsilon_1}{\varepsilon_2+2\varepsilon_1}$
Tinga [50]	$\frac{\varepsilon - \varepsilon_1}{\varepsilon_1} = \nu_2 \frac{\varepsilon_2 - \varepsilon_1}{\varepsilon_1 + n_2(\varepsilon_2 - \varepsilon_1) - n_1\nu_2(\varepsilon_2 - \varepsilon_1)}$
Wiener [51]	$\frac{\varepsilon - 1}{\varepsilon + n'} = \frac{\nu_2(\varepsilon_2 - \varepsilon_1)}{\varepsilon_2 + n'} + \frac{(1-\nu_2)(\varepsilon_1 - 1)}{\varepsilon_1 + n'}$

Simulations of the different models to predict the dielectric behaviour of composite samples were performance making use of the Origin 9.4 software. Figure 3.3.7 shows the dielectric constant as a function of filler volume fraction, considering $\varepsilon_1 = 9.18$ (experimentally measured) for the wax matrix and $\varepsilon_2 = 150$ for the BT filler, as provided by the supplier. All the theoretical models considered predict the same behaviour for $\nu_2 = 0$ $(\varepsilon = \varepsilon_1)$ and in the regime limit of $\nu_2 = 1$, the Maxwell-Garnett and Bruggeman (d = 3) models showing a dielectric constant of $\varepsilon = \varepsilon_2$. Although Maxwell-Garnett and Bruggeman (d = 3) models consider interactions between fillers and the applied field, the two models are unable to predict the dielectric constant the composites, as it is shown in Figure 3.3.7. The considered theoretical models show an increase of the dielectric constant for higher volume fractions until $\nu_2 = 1$, excepting the Maxwell-Garnett model, which predicts a vertical asymptote for $\nu_2 \approx 0.96$. The best modelling is obtained for the Tinga model which predicts a maximum dielectric constant for the composite of $\varepsilon' \approx 25.44$ for $\nu_2 > 0.5$ (horizontal asymptote).

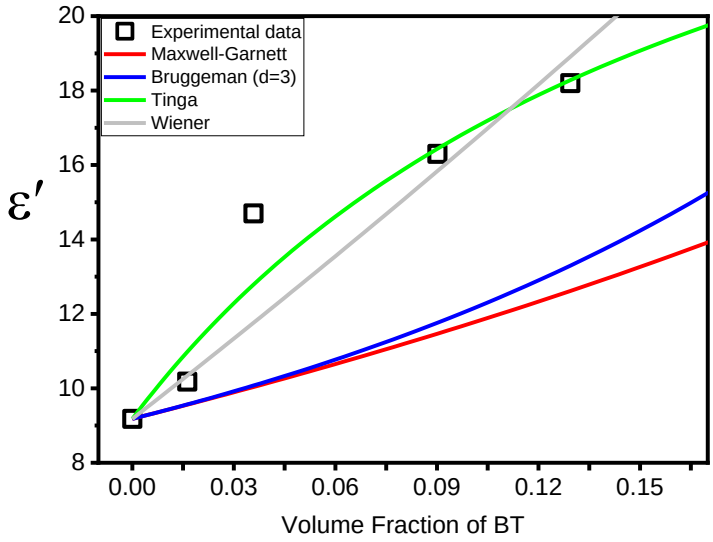

Figure 3.3.7. Experimental results and theoretical models (Maxell-Garnet, Bruggeman, Tinga and Wiener models) for BT/wax composites up to 50 wt.% BT content with a filler diameter of 100 nm. The experimental results correspond to a frequency of 1 kHz.

The experimental-theoretical difference was calculated as a relative percentage deviation ($\delta_r(\%) = \frac{|\varepsilon_{exp}-\varepsilon_{mod}|}{\varepsilon_{exp}} \times 100$), where ε_{exp} is the experimental data measured and ε_{mod} the predicted dielectric constant for Maxwell-Garnett and Bruggeman model and it is summarized in Table 3.3.2A). All these models predict dielectric constant with $\delta_r < 6.1\ \%$ for the 10BT/W composite but for higher filler contents, they are unable of predicting the experimental data. This means that filler-filler interactions only become important for higher filler content, as theoretically predicted. These results can be explained by the high difference between densities of the matrix and the filler as well as the increase of the space charge distribution and Maxwell-Wagner-Sillars contributions to the dielectric behaviour due to the high surface area of the filler [52]. SEM and EDX images (Figure 3.3.2 and 3.3.3) show that the agglomerations (both number and size) of BT increase with increasing of BT content which is related to the lower prediction capability of the theoretical models for higher filler content since the homogeneity condition underlying all models is not verified [45].

Table 3.3.2. - A) Relative percentage deviation of the Maxwell-Garnett and Brugemann models in function of the volume fraction and B) the factors n and n' for Tinga and Wiener models with the corresponding R-square obtained by computational iteration by fitting the experimental data.

A)	δ_r (%)

B)	Models	
	Wiener	Tinga

Models	10 wt.%	20 wt.%	40 wt.%	50 wt.%
Maxwell-Garnett	6.08	31.72	29.65	30.68
Bruggeman (d=3)	6.01	31.45	27.84	26.94

n_1	–	-0.42 ± 0.29
n_2	–	0.01 ± 0.03
n'	153.91 ± 42.19	–
R^2	0.91871	0.95035

The Tinga e Wiener models consider that the filler's shape and orientation play an important role in determining in a more precise way the dielectric behaviour of the composites. So, for these models, the experimental data were fitted to determine the n or n' factor, for the corresponding models, by computational iteration. Table 3.3.2B summarizes the obtained results, where the n or n' factor is presented with the respective R-square for the fitting procedure. Both models present good fitting parameters $(\mathrm{R}^2 > 0.9187)$ but the Tinga model presents a better prediction of the dielectric behaviour for the BT/wax composites. The n' factor in the Wiener model can be related to the filler ellipsoidal axis ratio and to the size of agglomeration and homogeneity of the sample. The models considered in this study are often used to predict the dielectric behaviour of polymeric-based composites [53] and the values of n or n' obtained are consistent with the SEM images, where filler agglomeration occurs. These values are consistent to the theoretical shape factor, where spherical fillers agglomerations take values near to 1/3 [54]. The shape factor value indicates the relative orientation of the agglomeration cluster concerning to the applied electric field [55].

3.3.3.3.2. Theoretical modelling of the composites as capacitors

In order to evaluate the developed composite materials as capacitors, a theoretical simulation was performed (Figure 3.3.8) to predict the spatial distribution of the electrical potential and the corresponding capacitance for a given composite geometry based on the Finite Elements Method (FEM). The 3D capacitor model is based on two metal electrodes separated by the dielectric material within an air volume since there can be fringing fields around the capacitor plates [56]. Under electrostatic conditions, it was assumed the equal potential in the entire surface of each electrode and the air and dielectric materials as perfect insulators. The theoretical model is based on the equations describing the charge conservation principle associated with the dielectric characteristics of the capacitor [57]. Stationary solutions are evaluated for each dielectric constant and geometry of the printed samples with a refined 100T mesh.

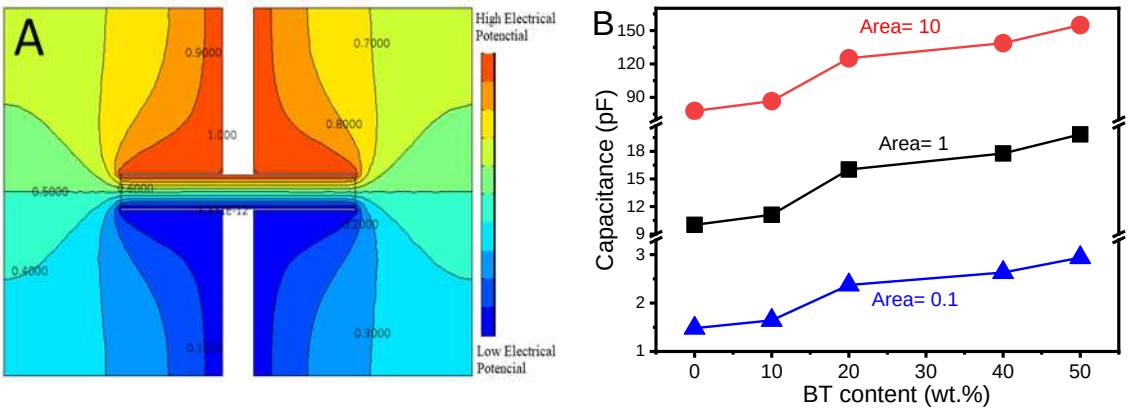

Figure 3.3.8. A) 2D illustration of the electrical potential and B) the computed capacitance for the simulated different dielectric areas as a function of BT content.

The capacitance and spatial distribution of the electrical potential (Figure 3.3.8A) were simulated considering the geometrical dimensions defined by the experimental composite samples (15x10 mm^2 and 2 mm of thickness) for the different BT contents (Figure 3.3.8B). It was also simulated the capacitance for dielectric areas of 0.1× and 10× the original sample size and the results are represented in Figure 3.3.8B. The 50BT/W composite can reach 155 pF of capacitance, using an area 10× the one experimentally used. To the scale-up of the polymeric films, the paraffin wax shows a larger dielectric constant with low-melting temperature as advantages, compared with commercial polymeric films to capacitors [58]. Thus, it is shown that the developed materials can be used in printed functional devices, including printed electronics [59], thermal applications [20] and paper (or other multifilament substrate) microfluidic and microelectronics [60], taking advantage of the hydrophobic character of wax and its simple printability [18, 21, 23].

3.3.4. Conclusions

Composites with dielectric properties have a wide range of applications, in particular, new formulations compatible with printed and moulded electronics are an area of increasing interest. Enviornmental-friendly processing also was used to samples manufacturing.

Homogeneous ceramic dispersion was obtained in the BT/wax composites in the function of the filler content, as shown by the SEM and EDX images. Agglomerates diameter increases to near 10 μm to 20 μm for lowest and largest composites, respectively. Their distribution into smaller agglomerates influences the mechanical properties with a similar Young modulus of the wax and 20BT/W composite

(7.9 and 7.8 MPa, respectively). The energy dissipated per cycle in compression mode up to 400 N shows similar behaviour for wax and 20BT/W, decreasing drastically for the first three cycles (first cycle with 100 $kJ.m^{-3}$), tending to stabilize after (fifth cycle with 30 $kJ.m^{-3}$). 20BT/W composite presents about less 40 % of dissipated energy than pristine wax. Besides compression in moulded materials, screen-printing samples were subject to bending cycles (100 cycles). Bending measurement shows that the flexibility of the screen-printed films is enough to support up to 4 mm of bending. In this way, the moulded and screen-printing samples are capable to support larger external stimuli and can be used in devices.

The dielectric constant of the pristine wax is near $\varepsilon \approx 9$, increasing for $\varepsilon \approx 18$ for 50BT/W composites, being about $\varepsilon \approx 18$ for 20BT/W composite. Similarly, to the dielectric constant, the losses increase with filler content, from tg $\delta \approx 0.01$ for wax to tg $\delta \approx 0.027$ for the largest composite. Theoretical models corroborate the experimental dielectric behaviour of the samples, being the models that consider the shape and orientation of the ceramic filler agglomerations crucial to predict the dielectric behaviour of the composites. Therefore, the Tinga model presents the best prediction of the dielectric behaviour for the BT/wax composites. Capacitive modelling based on FEM, shows that the 50BT/W composite can reach about 155 pF for a sample 10× larger than that used in experimental work (10×15×2 mm).

3.3.5. References

1. Drozdov, A.D., deClaville Christiansen, J., Modeling dielectric permittivity of polymer composites at microwave frequencies. Materials Research Bulletin, 2020; 126: 110818.

2. Mao, Z., Sun, H., Zhang, J., Selective distribution of SrTiO3 in co-continuous composites: An effective method to improve the dielectric and mechanical properties. Composites Part A: Applied Science and Manufacturing, 2021. 143: 106312.

3. Prateek, V., Thakur, K., Gupta, R.K., Recent Progress on Ferroelectric Polymer-Based Nanocomposites for High Energy Density Capacitors: Synthesis, Dielectric Properties, and Future Aspects. Chemical Reviews, 2016. 116(7): 4260-4317.

4. Song, Y., et al., Highly Efficient Electromagnetic Wave Absorbing Metal-Free and Carbon-Rich Ceramics Derived from Hyperbranched Polycarbosilazanes. The Journal of Physical Chemistry C, 2017. 121(44): 24774-24785.

5. Zhang, L., et al., Thermally stable polymer–ceramic composites for microwave antenna applications. Journal of Advanced Ceramics, 2016. 5(4): 269-276.

6. Raveendran, A., Sebastian, M.T., Raman, S., Applications of Microwave Materials: A Review. Journal of Electronic Materials, 2019. 48(5): 2601-2634.

7. Carvalho, E., et al., Piezoelectric Polymer Composites for Sensors and Actuators, in Reference Module in Materials Science and Materials Engineering. 2020, Elsevier.

8. Castro, H.F., et al., Printed Wheatstone bridge with embedded polymer based piezoresistive sensors for strain sensing applications. Additive Manufacturing, 2018. 20: 119-125.

9. Alcácer, V., Cruz-Machado, V., Scanning the Industry 4.0: A Literature Review on Technologies for Manufacturing Systems. Engineering Science and Technology, an International Journal, 2019. 22(3): 899-919.

10. Barras, R., et al., Printable cellulose-based electroconductive composites for sensing elements in paper electronics. Flexible and Printed Electronics, 2017. 2(1): 014006.

11. Zhang, D., et al., High energy density in P(VDF-HFP) nanocomposite with paraffin engineered BaTiO3 nanoparticles. Sensors and Actuators A: Physical, 2017. 260: 228-235.

12. Costa, P., et al., Recent Progress on Piezoelectric, Pyroelectric, and Magnetoelectric Polymer-Based Energy-Harvesting Devices. Energy Technology, 2019. 7(7): 1800852.

13. Chen, S., et al., Enhanced breakdown strength of aligned-sodium-titanate- nanowire/epoxy nanocomposites and their anisotropic dielectric properties. Composites Part A: Applied Science and Manufacturing, 2019. 120: 84-94.

14. Hu, H., et al., Recent advances in rational design of polymer nanocomposite dielectrics for energy storage. Nano Energy, 2020. 74: 104844.

15. Martins., P., Lopes, A.C., Lanceros-Mendez, S., Electroactive phases of poly(vinylidene fluoride): Determination, processing and applications. Progress in Polymer Science, 2014. 39(4): 683-706.

16. Brochu, P., Pei, Q., Advances in Dielectric Elastomers for Actuators and Artificial Muscles. Macromolecular Rapid Communications, 2010. 31(1): 10-36.

17. Liu, L., et al., Polyimide composites composed of covalently bonded BaTiO3@GO hybrids with high dielectric constant and low dielectric loss. RSC Advances, 2016. 6(90): 86817-86823.

18. Saji, V.S., Wax-based artificial superhydrophobic surfaces and coatings. Colloids and Surfaces A: Physicochemical and Engineering Aspects, 2020. 602: 125132.

19. Al-Salem, S.M., et al., Pyro-Oil and Wax Recovery from Reclaimed Plastic Waste in a Continuous Auger Pyrolysis Reactor. Energies, 2020. 13(8): 2040.

20. Gulfam, R., Zhang, P., Meng, Z., Advanced thermal systems driven by paraffin-based phase change materials – A review. Applied Energy, 2019. 238: 582-611.

21. Zhao, X., Hu, T., Zhang, J., Superhydrophobic coatings with high repellency to daily consumed liquid foods based on food grade waxes. Journal of Colloid and Interface Science, 2018. 515: 255-263.

22. White, J.R., et al., Piezoelectric paint: Ceramic-polymer composites for vibration sensors. Journal of Materials Science, 2004. 39(9): 3105-3114.

23. Liu, M., Zhang, C., Liu, F., Understanding wax screen-printing: A novel patterning process for microfluidic cloth-based analytical devices. Analytica Chimica Acta, 2015. 891: 234-246.

24. Li, Y., et al., Multifunctional BiFeO3 composites: Absorption attenuation dominated effective electromagnetic interference shielding and electromagnetic absorption induced by multiple dielectric and magnetic relaxations. Composites Science and Technology, 2018. 159: 240-250.

25. Kuang, B., et al., Chemical reduction dependent dielectric properties and dielectric loss mechanism of reduced graphene oxide. Carbon, 2018. 127: 209-217.

26. Zhang, N., et al., Design and microwave absorption properties of thistle-like CoNi enveloped in dielectric Ag decorated graphene composites. Journal of Colloid and Interface Science, 2019. 534: 110-121.

27. Xu, H., et al., Tunable dielectric properties of mesoporous carbon hollow microspheres via textural properties. Nanotechnology, 2018. 29(18): 184003.

28. Dey, C.C., et al., Electromagnetic-wave shielding promulgation of cluster like FZ@MWCNT composite incorporated in GO matrices by polarization relaxation and potential degradation. Materials Characterization, 2021. 172: 110884.

29. Wang, C., et al., Magnetic and dielectric properties of barium titanate-coated barium ferrite. Journal of Alloys and Compounds, 2009. 476(1): 560-565.

30. Hongxia, J., et al., Preparation and microwave adsorption properties of core–shell structured barium titanate/polyaniline composite. Journal of Magnetism and Magnetic Materials, 2013. 332: 10-14.

31. Araújo, M.C., Costa, C.M., Lanceros-Méndez, S., Evaluation of dielectric models for ceramic/polymer composites: Effect of filler size and concentration. Journal of Non-Crystalline Solids, 2014. 387: 6-15.

32. Bhimasankaram, T., Suryanarayana, S.V., Piezoelectric polymer composite materials. Current Science, 1998. 74(11): 967-976.

33. George, M., et al., A novel polyaniline (PANI)/ paraffin wax nano composite phase change material: Superior transition heat storage capacity, thermal conductivity and thermal reliability. Solar Energy, 2020. 204: 448-458.

34. George, M., et al., Long-term thermophysical behavior of paraffin wax and paraffin wax/polyaniline (PANI) composite phase change materials. Journal of Energy Storage, 2020. 31: 101568.

35. Jin, X., et al., Investigation on FTIR spectra of barium calcium titanate ceramics. Journal of Electroceramics, 2009. 22(1): 285-290.

36. Gumede, T.P., et al., Plasticization and cocrystallization in LLDPE/wax blends. Journal of Polymer Science Part B: Polymer Physics, 2016. 54(15): 1469-1482.

37. Trigui., A. Karkri, M., Krupa, I., Thermal conductivity and latent heat thermal energy storage properties of LDPE/wax as a shape-stabilized composite phase change material. Energy Conversion and Management, 2014. 77: 586-596.

38. He, Y., Heat capacity, thermal conductivity, and thermal expansion of barium titanate-based ceramics. Thermochimica Acta, 2004. 419(1): 135-141.

39. Cheng, B.L., et al., Mechanical loss and Young's modulus associated with phase transitions in barium titanate based ceramics. Journal of Materials Science, 1996. 31(18): 4951-4955.

40. Tewo, R.K., et al., Thermal and mechanical properties of investment casting pattern material based on paraffin wax fortified with LLDPE and filled with PMMA. AIP Conference Proceedings, 2020. 2289(1): 020053.

41. Wang, J., Severtson, S.J., Stein, A., Significant and Concurrent Enhancement of Stiffness, Strength, and Toughness for Paraffin Wax Through Organoclay Addition. Advanced Materials, 2006. 18(12): 1585-1588.

42. Karthik, M., Faik, A., D'Aguanno, B., Graphite foam as interpenetrating matrices for phase change paraffin wax: A candidate composite for low temperature thermal energy storage. Solar Energy Materials and Solar Cells, 2017. 172: 324-334.

43. Kobald, M., et al., Evaluation of Paraffin-based Fuels for Hybrid Rocket Engines, in 50th AIAA/ASME/SAE/ASEE Joint Propulsion Conference.

44. Offenzeller, C., et al., A dielectric coating for improved performance of capacitive sensors in all-polymer microfluidic devices. Microelectronic Engineering, 2020. 223: 111220.

45. Araujo, M.C., Costa, C.M., Lanceros-Mendez, S., Evaluation of dielectric models for ceramic/polymer composites: Effect of filler size and concentration. Journal of Non-Crystalline Solids, 2014. 387: 6-15.

46. Bergman, D.J., et al., The dielectric constant of a composite material-A problem in classical physics. Physics Reports, 1978. 43(9): 377-407.

47. Nan, C.W., Comment on "Effective dielectric function of a random medium". Physical Review B, 2001. 63(17): 3.

48. Jayasundere, N,. Smith, B.V., Dielectric-Constant for Binary Piezoelectric 0-3 Composites. Journal of Applied Physics, 1993. 73(5): 2462-2466.

49. Kittel, C., Introduction to Solid State Physics. 8° ed. 2005: Wiley India Pvt. Limited.

50. Tinga, W.R., Voss, W.A.G., Blossey, D.F., Generalized approach to multiphase dielectric mixture theory. Journal of Applied Physics, 1973. 44(9): 3897-3902.

51. Ahmad, Z., Prasad, A. Prasad., Prasad, K., A comparative approach to predicting effective dielectric, piezoelectric and elastic properties of PZT/PVDF composites. Physica B-Condensed Matter, 2009. 404(20): 3637-3644.

52. Mendes, S.F., et al., Effect of filler size and concentration on the structure and properties of poly(vinylidene fluoride)/$BaTiO_3$ nanocomposites. Journal of Materials Science, 2012. 47(3): 1378-1388.

53. Chamankar, N., et al., An experimental model for predicting the piezo and dielectric constant of PVDF-PZT nanocomposite fibers with 0-3 and 1-3 connectivity. Ceramics International, 2020. 46(15): 23567-23581.

54. Sihvola, A., Dielectric polarization and particle shape effects. Journal of Nanomaterials, 2007. 2007: 9.

55. Tuncer, E., Geometrical Description in Binary Composites and Spectral Density Representation. Materials, 2010. 3(1): 585-613.

56. Narimani, K., et al., Fabrication, modeling and simulation of high sensitivity capacitive humidity sensors based on ZnO nanorods. Sensors and Actuators B-Chemical, 2016. 224: 338-343.

57. Catalan-Izquierdo, S., et al., Capacitance evaluation on parallel-plate capacitors by means of finite element analysis. Renewable Energy and Power Quality Journal, 2009. 1(7): 613-616.

58. Tan, D.Q., Review of Polymer-Based Nanodielectric Exploration and Film Scale-Up for Advanced Capacitors. Advanced Functional Materials, 2020. 30(18): 1808567.

59. Won, S.M., et al., Natural Wax for Transient Electronics. Advanced Functional Materials, 2018. 28(32): 1801819.

60. Hamedi, M.M., et al., Integrating Electronics and Microfluidics on Paper. Advanced Materials, 2016. 28(25): 5054-5063.

3.4. Development of multifunctional waxes based on conductive nanofillers for sensing applications

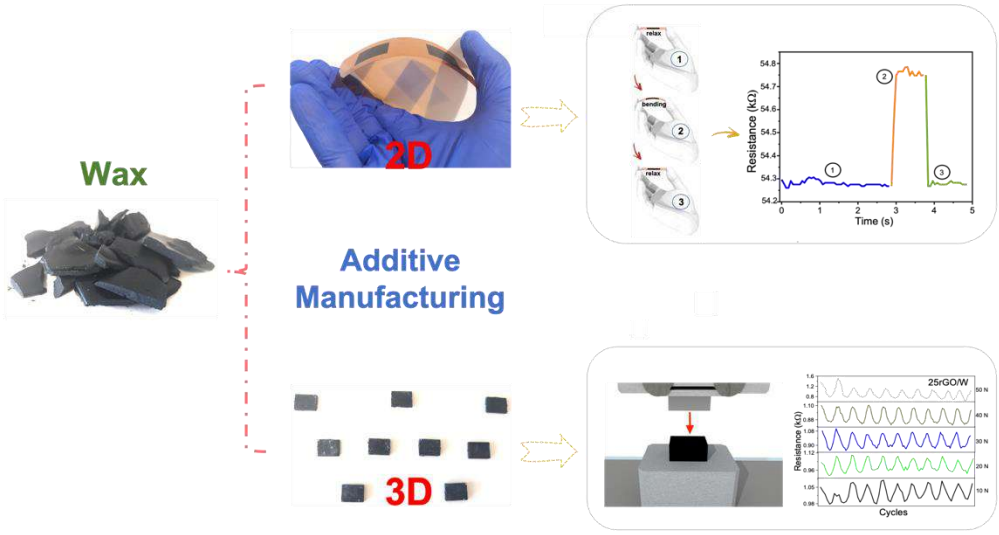

Multifunctional wax composites reinforced with carbon nanomaterials have been processed by additive manufacturing: 3D molding and screen-printing processes. Wax reinforced with carbon nanotubes or reduced graphene oxide leads to conductive and piezoresistive materials, the latter allowing to measure compression and bending deformations. Together with the good sensing properties, another advantage of the developed materials is the environmentally friendly processing. Carbon nanotube (CNT) and reduced graphene oxide (rGO) filled wax (W) composites were developed and proven to be suitable for screen-printing and molding techniques, allowing simple manufacturing of conductive and multifunctional materials. A homogeneous filler dispersion is essential to obtain smaller filler clusters within the wax. The applicability was demonstrated by developing a screen-printed sensor, allowing to detect bending movements, connected to a mobile device through an electronic system.

This chapter is based on following publication: R. Brito-Pereira, C.R Tubio, P.Costa, S. Lanceros-Mendez, Multifunctional wax based conductive and piezoresistive nanocomposites for sensing applications, Composites Science and Technology 213, 108892, (2021).

3.4.1. Introduction

Composites based on polymer matrices modified with nanofillers are increasing interest in the development of smart and multifunctional materials. The incorporation of specific fillers within the host matrix allows the combination, often in a synergetic way, of the intrinsic properties of the matrix with the functional properties of the specific fillers, incorporating electrical conductivity or magnetic response, among others, in the composite [1]. Thus, multifunctional composites have been developed with self-cleaning [2], self-healing [3, 4], or self-sensing [5, 6] properties based on low-density materials with simple, low-cost and environment-friendly processing [3].

Polymer-based composites can be tailored using a wide range of flexible matrices [7], conductive fillers [7, 8] and processing techniques [7, 9]. Elastomers, thermoplastic and thermosets can be properly combined with conductive micro- or nanoparticles to properly tailor conductive and piezoresistive characteristics materials [7, 10]. In particular, one of the most interesting functionalities is the electrical conductivity, due to the wide range of applications in electronics and related areas [11]. Thus, the development of conductive polymer composites has become an active research area in this field [1, 12]. Further, sensing characteristics can be implemented in conductive polymer composites, such as piezoresistive response, turning the materials suitable for force and deformation sensing [5].

Piezoresistive sensors are, together with temperature sensors, among the most used in applications such as robotic skins, transparent and wearable electronics, medical and structural health monitoring [7, 12]. An increasing number of studies have been focusing on developing piezoresistive flexible sensors with high sensitivity and deformability, mostly based on polymer composites [5].

In fact, carbon nanomaterials have been extensively used for the development of conductive and piezoresistive polymer composites, being carbon nanotubes (CNT) and graphene (rGO) the most promising candidates, to work as high sensitivity functional sensors [3]. Metallic nanofillers are also commonly employed for the development of conductive polymer-based composites [13], but graphene and CNT embedded in a polymer matrix lead to composites with lower percolation threshold, higher electrical conductivity and functional properties [1, 14]. Thus, CNTs are the most sought-after additive for realizing 3D-printed multifunctional composites [15]. Composites using conductive fillers and wax have been also developed [16, 17]. The piezoresistive sensibility (known as the Gauge Factor, GF) of polymer-based composites depends on the nature of the polymer, type of filler and filler content, as well as on the processing method and piezoresistive measurement mode [5, 7, 18]. Compression, bending or uniaxial strain are commonly used solicitation modes for applications [5, 7, 18], the piezoresistive sensibility being

also dependent on the applied stimulus. Higher GF is typically found near the percolation threshold [19] and for large strains in elastomeric composites, the electrical network of conductive fillers changing the electrical resistance more significantly under applied deformation [7]. The GF varies from low sensibility (GF< 1) to large sensibility (GF> 1000) in those composites evaluated in the tensile mode [7, 18]. Under compression, high sensibilities of GF> 50 [20] have been obtained as well as pressure sensibilities (PS) from some MPa^{-1} down to few kPa^{-1} [18, 20, 21]. Strain sensors evaluated in the bending mode, e.g. for electronic skin application, can show sensibilities ranging from GF<1 to GF >1000 [22]. Elastomeric or thermoplastic elastomer materials present larger piezoresistive sensibility combined with extraordinary mechanical properties, in particular with respect to the large deformations [21, 23].

Concerning the possible processing and device integration technologies, the IoT and Industry 4.0, promoting the ubiquity of sensors and their interconnectivity [24, 25], are also stimulating the production of sensing materials by additive manufacturing and, in particular, printing technologies such as screen- or inkjet-printing [11, 26, 27].

Despite their advantages, such as low assembly costs, large-area applications and the practical integration of these materials into functional devices [2], the widespread application of specific printing technologies, such as screen-printing, inkjet or direct writing of polymer-based composite materials is limited [28], among others, due to the need to use organic solvents during the printing process [29], raising some environmental concerns. In this context, wax-based materials appear as an alternative to traditional polymer host matrices, based on their relatively low-temperature melt processability (between 60 and 100 °C) [30], and for the possibility of being both from natural or synthetic sources [31]. Other suitable characteristics of waxes are being chemically inert, the negligible supercooling, low vapor pressure in the melt, self-nucleating, no phase segregation and being environmental-friendly and scalable for industrial applications [32, 33]. Functional wax composites have been thus developed based on different functional particles including conducting [34] and magnetic [35] nanoparticles. Environmental-friendly manufacturing (no need or non-dangerous solvents can be used to improve filler dispersion) and low-temperature processing can be used to develop functional composite materials for applications [36, 37]. Notwithstanding the possible use of natural wax, offering broad application potential based on their intrinsic biochemical properties, synthetic waxes are more chemically stable and allow higher resolutions when printed by 2D or 3D techniques [38-41]. Due to their moderate melting temperature, wax allows the 2D and 3D printing of multidimensional and multifunctional devices [35, 41, 42], including actuators [43], energy storage [44] and paper microfluidics [36, 45].

The demand for functional sensing materials considering eco-design principles and device integration by printing technologies [2] leads to the need for novel, environmentally friendlier and easy processable host matrices, being natural or synthetic wax one of the most interesting candidates [35, 45]. In this context, the present work explores the preparation of 2D and 3D multifunctional wax composites for conductive and piezoresistive sensing applications, being a contribution for the key scientific and technological priorities related to a digitalized and sustainable economy. Taking into consideration minimization of the environmental impact, ethanol was used to disperse the fillers and wax was melted at 100 °C for composites manufacturing.

3.4.2. Materials and Methods

3.4.2.1. Materials

Black dye wax cartridges were purchased from Xerox Corporation (Connecticut, USA). This solid ink wax composition is about 60 % of paraffin wax, 20 % of polyethylene resin, and about 10 % of black dye. As conductive fillers were used CNT, Nanocyl Company, NC7000 (length of 1.5 μm, a diameter of 9.5 nm and 90 % purity) and reduced graphene oxide, supplied by Graphenest Company, Portugal. The rGO has 2-30 layers with <10 nm of thickness and 1-20 μm of particle size [46]. All materials were used as received from the providers. Pure ethanol (99 %) was purchased from Sigma-Aldrich (Missouri, USA).

3.4.2.2. Preparation of the wax composites

For the preparation of the graphene/wax (rGO/W) and CNT/wax (CNT/W) composites (Figure 3.4.1), the corresponding filler was first added in the proper filler content (0, 2, 4, 6, 8, 10, 15, 20, 25 wt.% for rGO and 0, 0.25, 0.5, 1, 2, 4 wt.% for CNT) to 5 mL of pure ethanol (Figure 3.4.1i). The filler/ethanol solution was dispersed in an ultrasound bath (ii) for 3 h to ensure good dispersion and to prevent filler agglomeration. The nomenclature of the samples along the paper will be the following: filler content/matrix as, for example, 025CNT/W or 2rGO/W.

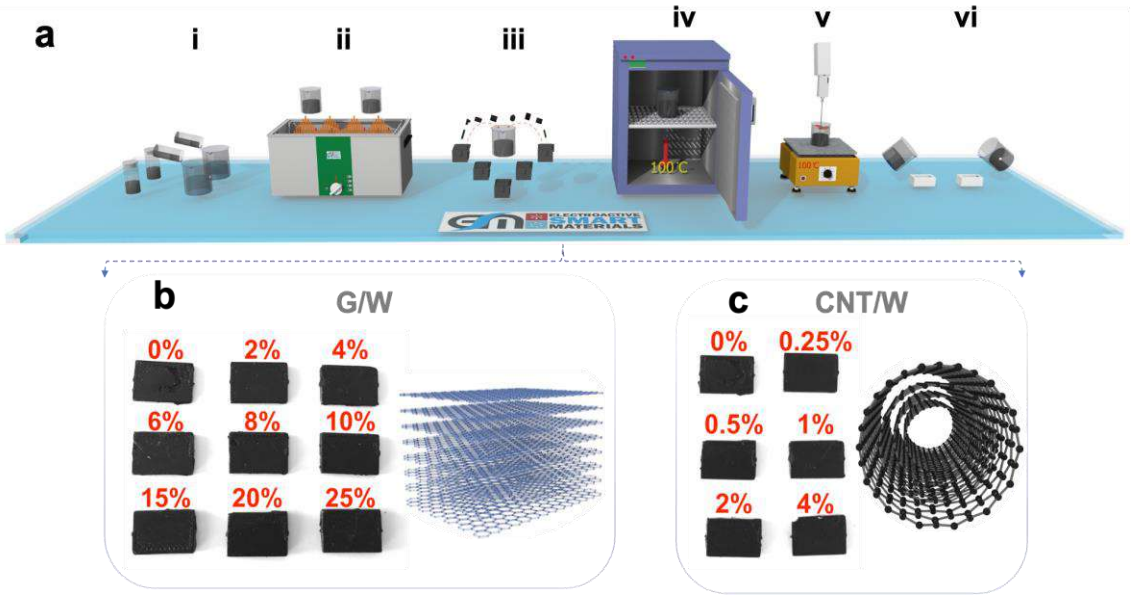

Figure 3.4.1. Experimental procedure used to prepare the wax (black dye) rGO/W and CNT/W composites a) and the prepared samples for several contents of rGO b) and c) CNT.

Afterward, a previously cut wax block (1.5 g) was added (iii) to the filler/ethanol solution and placed inside an oven (JP Selecta, Model 2000208) for 30 min (iv) at a temperature of 100 °C for wax melting embedding the fillers and then during 10 min for the complete removal of the solvent.

The filler/wax solution was removed from the oven and placed in a hot plate at the same temperature (100 °C) and mixed for 1 h at 100 rpm with the help of a mechanical Teflon stirrer (v) to ensure the homogeneity of the melt for the different composites.

These materials were then processed by two different techniques: molding (3D) and screen-printing (2D).

3.4.2.2.1. Molding

3D wax and wax composites were deposited in a printed ABS cubic mold (vi), with the inner dimensions of 1 cm^3 (Figure 3.4.1vi), allowing to obtain samples with the desired 3D structure.

3.4.2.2.2. Screen-printing

The possible 2D printing of the functional waxes on flexible substrates allows increasing their applicability [2]. Thus, filled wax inks with different filler contents were also applied by screen-printing (Figure 3.4.2i) at 100 °C (above wax melting temperature) to obtain films with an area of 20×8 mm. Commercial Kapton

(DuPont, 125 μm of thickness) was used as a flexible substrate, fixed in a hot plate (Prazitherm P272) for the printing process at 100 °C.

For the screen-printing of the samples, the screen (200 mesh of nylon on an aluminum frame) was placed at 1 mm distance from the hot plate surface and the previously melted wax-based ink (Figure 3.4.2i) was pressed with the screen stencil through the mesh to print the patters on the Kapton surface (Figure 3.4.2ii). It is to notice that the printed film was ready for use after removing it from the hot plate and allowing it to cool down at room temperature, with no further treatment.

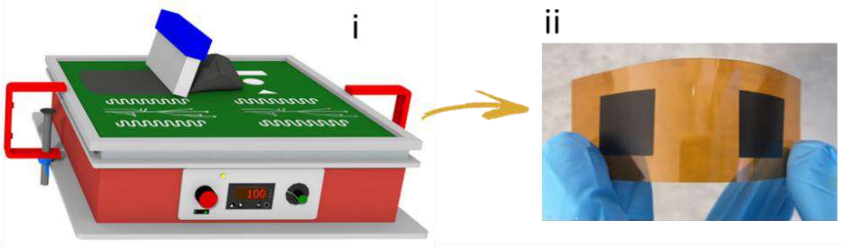

Figure 3.4.2. Illustration of the (i) screen-printing process of the wax composites (ii) on the flexible substrates (Kapton). The experimental process was carried out at 100 °C.

3.4.2.3. Physicochemical characterization

Morphological analysis was performed by SEM in order to evaluate the dispersion of the rGO and CNT fillers within the wax host matrix. Surface and cross-section images of the samples were obtained using a NanoSEM-FEI Nova 200 (FEG/SEM) at magnifications of 1 000× and 15 000×.

Chemical evaluation was carried out by FTIR spectroscopy using a Jasco FT/IR-4100 in the ATR mode. FTIR spectra were obtained in the spectral range from 4000 to 600 cm^{-1}, with 64 scans at 4 cm^{-1} of resolution.

Differential scanning calorimetry (DSC) was performed from 20 to 200 °C at a rate of 20 °C/min using a DSC200 F3 Maia (NETZSCH) set up under a dry nitrogen atmosphere.

Mechanical tests in the tensile mode were carried out using a universal testing machine (Shimadzu model AG-IS) using a load cell of 50 N. The samples prepared after a molding process, with a cubic shape of 1 cm^3, were analyzed in compression mode with a test velocity of 0.5 mm/min for 10 loading-unloading cycles up to forces from 10 to 50 N.

The volume electrical conductivity was determined in samples with 5 mm diameter gold electrodes deposited on both sides with a Polaron SC502 sputter coater. Gold electrodes present low electrical resistance, showing good adhesion to the samples surface and enough flexibility for the deformations

applied in the present work. The electrical conductivity was obtained by measuring the characteristic I-V curves in the voltage range from -1 V to +1 V at room temperature with a Keithley 6487 picoammeter/voltage source. The electrical conductivity (σ) was calculated considering the geometrical factors of the samples according to:

$$\sigma = \frac{l}{R.A} \tag{3.4.1}$$

where R is the electrical resistance, l is the sample thickness and A is the area of the electrodes.

Piezoresistive measurements were performed in compression and 4-point-bending modes using a universal testing machine Shimadzu model AG-IS with a 50 N load cell, measuring simultaneously the electrical resistance with an Agilent 34401A multimeter. The compression mode (Figure 3.4.3a) was used for composites manufactured by the molding method. The measurements were performed for 10, 20, 30, 40 and 50 N of maximum applied force at 0.5 mm/min deformation speed for 10 cycles. The electromechanical measurements were performed in the composites with graphene (25rGO/W) and CNT (05CNT/W and 4CNT/W).

The 4-point-bending mode (Figure 3.4.3b) was applied to the samples manufactured by screen-printing on Kapton substrates. The printed composite was glued to a polypropylene polymer flexible substrate with a thickness of 1 mm. The electrodes on the composite were printed with silver ink (Agar scientific, reference AGG3790) with an area of 15 mm × 8 mm (length×width). The electromechanical response was evaluated for the 25G/W sample from 0.1 to 5 mm of bending at 2 and 5 mm.min^{-1} deformation speed.

The electromechanical response, or piezoresistive sensibility, of the composites evaluated after compression (PS) and bending (GF) modes was evaluated using equations 3.4.3 and 3.4.4 [47, 48]:

$$PS = \frac{\Delta R/R_0}{P} \tag{3.4.3}$$

$$GF = \frac{\Delta R/R_0}{\Delta l/l_0} = \frac{d\rho/\rho_0}{\varepsilon} + 1 + 2\upsilon \tag{3.4.4}$$

where ΔR is the electrical resistance variation, R_0 the initial resistance value and P is the applied pressure. The Poisson coefficient is represented by υ (υ=0.37 [43]), l is the mechanical displacement, ρ the electrical resistivity and $\varepsilon = \Delta l/l_0$ the strain. For the 4-point-bending mode experiments, the strain

was calculated from the theory of pure bending, valid between the inner loading points and given by Equation 3.4.5 [47, 49].

$$\varepsilon = \frac{3dz}{5a^2} \tag{3.4.5}$$

where the thickness of sample and support, d ≈1.2 mm, vertical displacement, z, up to 5 mm, and distance between bending points, a = 15 mm, are represented in Figure 3.4.3b.

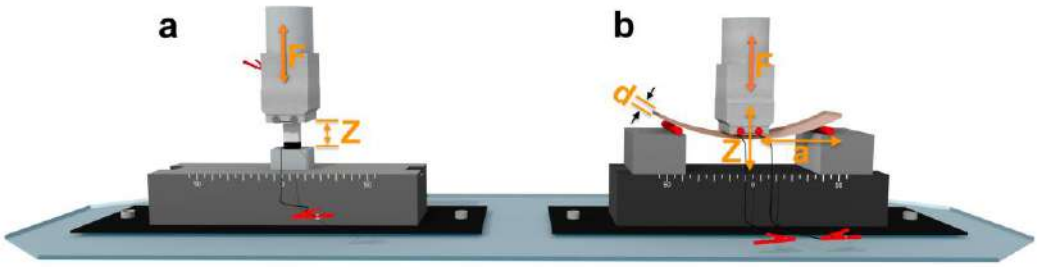

Figure 3.4.3. Schematic representation of the electromechanical measurements of the functional G/W and CNT/W composites. a) Cubic samples (volume of 1 cm^3) in compression mode up to a force of 50 N and b) 4-point-bending mode up to 5 mm deformation. The piezoresistive sensibility measured by the 4-point-bending method presents two contributions: the geometrical effect (1+2υ=1.74) and the intrinsic one that depends on the conductivity variation due to the fillers network reconfigurations [50].

3.4.3. Results and discussion

3.4.3.1. Morphological and thermal properties

The SEM surface images of the wax samples prepared by molding technique (3D) presents a homogeneous morphology, without the presence of voids or defects (Figure 3.4.4a). The same is observed in the cross-section SEM images for the corresponding CNT (Figure 3.4.4b and c) and rGO (Figure 3.4.4d (surface image), e, and f) composites. Thus, conductive fillers are homogeneously distributed in the wax host matrix by using ethanol for filler dispersion, as reported in the literature [37]. The solvent was then completely evaporated (boiling temperature ≈78 °C [51]) before wax melting (≈90 °C). This experimental procedure allows tailor novel composites with solid structure and homogeneous fillers dispersion, which is essential for the development of functional composites.

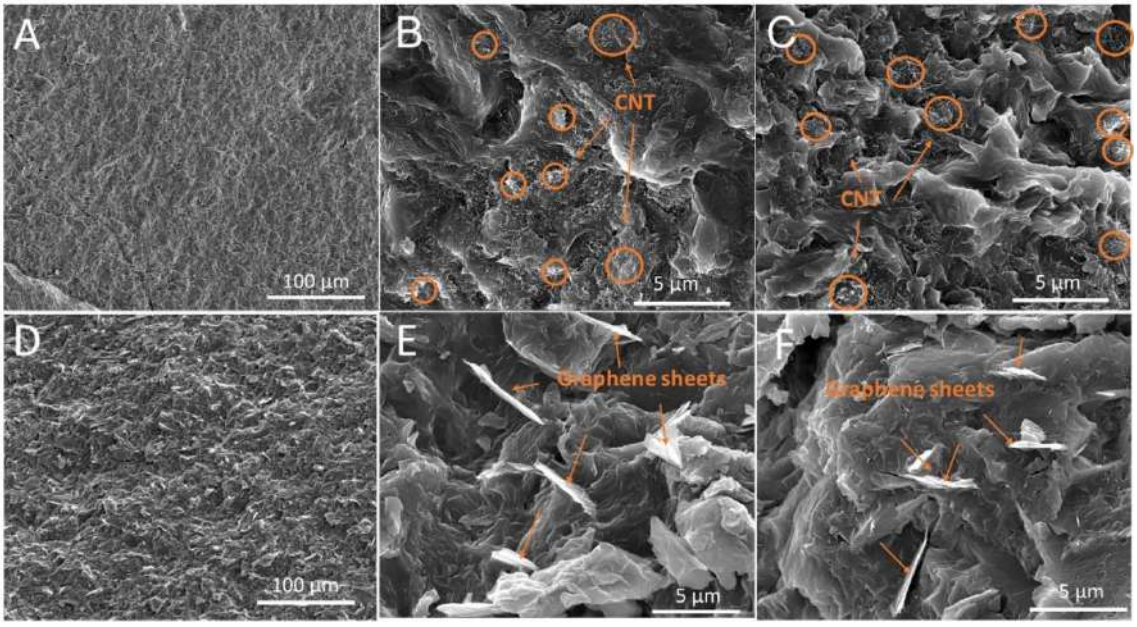

Figure 3.4.4. Representative SEM images of pristine wax a) and composites with CNT contents of 0.25 wt.% b) and 2 wt.% c) and rGO contents of 2 wt.% (d and e) and 25 wt.% f). a) and d) correspond to SEM surface images and b), c), e) and f) represent cross-section images of the samples. The magnifications used were 1 000× and 15 000×.

In fact, Figure 3.4.4b and c show that the CNT are dispersed within wax in small agglomerates. Graphene sheets show higher individual dispersion (Figure 3.4.4e and f) with smaller clusters, than for CNT composites (Figure 3.4.4b and c). The interwoven network of the bulk CNTs powder [37] is more difficult to disperse completely compared with the lower aspect ratio graphene oxide [52]. A similar degree of dispersion has been obtained independently of the filler content, for both fillers. Thus, an ultrasound bath of the filler/ethanol dispersion and mechanical stirring of the melt, represents a suitable procedure for the efficient dispersion of both fillers. The obtained results for CNTs and graphene dispersion are similar to the ones obtained in other polymer matrices [53].

The FTIR spectra of the wax composites are shown in Figure 3.4.5a. Pristine wax is composed by paraffin wax (50-60 %) and polyethylene resin (10-20 %), being the remaining dye material. The characteristic absorption peaks of the wax are shown in Figure 3.4.5a for wax and rGO or CNT composites for different filler contents.

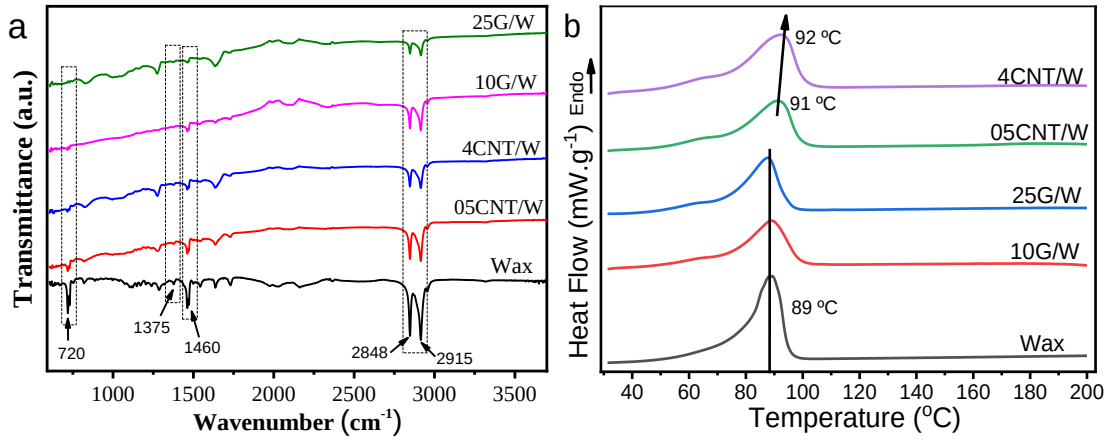

Figure 3.4.5. a) FTIR spectra and b) DSC thermograms for pristine wax and composites with 0.5 and 4 wt.% of CNT and 10 and 25 wt.% of rGO. Characteristic absorption bands of wax in the FTIR spectra are highlighted.

The characteristic absorption bands of wax are presented in Figure 3.4.5a, highlighting the most representative zones of interest [37]. The CH_2 and CH_3 stretching vibration are present at 2915 and 2848 cm^{-1}, respectively [37]. The in-plane bending vibration of CH_3 and CH_2 are identified at 1375 and 1460 cm^{-1}, respectively, and the rocking vibration of CH_2 at 720 cm^{-1} [37]. Composites with CNT and rGO does not lead to any shift in wavenumbers of the representative absorption bands of wax or in the appearance of new peaks, showing similar spectra than pristine wax excepting that the band intensities of the composites decrease with increasing filler contents [37]. Thus, no chemical interactions occur between the wax and the fillers.

The thermal properties of the wax and carbonaceous composites were evaluated by DSC thermograms (Figure 3.4.5b). The melting temperature (T_m) of the paraffin wax is at about 89 °C, being possible to range from between 40 to 60 °C for pure wax [30, 54] to higher temperature values depending on the polyethylene (PE) content (up to 20 %) in the final composition. Literature reports an increase from T_m ≈50 to 100 °C for the wax to wax/PE (60/40 weight percentage) blend [30]. It is to notice that the melting temperature of polyethylene is about T_m≈110 °C [30].

The melting temperature of the wax and the wax composites is similar, with variations within experimental error, independently of the filler content (Figure 3.4.5b). Nevertheless, it seems that a slight increase of the melting temperature of ≈2 to 3 °C occurs, with the inclusion of CNT. It has been reported that the thermal conductivity of wax composites shows a slight increase with increasing filler content [55], where the interfacial thermal resistance is a fundamental limitation of the thermal conductivity in insulator-

conductive composites [56]. The degradation behavior of wax is characterized by an onset temperature of 170 °C, a maximum rate degradation temperature at 250 °C and a full degradation at about 330 °C [37].

3.4.3.2. Mechanical and electrical properties

The mechanical properties under cyclic compression of the wax and wax composites reinforced with CNT or rGO for different applied forces up to 50 N present similar behaviors and are represented in Figure 3.4.6, for wax and 4CNT/W composites, as representative examples.

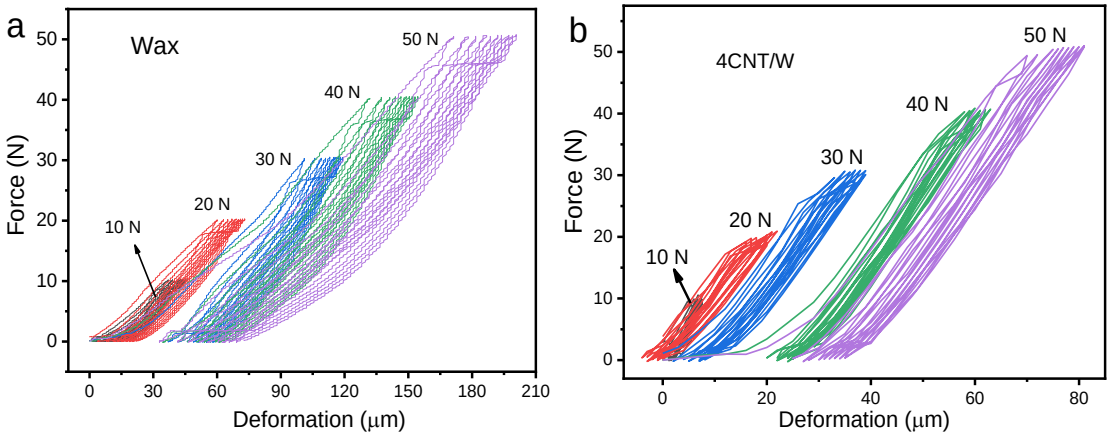

Figure 3.4.6. Illustration of the force-deformation characteristic mechanical curves under cyclic loading-unloading for wax (a) and for the 4CNT/W composite (b). Measurements were performed at several compression forces up to 50 N.

Wax and wax composites support forces up to 50 N, under continuous cyclic compression, without break, once they are ductile materials [57, 58]. The samples do not fully recover from each cycle, with the residual deformation increasing with increasing the number of cycles for each applied force, as it can be observed in Figure 3.4.6, indicative of plastic deformation. Increasing the maximum applied force from 10 to 50 N (corresponding from 0.1, to 0.5 MPa of stress, respectively) leads to an increase of the deformation from 30 to 200 μm (corresponding to 3 to 20 % of strain, respectively) and from 7 to 80 μm (corresponding to 0.7 and 8 % of strain, respectively) for wax and 4CNT/W composites, respectively. This represents an increase of the deformation from 3 to 20 % for wax and from 0.7 % to 8 % for the composite as a function of the applied force. The mechanical behavior is representative of the remaining composites,

the 25rGO/W sample having a higher tensile strength of about 10 % when compared to the 4CNT/W sample.

The current-voltage characteristics curves and the DC electrical conductivity of the composites reinforced with rGO and CNT are presented in Figure 3.4.7a and b, respectively, with the percolation threshold determined (inset in Figure 3.4.7b) for both type of fillers.

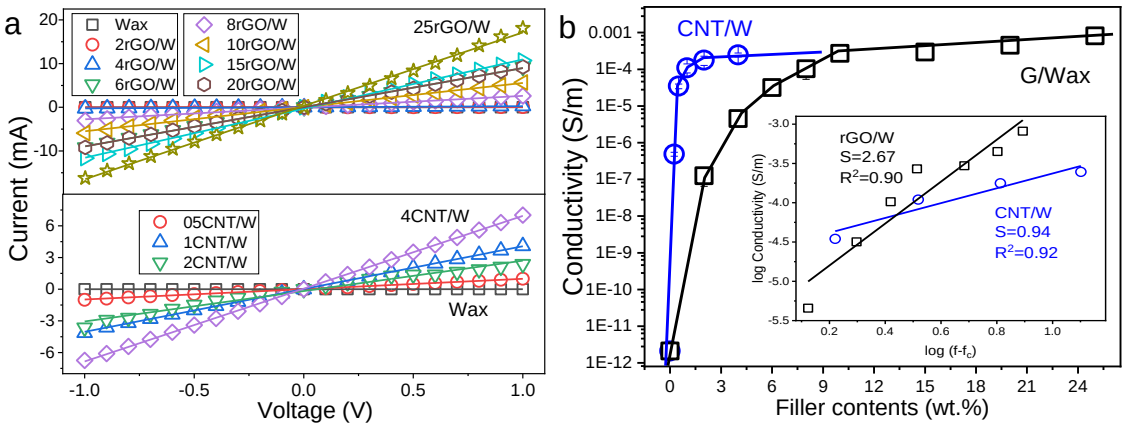

Figure 3.4.7. a) Characteristic I-V measurements of wax and the different wax composites with rGO (above) and CNT (below). b) Electrical conductivity of the wax composites reinforced with CNT and rGO up to 4 and 25 wt.%, filler content, respectively. Inset: determination of the percolation threshold.

Figure 3.4.7a shows that the current-voltage curves present a characteristic linear behavior for wax, CNT/W and rGO/W composites between -1 V to +1 V. The slope of the current-voltage curves increases with increasing filler content in the composite, as a consequence of the increased electrical conductivity, which shows a typical percolative behavior (Figure 3.4.7b) [59, 60]. The highest electrical conductivity values in polymer composites can range from 10^{-5} to 10^{2} $S.m^{-1}$, depending on materials, processing or filler contents [59, 60]. In the present work, the maximum electrical conductivity is 2.5×10^{-4} and 8.1×10^{-4} $S.m^{-1}$ for CNT and rGO filler contents of 3 and 20 wt.%, respectively.

The classic percolation threshold theory of the electrical conductivity (σ) as a function of filler content allows the determination of the percolation threshold for both composites, after equation 3.4.6 [61]:

$$\sigma = \sigma_0 (p - p_c)^s \tag{3.4.6}$$

where σ_0 is the filler conductivity, p the filler content, p_c the percolation threshold and s the universal critical exponent that depends on the system dimensionality, being 1 < s < 1.3 for a 2D network and 1.5

< s < 2 for a 3D network [61]. The experimental percolation threshold, similarly to the maximum conductivity, strongly depends on materials and processing conditions, being between 0.01 and 10 wt.% [60] for the large majority of polymer composites with high aspect ratio fillers. Larger aspect ratio and orientation of the fillers, functionalization, dispersion or aggregation have a strong influence on the electrical (also mechanical) properties [62].

Wax composites reinforced with CNT shows a lower percolation threshold near 0.3 wt.% that correspond to 0.29 volume percentage (vol%), whereas graphene composites show a higher percolation threshold near 3 wt.%, corresponding to 2.97 vol%. The obtained percolation threshold is in the order of the values obtained for related polymer-based composites [63]. Larger aspect ratio nanofillers lead to a decrease of the percolation threshold in wax composites, being in the typical range of related polymer composites [1, 60], CNT composites showing also lower percolation threshold compared to rGO composites [59]. The critical exponent depends on the system dimensionality, determined to be s = 1.33 or s = 2 for two or three dimensions, respectively [60]. In this work the critical exponent is s = 0.94 and 2.67 for CNT and rGO composites, respectively, corresponding to two dimensions for larger aspect ratio conductive fillers [27] and three dimensions for multilayer graphene [61, 64]. Literature, reports critical exponents between 1 and 4 for the large majority of composites [60], the value depending on filler type and dispersion. Filler dispersion into wax host matrix and intrinsic properties of the materials influences the electrical properties of the composites. SEM images (Figure 3.4.4) show a smaller CNT cluster and a higher individual dispersion of graphene into wax, which leads to the observed differences in the electrical response. Overall, CNT/wax composites show improved electrical properties and a lower threshold than rGO/wax composites.

3.4.3.3. Piezoresistive Properties

The piezoresistive response of the wax composites was evaluated under compression and bending modes, for molded (3D) and screen-printed (2D) samples, respectively. The piezoresistive sensibility was evaluated for composites with different filler contents: near the percolation threshold (0.5CNT/W) and for the highest filler contents (4CNT/W and 25rGO/W), as filler content is the main influence in the piezoresistive response of the composite [65].

The piezoresistive behavior of molded samples was tested under compression cycles and the screen-printed samples in 4-point-bending mode (Figure 3.4.8 and 3.4.9 respectively). Pressure sensibility (PS) and gauge factor (GF), calculated using equations 3.4.3 and 3.4.4, respectively, were used to quantify the piezoresistive sensitivity under compression and bending.

The electrical resistance variation under compressive 10 loading-unloading cycles for forces from 0 up to 10 to 50 N are similar for the composites, as shown in Figure 3.4.8a and b for the 05CNT/W and 25G/W composites, respectively.

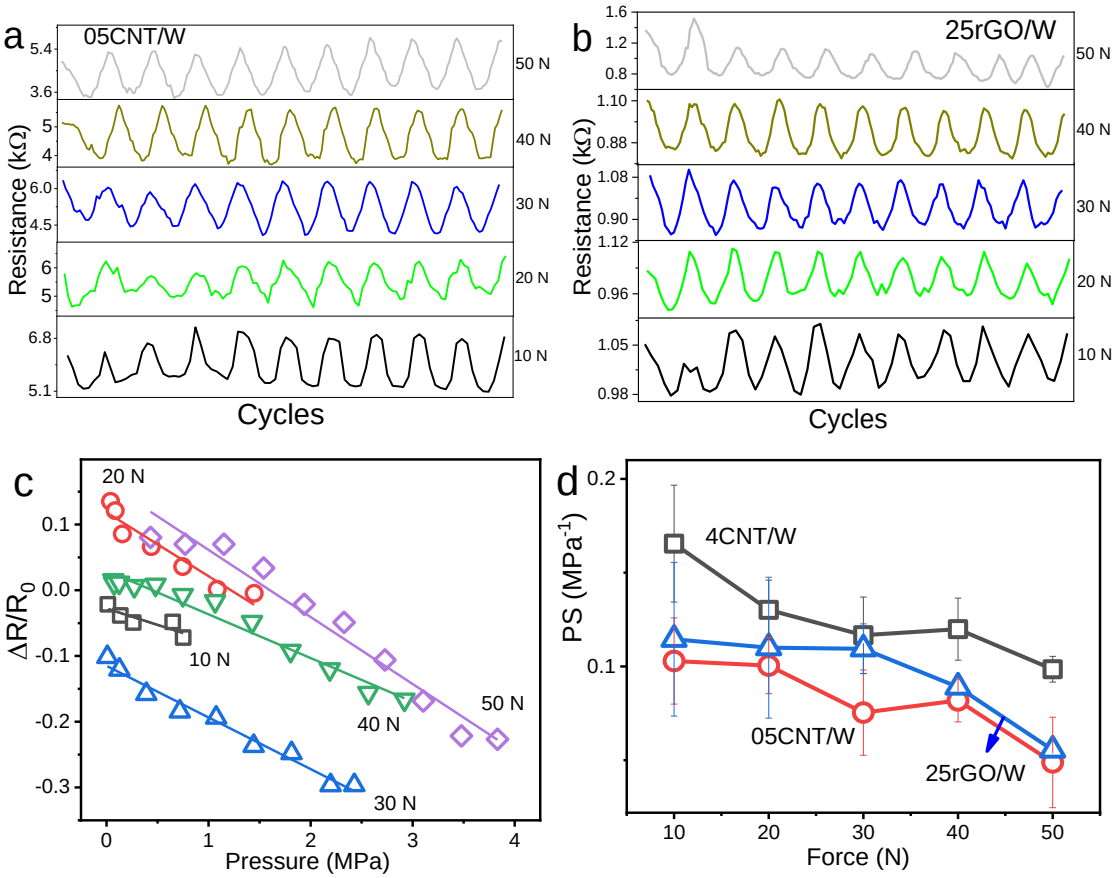

Figure 3.4.8. Piezoresistive response of the molded CNT/W and rGO/W composites. Compression cycles (10 cycles) for different applied maximum forces up to 50 N for a) 05CNT/W and b) 25rGO/W composites, respectively. Linearity of the electromechanical responses for (c) 05CNT/W and pressure sensibility (d) of the composites as a function of applied force, determined by average og the 10 cycles.

Figure 3.4.8a and b show that filler/wax composites can works perfectly as compression sensors up to an applied force of 50 N. CNT and rGO embedded into wax demonstrate linear piezoresistive properties under compression cycles (Figure 3.4.8c). The electrical resistance decreases with increasing pressure and returns to the initial resistance value when pressure is released, for different forces and reinforcement filler or filler content. The application of pressure leads to two factors contributing to the piezoresistive response of the material: geometrical contributions, due to the geometrical variation of the sample (thickness variation under applied compression), and intrinsic due to reconfiguration of the filler network. These two effects influence the electrical resistance, and consequently, the piezoresistive sensibility [29].

The sensibility of the materials, PS, is represented in Figure 3.4.8d, where it is observed a slight decrease of PS with increasing applied force. The 4CNT/W composite shows higher values for piezoresistive sensibility (0.17< PS < 0.1 MPa^{-1}) than the 05CNT/W or 25rGO/W samples (0.12 < PS < 0.05 MPa^{-1}) for both composites. All the presented values for sensibility are the average obtained over 10 cycles. The decrease of the piezoresistive response with increasing pressure, already reported for other composites [27], is attributed to the plastic deformation of the composites under compression cycles (it does not fully recover to the initial shape after pressure release, as demonstrated in Figure 3.4.6), and the electrical network created by the fillers into wax also present thus lower levels of reconfiguration under cycling. The PS performance is in line with related polymer composites, with sensibility in the order of MPa, being higher for lower applied pressure [27, 48, 66]. Larger pressure sensibilities can be obtained by further tailoring the morphology of the composites, such as porous microstructures or by varying the contact area [67].

The cycling stability (data not shown) of the samples was evaluated showing a stable and linear response for up to 100 cycles.

The suitability of the wax composites as sensor materials can be further explored for additive manufacturing, using screen-printing technique. The composite with 25 wt.% of rGO was screen-printed on Kapton, with excellent piezoresistive properties in bending mode for deformations up to 5 mm, as shown in Figure 3.4.9. Graphene composites show better viscosity for being screen-printed, without the use of solvents, reinforcing the environmentally friendly approach for sensor development.

Piezoresistive response is demonstrated in Figure 3.4.9a as a function of bending deformation up to 5 mm with excellent cycle response and stability as well as a suitable linear response between relative resistance change and deformation (Figure 3.4.9b).

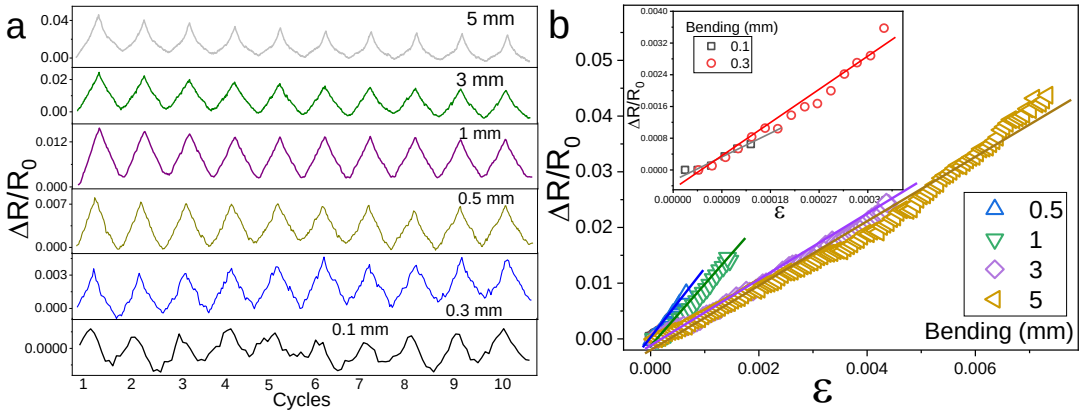

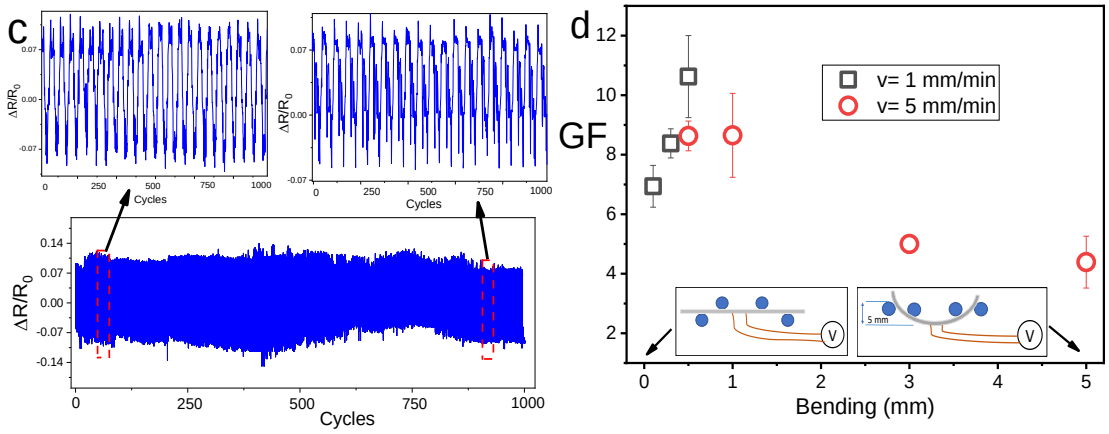

Figure 3.4.9. a) Piezoresistive bending response of the 25rGO/W samples for cycling deformations (10 cycles) from 0.1 to 5 mm and b) linear beahviour between strain (ε) and resistance changes ($\Delta R/R_0$). c) Cycling stability measurements for 1000 cycles at 5 mm of deformation (higlighted 25-30 cycles for the initial and the last cycles) and d) piezoresistive sensibility as a function of bending deformation up to 5 mm.

The graphene reinforcing wax composite presents excellent properties for functional sensing material and printability by screen printing. Linear behavior between bending and resistance change shows suitable linearity for deformations up to 5 mm and stability over cycling for 1000 cycles (Figure 3.4.9a-c). The piezoresistive sensibility under 4-point-bending (Figure 3.4.9d) is between $4.5 < GF < 11$, with excellent sensibility even for the lower deformations (0.1 mm). All the shown value is the average of the 10 cycles. This piezoresistive sensibility is up to 5 times larger than traditional strain gages (GF≈ 2 [12]) and larger than most composites using thermoplastic polymer matrices [68], but lower than for stretchable composites [68]. The piezoresistive sensibility has two main contributions: geometrical factor $(1 + 2\upsilon)$ and intrinsic resistivity change $(\frac{d\rho/\rho_0}{\varepsilon})$ (Equation 3). The geometrical factor is always present and depends on the Poisson coefficient ($\upsilon \approx 0.37$, for wax [43]) of the material. Thus, the piezoresistive geometrical contribution is about GF ≈1.75, meaning that intrinsic resistivity is the largest contribution of the piezoresistive response of the wax composites. Similar to compression tests, the resistance variations under cyclic bending are stable for at least 1000 cycles, maintaining the linear variation of the electrical resistance with the bending deformation (up to 5 mm). Together with the linearity and stability of the samples, the screen-printed 25rGO/wax composite printed over Kapton demonstrate excellent adhesion as demonstrated by standard peeling tests with adhesive tape in which no wax composite film is removed from the Kapton substrate.

The effect of the deformation speed in the piezoresistive response shows that the sensibility is higher for lower deformation speeds, decreasing from GF ≈11 to 9 with increasing deformation speed from 1 to 5

$mm.min^{-1}$, for the 0.5 mm bending test, as an example. Due to the viscoelastic characteristics of the composites, increasing deformation speeds lead to a lower recovery of the material to the original undeformed state, leading to lower variations per cycle of the conductive network, decreasing the sensibility of the material.

Thus, it is concluded that the developed functional wax composites show excellent piezoresistive sensibility, under compression and bending modes, being also suitable for printable applications.

3.4.4. Functional demonstration

The screen-printed 25rGO/W composite can be applied in a wide range of applications, from health care to structural health monitoring, when used at lower temperature ranges (up to 80 °C). One of the largest advantages of waxes are their simple processability conjugated with printed, that allows developing functional materials in a greener and precise form. Connected to an electronic system, it is demonstrated that the mechanical behavior of the material can be monitored in real-time through the resistance variation, as represented in Figure 3.4.10, where the bending cycles applied to the printed 25rGO/W sample are observed in the laptop computer.

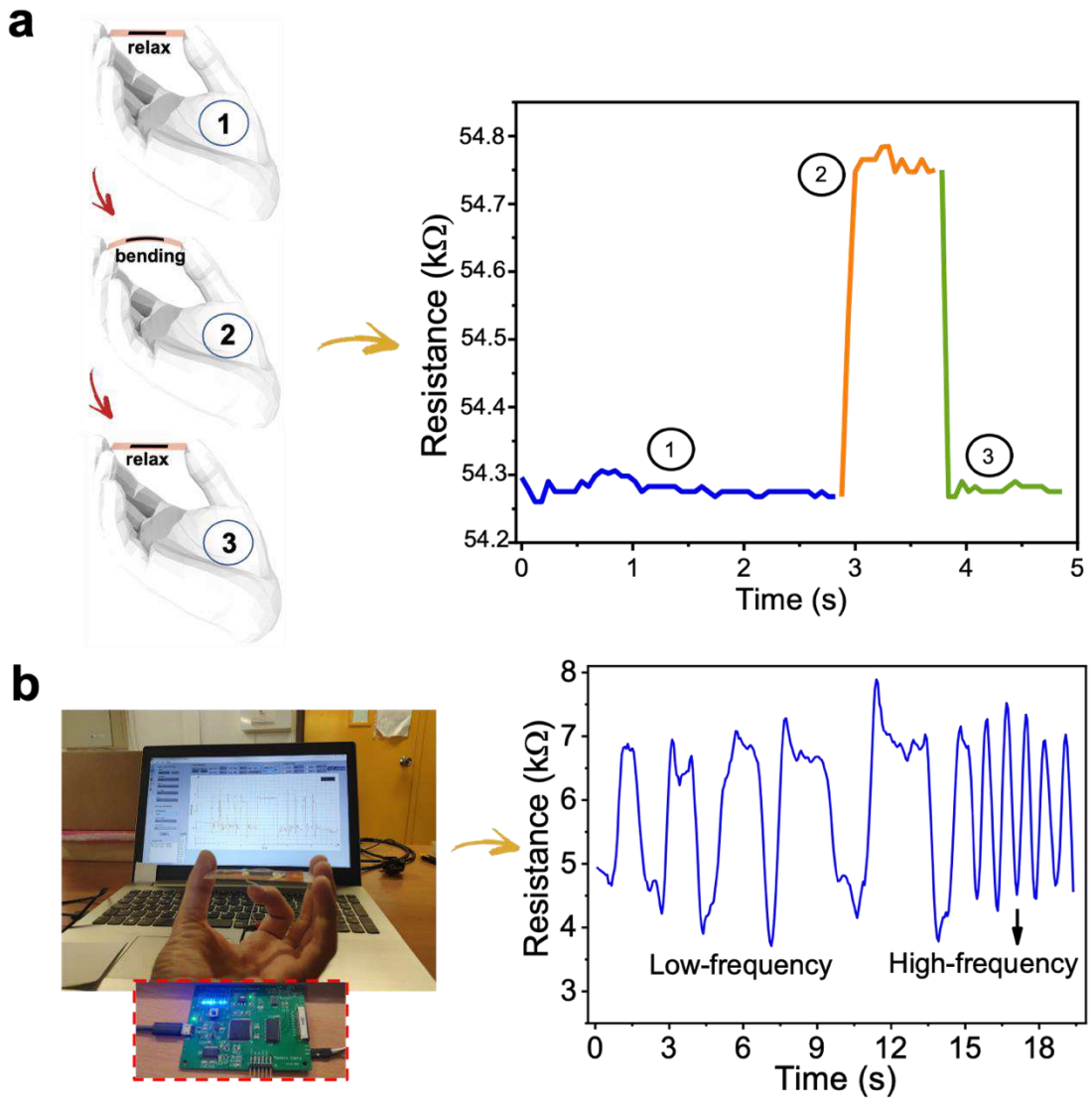

Figure 3.4.10. - a) Illustration of the wax composite working in the bending mode. b) Composite reinforced with 25 wt.% of graphene, processed by screen-printing, connected to the electronic circuit (left) measuring the bending stimulus applied to the sample (right).

The bending cycles on the sample are illustrated in Figure 3.4.10a, showing the resistance of the sample in the relaxed (1), bent (2) and relaxed (3) states. The developed readout electronic circuit (Figure 3.4.10b) relies on a voltage divider, composed of an appropriate reference resistance, which is determined by adjusting a digital potentiometer (Texas Instruments® TPL0501). An analog-to-digital converter present in the PIC32MX230F128L microcontroller from Microchip® is used to evaluate the voltage changes of the piezoresistive sensor, with prior system calibration on system power start-up. The voltage data points are kept in temporary memory. Furthermore, the electronic circuit allows USB communication through a serial port by using a USART-USB converter FT232RL from FTDI. The printed

sensors with 25 wt.% of rGO into the wax matrix works perfectly as bending deformation sensor, with large resistance changes between relaxed and bending modes, and present stable minimum and maximum resistance values (Figure 3.4.10c).

3.4.5. Conclusions

Wax is an outstanding environmentally friendly alternative as a host matrix for multifunctional composites, processable by additive manufacturing technologies. Wax reinforced with conductive nanocarbonaceous filler, including CNT and rGO, have been processed with suitable electrical, mechanical and electromechanical properties in compression and bending modes.

Composites have been prepared after filler dispersion in ethanol leading to good dispersion of the fillers. Composites with CNT show smaller agglomerates of about a few μm in diameter, which are smaller for the rGO composites. The aspect ratio and intrinsic conductivity of the CNT lead to a lower electrical percolation threshold (about 0.3 wt.%) when compared to rGO (about 3 wt.%) composites, with electrical conductivity values of the order of 10^{-4} $S.m^{-1}$ for both composites.

Cycling forces up to 50 N and bending deformations up to 5 mm are supported by the wax composites which show a high piezoresistive sensing response with excellent linearity and piezoresistive sensibility, being obtained GF from 4.5 to 11 in the bending mode and PS from 0.05 to 0.17 MPa^{-1} in the pressure mode, for screen-printed and molded samples, respectively. The composites also present a stable electrical resistance variation under continuous cycling.

Finally, an electronic system was developed to demonstrate the applicability of the materials on real-time bending deformations monitoring.

The stable response and larger resistance changes under deformation, together with the environmental-friendly processing (without the use of solvents) by printing or molding technologies, turn these composite materials an excellent alternative for a broad range of applications.

3.4.6. References

[1] Deng, H., et al., Progress on the morphological control of conductive network in conductive polymer composites and the use as electroactive multifunctional materials, Progress in Polymer Science 2014, 39(4): 627-655.

[2] Oliveira, J., et al., Polymer-based smart materials by printing technologies: Improving application and integration, Additive Manufacturing 2018, 21: 269-283.

[3] Chen, W. Yan, X., Progress in achieving high-performance piezoresistive and capacitive flexible pressure sensors: A review, Journal of Materials Science & Technology 2020, 43: 175-188.

[4] X. Hu., et al., Highly Stretchable Self-Healing Nanocomposite Hydrogel Reinforced by 5 nm Particles, ES Materials & Manufacturing 2018, 2: 16-23.

[5] Chung, D.D.L., et al., A review of multifunctional polymer-matrix structural composites, Composites Part B: Engineering 2019, 160: 644-660.

[6] Chen, J., et al., Recent Progress on Thermo-electrical Properties of Conductive Polymer Composites and Their Application in Temperature Sensors, Engineered Science 2020, 12: 13-22.

[7] L. Duan., D.R. D'Hooge., L. Cardon., Recent progress on flexible and stretchable piezoresistive strain sensors: From design to application, Progress in Materials Science 2019, 114: 100617.

[8] Lyu, L., et al., Overview of Electrically Conductive Polymer Nanocomposites toward Electromagnetic Interference Shielding, Engineered Science 2018, 2: 26-42.

[9] Zhang, D., et al., Overview of Ultrasonic Assisted Manufacturing Multifunctional Carbon Nanotube Nanopaper Based Polymer Nanocomposites, Engineered Science 2020, 10: 35-50.

[10] Zhou, L.-Y., Fu, J., He, Y., A Review of 3D Printing Technologies for Soft Polymer Materials, Advanced Functional Materials 2020, 30(28): 2000187.

[11] Castro, H.F., et al., Printed Wheatstone bridge with embedded polymer based piezoresistive sensors for strain sensing applications, Additive Manufacturing 2018, 20: 119-125.

[12] Costa, P., et al., Piezoresistive polymer blends for electromechanical sensor applications, Composites Science and Technology 2018, 168: 353-362.

[13] Singh, K., et al., Significance of nano-materials, designs consideration and fabrication techniques on performances of strain sensors - A review, Materials Science in Semiconductor Processing 2021, 123: 105581.

[14] Jiang, X., et al., Flexible conductive polymer composite materials based on strutted graphene foam, Composites Communications 2021, 25: 100757.

[15] Bekas, D.G., et al., 3D printing to enable multifunctionality in polymer-based composites: A review, Composites Part B: Engineering 2019, 179: 107540.

[16] George, M., et al., Long-term thermophysical behavior of paraffin wax and paraffin wax/polyaniline (PANI) composite phase change materials, Journal of Energy Storage 2020, 31: 101568.

[17] Song, W.-L., et al., Highly ordered porous carbon/wax composites for effective electromagnetic attenuation and shielding, Carbon 2014, 77: 130-142.

[18] Fiorillo, A.S., Critello, C.D., Pullano, S.A., Theory, technology and applications of piezoresistive sensors: A review, Sensors and Actuators A: Physical 2018, 281: 156-175.

[19] Yang, L., et al., One-pot preparation of porous piezoresistive sensor with high strain sensitivity via emulsion-templated polymerization, Composites Part A: Applied Science and Manufacturing 2017, 101: 195-198.

[20] L. Cheng, W., et al., A highly sensitive piezoresistive sensor with interlocked graphene microarrays for meticulous monitoring of human motions, Journal of Materials Chemistry C 2020, 8(33): 11525-11531.

[21] S. Li, R., et al., Highly sensitive and flexible piezoresistive sensor based on c-MWCNTs decorated TPU electrospun fibrous network for human motion detection, Composites Science and Technology 2021, 203: 108617.

[22] Park, B., et al., Dramatically Enhanced Mechanosensitivity and Signal-to-Noise Ratio of Nanoscale Crack-Based Sensors: Effect of Crack Depth, Advanced Materials 2016, 28(37): 8130-8137.

[23] He, Y., et al., A breathable, sensitive and wearable piezoresistive sensor based on hierarchical micro-porous PU@CNT films for long-term health monitoring, Composites Science and Technology 2020, 200: 108419.

[24] Aceto, G., Persico, V., Pescapé, A., Industry 4.0 and Health: Internet of Things, Big Data, and Cloud Computing for Healthcare 4.0, Journal of Industrial Information Integration 2020, 18: 100129.

[25] Lu, Y., Industry 4.0: A survey on technologies, applications and open research issues, Journal of Industrial Information Integration 2017, 6: 1-10.

[26] Kholghi Eshkalak, S., et al., A review on inkjet printing of CNT composites for smart applications, Applied Materials Today 2017, 9: 372-386.

[27] Dios, J.R., et al., Piezoresistive performance of polymer-based materials as a function of the matrix and nanofiller content to walking detection application, Composites Science and Technology 2019, 181: 107678.

[28] Ng, L.W.T., et al., Conformal Printing of Graphene for Single- and Multilayered Devices onto Arbitrarily Shaped 3D Surfaces, Advanced Functional Materials 2019, 29(36): 1807933.

[29] Gonçalves, B.F., et al., Development of water-based printable piezoresistive sensors for large strain applications, Composites Part B: Engineering 2017, 112: 344-352.

[30] T.P. Gumede, A.S., et al., Plasticization and cocrystallization in LLDPE/wax blends, Journal of Polymer Science Part B: Polymer Physics 2016, 54(15): 1469-1482.

[31] Tinto, W.F., et al., Chapter 22 - Waxes, in: S. Badal, R. Delgoda (Eds.), Pharmacognosy, Academic Press, Boston, 2017, pp. 443-455.

[32] Zhang, K., Han, B., Yu, X., Electrically conductive carbon nanofiber/paraffin wax composites for electric thermal storage, Energy conversion and management 2012, 64: 62-67.

[33] Cui, Y., et al., The experimental exploration of carbon nanofiber and carbon nanotube additives on thermal behavior of phase change materials, Solar Energy Materials and Solar Cells 2011, 95(4): 1208-1212.

[34] Cao, Z., et al., Physical wrapping of reduced graphene oxide sheets by polyethylene wax and its modification on the mechanical properties of polyethylene, Journal of Applied Polymer Science 2012, 126(5): 1546-1555.

[35] Brito-Pereira, R., et al., Reconfigurable 3D-printable magnets with improved maximum energy product, Journal of Materials Chemistry C 2020, 8(3): 952-958.

[36] Altundemir, S., Uguz, A.K., Ulgen, K. Ulgen., A review on wax printed microfluidic paper- based devices for international health, Biomicrofluidics 2017, 11(4): 041501.

[37] Han, L., et al., Effective Encapsulation of Paraffin Wax in Carbon Nanotube Agglomerates for a New Shape-Stabilized Phase Change Material with Enhanced Thermal-Storage Capacity and Stability, Industrial & Engineering Chemistry Research 2018, 57(39): 13026-13035.

[38] Liu, M., Zhang, C., Liu, F., Understanding wax screen-printing: a novel patterning process for microfluidic cloth-based analytical devices, Analytica chimica acta 2015, 891: 234-246.

[39] Wang, S., et al., Based chemiluminescence ELISA: lab-on-paper based on chitosan modified paper device and wax-screen-printing, Biosensors and bioelectronics 2012, 31(1): 212-218.

[40] Raoufi, M.A., et al., Fabrication of unconventional inertial microfluidic channels using wax 3D printing, Soft Matter 2020, 16(10): 2448-2459.

[41] Chi, J., et al., 3D Printing of Self-Organizing Structural Elements for Advanced Functional Structures, Advanced Materials Technologies 2018, 3(5): 1800003.

[42] Kyobula, M., et al., 3D inkjet printing of tablets exploiting bespoke complex geometries for controlled and tuneable drug release, Journal of Controlled release 2017, 261: 207-215.

[43] Mann, A., C.M. Bürgel., P. Groche., A Modeling Strategy for Predicting the Properties of Paraffin Wax Actuators, Actuators 2018, 7(4): 81.

[44] Guo, Z.H., et al., Stretchable Textile Rechargeable Zn Batteries Enabled by a Wax Dyeing Method, Advanced Materials Technologies 2020, 5(11): 2000544.

[45] Chiang, C.-K., Kurniawan, A., Kao, C.-Y., Single step and mask-free 3D wax printing of microfluidic paper-based analytical devices for glucose and nitrite assays, Talanta 2019, 194: 837-845.

[46] Franco, M., et al., Water-Based Graphene Inks for All-Printed Temperature and Deformation Sensors, ACS Applied Electronic Materials 2020, 2(9): 2857-2867.

[47] Arboleda, L., et al., Piezoresistive response of carbon nanotubes-polyamides composites processed by extrusion, Journal of Polymer Research 2013, 20(12): 326.

[48] Vicente, J., et al., Electromechanical Properties of PVDF-Based Polymers Reinforced with Nanocarbonaceous Fillers for Pressure Sensing Applications, Materials 2019, 12(21): 3545.

[49] Ferreira, A., et al., Relationship between electromechanical response and percolation threshold in carbon nanotube/poly (vinylidene fluoride) composites, Carbon 2013, 61: 568-576.

[50] Costa, P., et al., Polymer Nanocomposite-Based Strain Sensors with Tailored Processability and Improved Device Integration, ACS Applied Nano Materials 2018, 1(6): 3015-3025.

[51] Manzetti, S., et al., Methods for dispersing carbon nanotubes for nanotechnology applications: liquid nanocrystals, suspensions, polyelectrolytes, colloids and organization control, International Nano Letters 2019, 9(1): 31-49.

[52] Wu, N., et al., Synthesis of network reduced graphene oxide in polystyrene matrix by a two-step reduction method for superior conductivity of the composite, Journal of Materials Chemistry 2012, 22(33): 17254-17261.

[53] Ke, K., et al., Boosting electrical and piezoresistive properties of polymer nanocomposites via hybrid carbon fillers: A review, Carbon 2021, 173: 1020-1040.

[54] Mochane, M.J., Luyt, A.S., The effect of expanded graphite on the thermal stability, latent heat, and flammability properties of EVA/wax phase change blends, Polymer Engineering & Science 2015, 55(6): 1255-1262.

[55] Fredi, G., et al., Wax Confinement with Carbon Nanotubes for Phase Changing Epoxy Blends, Polymers 2017, 9(9): 405.

[56] Jakubinek, M.B., et al., Temperature dependence of thermal conductivity enhancement in single-walled carbon nanotube/polystyrene composites, Applied Physics Letters 2010, 96(8): 083105.

[57] Lee, R.S., et al., Mechanical properties of a composite wax model material simulating plastic flow of metals, Journal of Mechanical Working Technology 1984, 9(3): 301-312.

[58] Aleksandrova, E.A., e t al., Structural and Mechanical Properties of Paraffin Wax Composites, Chemistry and Technology of Fuels and Oils 2018, 54(1): 37-43.

[59] Punetha, V.D., et al., Functionalization of carbon nanomaterials for advanced polymer nanocomposites: A comparison study between CNT and graphene, Progress in Polymer Science, 2017, 67: 1-47.

[60] Bauhofer, W., Kovacs, J.Z., A review and analysis of electrical percolation in carbon nanotube polymer composites, Composites Science and Technology 2009, 69(10): 1486-1498.

[61] C. Bessaguet., et al., Electrical behavior of a graphene/PEKK and carbon black/PEKK nanocomposites in the vicinity of the percolation threshold, Journal of Non-Crystalline Solids 2019, 512: 1-6.

[62] Sahoo, N.G., et al., Polymer nanocomposites based on functionalized carbon nanotubes, Progress in Polymer Science 2010, 35(7): 837-867.

[63] Li, Y., et al., A review of the electrical and mechanical properties of carbon nanofiller-reinforced polymer composites, Journal of Materials Science 2019, 54(2): 1036-1076.

[64] Du, J., et al., Comparison of electrical properties between multi-walled carbon nanotube and graphene nanosheet/high density polyethylene composites with a segregated network structure, Carbon 2011, 49(4): 1094-1100.

[65] Ferrreira, A., et al., Electromechanical performance of poly(vinylidene fluoride)/carbon nanotube composites for strain sensor applications, Sensors and Actuators A: Physical 2012, 178: 10-16.

[66] Huang, J., et al., Flexible electrically conductive biomass-based aerogels for piezoresistive pressure/strain sensors, Chemical Engineering Journal 2019, 373: 1357-1366.

[67] He, J., et al., Recent advances of wearable and flexible piezoresistivity pressure sensor devices and its future prospects, Journal of Materiomics 2020, 6(1): 86-101.

[68] Duan, L., D'Hooge, D.R., Cardon, L., Recent progress on flexible and stretchable piezoresistive strain sensors: From design to application, Progress in Materials Science 2020, 114: 100617.

Chapter 4.

Validation of the developed technologies and materials for PADs applications

4.1. Wax printed magnetic origami paper as a platform for low cost disease multi-tool detection

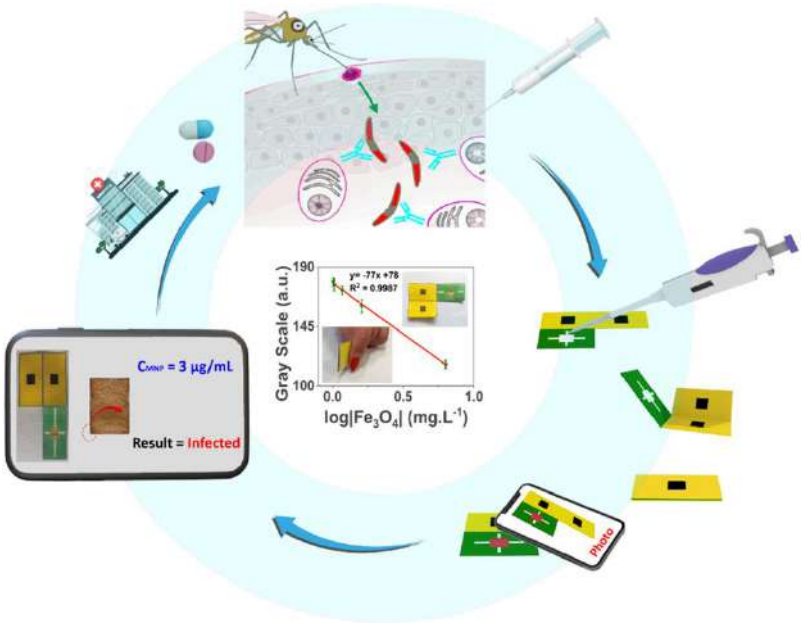

Infectious diseases kill over 10 million people each year. In low-resource locations, accurate and mechanically robust diagnostics platforms are crucial tools for detecting those who are in danger or need medical assistance. Nanomaterials, in particular magnetic nanoparticles, are playing increasingly important roles in such point-of-care testing platforms due to their specific and tunable magnetic properties. In this chapter, it is shown a printed magnetic origami paper for low cost infectious disease detection, based on Fe_3O_4 superparamagnetic nanoparticles (used as a magnetic model due to their magnetic properties). The μPAD is composed of two wax/NdFeB magnets, four hydrophilic channels, and a hydrophilic analysis rectangle, surrounded by hydrophobic wax. The flexibility, printability, low cost, sustainability, and multi-analysis possibilities of the developed platform foretell good possibilities in the realization of economically fair, user-friendly, mechanically robust and bendable, machinery-free, fast, accurate, precise, and highly specific multifunctional platforms for biomedical applications.

This chapter is based on following publication: R. Brito-Pereira, C. Ribeiro, A. Garcia Diez, C. Klapperich, P. Martins and S. Lanceros-Méndez, Printed magnetic origami paper as platform for low cost disease multi-tool detection: a chief weapon of offence (Submitted).

4.1.1. Introduction

In 1906, Sir William Osler, one of the more important founders of contemporary medicine, pointed out: "Diagnosis, not drugging, is our chief weapon of offence against infectious diseases" [1,2]. Such infectious diseases refer to transmissible illnesses that are caused by infectious pathogens, such as bacteria, viruses, fungi, and parasites, and are one of the major issues for global public health, being responsible for millions of mortalities each year, most of which occur in developing countries [3]. During the past decades, several severe viral infectious diseases, including influenza A (H1N1) flu, severe acute respiratory syndrome, Ebola hemorrhagic fever, Middle East respiratory syndrome, and Zika virus disease, have broken out in succession and made a huge impact to human health. Most recently, the coronavirus disease pandemic, caused by SARS-CoV-2, spread globally [4,5]. As of november 1st of 2022, it has caused more than 635 million infection cases and 6.6 million deaths worldwide (data obtained from https://www.worldometers.info/coronavirus/).

In the fight against such infectious diseases, and as anticipated by Sir William Osler more than a century ago, accomplishing a sensitive and well-timed diagnosis is imperative to allow a knowledgeable choice regarding the treatment procedure [6]. Thus, a fast and precise diagnosis will allow specialists not only to propose the appropriate medical procedure, but also significantly increases the quality of the overall patient prognosis [7]. In the particular case of highly infectious diseases, a fast diagnosis procedure is even more decisive once it can decrease the probability or even prevent supplementary infection within the population in contact with the infected individuals [8]. In this scenario, the WHO has highlighted the seriousness of μPADs, presenting a set of criteria for the selection of those POC platforms. Such conceptual requirements are abridged on the acronym ASSURED (Affordable, Sensitive, Specific, User-Friendly, Robust and rapid, Equipment free, Deliverable), that embodies the main characteristics needed for a suitable μPADs [9].

In general terms, a POC platform is designed to detect (either qualitatively or quantitatively) the presence of a specific biomarker characteristic of the malady at stake [1,10]. Most of the biomarker targets for infectious diseases can be grouped into three key categories [11]: i) pathogen genomics; ii) carbohydrate and protein antigens that have been produced by a certain pathogen; and iii) human immune response a certain infection, namely the pathogen-specific antibodies [1,12].

When it is intended to broaden the range of effective μPADs platforms, biomedical sensors should be produced with pre-defined characteristics. First, they must be capable to quantitatively identify specific biomarkers in complex environments such as mimetized fluids, feces, sputum, blood, or environmental

media, such as water and/or food [9]. Additionally, operational troubles can emerge when the non-trivial pathogenesis processes experienced by a high number of pathogens, such as parasites, bacteria, or viruses are taken into account. The different infectious agents that usually remain in the feces, sputum or blood can exhibit different stay times in these environments and/or can produce the respective biomarkers at distinct stages of their subsistence.

In this way, the ideal biomedical sensor is the one that can be tailored for several biomarkers, allowing it to sense numerous infectious agents during several stages in their entire life cycle. Moreover, μPADs diagnostic platforms should to be easily operated with no training (or at least with minimal preparation) in an application environment that that does not has a fully-equipped laboratory [9].

There are many different approaches for developing such diagnostic platforms, but the most effective are optical-, electrochemical-, magnetic-, and colorimetric-based modalities [9]. Those that are based in magnetic nanoparticles possess some advantages, being the signal quality (test opacity or biological interfects rarely obstruct/hinder the nanoparticle's response) the most relevant [1,13]. Additionally, magnetic nanoparticles can be custom-made to selectively bind/concentrate the biomarkers from their complex environment thought magnetic actuation, thus preventing signal contamination [14,15]. Traditionally, they are based on magnetic elements in their core such as magnetite, neodymium, nickel, manganese or iron, that are functionalized with biomolecules for a high variety of bioanalytical and biotechnology applications, being modified with specific receptors, using surface chemical groups such as epoxy, carboxyl, amine, or tosyl, for the identification/isolation of biomarkers including whole organisms, proteins and peptides, antibodies, and DNA, among others [1,16]. In the malaria's particular case, the magnetic detection does not require the use of functionalized magnetic nanoparticles due to the magnetic properties of disposal product made from the digestion of blood by some blood-feeding parasites [17,18].

Briefly, during the intraerythrocytic growth cycle of such malaria-related parasites and, upon haemoglobin's catabolism, free haem molecules are produced. With the objective to reduce the ferric iron's oxidative toxicity, the free haem structures are then polymerized into beta-haematin (a biomineral usually called haemozoin). Those haemozoin crystals exhibit a paramagnetic behaviour, and such characteristic can be used for the magnetic separation of late-stage parasites once they enclose bigger haemozoin biocrystals than both uninfected cells and early-stage parasites [17]. For such antibody-mediated cell separation, purification, and concentration, commercially available magnets have been successfully used [17]. So, in a global way, μPADs that are able to detect/quantify magnetic nanostructures can be used in the recognition of several diseases, either in the direct detection of the

magnetoactive waste deposits or by the use of magnetic particles that link to specific biomarkers [1,17,19,20]. From all magnetic nanostructures and due to its high saturation magnetization, reduced or zero value coercive field, water-dispersity, negligible toxicity, and capability of being surface functionalized with a high range of biomolecules that allow the linking with a high variety of biomarkers, Fe_3O_4 assumed itself as a suitable magnetic model to be used in such μPAD [21-24].

In this scenario, the present work proposes to validate a printed μPAD (Figure 4.1.1), by using paper substrates, hydrophobic & magnetic inks, and Fe_3O_4@H_2O suspensions as magnetic model. The detection and quantification of the magnetic entities will be made by 4 different approaches: i) infrared spectroscopy; ii) energy-dispersive X-ray spectroscopy; iii) vibrating sample magnetometry; and iv) color change (greyscale) on photographs taken by mobile phones.

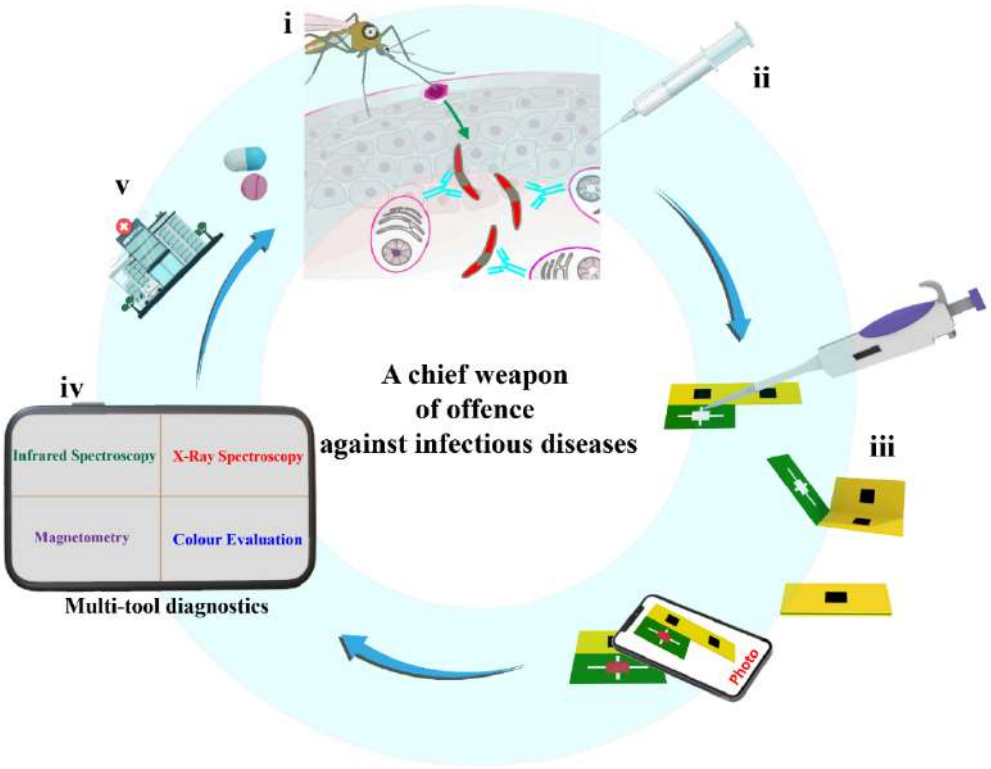

Figure 4.1.1. Proposed working principle of the printed magnetic origami portable analytical system applied to malaria: i) the infected mosquito bites a person; ii) a blood sample is collected from the person; iii) a few blood drops are placed on the testing rectangle and the printed magnets (black rectangles) concentrate the haemozoin crystals exhibiting a paramagnetic behaviour; iv) the detection of haemozoin crystals can be performed through four different techniques (Infrared spectroscopy; X-ray spectroscopy, Magnetometry, and Color evaluation); and v) the person who was bitten is free to go (in the case of a negative test) or referred for medical treatment (in the case of a positive test).

In the interest of providing portable, sustainable, environmentally friendly and low cost medical capabilities in low resource settings, this proof-of-concept study will use:

i) paper substrates (cellulose is one of the most widely used, inexpensive, and commonly available materials, with excellent biocompatibility [25-27]);

ii) printing technologies allowing the production of μPAD with waste reduction, scalable fabrication, and high design and manufacturing freedom [28-31];

iii) among the different inks and printing technologies, wax printing method [32,33] was chosen due to its high throughput fabrication and low technological needs to print complex three or two-dimensional (3D or 2D) structures for multipurpose systems, and also to the hydrophobic properties of wax;

iv) printed NdFeB swarf-based magnets in replacement of the traditional magnets used in POC devices (it was estimated that $1,3\times10^8$ to $1,5\times10^8$ kilograms of NdFeB magnets are produced per year globally, and 6–73 % of the magnet materials are wasted as swarf or powders [34,35]);

v) Fe_3O_4 nanoparticles due to its high chemical stability, biocompatibility, low toxicity in human body, low sensitivity to oxidation, stable ferromagnetic response, and green-synthesis possibility [24,36-39];

vi) mobile phone-based diagnostics aiming to ensure tools that are safe, cost-effective, and user-friendly (today, the images obtained by mobile phones, particularly smartphones, can achieve resolution sufficient to image cells with below 10-μm resolution and even bacteria, providing a cost-effective alternative to traditional microscopic techniques due to their ubiquity) [40,41].

4.1.2. Methods

4.1.2.1. Materials and reagents

Whatman n°1 cellulose paper (≈100 μm thick) was purchased from Sigma-Aldrich (Missouri,USA). NdFeB crushed ribbon powder/swarf, MQFP-15-7 (D50= 5 μm)-Reference number 20065-089, was obtained from Magnequench GmbH (Tübingen, Germany). Wax cartridges were obtained from Xerox Corporation (Connecticut, USA).

$FeCl_3{\cdot}6H_2O$ (99 %), $FeCl_2{\cdot}4H_2O$ (99 %), sodium oleate (82%), aqueous NH_4OH solution (28-30 %), concentrated NH_3, cyclohexane (99.8%), and pure ethanol (99%) were obtained from Sigma-Aldrich (Missouri, USA). Ethanol (96%) was purchased from Carlo Erba (Barcelona, Spain). All materials were used as received from the providers.

4.1.2.2. Fabrication and preparation

4.1.2.2.1. Synthesis of Fe_3O_4 nanoparticles

The Fe_3O_4 nanoparticles were synthesized using a previously optimized method as reported elsewhere [42]. In short, $14x10^{-3}$ mol of Fe^{3+} precursor and $8\ x10^{-3}$ mol of Fe^{2+} precursor were dissolved in 10 mL of ultrapure H_2O (Milli-Q). A 10 mL solution with 0.5 g of sodium oleate was then slowly added, step that was succeeded by a quick addition of 15 mL of concentrated NH_3 solution. The hydrothermal cure was performed at 200 °C for 24 hours. The treatment's product was collected through decantation, meticulously washed with ultrapure H_2O (Milli-Q) and finally dried at room-temperature (≈25 °C) for 12 hours at ≈80 kPa. The resulting dry powder was once more dispersed in cyclohexane and centrifuged at 3000 rpm for 10 minutes, being then observed the precipitation of the Fe_3O_4 nanoparticles. The centrifuged Fe_3O_4 nanoparticles were dried at room-temperature (≈25 °C) for 12 hours at ≈80 kPa and, finally, homogenized in an agate mortar through the use of a pestle.

4.1.2.2.2. Fe_3O_4@H_2O testing suspensions:

In order to evaluate the concept proposed in this work, five different mixtures of Fe_3O_4 and H_2O were produced (with Fe_3O_4 concentrations of 0.8 $mg.ml^{-1}$; 0.2 $mg.ml^{-1}$; 0.05 $mg.ml^{-1}$; 0.0125 $mg.ml^{-1}$; and 0.003125 $mg.ml^{-1}$) by adding the desired content of Fe_3O_4 into 10 ml of ultrapure H_2O (Milli-Q). The mixture was homogenized within a Vortex (Vortex Genie 2, Scientific Industries).

4.1.2.2.3. Printing of the magnetic origami portable analytical system (MOPAS)

Magnetic Ink Preparation: For the preparation of the wax/NdFeB ink, the NdFeB particles were first added (85 wt.%) to pure ethanol (5 mL) and the mixture was placed into an ultrasonic bath for 3 h to ensure proper dispersion and to avoid agglomeration between NdFeB particles (Figure 4.1.2a-d).

Afterwards, the previously cut Xerox wax (45 g) was added to the mixture (to obtain final NdFeB weight percentage -wt.% of 85) and placed inside an oven (JP Selecta, Model 2000208) for 30 min at a temperature of 120 °C, ensuring polymer melting and full solvent's evaporation.

The mixture was then removed from the oven, placed on a hot plate (Prazitherm P272) at a temperature of ≈120 °C and mixed for 1 hour with the help of a mechanical Teflon stirrer to ensure a high homogeneity on the wax/NdFeB mixture. Finally, the melted mixture was poured into a homemade aluminum mold, specifically shaped (159 mm x 133 mm x 44 mm) and manufactured to be compatible with a commercial

wax printer (Xerox ColorQube 8880). The mixture was allowed to cool down to room temperature (25 °C, ≈10 minutes) to solidify in the required shape. Then, the mould was disassembled, being the developed magnetoactive cartridge ready to be introduced into the printer. The MOPAS (Figure 4.1.2e-g) design was created using computer-assisted design software (Sketchup 2017) and printed with a Xerox ColorQube 8880 printer (during the printing procedure the cartridge is at 120 °C). After printing, the samples were placed on a hot plate (Prazitherm P272) for a thermal cure at 80 °C or 30 °C for 2 minutes, allowing the wax to penetrate the paper substrates all the way through till the opposing surface, and creating the walls required for the fluids to flow by capillary action on the hydrophilic paper substrates.

Finally, the wax/NdFeB magnets of the MOPAS were magnetized at 50 °C for 2 hours on an ADE 3473–70 Technologies VSM (DC magnetic field = 2 T).

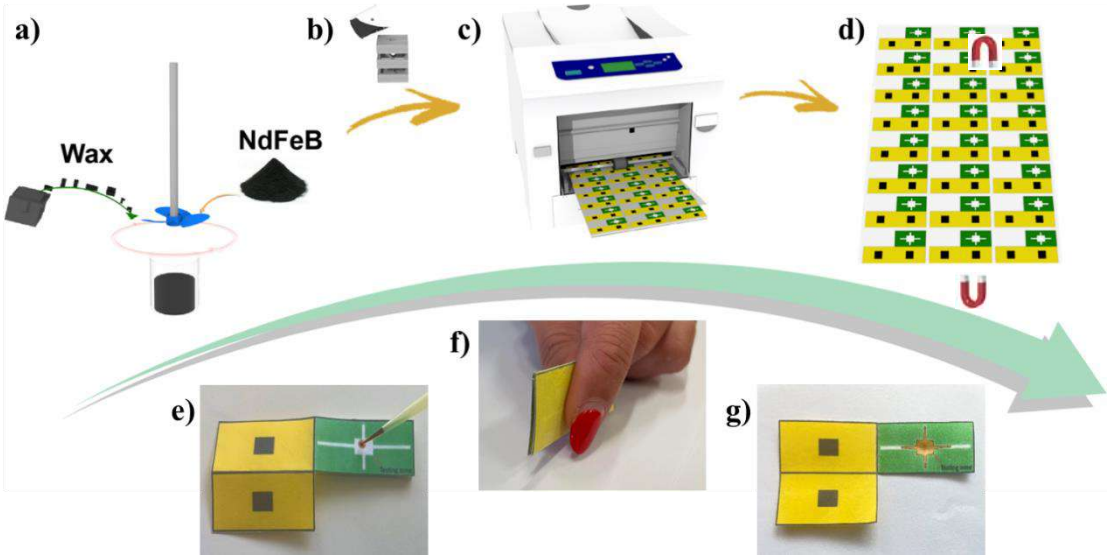

Figure 4.1.2. Experimental scheme (a-d) regarding the printing of the MOPAS. a) Mechanical mixing of the Wax and/or Wax-NdFeB inks; b) Molding process of the Wax and/or Wax-NdFeB cartridges; c) Printing of the MOPAS on a Whatman n°1 cellulose paper substrate using a Xerox ColorQube 8880 printer; d) A4 Whatman n°1 cellulose paper sheet with 23 printed MOPAS. MOPAS working principle (e-g): e) initial coniguration and dropping the Fe_3O_4@H_2O suspension (50 µl) on the center of the white rectangle (10mm x 7mm); f) folded MOPAS configuration; and g) Fe_3O_4@H_2O suspension flowing through the escaping channels (4 white lines: 26mm x 1mm) without the action of the printed wax/NdFeB magnets (10mm x 7mm).

The structure (Figure 4.1.2) of the MOPAS is composed by 2 hydrophobic wax/NdFeB magnets (2 black rectangles) printed on the paper@wax substrate (yeellow rectangles: 43 mm x 20 mm), an hydrophobic paper@wax substrate (green rectangle: 43mm x 20mm), an hydrophylic paper zone (white rectangle), and hydrophilic water escape zone (white cross). 50 µl of the Fe_3O_4@H_2O suspension are dropped in the

center of the white rectangle (Figure 4.1.2e). When the origami is folded (Figure 4.1.2f) the wax/NdFeB magnets will exert a magnetic force on the Fe_3O_4 particles drawing them to the white square while the water escapes through the white channels. Figure 4.1.2g reveals Fe_3O_4@H_2O suspension flowing through the escaping channels when the origami structure is not folded.

4.1.2.3. Physicochemical characterization

The different fluid drops (Wax, Wax/NdFeB and Fe_3O_4@H_2O) were deposited on the surface of the different substrates (paper and paper@wax), and the contact angles were evaluated using a Data Physics OCA20 instrument. Both mean contact angle and standard deviation were obtained through the measurement of four different drops for each sample.

Rheological properties were evaluated using an AresG2 rheometer equipped with a flat plate geometry (40 mm) and a gap of 500 μm. A steady shear flow test was performed at 100 °C, with a shear rate range between 0 and 500 s^{-1}, and the ink's viscosity vs shear rate graph was obtained. An amplitude sweep test was also performed to evaluate the effect of oscillation strain on the ink rheological behaviour.

The morphology of the printed composites was assessed with an ultra-high resolution Field Emission Gun Scanning Electron Microscopy (NOVA 200 Nano SEM purchased from FEI Company) with a secondary electron detector (acceleration voltage of 10kV). Before SEM, samples were coated with a ≈25 nm thick Au-Pd (80-20 wt.%) layer, using a high resolution sputter coater (208HR model purchased from Cressington Company), combined with a High Resolution Thickness Controller (model MTM-20 purchased from Cressington). The thickness of the layers was calculated from 5 images with 10 measurements each by using the ImageJ software. Atomic contrast images ware obtained with a Backscattering Electron Detector (BSED) at an acceleration voltage of 15 kV. Chemical analyses and EDX Mapping were performed by the Energy Dispersive Spectroscopy (EDS) through the use of a Si(Li) detector(EDAX) at an acceleration voltage of 20 kV.

The adhesion of the different layers of the composite was investigated with an adapted tape peel test [43] carried out on samples with a size of 1 cm x 1 cm. Briefly, an adhesive tape (3 M Scotch® Magic™ tape 810) was pressed on the surface of the printed samples with different forces (100 N, 150 N, 200 N and 300 N for 30 seconds) using a Shimadzu AG-IS universal test set-up, in compression mode at 2 $mm.min^{-1}$. Then, the tape was removed from the sample at the same velocity, while monitoring the force applied on the sample. The different tape samples were weighed before and after each test, to determine the mass loss.

The room-temperature stress–strain measurements in tensile mode at a deformation rate of 0.5 $mm.min^{-1}$ were performed with an Autograph AG-IS (Shimadzu) 500 N in order to assess the mechanical properties of samples. The Young's modulus, Y, was calculated in the linear regime of the stress–strain curves after Hooke's law:

$$\sigma s = Y \cdot \varepsilon s \quad (4.1.1)$$

Magnetic hysteresis loops were measured at room temperature, from -2T to 2T, using an ADE 3473–70 Technologies VSM.

Transmission electron microscopy (TEM) studies were performed using probe aberration-corrected Titan ChemiSTEM (FEI) electron microscope, operated at 200 kV. The average size of nanoparticles was estimated using the Image J software by counting more than 250 nanoparticles.

Powder X-ray diffraction (XRD) data were collected on a X'Pert PRO diffractometer (PANalytical) set at 45 kV and 40 mA, and equipped with Cu Kα radiation (λ=1.541874 Å) and a PIXcel detector.

A Bruker Alpha II FTIR spectrometer with a diamond attenuated total internal reflectance (ATR) accessory was used to perform the Fourier Transformed Infrared measurements (FTIR-ATR). The FTIR-ATR spectra of the different samples were acquired at room temperature from 400 to 4000 cm^{-1} and collected after 64 scans with a spectral resolution of 4 cm^{-1}. The Whatman paper was used as background for the measurement of the different samples.

4.1.3. Results and discussion

Aiming to test both Wax and Wax/NdFeB spreading on the cellulose substrate, and also to evaluate the hydrophobicity of the $Fe_3O_4@H_2O$ suspension on both cellulose and cellulose with impregnated wax (paper@wax) substrates, essential for a successful printing [44,45] and disease detection, respectively, contact angle experiments have been conducted (Table 4.1.1).

Table 4.1.1. - Contact angle between Wax and Wax/NdFeB inks and the paper substrate at 30 °C and 80 °C, and between $Fe_3O_4@H2O$ suspension and the 2 different substrates: paper and paper@wax.

Liquid	Substrate temperature	
	30 °C	80 °C
Wax		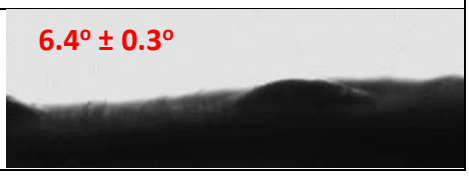

Wax/NdFeB	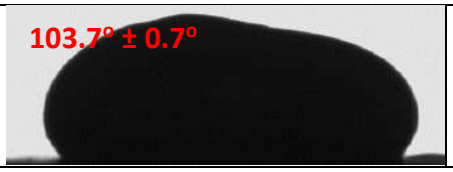	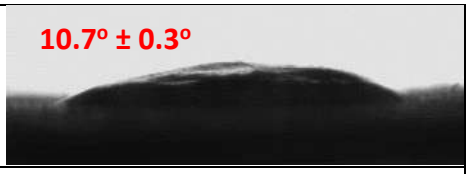
	Substrate	
	Paper	Paper@wax
$Fe_3O_4@H_2O$	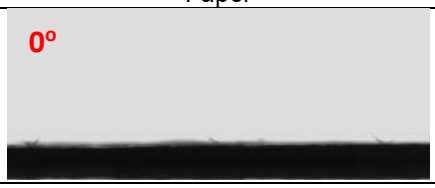	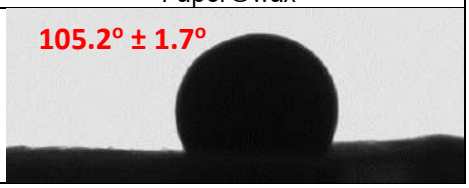

Table 4.1.1 reveals that increasing the paper substrate temperature from 30 °C to 80 °C, led to an increase in the Wax and Wax/NdFeB impregnation, demonstrated by the decrease in the contact angle values, from 126.8° ± 0.4° to 6.4° ± 0.3° in the case of Wax, and from 103.7° ± 0.7° to 10.7° ± 0.3° in the case of the Wax/NdFeB. This phenomenon is explained by the abrupt decrease in the viscosity of wax-related materials for temperatures above 80 °C [46]. To mitigate such event and to ensure a high impregnation of Wax and Wax/NdFeB on the paper, the substrate will be set to 80 °C during the printing procedure.

Table 4.1.1 also shows that the impregnation of the paper substrate with Wax leads to a hydrophobic barrier (contact angle of 105.2° ± 1.7°) that promotes the complete absorption of the $Fe_3O_4@H_2O$ on the cellulose hydrophilic channels/testing zone. The increased hydrophobicity of the Wax@paper structure is explained by the introduction of esters of long-chain fatty alcohols, acids, and long-chain alkanes into the paper structure [47].

In order to evaluate the printability, the rheological characteristics and the viscosity of both inks, Wax and Wax/NdFeB, are presented in Figure 4.1.3.

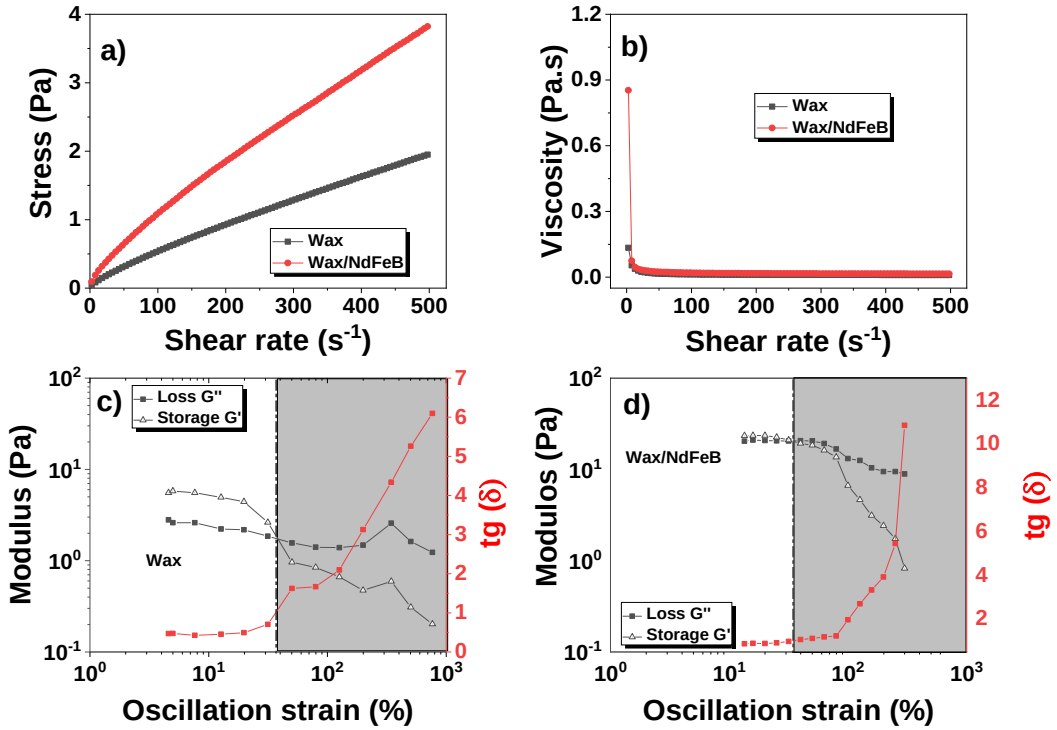

Figure 4.1.3. a) Shear stress vs. shear rate of the Wax and Wax/NdFeB inks at 120 °C. b) Viscosity values of the Wax and Wax/NdFeB inks as a function of the shear rate at 120 °C. c) Wax ink's storage (G') and loss (G'') modulus, and tg (δ) values as function of oscillation strain at 120 °C. d) Wax/NdFeB ink's storage (G') and loss (G'') modulus, and tg (δ) values as function of oscillation strain at 120 °C. Please note that during the printing procedure the cartridge is at 120 °C.

It is observed that as the shear rate increases, the shear stress also increases (Figure 4.13a) and the viscosity decreases (Figure 4.1.3b) for both Wax and Wax/NdFeB inks. When the shear rate is applied, the ink components are reordered to accommodate the shear rate. As a consequence, the overall shear force is smaller for lower shear rates due to the slow response time of the inks: whereas for the smaller shear rates the ink components have enough time to reorder, increasing shear rates lead to lower reorganization times and higher induced stress [48].

This makes the viscosity of the Wax and Wax/NdFeB inks very similar (difference less than 0.06 $Pa.s^{-1}$ for shear rates higher than 50 s^{-1}), ensuring a printing quality of the developed Wax/NdFeB inks similar to the one of neat Wax ink.

Furthermore, an amplitude sweep test was performed to evaluate the effect of oscillation strain on the ink's rheological behaviour. Figures 4.1.3c-d show the storage modulus (G') representing the elastic behaviour of the material (the energy is kept in the deformed material by stretching and extending the internal superstructures without hindering the interactions and without destroying or overstretching the

material), and the loss modulus (G"), representing the viscous behaviour of a material (energy lost as heat through internal friction when flowing) [49,50]. When the material is later released from stretching, the unemployed stored energy acts as a driving force resetting the structure into its original shape. When G'' equalled G' the gelation point is reached. The ratio between the loss and the storage modules is the tg (δ), often called damping, and it is a measure of the energy dissipation of a material. It is observed that the loss modulus (G'') values are lower than the storage modulus (G') values, exhibiting a solid-like behaviour (G'>G'') for oscillations strains higher than 50 % in both Wax and Wax/NdFeB inks [49-51]. Additionally, it was detected a plateau value of the storage modulus, associated to the elastic behaviour, for oscillations strains up to 30 %, which is characteristic of a ink with high elasticity [52,53]. Overall, the results presented in Figure 4.1.3 ensure that both inks are suitable for printing and that those inks possess high elasticity for oscillations strains up to 30 %, allowing print resolutions of 2400 FinePoint and printing speeds of higher than 11 pages per minute [54].

Figure 4.1.4. Schematically represents the working principle of the origami structure: the yellow and green zones evidence the hydrophobic wax/paper zones; the black rectangles the magnetic attraction zones composed by the Wax/NdFeB magnets; the white rectangle the hydrophilic testing zone; and the white hydrophilic cross the water escape zone (i).

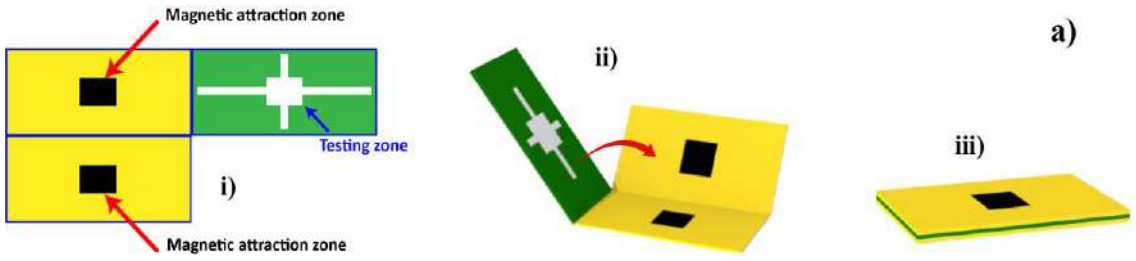

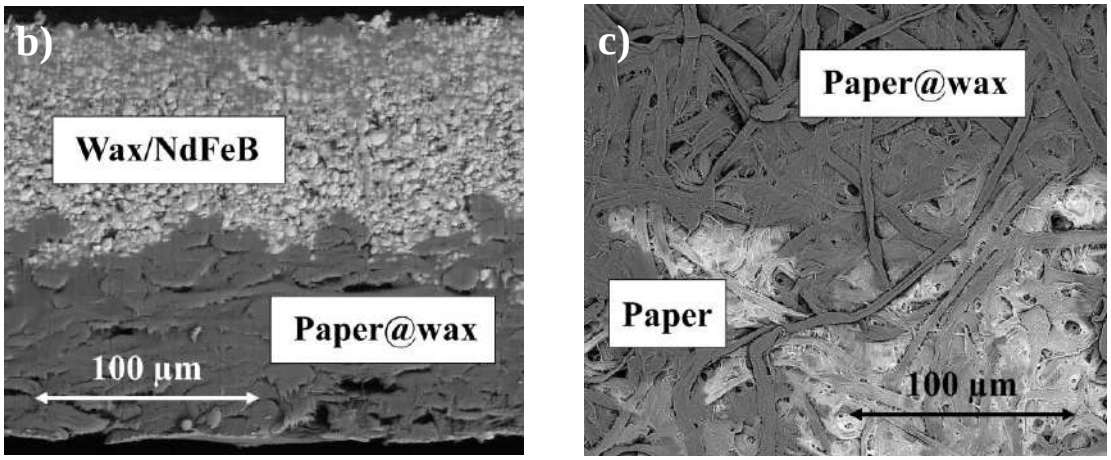

Figure 4.1.4. a) Proposed printed MOPAS: i) the black squares represent the printed Wax/NdFeB magnets, the yellow rectangles represent the wax layer printed on the paper substrates and adjacent to the Wax/NdFeB magnets, the green rectangle represents the hydrophobic wax layer printed on the paper substrates and adjacent to the testing zone, and the white cross represents the hydrophilic testing zone; ii) the testing rectangle can be placed between the two printed magnets; being ready for the multi-tool diagnostics evaluation. b) Cross-section SEM image of the Wax/NdFeB-Wax interface. c) Surface SEM image of the hydrophilic (wax)-hydrophobic (paper) interface.

After the Fe_3O_4@H_2O suspension drop being placed on the testing zone, the origami is folded so that Wax/NdFeB magnets are located just below/above the testing zone rectangle (ii). The magnetic attraction between the Wax/NdFeB magnets and the Fe_3O_4 nanoparticles will cause them to be lodged mainly in the white testing rectangle and water to flow out through the escape channels (iii).

Figure 4.1.4b displays a cross-section SEM image highlighting the interface between the Wax/NdFeB layer (top section, clearer) and the paper@wax layer (down section, darker) of the black rectangles zone. In turn, Figure 4.1.4c shows a surface SEM image that highlights the interface between the hydrophobic yellow zone (wax) and the hydrophilic white zone (paper). Both SEM images ensure that all functional layers are properly separated, being therefore suitable to perform their function in the final device.

In order to verify how the printing process and corresponding thermal treatment (cure at 80 °C for 2 minutes) affects the overall mechanical properties of the paper, stress-strain measurements were performed in tensile mode (Figure 4.1.5).

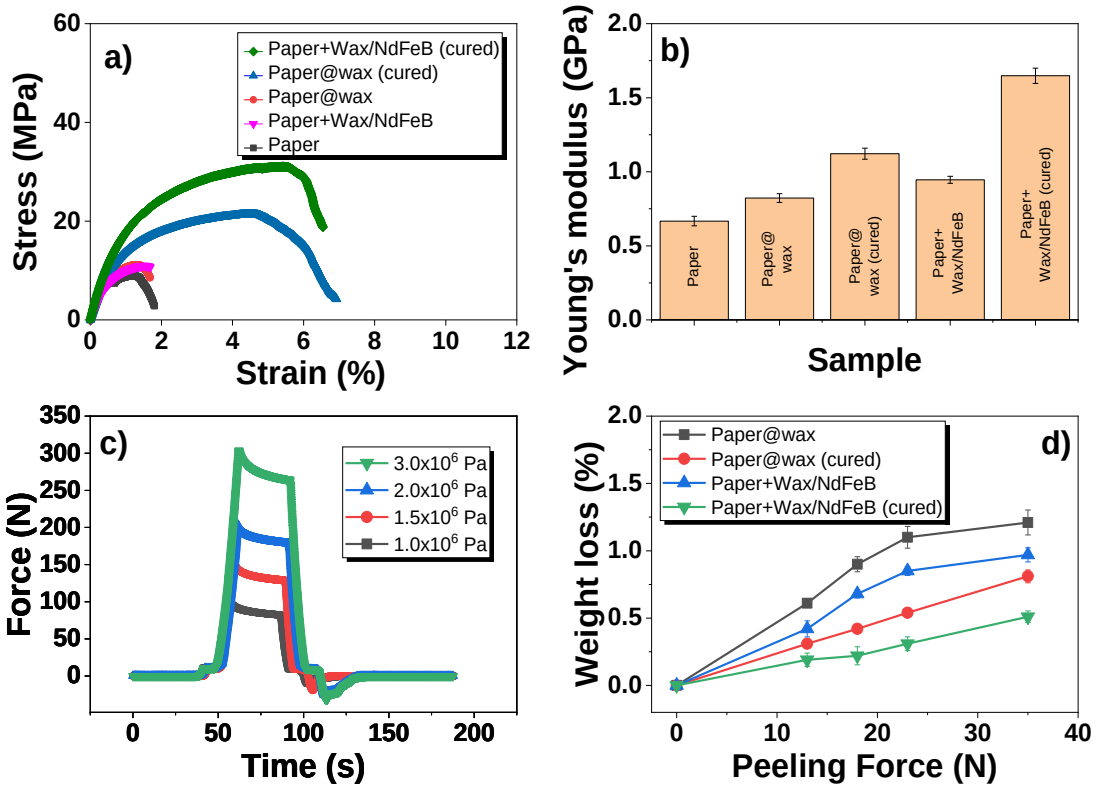

Figure 4.1.5. a) Stress-strain curves obtained at room-temperature (30 °C) for the different samples. b) Young's Modulus values obtained from (a). c) Force profile of the peeling test for the different samples as a function of time and pressure. d) Weight loss for the different samples as a function of the peeling force.

From the linear regime of the Figure 4.1.5a curves, the Young's modulus was obtained by applying Hooke's law (Equation 4.1.1), the obtained values being represented in Figure 4.1.5b. In neat paper it is usually observed just a small or even no plastic deformation, being detected a fracture near the end of the linear elastic region of the curve. All the Paper@wax samples exhibit both higher stress and strain at the breaking strain giving a clear indication of the modification of the mechanical properties of the paper, leading to more ductile samples. Similar modification was detected when the NdFeB particles are added to the wax matrix. All the above observations are independent of thermal cure temperature (80 °C or 30 °C).

Such indications are reinforced with the increase of the Young's Modulus with the addition of wax to the paper substrate (25 %); with the addition of Wax/NdFeB into the paper substrate (42 %); and with the application of the curing process (55 %). The observed increase of the Young's Modulus is attributed by the incorporation of the wax on the fibrilar structure of the paper [55]; and by the higher Young's Modulus of the NdFeB particles (higher than 100 GPa: value provided by the supplier).

In order to study the adhesion stability of the printed layers, peeling tests (Figure 4.1.5c-d) have been performed on the different composite types. The force profile during the peeling test for the printed layers (Figure 4.1.5c) reveals that the highest compression force (300 N) also led to the highest peeling force (35 N) and the lowest compression force (100 N) led to the lowest peeling force (13 N). In turn, Figure 4.1.5d reveals that the weight loss increases with increasing compression force, being maximized for samples submitted to higher peeling forces (≈1.21 %) and minimized for samples submitted to lower peeling forces (≈0.4 %). In a second round of tests, none of the samples experienced weight loss. The samples submitted to the curing process exhibited lower weight loss (less than 0.79 %).

The results presented in Figure 4.1.5c-d confirm that the printing process was effective in leading to stable mechanical coupled layers.

The final origami structure was fabricated by using the optimized thermal curing process 80 °C for 2 minutes.

Figure 4.1.6 shows the evaluation of the magnetic structures used in the present study (a: room-temperature magnetic properties of the synthesized Fe_3O_4 nanoparticles, NdFeB powder, and wax/NdFeB; b: EDX image of the wax/NdFeB layer; c: TEM image of the synthesized Fe_3O_4 nanoparticles; d: size distribution of the synthesized Fe_3O_4 nanoparticles).

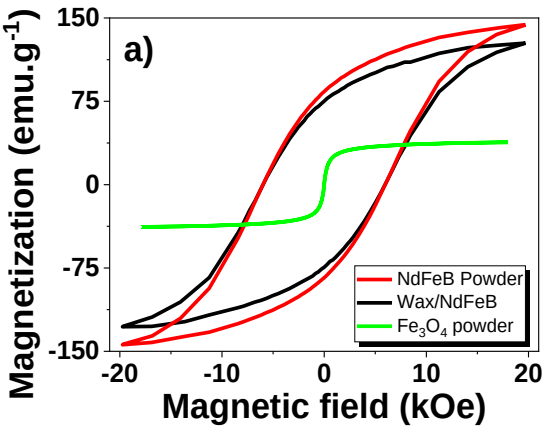

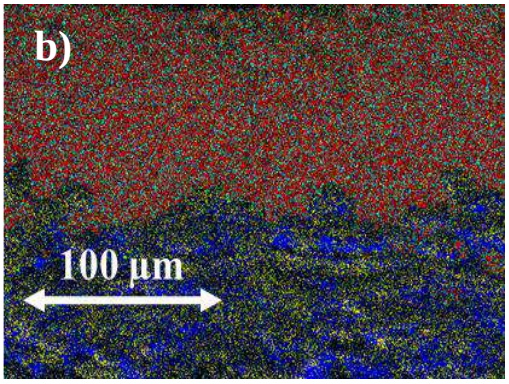

B, C, O, Nd, Fe

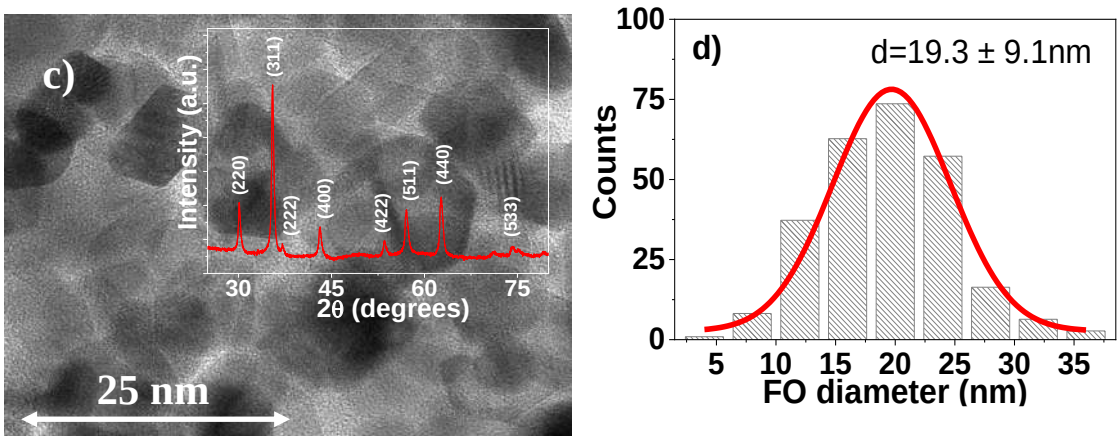

Figure 4.1.6. a) Room-temperature magnetization as a function of the applied DC magnetic field for the NdFeB powder, the wax/NdFeB printed magnet and, for the Fe_3O_4 powder. b) Color map obtained by EDS in the same sample and location of Figure 5b): Green: B; blue: Carbon; Yellow: Oxygen; Cyan: Nd; and Red: Iron. c) TEM image of Fe_3O_4 nanoparticles. The inset reveals the corresponding X-ray diffractions pattern. d) Size distribution of the Fe_3O_4 nanoparticles.

The Fe_3O_4 plot shows almost a complete absence of hysteresis, remanence and coercivity consistent with the single domain or superparamagnetic behaviour, once room temperature is above the blocking temperature and the magnetic moment of the particle is free to rotate in response to the applied magnetic field [56]. Regarding the NdFeB-related hysteresis cycles, the plots reflects a typical ferromagnetic behaviour with blocked magnetic moments within the micropowders for both the neat NdFeB powder and the Wax/NdFeB composite, all of them with a coercivity of ≈0.6 T. Additionally, the shape and magnetization maximum values of the hysteresis loops demonstrate that NdFeB powders are randomly oriented within the wax matrix. The difference between the saturation magnetization (at 20 kOe) of the NdFeB powders (≈144 $emu.g^{-1}$) and the one exhibited by the wax/NdFeB composite (≈124 $emu.g^{-1}$), and following a method proposed [57], allows to calculate that the weight concentration of NdFeB particles in the wax/NdFeB composite, which is ≈86 %, showing that no particles are shown during the samples and device processing.

TEM images show (Figure 4.1.6c) a nearly spherical shape for the synthesized Fe_3O_4 nanoparticles with average diameters of 19.3 ± 9.1 nm (Figure 4.1.6d). Since the size of the magnetic nanoparticles is below the superparamagnetic limit (≈25 nm) [58] a superparamagnetic behaviour was detected in Figure 4.1.6a [42]. In the XRD patterns (inset in Figure 4.1.6c) no peaks corresponding to impurities are detected, being observed an inverse cubic spinel structure with space group Fd-3m [59,60]. The narrow sharp peaks reveal the high purity of the synthesized Fe_3O_4 nanoparticles [42,60].

4.1.4. Proof-of-concept

The origami device has been submitted to functional experiments in order to prove the multifunctional detection capability: detection of the nanoparticles through EDX (Figure 4.1.7a-b); detection through VSM (Figure 4.1.7c-d); detection through FTIR (Figure 4.1.7e-f); and color detection through a mobile phone camera (Figure 4.1.7g-h).

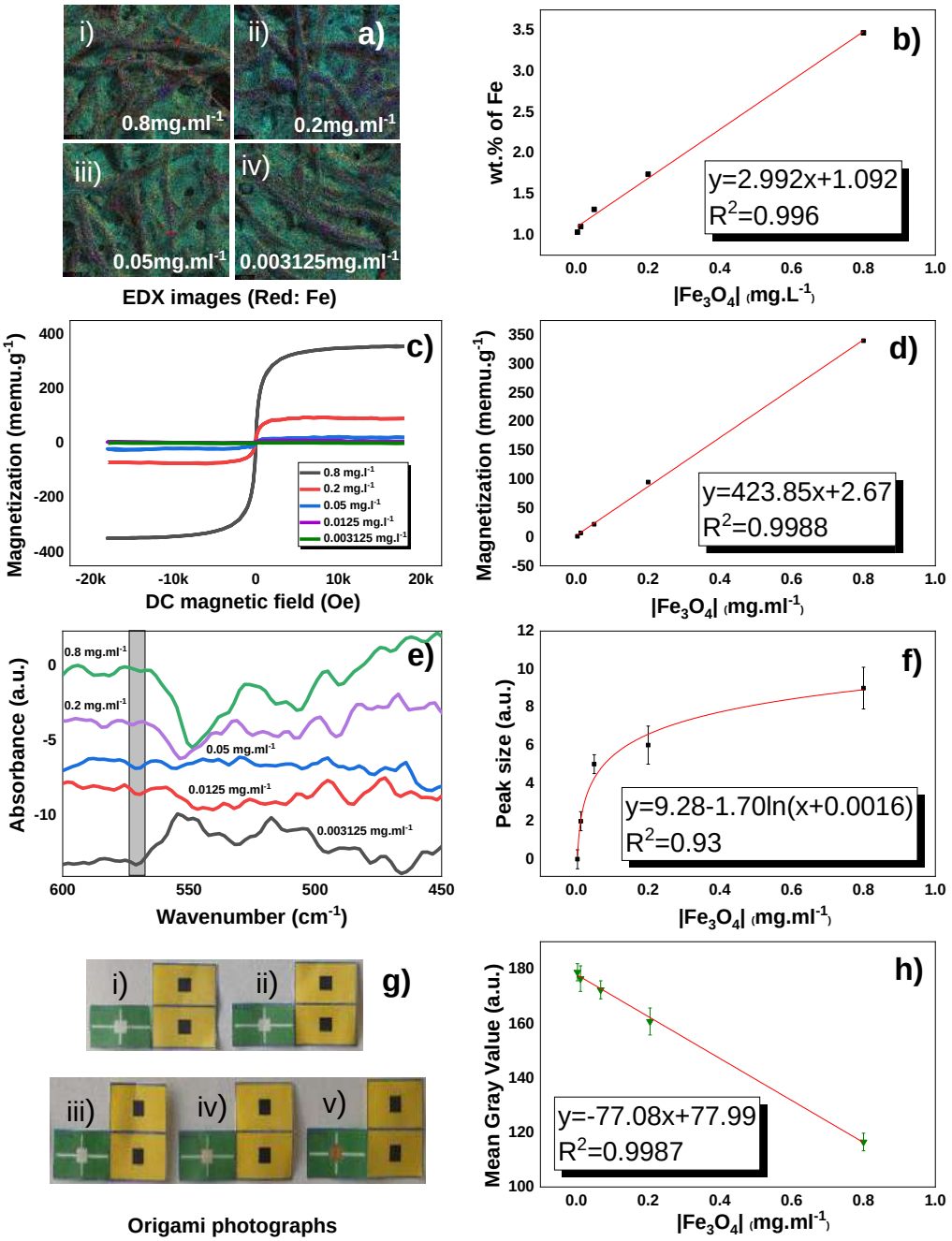

Figure 4.1.7. a) Color map obtained by EDS in the testing zone rectangle into which were added 50 µl of the mixture with Fe_3O_4 content of: iv) 0.8 mg.ml^{-1}; iii) 0.2 mg.ml^{-1}; ii) 0.05 mg.ml^{-1}; and i) 0.003125 mg.ml^{-1}. b) Relation between Fe wt.% in the testing zone rectangle (obtained from EDS) and the Fe_3O_4

concentration. c) Room-temperature magnetization as a function of the applied DC magnetic field for the testing zone rectangle into which were added 50 μl of the mixture with Fe_3O_4 content of: 0.8 $mg.ml^{-1}$; 0.2 $mg.ml^{-1}$; 0.05 $mg.ml^{-1}$; 0.0125 $mg.ml^{-1}$; and 0.003125 $mg.ml^{-1}$. d) Relation between the saturation magnetization (at 20 kOe) found on the testing zone rectangle and the Fe_3O_4 concentration. e) Infrared absorbance vs. wavenumber for the testing zone rectangle into which were added 50 μl of the mixture with Fe_3O_4 content of: 0.8 $mg.ml^{-1}$; 0.2 $mg.ml^{-1}$; 0.05 $mg.ml^{-1}$; 0.0125 $mg.ml^{-1}$, and 0.003125 $mg.ml^{-1}$. f) Relation between the 530 cm^{-1} FTIR band (reported as representing Fe-O vibrations in Fe_3O_4) absorbance and the Fe_3O_4 concentration on the drop added to the testing zone rectangle. g) Mobile phone photographs (iPhone 12) of the origami testing platform into which were added 50 μl of the mixture with Fe_3O_4 content of: v) 0.8 $mg.ml^{-1}$; iv) 0.2 $mg.ml^{-1}$; iii) 0.05 $mg.ml^{-1}$; ii) 0.0125 $mg.ml^{-1}$, and i) 0.003125 $mg.ml^{-1}$. h) Relation between the mean grey value (obtained through image J software) and the Fe_3O_4 concentration of the drop added to the testing zone rectangle.

EDX analysis carried out in the testing zone square allowed to relate the Fe wt.% with the concentration of the different $Fe_3O_4@H_2O$ suspensions with high linearity (R^2 = 0.996; Figure 4.1.7a-b). Such linearity was improved to 0.998 when VSM measurements were used to relate the saturation magnetization obtained in the testing zone square (in which they were previously added the different $Fe_3O_4@H_2O$ drops) with the concentration of the different $Fe_3O_4@H_2O$ suspensions (Figure 4.1.7c-d).

Taking advantage of previous studies reporting that the FTIR band located at 565 cm^{-1} - 580 cm^{-1} is related with Fe-O stretching in highly crystalline Fe_3O_4 nanoparticles [61], the spectra of the different testing squares was been used to relate the absorbance of the 565 cm^{-1} - 580 cm^{-1} band with the Fe_3O_4 wt.% (Figure 4.1.7e-f). Such approach proved to be the one with the lowest correlation, yet it proved to be effective in detecting Fe_3O_4 concentrations as small as 3.125 $\mu g.ml^{-1}$.

As the Fe_3O_4 nanopowders introduce a brown-black color to the white substrates [62], the images taken with a mobile phone and later analysed with the image J software (mean grey value: Figure 4.1.7g-h) allowed to almost match the maximum linearity of the VSM approach. Such method is quite simple and only requires a mobile phone equipped with a camera and a photo analysis software.

Thus, it is confirmed that the proposed MOPAS allows to detect magnetic nanoparticles in mixtures with low Fe_3O_4 wt.% (3.125 $\mu g.ml^{-1}$) with the use of a small amount of testing liquid (50 μl), exhibiting a limit of detection lower than 156 μg of Fe_3O_4. Those features can be further optimized with the use of the use of surface-functionalized magnetic nanoparticles that link to biomarkers or magnetoactive disposal products, being therefore a powerful platform for the development of biomedical μPADs.

4.1.5. Conclusions

In conclusion, this work presents the development, fabrication and evaluation of a flexible point-of-care device upgraded with *in situ* magnetic concentration capability. When compared with magnetic flow detectors currently found on the market and fabricated on rigid substrates, the advantages of the proposed platform are the economic viability of the fabrication and the mass production allowance as a result of the low cost, printability and lightweight of the device (less than 100 mg). The mechanical properties of the device (flexibility, foldability, and 0.5-2 GPa Young's Modulus) and printing stability/durability, provide the required long-term stability of the POC multifunctional platform for practical applications. The content of the Fe_3O_4 within the analysis rectangle was determined through energy-dispersive X-ray spectroscopy, vibrating sample magnetometry, infrared spectroscopy; and color change (greyscale) in photographs taken by a mobile phone, with linearity of 0.996, 0.998, 0.930, and 0.998, respectively, for Fe_3O_4@H_2O mixtures with Fe_3O_4 wt.% up to 3.125 $\mu g.ml^{-1}$ (50 µl of Fe_3O_4@H_2O), being determined a limit of detection lower than 156 µg of Fe_3O_4.

The proposed device provides a state-of-the-art solution to incorporate printed magnets on a flexible µPAD platform that can serve as a platform for the implementation of the detection of a high range of diseases (with magnetoactive disposal products or with the use of biomarkers) in a new type of multifunctional biomedical device that combines X-ray spectroscopy, vibrating sample magnetometry, infrared spectroscopy; and color change sensitivities. Thus, the proposed printed magnetic origami paper represents a lightweight, sustainable, printable and low cost platform for a successful disease detection procedure.

4.1.6. References

1. Markwalter, CF., et al., Inorganic Complexes and Metal-Based Nanomaterials for Infectious Disease Diagnostics. Chemical Reviews (2019) 119: 1456-1518.

2. Osler, W. Aequanimitas., With Other Addresses to Medical Students, Nurses and Practitioners of Medicine. (Creative Media Partners, LLC, 2018).

3. Karlikow, M., et al., Field validation of the performance of paper-based tests for the detection of the Zika and chikungunya viruses in serum samples. Nature Biomedical Engineering (2022) 6: 246-256.

4. Deng, J., et al., Nanosensors for Diagnosis of Infectious Diseases. ACS Applied Bio Materials (2021) 4: 3863-3879.

5. Wang, Z., et al., Exosomes decorated with a recombinant SARS-CoV-2 receptor-binding domain as an inhalable COVID-19 vaccine. Nature Biomedical Engineering (2022) 6: 791-805.

6. Chandrasekaran, SS., et al., Rapid detection of SARS-CoV-2 RNA in saliva via Cas13. Nature Biomedical Engineering (2022) 6: 944-956.

7. Zhu, T., Watkinson, P., Clifton, DA., Smartwatch data help detect COVID-19. Nature Biomedical Engineering (2020) 4: 1125-1127.

8. Bloom, JS., et al., Massively scaled-up testing for SARS-CoV-2 RNA via next-generation sequencing of pooled and barcoded nasal and saliva samples. Nature Biomedical Engineering (2021) 5: 657-665.

9. Pashchenko, O., et al., Comparison of Optical, Electrochemical, Magnetic, and Colorimetric Point-of-Care Biosensors for Infectious Disease Diagnosis. ACS Infectious Diseases (2018) 4: 1162-1178.

10. Michael, I., et al., A fidget spinner for the point-of-care diagnosis of urinary tract infection. Nature Biomedical Engineering (2020) 4: 591-600.

11. Sedlmayer, F., Aubel, D., Fussenegger, M., Synthetic gene circuits for the detection, elimination and prevention of disease. Nature Biomedical Engineering (2018) 2: 399-415.

12. Tram, DTN., et al. Advances in nanomaterials and their applications in point of care (POC) devices for the diagnosis of infectious diseases. Biotechnology Advances (2016) 34: 1275-1288.

13. Perlman, O., et al., Quantitative imaging of apoptosis following oncolytic virotherapy by magnetic resonance fingerprinting aided by deep learning. Nature Biomedical Engineering 2022; 6: 648-657.

14. Song, G., et al., Carbon-coated FeCo nanoparticles as sensitive magnetic-particle-imaging tracers with photothermal and magnetothermal properties. Nature Biomedical Engineering 2020; 4: 325-334.

15. Rickard, JJS., et al., Rapid optofluidic detection of biomarkers for traumatic brain injury via surface-enhanced Raman spectroscopy. Nature Biomedical Engineering 2020; 4: 610-623.

16. Chen, HH., et al., A nanoparticle probe for the imaging of autophagic flux in live mice via magnetic resonance and near-infrared fluorescence. Nature Biomedical Engineering 2022; 6: 1045-1056.

17. Kim, CC, Wilson, EB, Derisi, JL. Improved methods for magnetic purification of malaria parasites and haemozoin. Malaria Journal 2010; 9.:17

18. Bhamla, MS., et al., Hand-powered ultralow cost paper centrifuge. Nature Biomedical Engineering.2017; 1, 0009

19. Carinelli, S., et al., Biomarker detection of global infectious diseases based on magnetic particles. New Biotechnology 2015; 32: 521-532.

20. Iranmanesh, M, Hulliger, J. Magnetic separation: Its application in mining, waste purification, medicine, biochemistry and chemistry. Chemical Society Reviews 2017; 46: 5925-5934.

21. Thanh, BT., et al., Immobilization of Protein A on Monodisperse Magnetic Nanoparticles for Biomedical Applications. 2019; Journal of Nanomaterials.

22. Ganapathe, LS., et al., Magnetite (Fe3O4) nanoparticles in biomedical application: From synthesis to surface functionalisation. Magnetochemistry 2020; 6: 1-35.

23. Cheng, FY., et al., Characterization of aqueous dispersions of Fe_3O_4 nanoparticles and their biomedical applications. Biomaterials 2005; 26: 729-738.

24. Ghazanfari, MR., et al., Perspective of Fe_3O_4 Nanoparticles Role in Biomedical Applications. Biochemistry Research International 2016.

25. Jia, D., et al., Highly smooth, robust, degradable and cost-effective modified lignin-nanocellulose green composite substrates for flexible and green electronics Composites Part B: Engineering 2016; 236:109803

26. Lou, Z., et al., Biomass-Derived Carbon Heterostructures Enable Environmentally Adaptive Wideband Electromagnetic Wave Absorbers Nano-Micro Letters 2022; 14:11.

27. Zhang, T., et al., A paper-based assay for the colorimetric detection of SARS-CoV-2 variants at single-nucleotide resolution. Nature Biomedical Engineering 2022; 6: 957-967.

28. Oliveira, J., et al., Polymer-based smart materials by printing technologies: Improving application and integration. Additive Manufacturing 2018; 21: 269-283.

29. Zhao, TH., et al., Printing of Responsive Photonic Cellulose Nanocrystal Microfilm Arrays. Advanced Functional Materials 2019; 29: 1804531

30. Siqueira, G., et al., Cellulose Nanocrystal Inks for 3D Printing of Textured Cellular Architectures. Advanced Functional Materials 2017; 27: 1604619

31. Yu C., et al., Recent Advances in Design of Flexible Electrodes for Miniaturized Supercapacitors. Small Methods 2020;.4:1900824

32. Brito-Pereira R., et al., Reconfigurable 3D-printable magnets with improved maximum energy product. Journal of Materials Chemistry C 2020; 8: 952-958.

33. Dixon, C, Lamanna, J, Wheeler, AR. Printed Microfluidics. Advanced Functional Materials 2017; 27:1604824

34. Chowdhury NA., et al., Sustainable Recycling of Rare-Earth Elements from NdFeB Magnet Swarf: Techno-Economic and Environmental Perspectives. ACS Sustainable Chemistry and Engineering 2021; 9: 15915-15924.

35. Costis S., et al., Recovery potential of rare earth elements from mining and industrial residues: A review and cases studies. Journal of Geochemical Exploration 2021; 221: 106699

36. Gawande, MB, Branco, PS, Varma, RS. Nano-magnetite (Fe_3O_4) as a support for recyclablecatalysts in the development of sustainable methodologies. Chemical Society Reviews 2013; 42: 3371-3393.

37. Nicolas-Boluda., et al., Self-Assemblies of Fe_3O_4 Nanocrystals: Toward Nanoscale Precision of Photothermal Effects in the Tumor Microenvironment. Advanced Functional Materials 2021;. 31: 2006824

38. Chen X., et al., Electrospinning Multilayered Scaffolds Loaded with Melatonin and Fe_3O_4Magnetic Nanoparticles for Peripheral Nerve Regeneration. Advanced Functional Materials 2020; 30: 2004537

39. McCoey, JM., et al., Quantum Magnetic Imaging of Iron Biomineralization in Teeth of the Chiton Acanthopleura hirtosa. Small Methods 2020; 4: 1900754

40. Knowlton, S., et al., 3D-printed smartphone-based point of care tool for fluorescence- and magnetophoresis-based cytometry. Lab on a Chip 2017; 17: 2839-2851.

41. Kim, J., et al., A soft and transparent contact lens for the wireless quantitative monitoring of intraocular pressure. Nature Biomedical Engineering 2021; 5: 772-782.

42. Martins, P., et al., Tailored Magnetic and Magnetoelectric Responses of Polymer-Based Composites. ACS Applied Materials and Interfaces 2015; 7: 15017-15022.

43. Hao, T., et al., Highly robust, transparent, and conductive films based on AgNW-C nanowires for flexible smart windows. Applied Surface Science 2021; 559:149846

44. Krainer, S., Smit, C., Hirn, U., The effect of viscosity and surface tension on inkjet printed picoliter dots. RSC Advances 2019; 9: 31708-31719.

45. He, B., et al., The roles of wettability and surface tension in droplet formation during inkjet printing. Scientific Reports 2017; 7: 11841

46. Alade, OS., et al., Novel Approach for Improving the Flow of Waxy Crude Oil Using Thermochemical Fluids: Experimental and Simulation Study. ACS Omega 2020; 5: 4313-4321.

47. Saji, VS., Wax-based artificial superhydrophobic surfaces and coatings. Colloids and Surfaces A: Physicochemical and Engineering Aspects 2020; 602: 1251325

48. Rapp, BE., Chapter 9 - Fluids. In: Rapp BE (ed). Microfluidics: Modelling, Mechanics and Mathematics. 2017, pp 243-263.

49. Murata, H., Rheology - Theory and Application to Biomaterials. (INTECH Open Access Publisher, 2012.

50. Shakeel, A., Kirichek, A., Chassagne C., Effect of pre-shearing on the steady and dynamic rheological properties of mud sediments. Marine and Petroleum Geology 2020; 116: 104338.

51. M'Barki, A., Bocquet, L., Stevenson, A., Linking Rheology and Printability for Dense and Strong Ceramics by Direct Ink Writing. Scientific Reports 2017; 7: 6017

52. Lewis, JA., Direct ink writing of 3D functional materials. Advanced Functional Materials 2006; 16: 2193-2204.

53. Dabbaghi M., et al., Viscoelastic and deformation characteristics of structurally different commercial topical systems. Pharmaceutics 2021; 13: 1351

54. Xerox. Xerox® ColorQube® 8580/8880Color PrinterImprimante CouleurUser Guide. https://usermanual.wiki/Xerox/XeroxColorqube8880UsersManual684582.347452995/html#pf3; 2015.

55. Madhuranthakam, CMR., Pandiyan, S., Penlidis, A., Performance Evaluation of Nonacosan-10-ol-Based Polyethylene Packaging Material Using Molecular Dynamics Simulations. Polymers 2022; 14: 1779

56. Martins, P., et al., Dielectric and magnetic properties of ferrite/poly(vinylidene fluoride) nanocomposites. Materials Chemistry and Physics 2012; 131: 698-705.

57. Gonçalves, R., et al., Development of magnetoelectric $CoFe_2O_4$ /poly(vinylidene fluoride) microspheres. RSC Advances 2015; 5: 35852-35857.

58. Krishnan, KM., et al., Nanomagnetism and spin electronics: materials, microstructure and novel properties. Journal of Materials Science 2006; 41: 793-815.

59. Liu, XD., et al., Hydrothermal synthesis of superparamagnetic Fe_3O_4 nanoparticles with ionic liquids as stabilizer. Materials Research Bulletin 2015; 62: 217-225.

60. Houshiar, M., et al., Synthesis of cobalt ferrite $CoFe_2O_4$ nanoparticles using combustion, coprecipitation, and precipitation methods: A comparison study of size, structural, and magnetic properties. Journal of Magnetism and Magnetic Materials 2014; 371: 43-48.

61. Chipara, DM., et al., PVDF-Fe3O4 nanocomposites: spectroscopic investigations. Journal of Polymer Research 2022; 29: 48907

62. Pfaff, G., Iron oxide pigments. Physical Sciences Reviews 2021; 6: 535-548.

4.2. Wax printable conductive and low-power thermal actuator paper-based analytical device

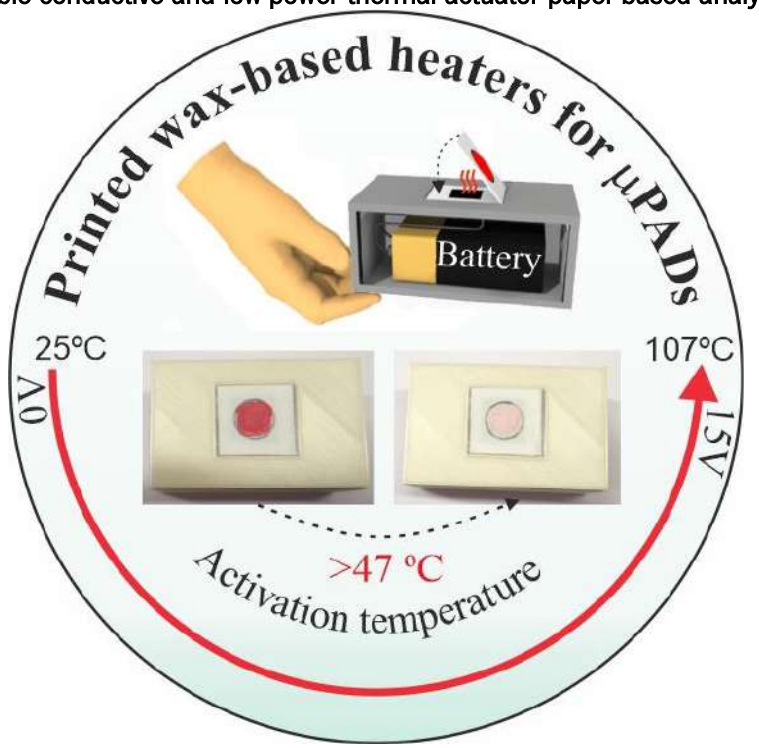

In this chapter is developed a paper-based analytical device printed with multifunctional hydrophobic composites based on conductive graphene nanoplatelets (GNP) integrated into the wax matrix to allow a dual role of barrier and heater, the latter being required in a large variety of temperature-sensitive reactions and applications of microfluidic technology. The benefits of μPADs allied to the increased functionality and performance of the developed wax, hold great promise to meet the requirements for a next generation of versatile, effective and accurate μPADs for an increasing number of applications.

This chapter is based on the following work: R. Brito-Pereira, C. Ribeiro, P. Costa, V. Correia, V. F. Cardoso, S. Lanceros Mendez, Graphene based printable conductive wax for low-power thermal actuation on microfluidic paper-based analytical devices. (Submitted).

4.2.1. Introduction

Paper has been a base material for many applications for centuries. It is based on cellulose, which is a renewable polymer, produced by trees, plants and some non-pathogenic bacteria [1]. Besides being affordable and widely available, this polymer features interesting physicochemical properties such as biocompatibility, flexibility, low weight and hydrophilicity by nature, which results in an effortless fluid flow by capillary action with no need for external pumps or pressure [2,3]. Moreover, it allows modification with a variety of functional groups to perform specific analytical assays [4]. These assets make it suitable for the development of devices, including the μPADs, a concept that was introduced in 2007 by Whitesides and co-workers when photolithography was employed to patterned paper and colorimetric analyses were implemented [5]. Although Whatman n°1 paper is the gold standard used microfluidic substrate, other versions such as Whatman n°4, nitrocellulose, bacteria cellulose nanopaper and nylon membranes are also used to develop μPADs [6]. Recently, new polymer-based materials with promising and tailorable physicochemical properties, including controllable flow rates, have been introduced and successfully tested as alternative to the commonly used microfluidic paper substrates [7–10].

μPADs have been initially developed for resources limited environments, in-field applications or for their use in private homes, as they fulfil the ASSURED criteria defined by the WHO and being therefore suitable for PADs development [4]. Thus, their potential has expanded to such an extent that nowadays this technology is used in numerous applications worldwide such as clinical [1], veterinary [11], food industry [12], agriculture [13], biodefense [14], energy [15] and environmental purposes [16], among others [17–19]. Its popularity is due to the fact that μPADs present several advantages comparatively to traditional microfluidic devices made of silicon, glass or polymer (e.g. PDMS), as well as to the conventional laboratory techniques, including low cost, low sample volume consumption, ease of use, portability, in situ measurement, high sensitivity, and no need for sophisticated laboratory equipment and trained user [20,21]. Moreover, they can be used not just in lateral flow assays but also for multiplex analysis and complex analysis requiring multiple steps (e.g. sample transport, pre-treatment, mixing, reaction, separation) [22,23]. Thus, significant growth of academic research on paper-based analytical fabrication methods and integrated tools (e.g, optical sensors, pressure sensors, micropumps, microvalves, heaters, temperature sensors, among others [24]) has been observed for the past decade to increase their functionality and performance. This will allow the development of effective, accurate and standardize μPADs and promote their commercialization, maintaining simplicity and without compromising its cost [25-27].

For instance, given the hydrophilic nature of paper, hydrophobic boundaries with specific patterns are often required to restrict the fluid flow of samples and reagents to specific pathways of the hydrophilic substrate [28]. To address these goals, different strategies have been used such as photolithography, wax printing, inkjet printing and screen-printing. Folding several layers of patterned paper, origami inspired, has also been employed to obtain three-dimensional (3D) μPADs. Several review articles address these techniques in detail [2,22,29–31]. Each of those approaches has its own benefits and limitations, so the choice is often based on cost, substrate, fabrication time, equipment availability and also specific application demands. Photolithography used a chemical photoresist to infiltrate the paper substrate and create the barrier by exposing the substrate to light through a photomask. This technique presents good resolution but suffer from the cost of the photoresist and organic solvent, fragile nature of the resulting devices and possible production of background signals [4]. A technique that has become popular to pattern channels in μPADs is wax printing. Although the printing resolution cannot catch up with photolithography, the production steps are simpler, faster and cheaper, being, thus, best suited for large scale production [32]. It involves a three-step method including the pattern drawing using an appropriate software, the paper printing using a commercial wax printer and the heating step to allow impregnation of the wax through the paper to the opposite surface [33]. Moreover, wax-based devices are mechanically resistant and are compatible with lamination, allowing to fabricate complex two (2D) or 3D structures for multipurpose applications [28].

Nonetheless, despite the excellent quality of wax printing that makes it one of the materials and techniques most used in the manufacture of uPADs systems, its function is passive, working only as boundaries to delineate hydrophilic channels without any action on the fluids. On the other hand, thermal actuators are commonly needed in microfluidic technology for precise temperature-sensitive reactions and applications such as colorimetric analytic analysis [9,34], cell culture [35,36], polymerase chain reaction [37,38], cell lysis [39,40], among others technological applications. However, they are still not well developed for μPADs. As instance, heaters were implemented in μPADs in the forms of non-contact inductive heater [41], laser heater [42,43], infrared heater [44], and microwave heater [45,46], among others, being resistive heaters [24,47,48] the most commonly used due to their low fabrication cost and mature fabrication process. However, they required additional processing techniques for their proper integration into μPADs.

In this context, the present work reports on the implementation of active functionalities to the hydrophobic wax through the integration of conductive graphene fillers, on behalf of their electrical and thermal conductivity and good mechanical properties [49–51]. Conductive wax inks and printed patterns have

been developed, the latter with the individual or dual function of barrier and heater using a simple, single and rapid fabrication method.

4.2.2. Experimental

4.2.2.1. Materials

Whatman n°1 cellulose paper was purchased from Sigma-Aldrich (Missouri, USA). Graphene nanoplatelets (referred as GNP) were supplied by Graphenest Company, Portugal. The GNP is characterized by 2-30 layers with <10 nm of thickness and 1–20 μm of particle size. Wax cartridges were obtained from Xerox Corporation (Connecticut, USA). Thermochromic Inks were purchased from SFXC-Good Life Innovations Ltd (Denton Island, UK), namely: two temperatures responsive thermochromic inks – red to more translucent (light rose) when activated at temperatures higher than 28 °C and 47 °C, respectively, and temperature responsive thermochromic ink – green to yellow when activated at temperature higher than 28 °C. Pure ethanol (99 %) was obtained from Sigma-Aldrich (Missouri, USA). 1.5, 9 and 12 V alkaline batteries were supplied from a local store. All materials were used as received from the providers.

4.2.2.2. Experimental methods

4.2.2.2.1. Conductive wax preparation

For the preparation of the GNP/Wax composites, GNP was added to 15 mL of pure ethanol at a defined concentration. The solutions were placed in an ultrasonic bath (Fisherbrand, FB15056) for 3 h to avoid agglomeration between GNP and ensure their proper dispersion. Previously cut Xerox wax of ≈45 g was then added to the mixture (to obtain a final GNP weight percentage of 5, 10, 15 and 20 wt.%) and placed in an oven (JP Selecta, 2000208) for 30 min at a temperature of 120 °C, to ensure suitable polymer melting and complete evaporation of the solvent. Then, the GNP/Wax mixture was removed from the oven and placed in a hot plate (Prazitherm P272) at the same temperature and mixed with the help of a mechanical Teflon stirrer (Heidolph RZR 1) for 1 h at 100 rpm to ensure the homogeneity of the melt composites. Finally, each melted mixture was poured into a homemade aluminium mould, specially designed and manufactured to ensure a shape compatibility with a commercial wax printer (Xerox

Colorqube 8880). The mould was allowed to cool down to room temperature (≈25 °C) for 10 min and dissembled, being the obtained solidified GNP/Wax cartridges ready to be introduced into the printer.

4.2.2.2.2. Printing process

Various neat wax and GNP/Wax designs were created, according to the intended application (described below), using a computer-assisted design software (Sketchup 2017) and printed with a Xerox ColorQube 8880 printer (during printing the cartridge melts at temperature higher than 100 °C) on the Whatman n°1 cellulose paper substrates (uncured samples). After printing, the samples were placed on a hot plate for a thermal cure at 100 °C for 5 min (cured samples), allowing the wax to penetrate the substrates all the way through to the opposing surface. Uncured and cured samples will be referred in the figures as "Unc." and "C.", respectively.

4.2.2.2.3. Physicochemical characterization

Rheological properties of different prepared waxes were evaluated using an AresG2 rheometer equipped with a flat plate geometry (40 mm) and a gap of 500 μm. A steady shear flow test was carried out at 100 °C, with a shear rate range from 0 to 500 s^{-1}. Accordingly, the melted waxes' viscosity as a function of the shear rate was obtained.

Moreover, drops with approximately ≈10 μL from different melted prepared waxes (≈100 °C) were deposited on the surface of Whatman n°1 paper at a temperature of 30 and 80 °C, and the contact angles were evaluated using a Data Physics OCA20 instrument. Four measurements were performed in each case at different locations, the contact angles being reported as the average and standard deviation.

The surface and cross-section morphology of printed uncured and cured waxes was assessed with a NanoSEM - FEI Nova 200 (FEG/SEM) scanning electron microscope at 10 kV. Before SEM, samples were gold coated by magnetron sputtering using a Polaron SC502 sputter coater.

The mechanical properties of the different printed waxes on Whatman n°1 paper were obtained by uniaxial stress–strain measurements in tensile mode at a deformation rate of 0.5 $mm.min^{-1}$ and at room temperature (≈25 °C) using a Shimadzu model AG-IS and a load cell of 500 N. Three assays were carried out for each sample. The Young's modulus, Y, was calculated in the linear regime of the stress (σs)–strain (εs) curves after Hooke's law (equation 4.2.1):

$$\sigma s = Y \cdot \varepsilon s \quad (4.2.1)$$

The adhesion of the different printed waxes on Whatman n°1 paper was studied with an adapted tape peel test [52] performed on samples with an area of 10×10 mm^2. For that, an adhesive tape (3 M Scotch® Magic™ tape 810) was pressed on the surface of the printed samples with different forces (50, 100, 150 and 200 N for 30 s) using a Shimadzu AG-IS universal test set-up, in compression mode at 2 $mm.min^{-1}$. After that, the tape was removed from the sample at the same speed, while monitoring the force applied to the sample. Each sample was weighed before and after each assay, to determine the mass loss.

Sheet resistance measurements were performed using silver paint electrodes (AGG3790, Agar Scientific) with area of 2 × 1 mm^2 and distance of 10 mm between them. The DC electrical voltage was varied from -10 to +10 V in steps of 1 V measuring the current using a Keithley 487 picoammeter/voltage source. The surface electrical resistivity (r) and conductivity (s) was determined from the linear slope of the I-V curves after equation 4.2.2:

$$\sigma = \frac{1}{\rho} = \frac{1}{R}\frac{d}{l} \quad (4.2.2)$$

where R is the electrical resistance, d the distance and l the length of the electrodes.

Thermal measurements were performed on printed wax lines (1 mm width) on Whatman n°1 paper. A temperature probe type K (-40 °C to 260 °C, ± 0.75 %) UNI-T UTT10K connected to Rigol DM3068 Digital Multimeter was used. A DC Power Supply, 21N155 Hikari HF-3203S, ranging from 0 to 15 V, was used to supply and control the energy provided to the printed lines. Moreover, the temperature was measured as a function of time (30 s) and at a distance of 1 and 2 mm (after 10 s) in order to study the propagation of the heating through the paper.

4.2.2.3. Functional proofs of concept

Two functional proofs of concepts were demonstrated (Figure 4.2.1). The first one consists on Whatman n°1 paper devices with arrays of 6 parallel channels (2 mm width) delimited by neat wax and conductive 20 wt.% GNP/Wax lines (1 mm width) allowing for individualized actuation with different electrical voltages (Figure 4.2.1a). In this case, a unique DC Power Supply was used and applied to different conductive lines. Two different thermochromic inks (yellow and red) with different activation temperatures at 28 °C and 47 °C were used for this purpose.

The proof-of-concept consists in the development of a portable printed folded Whatman n°1 paper device, in which a 20 wt.% GNP/Wax conductive square (100 mm^2) is connected to a small battery (1.5, 9 or

12 V) to provides heat to fluids (in this specific case thermochromic inks) contained in the circular testing area (8 mm diameter) delimited by neat wax (Figure 4.2.1b). To build the structure that incorporates the different alkaline batteries and supports the paper device, 3D printing was used (*Prusa* i3 3MK3) to obtain an adequate polylactic acid (PLA) support. Two different thermochromic inks (both red) with different activation temperatures at 28 ◦C and 47 ◦C were used to visually evaluate and validate the developed system. Further, a thermal imaging camera (HT 19-HTi) was also employed in both proof-of-concepts.

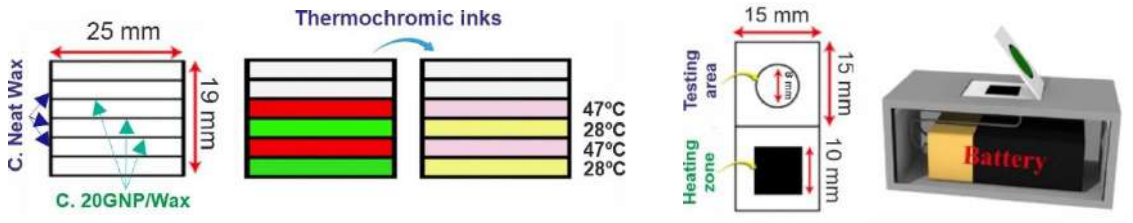

a) b)

Figure 4.2.1. Representative illustration of the a) Whatman n°1 paper devices with arrays of 6 parallel channels and b) portable printed folded Whatman n°1 paper device, in which a conductive square is connected to a small battery.

4.2.3. Results and discussion

In order to evaluate ink printability, the viscosity of the produced samples was evaluated as a function of shear rate through a steady shear test (Figure 4.2.2a).

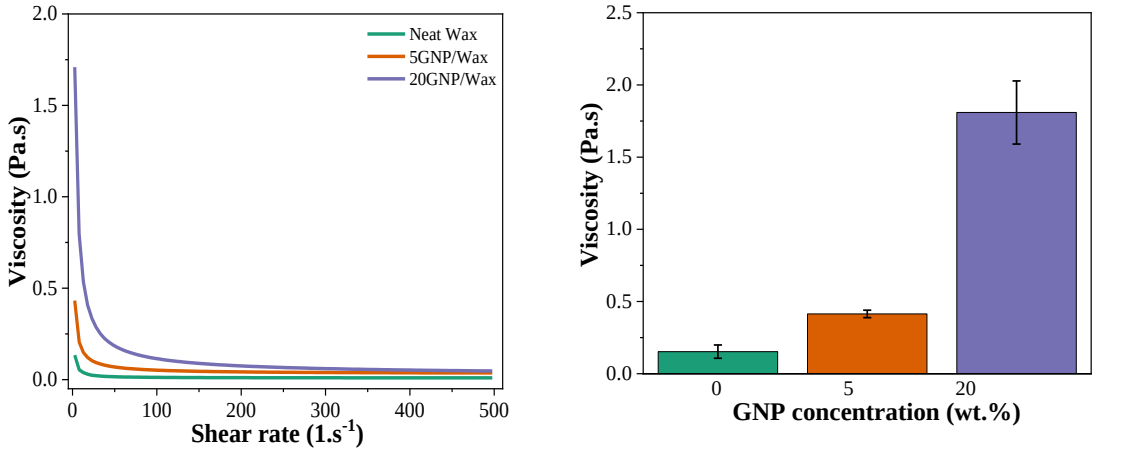

a) b)

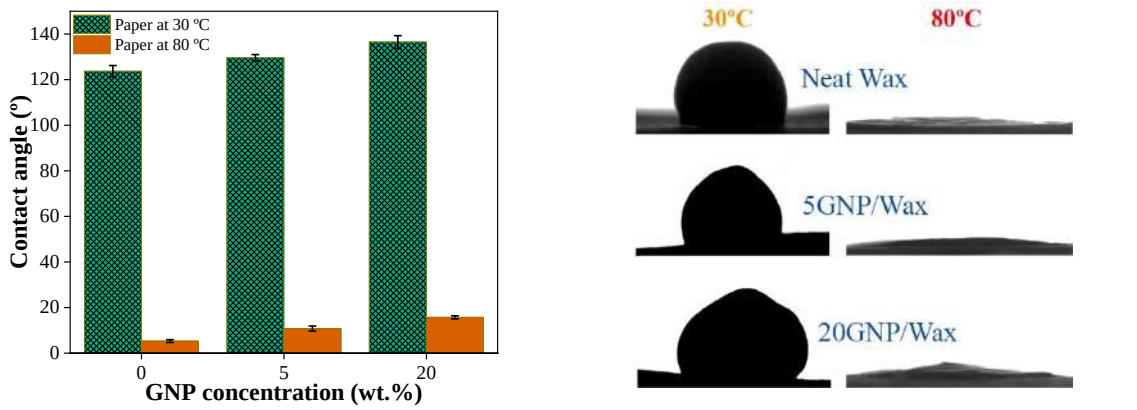

c) d)

Figure 4.2.2. a) Variation of viscosity of the inks as a function of shear rate for solutions with different melted GNP/Wax concentrations. b) Viscosity at 2 s^{-1} shear rate for solutions with different melted GNP/Wax concentrations. c) Contact angle between different melted GNP/Wax concentration drops and paper at 30 °C (left) and 80 °C (right); d) corresponding representative photograph's of the waxes in contact with paper.

The results demonstrated a typical shear thinning behaviour for the different melted waxes, independently of the filler concentration, as the viscosity decreases by increasing the shear rate. It is also verified that for higher shear rates, all waxes present similar viscosities, ensuring a printing quality of the developed GNP/Wax similar to the one of melted neat wax. Ono the other hand, the viscosities are quite different at lower shear rates, based on the different filler content and the interaction of the GNP loading with the polymer matrix. In this way, the viscosity of the different melted waxes at the shear rate of 2 s^{-1} is compared and presented in the Figure 4.2.2b. The melted neat wax presents the lowest viscosity (0.15 ± 0.05 Pa.s) and the melted wax with higher concentration of GNP (20 wt.%) the higher viscosity value (1.81 ± 0.22 Pa.s).

In order to evaluate the spreading of the produced waxes on the Whatman n°1 cellulose paper, contact angle experiments were conducted with the paper at temperatures of 30 °C and at 80 °C (Figure 4.2.2c-d). It is shown that increasing paper substrate temperature from 30 to 80 °C leads to an increase of the impregnation of all the waxes, as indicated by the variation of the contact angle from 123.7° ± 2.5° to 5.3° ± 0.6° in the case of neat wax, from 129.6° ± 1.4° to 10.8° ± 1.1° in the case of 5 wt.% GNP/Wax and from 136.5° ± 2.8° to 15.7° ± 0.7° in the case of the 20 wt.% GNP/Wax. Therefore, to ensure a high impregnation of the printed waxes on the paper substrate, they will be thermally cured at a temperature higher than 80 °C after the printing procedure.

Representative SEM images of surface and cross-section of Whatman n°1 paper substrate, printed and cured neat wax and printed and cured conductive 5 and 20 wt.% GNP/Wax on paper are presented in Figure 4.2.3. All waxes were properly cured to cross the paper substrate all the way through the opposite surface, so barriers can fully contain fluids if needed.

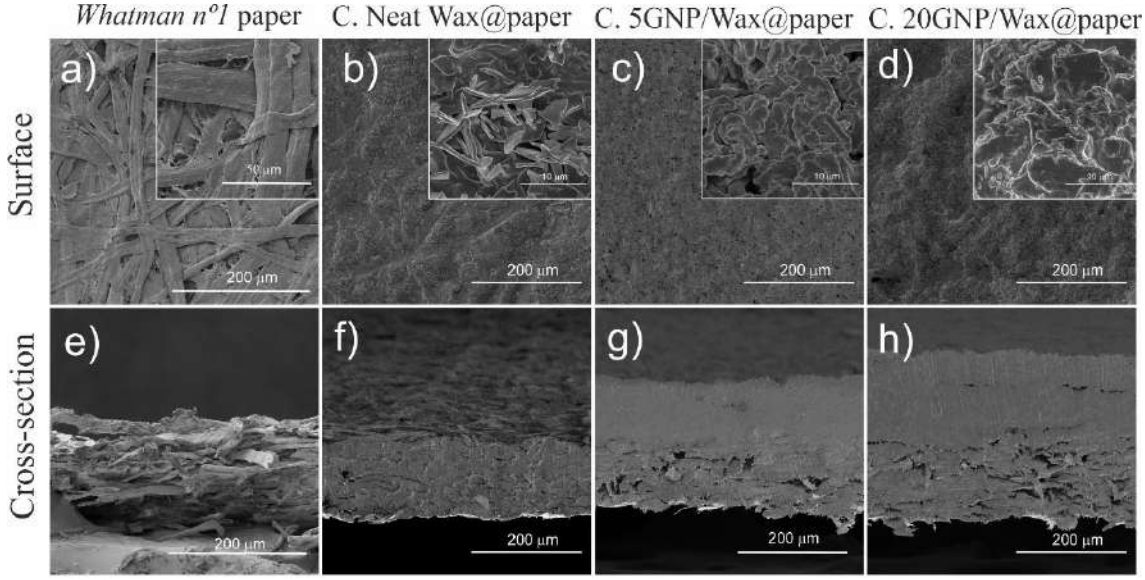

Figure 4.2.3. Representative surface SEM images of a) Whatman n°1 paper; b) printed cured neat wax on paper; c) Printed cured 5 wt.% GNP/Wax on paper; d) printed cured 20 wt.% GNP/Wax on paper. e)-h) Respective representative cross-section images.

Whatman n°1 substrates are characterized by non-oriented and flattened cellulose fibres (Figure 4.2.3a), which are associated with the fabrication process employed in the manufacture of paper, as reported in [7]. This fibrillar microstructure is evidenced in the transverse image illustrated in Figure 4.2.3e. On the other hand, a rough surface (Figure 4.2.3b) and compact transversal section (Figure 4.2.3f) is obtained after the printing and cure of neat wax on paper, demonstrating an adequate impregnation of the wax through the substrate to the opposite surface, in relation with the contact angle results (Figures 4.2.2c and d). The addition of GNP fillers to the wax has a larger morphological influence on the cross-section. In fact, while the surface remains rough and hydrophobic with the addition of GNP fillers to the wax (Figures 4.2.3c and d), the larger the concentration of fillers, the larger the thickness presented by the samples (Figures 4.2.3g and h). These results demonstrate that GNP fillers present difficulty to cross the substrate and remain mostly on the substrate surface, which may be due to the combined effect of the GNP dimensions and the fibrillar paper substrate with reduced pore size, resulting on a very compact layer of composite wax at the surface of the substrate. Nonetheless, as demonstrated in the contact angle

results (Figures 4.2.2c and d) and in the proofs of concepts discussed later (Section 3.2), the hydrophobic barriers needed to contain fluids are guaranteed.

To evaluate how the printing process and the corresponding thermal treatment (curing process) affects the mechanical properties of the printed substrates, peeling assays (Figures 4.2.4a and b) and stress-strain measurements (Figures 4.2.4c and d) in tensile mode were carried out. Uncured prints can find application when the conductive waxes, i.e. heater, do not need to cross the entire substrate and work as fluid barriers, as occurred in the second proof-of-concept. However, it can negatively affect the mechanical properties, as it will be shown in the following, so that the need for curing must be properly evaluated according to the application.

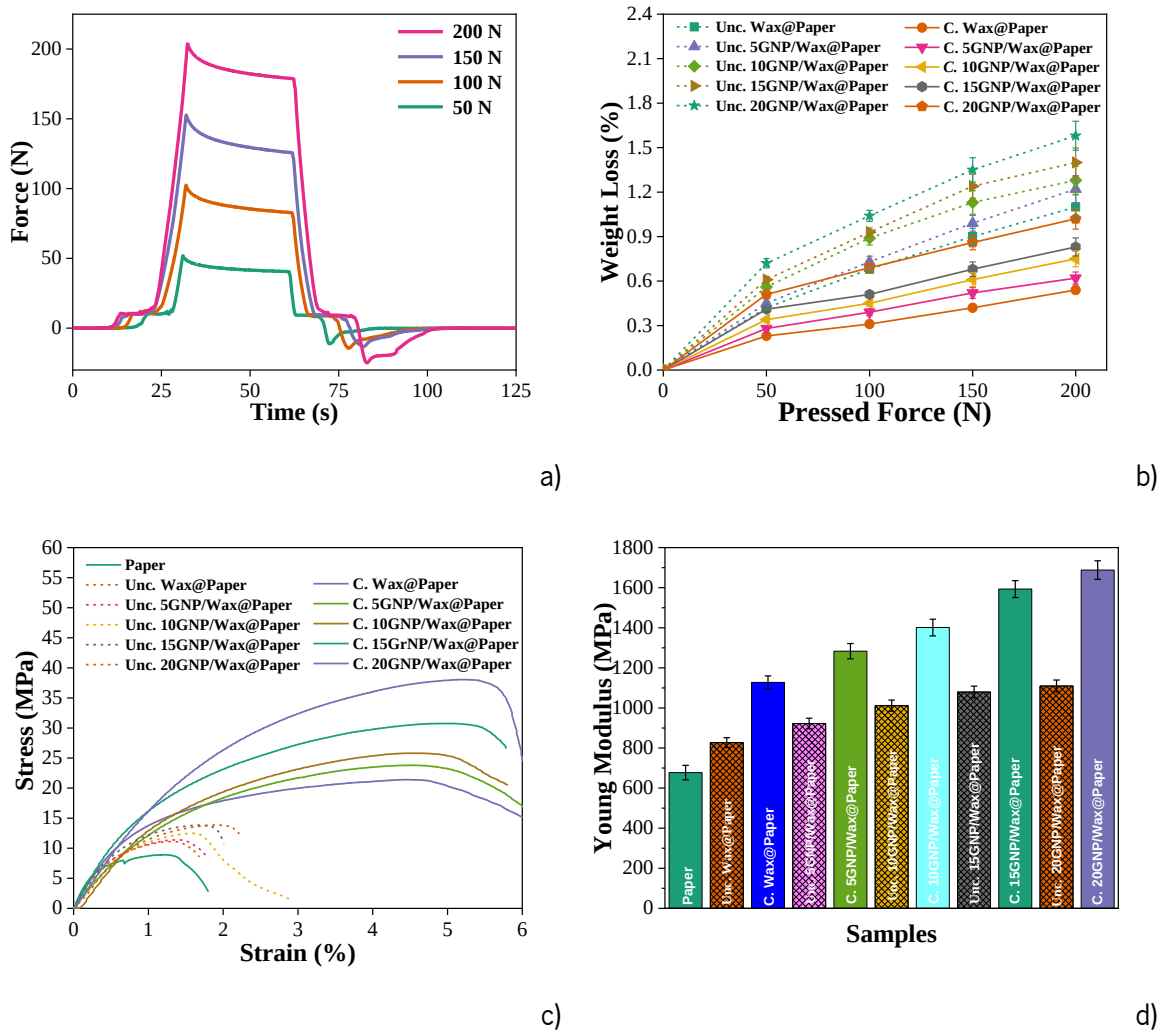

Figure 4.2.4. a) Force profile of the peeling assays for the various wax printed samples as a function of time and compression force; b) respective weight loss after the peeling assays as function of the compression force; c) stress-strain curves for the various wax printed samples obtained at room temperature; d) respective Young's modulus values obtained from a).

The force profile during the peeling assays for the printed layers (Figure 4.2.4a) shows that the lowest compression force of 50 N leads to the lowest peeling force of ≈11 N, while the highest compression force of 200 N leads to the highest peeling force of ≈25 N. Regarding Figure 4.2.4b, it is shown that increased compression forces lead to increased weight loss, regardless the sample. Moreover, the benefits of thermal treatment on the stability of the wax print is demonstrated, with less weight loss in the cured samples. A maximum of ≈1.02 % is loss for the cured 20 wt.% GNP/Wax at a compression force of 200 N (≈1.58 % for the respective uncured sample) whereas a minimum of ≈0.27 % is loss in the case of cured 5 wt.% GNP/Wax (≈0.45 % for the respective uncured), very close to the value of ≈0.23 % for the cured neat wax (≈0.44 % for the respective uncured). Although some weight loss is evidenced, which is more pronounced for high compression forces and uncured waxes, the results confirm the mechanical stability of the printed waxes, as the observed weight loss does not compromise the mechanical and functional characteristics of the samples. Further, none of the samples experienced weight loss in a second round of assays. Accordingly, the proofs of concepts will be performed using cured waxes.

The characteristic stress-strain curves of the processed samples are presented in Figure 4.2.4c. From the liner regimes of the curves, the Young's modules were obtained for each sample applying Hooke's law and the values are presented in Figure 4.2.4d. Commercial Whatman n°1 paper features almost no plastic regime, with a fracture near the end of the linear elastic region of the curve. On the other hand, all printed paper samples present both higher stress and strain at the breaking point. This increase proves to be significantly higher when the wax is thermally cured, indicating a clear improvement of the mechanical properties. Comparable improvements are detected with the increase of GNP filler concentration in the wax. The analysis of the Young's modules obtained in the linear mechanical regime, where the materials are generally used, allow to reinforce the previously mentioned conclusions. In fact, increasing GNP filler concentration in the wax leads to higher Young's modules, the increase being much more significant when the wax is cured. An increase of ≈67 % is obtained in the cured wax compared to the neat paper. Moreover, the addition 20 wt.% GNP to the wax and the curing process allow an increase of ≈49 % compared the cured neat wax and ≈148 % compared to the neat paper. Regarding the relevance of thermal curing in the mechanical properties and analysing the samples composed by 20 wt.% GNP/Wax, an increase of ≈53 % is obtained after curing. The increase of the Young's modulus can thus be explained by the impregnation of wax in the fibrillary structure of the Whatman n°1 paper in combination with the addition of GNP fillers (with a large Young's modulus of 20-60 GPa [53]) and the corresponding filler-matrix interaction.

The sheet electrical resistance of wax and the corresponding composites up to 20 wt.% are presented in Figure 4.2.5a.

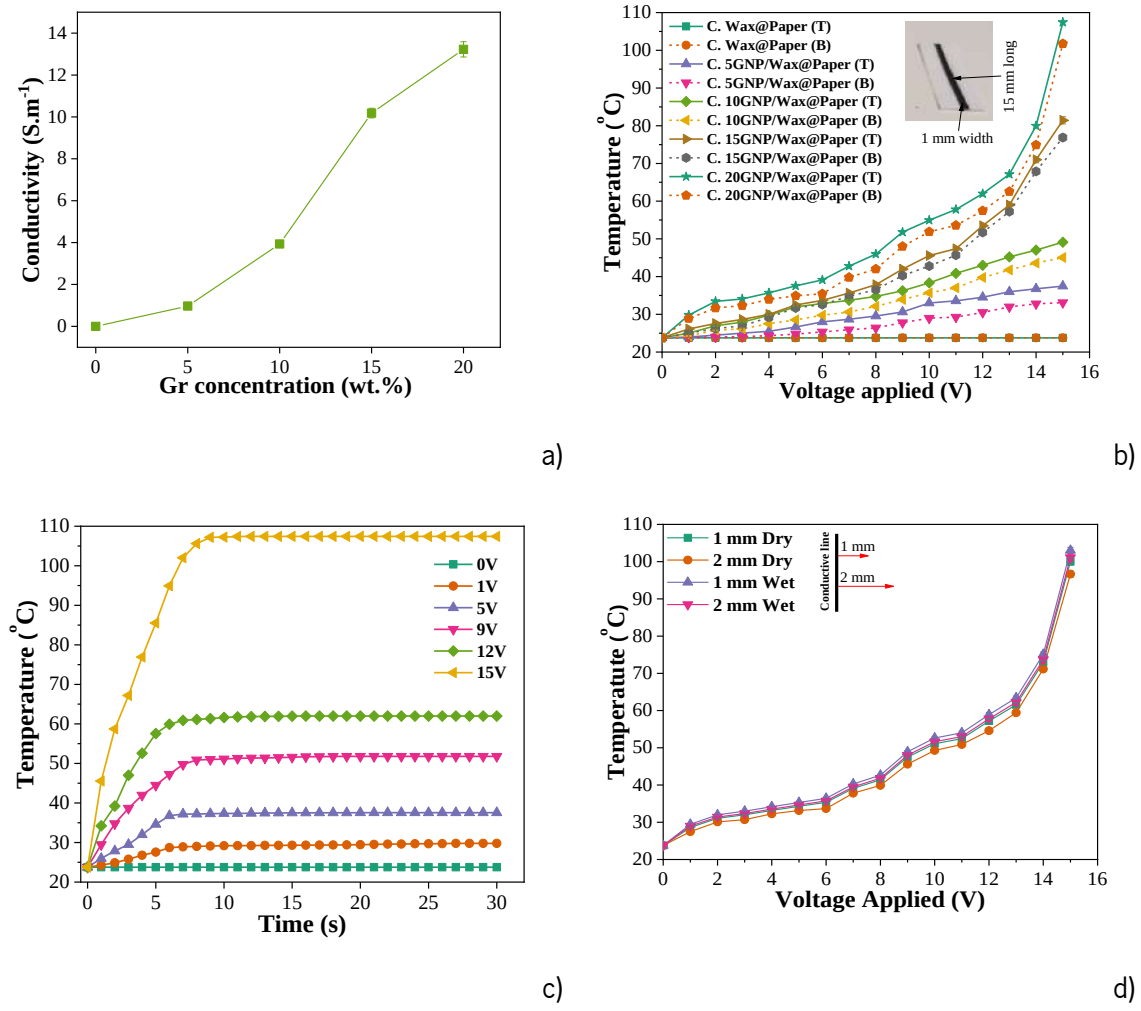

Figure 4.2.5. a) Electrical conductivity values of the various wax based printed samples as a function of GNP concentration. b) Temperature at the top (T) and bottom (B) of the different GNP/Wax lines printed and cured on Whatman n°1 paper as function of the applied voltage. c) Temperature variation as a function of time for various applied voltages measured at the top of the printed and cured 20 wt.% GNP/Wax lines. d) Temperature measured at the top of the substrate in the dry and wet state as function of the applied voltage, 1 and 2 mm away from the printed and cured 20 wt.% GNP/Wax lines.

The electrical conductivity of the neat wax is near 2.1×10^{-12} $S.m^{-1}$ increasing about 12 orders of magnitude with increasing filler content up to a value of ≈13.2 $S.m^{-1}$ for the sample with a filler content of 20 wt.%. This increase in the electrical conductivity will have a direct effect on the generated heat capacity, as described in the following.

By means of a temperature probe, thermal measurements at the top and bottom of the different GNP/Wax lines (2x10 mm) printed and cured on Whatman n°1 paper were measured as function of the electrical voltage, after 30 s (Figure 4.2.5b). As expected, no heating is generated by neat wax, regardless the measuring surface. On the other hand, in all composite waxes, the higher the applied voltage, the higher the heating generated by the conductive lines. The temperature increase shows to be higher on the upper surface of the printed line (T) compared to the inner surface of the line (B), i.e. bottom surface of the substrate, which confirms that there is a higher accumulation of GNP fillers on the surface of the print, as previously demonstrated in the contact angle measurements (Figure 4.2.2d) and SEM images (Figures 4.2.3e-h). A maximum temperature of ≈107 °C was measured at the top of the cured 20 wt.% GNP/Wax line (≈102 °C below) for an applied voltage of 15 V, while a value of ≈37 °C was obtained at the top of the cured 5 wt.% GNP/Wax line (≈32 °C below) for the same applied voltage. Higher voltages were not evaluated due to the thermal sensitivity of the Whatman N°1 substrate, which is based on cellulose. However, more thermally resistant membranes, such as PVDF and their copolymers [8,54], can be an option if higher heating is required. Applying the voltage with alkaline batteries of 1.5, 9 and 12 V, temperatures of ≈31.5, 51.6 and 62.1 °C were obtained at the top of the cured 20 wt.% GNP/Wax line, respectively. These results are interesting for applications in several fields, since it is demonstrated that it is possible to adjust and control the heating generated through the proper selection of the applied electrical signal and/or the concentration of GNP fillers in the wax.

Another interesting conclusion illustrated in Figure 4.2.5c is that the maximum temperature is achieved in a few seconds (≈9 s), remaining stable over time. Figure 4.2.5c reports on 20 wt.% GNP printed lines after curing.

Finally, temperature was measured at a fixed distance from the conducting lines, namely at 1 and 2 mm to evaluate the heat loss through the paper. These dimensions were chosen considering that in μPADs, the channels have a very small width (mm or below) in order to allow adequate passive flows without the need for external pumps or pressure. The results are shown in Figure 4.2.5d for a conducting line of cured 20 wt.% GNP/Wax. Comparing with the results presented in Figure 4.2.5b, it is concluded that there is a small heat transfer, which is more accentuated when the paper is dry when compared to the wet state. This is explained by the fact that wet paper feature a higher thermal conductivity than dry paper, receptively [55,56]. For the maximum applied voltage of 15 V, a temperature variation of ≈4 and ≈7 °C (from the initial ≈107 °C at the top of the line) occurs at a distance of 1 mm from the line in the wet and dry states, respectively. At a distance of 2 mm, the temperature variation presents values of ≈6 and ≈10 °C in the wet and dry state, respectively. Those variations have to be taken into consideration when

precise temperature control is required and μPADs design and dimensions have to be optimized to account for those temperature gradients.

4.2.3.1. Proofs of concept validation

Thermochromic inks have the ability to change colour when heated above a certain temperature. This concept was employed in μPADs devices made of Whatman n°1 paper substrates and patterned using printed and cured neat wax and 20 wt.% GNP/Wax lines (Figure 4.2.6a). In this system, red and green thermochromic inks were used, changing to more translucent (light rose) and yellow at temperatures higher than 47 °C and 28 °C, respectively (Figure 4.2.6b). Different conductive lines were activated by means of a DC power supply at 12 V (Figure 4.2.6c) and 15 V (Figure 4.2.6d).

At room temperature (≈25 °C), the thermochromic inks feature a clear green and red colour (Figure 4.2.6b). When a voltage of 12 V is applied to the three lower conductive lines, a maximum temperature of ≈64.3 °C was measured using the thermal imaging camera, near the ≈61.9 °C obtained by means of the temperature probe (Figure 4.2.5b). This result in a colour change of the inks presented in the three lower channels means that the thermochromic activation temperatures are reached. On the other hand, the upper channel features a clear colour gradient from translucent red to bright red (light rose) also indicating a temperature gradient between values above and below the activation temperature. Thus, it becomes evident that there is a reduction in temperature with increasing distance between the reaction channel and the superior conductive line, as expected and previously concluded in Figure 4.2.5d. When the voltage is increased to 14 V and applied to the four lower conductive lines, all inks undergo colour changes, with a maximum temperature of ≈83.9 °C measured with the thermal imaging camera, near the ≈80.1 °C obtained using the temperature probe, much higher than the activation temperature of both thermochromic inks.

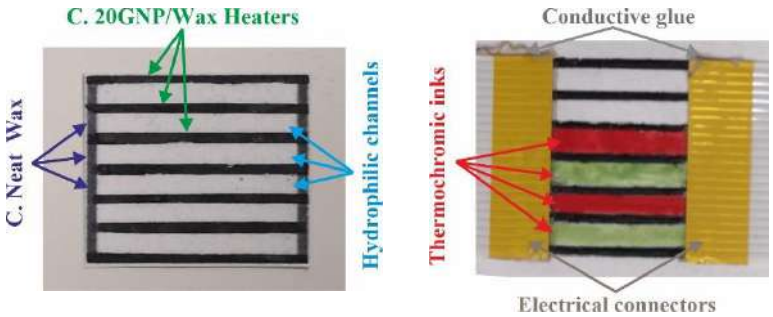

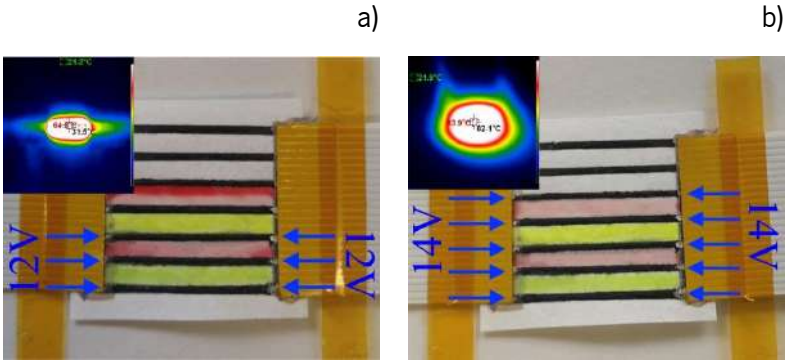

Figure 4.2.6. Photographs of a) μPADs system with individual hydrophilic channels delineated by printed and cured hydrophobic neat wax and hydrophobic conductive 20 wt.% GNP/Wax lines; b) two thermochromic inks at room temperature (red activated at > 47 °C and green activated at >28 °C); Resulting colour changes when specific conductive lines are subject to an electrical voltage of c) 12 V and d) 14V indicated by the blue arrows. Corresponding thermal images in inset.

To further strengthen the capabilities of the manufactured materials as well as their suitability for μPADs applications, a second proof-of-concept was carried out using alkaline batteries of 1.5, 9 and 12 V instead of a DC power supply. For that, a 3D printed support was manufactured to include the battery inside and protect it from possible moisture and short circuit. The disposable μPADs consist of a folded Whatman n°1 paper with a rectangular heater made of 20 wt.% GNP/Wax underneath a circular testing area delimitated by neat wax, where the thermochromic ink is placed (Figure 4.2.7a). Although there was no need for post-thermal cure of the conductive wax since in this case it works only as heater, the entire system was cured to increase the mechanical stability of the printed waxes and thus of the μPADs, as concluded in Figures 4.2.4a and b. In this case, two red thermochromic inks were used with activation temperatures at 28 °C (Figure 4.2.7b) and 47 °C (Figure 4.2.7c), respectively.

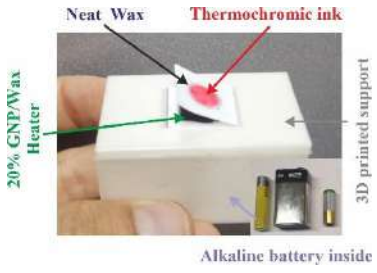

a)

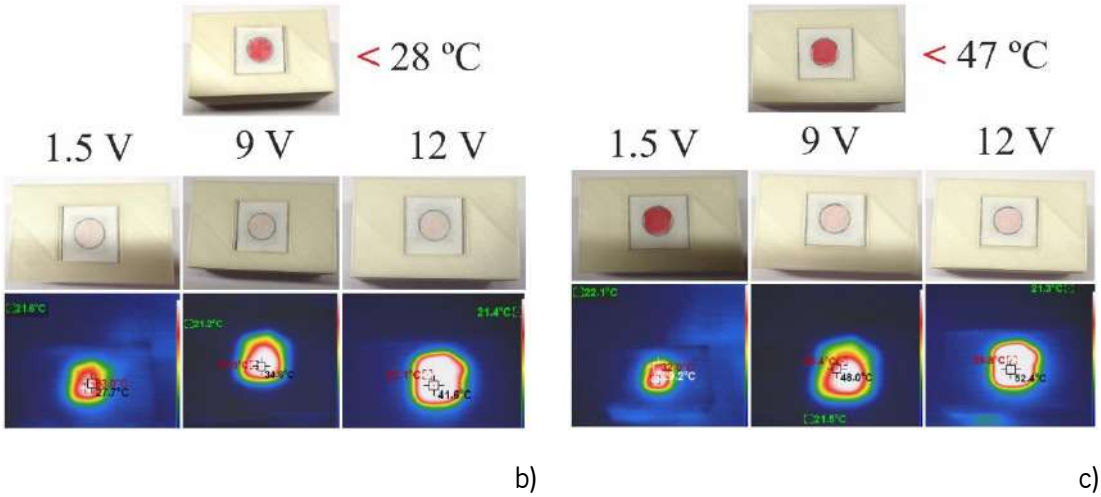

Figure 4.2.7. Photographs of a) portable printed folded Whatman n°1 paper devices, in which a 20 wt.% GNP/Wax square is connected to a battery (1.5, 9 or 12 V) placed inside the 3D printed support, in order to provide heat to the thermochromic ink contained in the circular testing area delimited by neat wax; b) thermochromic ink (activated at 28 °C) with conductive square subjected to a voltage of 1.5, 9 and 12 V and corresponding thermal images; c) thermochromic ink (activated at 47 °C) with conductive square subjected to a voltage of 1.5, 9 and 12 V and corresponding thermal images.

Regarding the results presented in Figure 4.2.7b, the ink with an activation temperature of 28 °C changes colour regardless the battery used from a bright red to a more translucent red (light rose.) At 1.5 V, 9 and 12 V applied voltages, maximum temperatures of ≈32.0, 50.5 and ≈59.8 °C are measured using the thermal imaging camera, close the values of ≈31.5, 51.6 and 62.1 °C obtained by means of the temperature probe (Figure 4.2.5b), respectively, which are higher than the activation temperature of the ink, which is in line with the obtained results. On the other hand, the heating generated by the 1.5 V battery is not enough to change the colour of the ink with an activation temperature of 47 °C, as shown in Figure 4.2.7c. The two batteries with higher potential allow to generate enough temperature variation for a colour transition, with the values previously described.

These aforementioned proofs of concept can be further tailored according to the application, e.g. by varying µPADs design, GNP/Wax concentration, or applied voltage, but nevertheless convincingly validate the concept of multifunctional conductive wax development for portable µPAD systems, allowing to work simultaneously as hydrophobic barriers and heaters, using a simple, rapid and low cost fabrication method with reproducible response.

4.2.4. Conclusions

This work reports on the development of multifunctional waxes based on the integration of conductive graphene nanoplatelets (GNP) into the wax matrix for μPAD applications. This approach allows the wax to work simultaneously as hydrophobic barriers, its commonly used property to delimit boundaries into hydrophilic paper substrates, and also as heater for temperature-sensitive applications. The process of wax patterning in paper involves a single, simple and fast printing method allowing cost-effective tailorable production. Moreover, portability is assured by the possibility of using lightweight and low-power actuation systems such as alkaline batteries. Wax prints with mechanical stability and adequate impregnation through the paper were obtained after proper post-thermal cure. Tailorable temperatures ranging from room temperature to ≈107 °C were achieved by varying GNP weight content up to 20 wt.% and applied electric potential up to 15 V. Moreover, thermochromic inks with the ability to change colour above a certain activation temperature were used in pre-designed and printed wax-based μPADs to validate heating reproducibility and low-power thermal actuation.

The proposed printable wax composites with improved functionality and performance, allied to the benefits of μPADs, provide a novel and simple solution to meet the increased requirements of complex multi-step analysis, with the ultimate goal of promoting their standardization and further commercialization.

4.2.5. References

[1] Ratajczak, K., Stobiecka, M., High-performance modified cellulose paper-based biosensors for medical diagnostics and early cancer screening: A concise review, Carbohydr. Polym. 2020; 229:115463.

[2] Xia, Y., Si, J., Li, Z., Fabrication techniques for microfluidic paper-based analytical devices and their applications for biological testing: A review, Elsevier Ltd. 2016, 774-789.

[3] Sher., M., et al., Paper-based analytical devices for clinical diagnosis: recent advances in the fabrication techniques and sensing mechanisms, Expert Rev. Mol. Diagn. 2017; 17:351–366.

[4] Noviana, E., et al., Electrochemical paper-based devices: Sensing approaches and progress toward practical applications, Lab Chip. 2020; 9:34.

[5] Martinez, A.W., et al., Patterned Paper as a Platform for Inexpensive, Low-Volume, Portable Bioassays, Angew. Chemie. 2007; 119:1340–1342.

[6] Carneiro, M.C.C.G., et al., Colorimetric Paper-Based Sensors against Cancer Biomarkers, Sensors. 2022; 22:3221.

[7] Pimentel, E.S., et al., Tailoring Electrospun Poly(l -lactic acid) Nanofibers as Substrates for Microfluidic Applications, ACS Appl. Mater. Interfaces. 2020; 12: 60–69.

[8] Brito-Pereira, R., et al., Fluorinated Polymer Membranes as Advanced Substrates for Portable Analytical Systems and Their Proof of Concept for Colorimetric Bioassays, ACS Appl. Mater. Interfaces. 2021; 13:18065–18076.

[9] Brito-Pereira, R., et al., Natural based reusable materials for microfluidic substrates: The silk road towards sustainable portable analytical systems, Appl. Mater. Today. 2022; 28: 101507.

[10] Brito-Pereira, R., et al., Biodegradable polymer-based microfluidic membranes for sustainable point-of-care devices, Chem. Eng. J. 2022; 448:137639

[11] Busin, V., et al., Opportunities and challenges for the application of microfluidic technologies in point-of-care veterinary diagnostics, Mol. Cell. Probes. 2016; 30:331–341.

[12] Papatheodorou, S.A., et al., Application of microfluidic paper-based analytical devices (μPADs) for food microbial detection , J. Sci. Food Agric. 2022; 11822.

[13] Yang, N., et al., Error analysis for pesticide detection performed on paper-based microfluidic chip devices, in: Mod. Phys. Lett. B. 2017; 31:19-21.

[14] Musile, G., et al., Paper-based microfluidic devices: On-site tools for crime scene investigation, TrAC - Trends Anal. Chem. 2021; 143: 116406.

[15] F. Sharifi, S., et al., Paper-based devices for energy applications, Renew. Sustain. Energy Rev. 2015; 52: 1453-1472

[16] Meredith, N.A., et al., Paper-based analytical devices for environmental analysis, Analyst. 2016; 141 1874–1887.

[17] Adkins, J., Boehle, K., Henry, C., Electrochemical paper-based microfluidic devices, Electrophoresis. 2015; 36 1811–1824.

[18] Fu, L.M., Wang, Y.N., Detection methods and applications of microfluidic paper-based analytical devices, TrAC - Trends Anal. Chem. 2018; 107: 116406.

[19] Smith, S., et al., The potential of paper-based diagnostics to meet the ASSURED criteria, RSC Adv. 2018; 8: 34012–34034.

[20] Lim, W.Y., Goh, B.T., Khor, S.M., Microfluidic paper-based analytical devices for potential use in quantitative and direct detection of disease biomarkers in clinical analysis, J. Chromatogr. B Anal. Technol. Biomed. Life Sci. 2017; 1060: 424-442

[21] Selvakumar, B., Kathiravan, A., Sensory materials for microfluidic paper based analytical devices - A review, Talanta. 2021; 235: 122733

[22] Lim, H., Jafry, A.T., Lee, J., Fabrication, flow control, and applications of microfluidic paper-based analytical devices, Molecules. 2019, 24: 9.

[23] Mazurkiewicz, W., et al., Paper-Based Electrochemical Sensors and How to Make Them (Work), ChemElectroChem. 7 2020, 14 2939-2956.

[24] Atabakhsh, S., Latifi Namin, Z., Jafarabadi Ashtiani, S., Paper-based resistive heater with accurate closed-loop temperature control for microfluidics paper-based analytical devices, Microsyst. Technol. 2018, 24: 3915–3924.

[25] Zhang, D., et al., Paper-Based Microfluidic Sensors for Onsite Environmental Detection: A Critical Review, Crit. Rev. Anal. Chem. 2022, 52: 1432-1449.

[26] Akyazi, T., Basabe-Desmonts, L., Benito-Lopez, F., Review on microfluidic paper-based analytical devices towards commercialisation, Anal. Chim. Acta. 2018, 1001: 1–17.

[27] Sachdeva, S., Davis, R.W., Saha, A.K., Microfluidic Point-of-Care Testing: Commercial Landscape and Future Directions, Front. Bioeng. Biotechnol. 2021, 8: 602659.

[28] Brooks, J.C., Mace, C.R., Scalable Methods for Device Patterning as an Outstanding Challenge in Translating Paper-Based Microfluidics from the Academic Benchtop to the Point-of-Care, J. Anal. Test. 2019, 3: 50–60.

[29] Jiang, X., Fan, Z.H., Fabrication and Operation of Paper-Based Analytical Devices, Annual Review of Analytical Chemistr. 2016, 9: 203-222

[30] Sriram, G., et al., Paper-based microfluidic analytical devices for colorimetric detection of toxic ions: A review, TrAC - Trends Anal. Chem. 2017, 93 212-227.

[31] Singhal, H.R., et al., One-dollar microfluidic paper-based analytical devices: Do-It-Yourself approaches, Microchem. J. 2021, 165 106126.

[32] Han, T., et al., Microfluidic Paper-based Analytical Devices in Clinical Applications, Chromatographia. 2020, 83:693–701.

[33] Altundemir, S., Uguz, A.K., Ulgen, K., A review on wax printed microfluidic paper-based devices for international health, Biomicrofluidics. 2017, 11:041501.

[34] Cardoso, V.F., et al., Polymer-based acoustic streaming for improving mixing and reaction times in microfluidic applications, RSC Adv. 2014, 4: 4292 - 4300.

[35] Chang, H.F., Chou, S.E., Cheng, J.Y., Electric-field-induced neural precursor cell differentiation in microfluidic devices, J. Vis. Exp. 2021, 170: e61917.

[36] Kojima, M., et al., Development of micro heater array system for cell manipulation, in: 2017 IEEE Int. Conf. Cyborg Bionic Syst. CBS 2017.

[37] Hong, S.H., et al., Automated optimization of double heater convective polymerase chain reaction devices based on CFD simulation database and artificial neural network model, Biomed. Microdevices. 2021, 23: 20.

[38] Lee, D.S., Choi, O.R., Choi, Y., A microheater on polyimide substrate for hand-held realtime microfluidic polymerase chain reaction amplification, Micro Nano Syst. Lett. 2019, 7: 18.

[39] Privorotskaya, N., et al., Rapid thermal lysis of cells using silicon-diamond microcantilever heaters, Lab Chip. 2010, 10: 1135-1141.

[40] Govindarajan, A. V., et al., A low cost point-of-care viscous sample preparation device for molecular diagnosis in the developing world; An example of microfluidic origami, Lab Chip. 2012, 12: 174-181.

[41] Mondal, S., Venkataraman, V., Novel fluorescence detection technique for non-contact temperature sensing in microchip PCR, J. Biochem. Biophys. Methods. 2007, 5:773-777.

[42] Chen, J., et al., Laser-Induced Graphene Paper Heaters with Multimodally Patternable Electrothermal Performance for Low-Energy Manufacturing of Composites, ACS Appl. Mater. Interfaces. 2020, 12:23284–23297.

[43] Wang, G., et al., High-Performance Flexible Heater with Command-Responding Function Attained by Direct Laser Writing on Nomex Paper, IEEE Electron Device Lett. 2022, 43: 462-465.

[44] Hagan, K.A., et al., An integrated, valveless system for microfluidic purification and reverse transcription-PCR amplification of RNA for detection of infectious agents, Lab Chip. 2011, 11: 957-961.

[45] Shaw, K.J., et al., Rapid PCR amplification using a microfluidic device with integrated microwave heating and air impingement cooling, Lab Chip. 2010, 10: 1725-1728.

[46] Ohtsu, Y., et al., Development of a novel hybrid microwave-heater reactor for paper-based waste treatment, J. Mater. Cycles Waste Manag. 2010, 12: 25–29.

[47] Jang, N.S., et al., Simple Approach to High-Performance Stretchable Heaters Based on Kirigami Patterning of Conductive Paper for Wearable Thermotherapy Applications, ACS Appl. Mater. Interfaces. 2017, 9: 19612–19621.

[48] Atabakhsh, S., Jafarabadi Ashtiani, S., Thermal actuation and confinement of water droplets on paper-based digital microfluidics devices, Microfluid. Nanofluidics. 2018, 22: 43.

[49] Danial, W.H., Abdul Majid, Z., Recent advances on the enhanced thermal conductivity of graphene nanoplatelets composites: a short review, Carbon Lett. 2022, 32: 1411–1424.

[50] Silva, M., et al., Biomedical films of graphene nanoribbons and nanoflakes with natural polymers, RSC Adv. 2017, 7: 27578-27594.

[51] Kim, H.S., et al., Thermal conductivity of polymer composites with the geometrical characteristics of graphene nanoplatelets, Sci. Rep. 2016, 6: 26825.

[52] Brito-Pereira, R., et al., Printed multifunctional magnetically activated energy harvester with sensing capabilities, Nano Energy. 2022, 94:106885.

[53] Feng, C., Wang, Y., Yang, J., Effects of reorientation of graphene platelets (gpls) on young's modulus of polymer composites under bi-axial stretching, Nanomaterials. 2018, 8: 27.

[54] Ribeiro, C., et al., Electroactive poly(vinylidene fluoride)-based structures for advanced applications, Nat. Protoc. 2018, 13: 681–704.

[55] Lavrykov, S.A., Ramarao, B. V., Thermal Properties of Copy Paper Sheets, Dry. Technol. 2012, 30: 297-311.

[56] Szodrai, F., Lakatos, Á., Effect of wetting time in the sorption and in the thermal conductivity of the most commonly used structural materials, Build. Serv. Eng. Res. Technol, 2017, 38: 4.

Chapter 5.

Conclusions and future works

5.1. Conclusions

Portable analytical devices represent a promising platform for the development of portable, disposable and low-cost analytical tools in different application areas. However, their commercialization is still limited, mainly because of their poor ability to achieve complex fluid and analyte handling tasks, and also because of their low storage stability or their limited mechanical proprieties when wet and which will strongly affect their performance.

This thesis provides solutions based on advanced materials in order to offer alternatives to the commercially passive materials used in printing technologies.

Novel microfluidic substrates with tailored morphology, surface hydrophilicity and capillary flow rate were developed as alternatives/complements for the commonly used paper substrates. Electrospun poly(l-lactic acid) based membranes, were tailored in different morphologies, which is beneficial in order to reach specific applications requirements, which can be difficult to obtain with the current commercially available paper substrates. Moreover, the developed materials are biocompatible, showing good wet strength and appropriate thermal properties to be used as substrates for the fabrication of microfluidic substrates using wax printing technology. The substrates were evaluated as a platform for colorimetric detection of glucose, showing linearity with correlation coefficients R^2 of 0.990. The suitability of plasma-treated poly(vinylidene fluoride-co-trifluorethylene) membranes for microfluidic applications was demonstrated based on their tailorable morphology, tailorable capillary flow rate (from 35.7 ± 2.5 $mm.min^{-1}$ to 88.3 $mm.min^{-1}$), high wax print quality and excellent mechanical properties (Young's modulus from 71.4 ± 2.9 to 163.4 ± 5.1 MPa in the wet state), allowing to match process requirements of specific technological applications. Following the pursuit to build biodegradable systems, poly(D,L-lactic- co-glycolide) membranes showed potential to be used as microfluidic substrates, allowing tailorable morphologies, including porous, randomly and oriented fiber-based membranes, and surface hydrophilicity modification to generate spontaneously passive flows and controllable capillary flow rates from 36.2 ± 4.2 to 84.1 ± 5.2 $mm.min^{-1}$. Moreover, the membranes show good mechanical properties even in a wet state (111.1 ± 9.9 MPa, 140.2 ± 9.3 and 189.3 ± 9.0 MPa for temperature-induced phase separation (TIPS), randomly oriented electrospun fibres (ES-RO) and oriented electrospun fibres (ES-O) and high biocompatibility. Their biodegradability is an important feature for the development of a new generation of portable analytical devices according to the circular economy paradigm, reaching degradation values of 90 % in just 6 weeks. Then, taking into account the objective of creating systems with a low environmental footprint and taking advantage of natural resources, Bombyx mori cocoons and electrospun silk fibroin were used to manufacture sustainable PADs. Bombyx mori cocoons show

superhydrophilicity, capillary flow rates of 44.8 ± 3.75 $mm.min^{-1}$, mechanical resistance, with Young's modulus values of 592.13 MPa (dry conditions) and 377.2 ± 14.39 MPa (wet conditions) and the possibility to perform different tests with the same substrate using a simple cleaning procedure, showing that reuse is possible without compromising substrate and printed microstructure and, therefore, system functionality.

Each polymer substrate that was developed, brought different characteristics and advantages in relation to paper substrates, which allows the manufacture of PADs that are more resistant, more sustainable and more efficient.

Regarding the functionalization of the hydrophobic waxes, Fe_3O_4 nanoparticles were used in order to provide the wax's magnetic properties. The Fe_3O_4 modified wax was nano-impregnated into a paper by a thermal process, leading to a magnetic paper with improved stress and strain at rupture and Young's modulus, 30 MPa, 4.5 % and 2 GPa, respectively, when compared to neat paper, 15 MPa, 3.5 % and ≈1 GPa, respectively. Furthermore, this method provides a paper with a 0.2 $emu.g^{-1}$ magnetic saturation, allowing it to work as a bending actuator with a bending of 12 mm at an applied magnetic field of 105 mT. This methodology was then utilized to employ wax printing with magnetic wax ($CoFe_2O_4$/wax) to print and functionalize a self-powered magneto-mechano-electric printed device. The printed magnetoactive device revealed the capabilities of harvesting magnetic energy with a maximum output power density of 9.7 $mW.cm^{-3}$ as well as detecting magnetic fields with a R^2 of 0.999 and a sensitivity of 30 $V.T^{-1}$. This sensing/harvesting performance offers great potential for applications in wearable electronics devices, Internet of Things-related applications and for low-cost analytical tools. Functional wax reinforced with barium titanate (BT) composites was also developed with an increase of the dielectric constant from about $\varepsilon = 9$ for the pristine wax up to $\varepsilon = 18$ for the composite with 50 wt.% BT. The moulded composite wax showed a Young modulus of ≈7.8 MPa in compression mode. Further, it supported forces up to 400 N under compression and strains up to 20 %. Mechanical hysteresis decreased drastically for the first cycles, stabilizing at 30 $kJ.m^{-3}$ in the fifth cycle. Wax and the corresponding dielectric composites were printed over a PET substrate and support bending deformation up to 4 mm of bending for 100 cycles. Fully printed systems with conductive properties can bring extremely important functionalities to many portable analytical devices applications. For this purpose, wax-based composites with different conductive fillers such as CNT or rGO were also developed. Low electrical percolation thresholds with 0.3 and 3 wt.% filler content were obtained for CNT/W and rGO/W composites, respectively, with maximum electrical conductivity of 2.5×10^{-4} $S.m^{-1}$ for both fillers. Further, good filler dispersion and mechanical properties have been obtained for all samples. The composites were evaluated as sensing materials with good

linearity between applied force and resistance variation. The piezoresistive sensibility is GF < 11 (5 mm of bending) and PS < 0.17 MPa^{-1} (50 N of pressure), being suitable for the development of sensing applications.

Finaly, the developed materials were used for integration into proof-of-concept applications. A printed magnetic origami paper as a platform for low-cost disease multi-tool detection was developed using wax-printing. A fully functional magnetic system with two Neodymium (NDFeB)/Wax magnets was fabricated for the analysis of magnetic entities. The weight content (wt.%) of the Fe_3O_4 on the analysis area was determined through energy-dispersive X-ray spectroscopy, vibrating sample magnetometry, infrared spectroscopy; and color change (grey scale) on photographs taken by mobile phones, with a linearity of 0.996, 0.998, 0.930, and 0.998, respectively. It is shown that the device is able to detect magnetic nanoparticles in mixtures with low Fe_3O_4 wt.% (3.125 $\mu g.ml^{-1}$) with the use of a small amount of testing liquid (50 µl), exhibiting a limit of detection lower than 156 µg of Fe_3O_4.

As several applications in biotechnology require temperature-sensitive reactions, a fully wax-printed heating system was developed based on multifunctional hydrophobic composites combined with conductive graphene nanoplatelets integrated into the wax matrix to allow a dual role of barrier and heater. Wax prints with notable mechanical stability and adequate impregnation through the paper were obtained after proper post-thermal cure. Also, controlled temperatures ranging from room temperature to ≈107 °C were achieved (after only 10 s) through the proper selection of the GNP concentration (up to 20 wt.%) and an applied electric field (up to 15 V).

This work successfully demonstrates that new active polymers and multifunctional hydrophobic waxes can be an alternative to current materials and solutions for the manufacture of more efficient, multifunctional and affordable portable analytical devices and microfluidic paper analytical devices.

5.2. Future work

This work demonstrated that new polymeric microfluidic substrates and new multifunctional hydrophobic waxes are promising candidates for the development of more efficient PADs and µPADs. However, it is essential to continue this line of research to better understand how the developed materials will support different applications. In particular, the following tasks are proposed as future works:

- Take advantage of the electroactive properties of the developed substrates to increase the performance of current devices;

- Develop new polymer substrates based on natural polymers, such as lignin, collagen, chitosan or new types of cellulose, which can bring new solutions and turn PADs and μPADs more compatible with the 2030 agenda in terms of the circular economy;

- Develop wax-based hydrophobic inks with embedded semiconductor particles, which can increase the variety of applications available in the current devices, towards functional printed electronic systems;

- Replace synthetic-based waxes such as the Xerox commercial wax, with natural-based waxes i.e. beeswax, carnauba wax or myrica wax, with different melting temperatures;

- Combine the tailored polymeric substrates and the new multifunctional waxes to take full advantage of the unique characteristics provided by the use of active components both in the support material and in the printing material. These PADs can combine colorimetry with an electrochemical response.